Electronic Excitations in Solids Studied with Static and Time Resolved X-ray Spectroscopy.

Dissertation zur Erlangung des Doktorgrades an der Fakultät für Mathematik, Informatik und Naturwissenschaften Fachbereich Physik der Universität Hamburg

vorgelegt von

Florian Hieke

Hamburg, 2017

Gutachter der Dissertation:	Prof. Dr. Wilfried Wurth
	Prof. Dr. Adrian Cavalieri
Gutachter der Disputation:	Prof. Dr. Daniela Pfannkuche
	PD Dr. Tim Laarmann
	JProf. Dr. Thorsten Uphues
Datum der Disputation:	3. Februar 2017
Datum der Veröffentlichung:	April 2017
Vorsitzender des Prüfungsausschusses:	Prof. Dr. Daniela Pfannkuche
Vorsitzender des Promotionsausschusses Physik:	Prof. Dr. Wolfgang Hansen
Dekan der Fakultät:	Prof. Dr. Heinrich Graener

Abstract

Spectroscopy with x-rays allows to determine the electronic structure of condensed matter, and thereby the electronic contribution to physical properties of solids. Within this thesis time resolved and static x-ray spectroscopic methods are applied in different experiments.

The fast thermalization of photo excited electrons in a gallium arsenide semiconductor (GaAs) after absorption of a short x-ray pulse is investigated. Therefore short pulses of x-rays from the Free Electron Laser (FEL) FLASH are applied in a jitter free, x-ray pump x-ray probe time resolved Photoemission experiment (TR-PES) on GaAs samples. Delay and pump-fluence dependent effects, caused by pump pulse induced vacuum spacecharge in the TR-PES experiment, are modeled with numerical simulations and the results of the simulations are used to correct the experimentally obtained data. A transient rise of the local potentials at the gallium sites is found, which is characterized by a fast rising and 500 fs lasting increase of the Ga3d core level binding energy.

The second focus of this work lies in the investigation of the metal-to-insulator phase transition (Verwey transition) in the iron oxide magnetite (Fe_3O_4). With resonant inelastic x-ray scattering (RIXS) at the iron $M_{2,3}$-absorption edge of magnetite at different temperatures, a signature of the Verwey transition in magnetite is found and experimentally characterized. A qualitative comparison of the obtained excitation spectra, with the calculated x-ray absorption spectrum suggests, that the measured excitation spectra are in agreement with the proposed existence of three iron sites spanning orbital molecules (trimerons) in magnetite. Towards time resolved RIXS investigations (TR-RIXS) of the Verwey transition in magnetite at a seeded FEL, an experimental endstation was brought to operation. Excitation spectra of an easy-to-prepare $KCoF_3$ sample were recorded in a first RIXS experiment at the seeded FEL FERMI.

Kurzzusammenfassung

Elektronische Anregungen in Festkörpern untersucht mit statischer und Zeit-aufgelöster Röntgenspektroskopie.

Spektroskopie mit Röntgenstrahlung ermöglicht die Bestimmung der elektronischen Struktur von Festkörpern und dadurch den elektronischen Beitrag zu physikalischen Eigenschaften der selben. Im Rahmen dieser Arbeit werden verschiedene Experimente vorgestellt in denen unterschiedliche Zeit-aufgelöste und statische Röntgenspektroskopie Methoden verwendet werden.

Die schnelle Thermalisierung von angeregten Elektronen im Halbleiter Gallium Arsenid (GaAs) nach Absorption eines kurzen Röntgenpulses wird untersucht. Hierfür werden die kurzen Röntgenpulse des Freie Elektronen Lasers (FEL) FLASH verwendet, um ein perfekt synchronisiertes, Röntgenstrahlungs-Anregung Röntgenstrahlungs-Abfrage Zeit aufgelöstes Photoelektronenspektroskopie Experiment (TR-PES) an GaAs Proben durchzuführen. Zeit- und Anregungs-Intensitätsabhängige Effekte, verursacht durch die von den Anregungspulsen induzierte Vakuumraumladung im TR-PES Experiment, werden mit numerischen Simulationen vorherbestimmt und mit den Ergbenissen der Simulationen die experimentel bestimmten Daten korrigiert. Ein vorrübergehende Änderung der elektrischen Potenziale innerhalb der erstenn 500 fs nach Anregung wird bestimmt und charakterisiert durch Veränderungen in der Bindungsenergie der Gallium 3d Rumpf-Elektronen Niveaus.

Der zweite Schwerpunkt dieser Arbeit liegt auf der Untersuchung des Metal-Isolator Phasenüberganges (Verwey-Übergang) im Eisenoxid Magnetit (Fe_3O_4). Mit resonanter inelastischer Röntgenstreuung (RIXS) an der Eisen $M_{2,3}$ Absorptionskante von Magnetit bei unterschiedlichen Temperaturen, wird eine Signatur des Verwey-Übergangs bestimmt und experimentell charakterisiert. Ein qualitiativer Vergleich der experimentel bestimmten Anregungsspektren mit dem berechneten Röntgenabsorptionsspektrum zeigt, dass die gemessenen Spektren verträglich mit der Existenz von den vorgeschlagenen, aus drei Eisen Ionen bestehenden Orbital-Molekülen (orbital molecules) in Magnetit (trimerons) sind. Mit dem Ziel Zeit-aufgelöster RIXS Experimente (TR-RIXS) am Verwey-Übergang in Magnetit an einem extern induzierten ("seeded") Freie Elektronen Laser, wurde ein neues Experiment aufgebaut. Das Anregungsspektum einer einfach zu präparierenden $KCoF_3$ Probe wurde in einem ersten RIXS Experiment am FEL FERMI bestimmt.

Contents

Preface

The physics of the solid state has an essential contribution to our daily live, as we are surrounded and formed of condensed matter. When atoms get close, it is energetically favorable to share the valence electrons and form solids. Upon this formation of stiff lattices and macroscopic crystals, properties arise which are more than the sum of properties of the individual atoms. These collective properties of nuclei and electrons in the solid, makes the field of solid state research very broad and interesting.

Many properties of condensed matter can be attributed to the electronic subsystem. Color, which is determined by excitations of electrons from occupied to unoccupied electronic levels, and electrical conductivity, influenced by the filling of these levels, are only two examples[1][2]. While lot's of effects are well understood and can be modeled by theoretical calculations, the variety of observed phenomena which lack a conclusive explanation is big as well. Two examples having special attention in the last years are the high temperature super conductivity in some transition metal oxides[3] or catalytical processes on metallic surfaces[4]. Beside these examples, it lies in the nature of science to always find unresolved questions. With x-ray spectroscopy it is possible, to search for answers in the electronic structure. Research with static x-ray spectroscopy experiments helped to form our todays knowledge on solids[5]. A variety of x-ray based methods can provide information about the occupied electronic levels (e.g. photoemission spectroscopy[6]) or possible excitations pathways of the bound electrons (e.g. inelastic x-ray scattering[7]). Technological advances in the field of short pulsed x-ray sources allow to investigate electronic excitations on time scales at which electronic motion happens in the atto- and femtoseconds. By applying pump probe schemes, it is possible to investigate the real time evolution of electronic structure and monitor e.g. charge transfer from surfaces to molecules or the photoelectric effect[8][9][10][11].

Within this thesis, two contributions to the understanding of solid state effects utilizing x-ray spectroscopic methods are summarized. In Part I, a time resolved Photoemission experiment at a photo excited semiconductor unravels a signature of electron thermalization using the higher harmonics in the x-ray spectrum of a Free Electron Laser. The second Part II summarizes static Resonant inelastic x-ray scattering studies on magnetite and proof-of-principle experiments towards time resolved studies at a seeded Free Electron Laser on this system. Each of the two parts is introduced separately and contains a review of methods and background information. In between, a short comment on the link between the two parts is given. At the end of this thesis a short conclusion summarizes the thesis and highlights perspectives for future research.

Part I.

Nonequilibrium Electron Dynamics - Electron Thermalization in Gallium Arsenide after X-ray Excitation.

1. Introduction

Dynamical effects and excitations play an important role in nature and applied technologies. Many fundamental aspects of our world, such as chemical processes and any kind of transport rely on dynamical reaction chains. For example the switching of a CMOS transistor is the controlled transport of electrons to different regions within a nano-scale heterostructure. In future data storage devices and logical processors, the dynamical aspects of such transport processes step in the foreground and will limit the size reductions[12]. The time-scale at which relevant electronic processes occur and excitations have to be steered, approaches hereby the regime of pico- and femtoseconds. Using short pulses of light to control and initiate electronic excitations is due to the short pulses available in modern laser sources, a promising pathway to go beyond the limits of nowadays technology for steering electronic transport and switching[13][14]. Apart from technological interests, the appearance of light induced phases in solid state systems[15] underlines the relevance of studies of dynamical processes also for fundamental research. An example for such a light induced state, is the change in optical reflectivity of semiconductors after absorption of short pulses of x-ray light[16]. This light induced change in reflectivity is applied in cross correlation devices at Free Electron Lasers for timing diagnostics in pump-probe experiments with pulses of few tens of femtoseconds duration, because the transition is very fast. While the technique is applied routinely, a full microscopic picture of the ongoing processes in the sample leading to energy dissipation in the semiconductor, is still missing.

In the above examples for light induced processes, the underlying very fast interaction of light with condensed matter starts with the absorption of the light field energy by the electrons. The dissipation of this energy from the photo excited electronic system throughout its environment is what essentially describes the subsequent dynamics of the light-matter interaction. While the initial energy absorption occurs within the duration of the light pulse, which can be as short as attoseconds[8], the energy dissipation will last easily several nanoseconds[17]. One of the first steps along the energy dissipation, is the thermalization of the photo excited electrons into a high-temperature equilibrium state. It is dominated by electron-cascades and electron-electron scattering events[18]. Little experimental observations exist about the microscopic processes that take place during this thermalization process within first few picoseconds after absorption.

With time-resolved Photoemission experiments (TR-PES) it is possible to probe the electronic configuration at specific sites of the object under study. By using the short x-ray pulses of Free Electron Lasers, it is possible to achieve time resolution below 100 fs allowing research on the timescales of the afore mentioned thermalization processes. Hereby only Free Electron Laser sources can pro-

vide high enough frequency for simultaneous probing and excitation with high energy photons in the extreme ultraviolet regime[19]. The choice of XUV light as the initial pump frequency is close to the application case of the mentioned cross correlation devices and is a good choice also because only excitation with high photon energy pulses guarantees highly non-thermal distributions in the electronic system. With TR-PES at a Free Electron Laser, it is possible to investigate transient changes of the electronic potentials at specific ionic sites during the thermalization process of the highly non-thermally photoexcited electrons.

In this part of my thesis, a contribution to the understanding of the dynamical footprint of the electron thermalization process on the electronic potentials in the prototype semiconductor Gallium arsenide after absorption of a short pulse of extreme ultraviolet radiation from the Free Electron Laser source FLASH is summarized. With TR-PES the transient variations of the electronic potentials at the Gallium sites during the first 1.5 ps after excitation with a short XUV pulse are investigated.

The TR-PES experiments are performed by making use of the split and delay unit provided at the PG2 beamline of the Free Electron Laser FLASH at DESY in Hamburg. For being able to pump and probe with the XUV radiation of the Free Electron Laser (FEL) we make use of the first (pump, $h\nu_{\mathrm{pump}} = 40\,\mathrm{eV}$) and third harmonic (probe, $h\nu_{\mathrm{probe}} = 120\,\mathrm{eV}$) in the photon energy spectrum of the FEL. In the first two chapters 2 and 3 of this part, the relevant knowledge on the experimental technique and setup and the state of research upon the dynamics in Gallium arsenide after XUV excitation are reviewed. After that, in chapter 4 numerical simulations are performed and summarized to investigate the role of pump beam induced spacecharge in a TR-PES experiment. At the end of this part in chapter 5 the final results of the TR-PES experiment at different pump fluences are summarized and discussed.

2. Literature Review

For studying the electronic excitations in solids, photoemission spectroscopy is an excellent choice. By making use of the photoelectric effect it allows to measure the occupied electronic density of states. The latter one is depending on the exact atomic number and chemical environment allowing site specific measurements. Used in combination with short pulsed x-ray sources it allows to resolve processes which occur as fast as the pulse length of the light source. To gain insights into the electron dynamics in Gallium arsenide after being excited with a short XUV pulse we performed time resolved Photoemission Experiment (TR-PES) at the Free Electron Laser FLASH. The Free Electron Laser FLASH pulse lengths lies during our experiments $\tau_{\mathrm{FEL}} = (170 \pm 100)$ fs and therefore allows to resolve electronic excitations in the time domain. To realize this pump probe experiment we used the wavefront cutting "split and delay unit" (SDU) at the PG2-beamline at the Free Electron Laser FLASH in Hamburg. The sample is excited with the first harmonic of the FEL and probed by photoemission with the third harmonic. In the following chapter I summarize general aspects of the TR-PES technique. As a second focus of this chapter I present a review of the state of theoretical and experimental research on the dynamical response of Gallium arsenide after short pulsed excitation.

2.1. The Time Resolved Photoemission Technique

The time resolved Photoemission spectroscopy technique (TR-PES) is the extension of the very well established Photoemission spectroscopy (PES) into the time domain. In the following section I will briefly point out the general strength of PES. After that, I introduce the concept of the TR-PES approach and discuss vacuum spacecharge effects, which are a particular experimental aspect of the TR-PES experiment arising from the use of ultrashort pulses as photon source.

2.1.1. Photoemission Spectroscopy (PES)

Photoemission or Photoelectron spectroscopy (PES) is a well established technique for studying the chemical and electronics state of materials[20][21][22]. It is based on the photoelectric effect which relates the kinetic energy of photoelectrons with the binding energy in the material[23]:

$$E_{\mathrm{kin}} = h\nu - E_{\mathrm{binding}} - \phi_{\mathrm{W}}. \tag{2.1}$$

Here $h\nu$ is the photon energy of the incident light, $E_{\mathrm{kin/Binding}}$ the kinetic/binding energy of the electrons in vacuum/the material[1] and ϕ_{W} the work function of the material. As the binding energy of electrons in atoms depends on both, the local structure (e.g. number of nuclei, charge state) as well as the environment (e.g. nearest neighbors, long-range order environment) it's study with PES allows insights onto the state of matter[24]. Many textbooks (e.g. by Stefan Hüfner[20]) and review articles (e.g. by Charles Fadley [6]) are available, that summarize the contribution of PES to the picture of matter we are having today.

Temporal Picture - The three step model

To understand the limitations of time resolved Photoemission in terms of time resolution, the natural time scales of the technique have to be kept in mind. In fact, the process of Photoemission is a dynamic phenomenon and can be described with four successive steps[20]:

1. photo excitation of the photoelectron
2. travel to the surface
3. escape to vacuum
4. (travel to the analyzer)

The steps 1-3 are the so called "three step model of Photoemission". It is an obvious simplification of a theoretically far more complex phenomenon which in principle requires quantum mechanical descriptions to be taken into account[25]. Nevertheless the simplified perspective proposed with the three step model can be used to describe the process and the related time scales: Step 1, describing the initial scattering of photon and atom is described by the Wigner time which lies in the order of Attoseconds[26][27]. The combined duration of all three steps could be revealed in streaking experiments to last $\leq 100\,\mathrm{as}$[8][28][29]. The excact duration of the emission process depends on the kinetic energy of the photoelectrons, but the timescale of few 100 as for the combined steps 1 to 3 is a good assumption for all kinetic energies.

In contrast to that, the duration of step 4 solely depends on the kinetic energy of the photoelectrons and lies in the nanoseconds time domain. In our case (1.6m long time of flight spectrometer) an electron with $E_{\mathrm{kin}} = 100\,\mathrm{eV}$ [10 eV] will travel 268 ns [853 ns][2] to reach the detector.

2.1.2. Extension Into The Time Domain - Time Resolved PES (TR-PES)

Pump-probe experiments, possible with short pulses of light, allow to study the dynamical response of a system and the real time observation of processes, which are too fast to be captured "live". The basic idea is to excite the system under study very fast, e.g. with an ultrashort pulse of

[1] The binding energy in a solid is referenced to the Fermi energy.

[2] The time t needed for an electron with mass m_{e} and kinetic energy E_{kin} to travel the distance s is $t = \sqrt{m_{\mathrm{e}}/(2 \cdot E_{\mathrm{kin}})} \cdot s$.

light, followed by a delayed and very fast taken snapshot of the system. A variation of the delay and subsequent analysis of the recorded data gives the temporal evolution of the system under study after being excited. The time resolution of the experiment depends on the duration of both, excitation and snapshot-taking. Since pulsed light sources with photon energies suitable for PES are available, such pump-probe experiments on solids are done with PES as probe-technique and e.g. IR-lasers as pump[30].

The inclusion of the time domain into the PES opened the field of time resolved PES (TR-PES). At early times, due to the lack of pulsed x-ray sources, by using two-Photon Photoemission (2PPE) or HHG-based UV-PES. The contributions within these field are reviewed e.g. in [31][32] or [33]. While laser based techniques as 2PPE and HHG-based UV-PES are limited to valence states and weakly bound core states, the developments of XUV/x-ray Free Electron Lasers allowed a variety of studies on the sub-ps dynamics of deeply bound core-level electrons of metals, correlated systems and surface-adsorbate systems after excitation by IR-laser pulses[34][10][35][36]. Another approach to probe dynamical effects with photoemission are streaking experiments. The streaking technique is a pump probe technique which makes use of the time dependence of the electrical field strength at carrier envelope phase (CEP) stabilized laser pulses. With streaking techniques applied to gas-phase samples and solids, time resolutions below several 100 as (10^{-18} s) are achieved[8][28][37][38]. The streaking technique can not be applied to study pump induced effects. Instead it allows to study natural time scales of processes as e.g. the travel time of electrons through monolayers of magnesium[11].

Compared to PES using continuous light sources, additional experimental complications arise in TR-PES from the usage of pulsed light sources. The high peak intensity leads to high Photoelectron densities in front of the sample appearing within a very short duration of time. These high charge densities, often termed as vacuum spacecharge, influence the energy distribution under studies. In the next section I comment on the influence of these vacuum spacecharge effects.

2.1.3. Vacuum Space Charge at PES from Pulsed Light Sources

General Influence of Electromagnetic Fields in PES

Due to their electrical charge, electrons will experience Lorentz forces induced by electrical and magnetic fields between sample and analyzer:

$$\vec{F} = \vec{F_{\mathrm{E}}} + \vec{F_{\mathrm{B}}} = q\vec{E} + q\vec{v} \times \vec{B}. \tag{2.2}$$

Here $\vec{E}$ denotes the electrical field, $\vec{B}$ the magnetic field strength, $\vec{v}$ the velocity and q the charge of the electron. These force will alter the kinetic energy E_{kin}. An unwanted error in the PES technique. To reduce the measurement error, external fields are minimized in the experimental setup. The earth magnetic field is screened with a Mu-Metal shield surrounding the inner part of the vacuum vessel (see section 3.3). Beside external fields, the PES processes is accompanied by electrical fields which can not be screened. Namely these are Vacuum space charge fields. The

influence of these spacecharge fields onto the detected kinetic energies is discussed in the following section.

Fields Induced by the Photoelectrons

Photoabsorption and subsequent electron emission liberates Photoelectrons from the sample. The spatial arrangement of these Photoelectrons can be described as a charge density in front of the sample ϱ^{PES} which leads to an electric field in the vacuum:

$$\vec{E}_{\mathrm{spacecharge}}(\varrho^{\mathrm{PES}}) = \frac{1}{4\pi\varepsilon_0\varepsilon_r}\int \varrho^{\mathrm{PES}}(\vec{r'})\frac{\vec{r}-\vec{r'}}{|\vec{r}-\vec{r'}|^3}dx'dy'dz'. \tag{2.3}$$

It is $\varepsilon_0/\varepsilon_r$ the vacuum/relative permittivity, $\varrho(\vec{r})$ the charge density at position $\vec{r}$ and x, y, z the three spatial dimensions.

The influence of these spacecharge fields onto the measured kinetic energy distribution of detected electrons is usually separated into two components:

- Shift of the measured kinetic energy with respect to the expected: $\Delta E_{\mathrm{kin}}^{\mathrm{spacecharge}}$
- Linewidth broadening $\Delta\Gamma^{\mathrm{spacecharge}}$.

The detected lines will be found with final kinetic energy $E_{\mathrm{kin}}^{\mathrm{detected}}$ and linewidth $\Gamma_{\mathrm{FWHM}}^{\mathrm{detected}}$:

$$E_{\mathrm{kin}}^{\mathrm{detected}} = E_{\mathrm{kin}}^{\mathrm{initial}} + \Delta E_{\mathrm{kin}}^{\mathrm{spacecharge}} \tag{2.4}$$

$$\Gamma_{\mathrm{FWHM}}^{\mathrm{detected}} = \sqrt{\left(\Gamma_{\mathrm{FWHM}}^{\mathrm{initial}}\right)^2 + \left(\Delta\Gamma_{\mathrm{FWHM}}^{\mathrm{spacecharge}}\right)^2} \tag{2.5}$$

Here $E_{\mathrm{kin}}^{\mathrm{initial}}$ describes the kinetic energy which is expected from the standard equation of PES in case of PES without influence of spacecharge fields (eq. 2.1). The linewidth of the analyzed state expected without spacecharge contributions is described with $\Gamma_{\mathrm{FWHM}}^{\mathrm{initial}}$.

Probe Spacecharge

Many experimental studies are published concerning vacuum spacecharge effects in PES from pulsed light sources. Examples can be found for PES using Laser systems[39][40][41][42][43], Synchrotrons[44], HHG Laser Systems[45][46] and Free Electron Lasers [34][47][48][35].

In [49] Hellmann et al. present an analysis of experimental data from FEL and laser based PES experiments combined with numerical simulations of the spacecharge effects. As a result they find a power-law dependency of the measured probe-spacecharge energy shifts and broadening on the ratio of totally emitted number of electrons N_C ("cloud electrons") to beam diameter d_0 (see figure 2.1). The same results were found by Verna et al. in [50].

It has to be kept in mind, that most of the electrons in the PES experiments are contained in the low energy secondary electron tail[51]. The contribution of these low energy electrons plays the key role for both, broadening and shift of the detected Photoelectrons[49][50][52].

In addition to that Schönhense et al. differentiate in [52] between a deterministic spacecharge influence and an increase of the phase-space volume leading to an stochastic spacecharge contribution. The kinetic energy shift is assigned a deterministic behavior and the broadening a stochastic one.

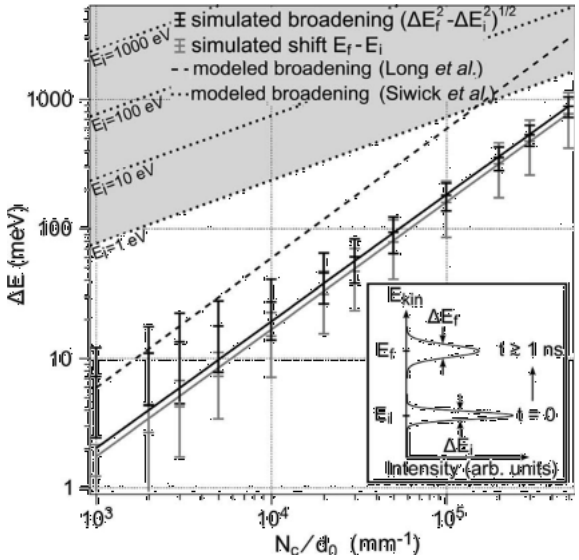

Figure 2.1.: Figure from Hellmann et al. [49]/url. The spacecharge induced shift (gray data points) and broadening (black data points) extracted from simulations with varied number of electrons is plotted as a function of the linear electron density N_C/d_0. Additionally two different theoretical models are included with dashed and dotted lines (see legend and original paper descriptions for more details). It was found, that the predictions made by the models overestimate the simulated broadening. A linear fit (lines through the marks) of the simulated data points results in a power-law dependency of both, shift and broadening: $\Delta E_{\text{shift}} \propto \left(\frac{N_C}{d_0}\right)^{0.98}$ and $\Delta E_{\text{broad}} \propto \left(\frac{N_C}{d_0}\right)^{0.98}$.

Pump Spacecharge

In a TR-PES pump-probe measurement not only one, but two light pulses will hit the sample. Photoelectrons will be emitted due to Photoemission of both. Either due to direct[23] or through multi-photon absorption[45]. The additional spacecharge density ϱ_{pump} will influence the Photoelectrons under study. IR pump TR-PES experiments with a detailed analysis of the IR induced spacecharge effects are presented in [53][54][36][35].

Oloff et al. show in [53] that a mean field approach can reproduce the experimentally observed spacecharge shifts and their dependence on the pump-probe delay in an IR pump TR-PES experiment performed at an HHG Laser setup (see figure 2.2). The observed spacecharge induced shifts and broadenings depend on the pump beam intensity which is proportional to the amount of pump photoelectrons. Also their spectral and spatial distribution plays a role. Additionally to that, it depends on the time delay between pump- and probe x-ray pulse.

The observed shift of the delay trace in figure 2.2 is not symmetric for positive and negative delays and biggest at the temporal overlap of pump and probe beam (see also [35]). For negative-delay sides of the delay traces a linear relation between the pump beam spot diameter and the exponential grow rates was found. The positive-delay rates instead could not be linked to the spot diameter. With the model of Oloff et al. it was not possible to predict the broadening of the spectrum.

To make predictions concerning both, the pump spacecharge induced broadening and the delay-dependence as e.g. in [35], one can make use of numerical integration codes which solve the integrals of equation 2.3 numerical for all relevant positions $\vec{r}$ and pump-probe time delays Δt.

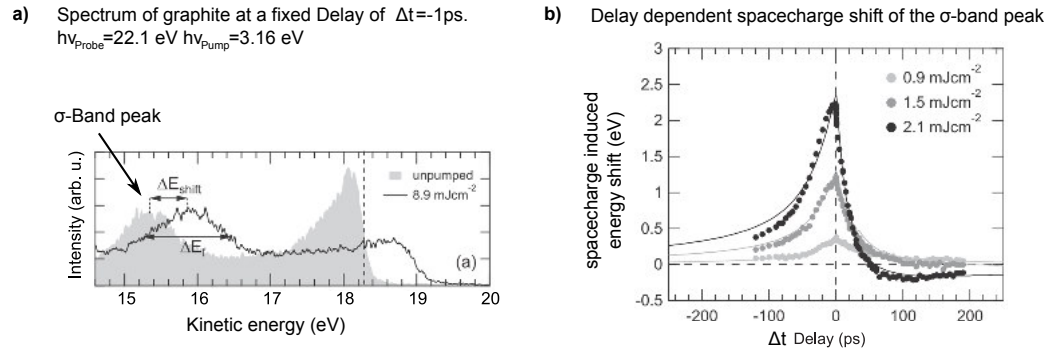

Figure 2.2.: Reprinted from Oloff et al. [53]. a) Valence band spectrum of the highly oriented pyrolytic graphite sample (HOPG) without (black) and with UV pump pulse on the sample (gray filled). Due to the spacecharge of the pump pulse the spectrum gets shift. b) Spacecharge induced shift of the σ-band peak of HOPG for different delays of the HHG probe- to the UV pump pulse for different laser fluences. Mean field based calculations of the spacecharge effects with a simplified model are presented with solid lines. Both, calculation and experimental data show a delay dependence of the spacecharge shift which is asymmetric around time zero.

Mirrorcharge Effects

The potential resulting from the Photoelectrons in the vacuum will, in case of a metallic sample, cause the appearance of a mirror-charge/image-charge on the sample surface. This mirror-charge will partly compensate the shifts and broadenings compared to the case without mirrorcharge. This was in detail shown by Zhou et al. in [44]. In case of Photoemission from a semiconductor the mirrorcharge effects are less pronounced. Therefore a general increase of the spacecharge shifts for PES from semiconductors is expected compared to that from metallic samples.

Implications for TR-PES experiments

The influence of spacecharge effects onto the achievable energy resolution has to be taken into account when planing and performing a photoemission experiment with pulsed light sources. Concerning probe spacecharge the experimentalist has to search for compromise between probe fluencies

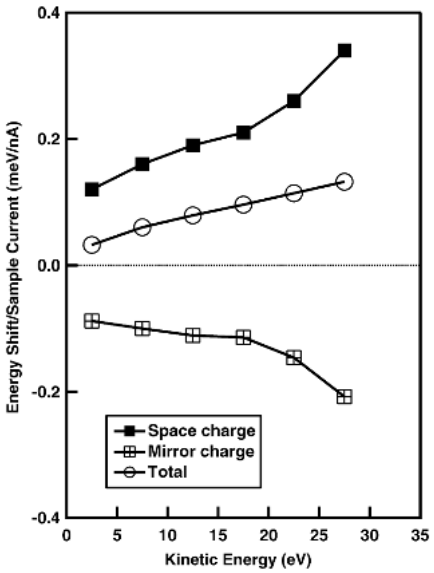

Figure 2.3.: Reprinted from Zhou et al. [44]. The simulated energy shift (normalized to the sample current) of a test distribution with different initial kinetic energies is shown with open circles. The effect of mirror-charges at the sample surface were included in the simulations. The contributions of space-/mirror-charge fields to the shift are shown with black solid/open squares.

as low as the required energy resolution demands, but still high enough to allow acquisition within a reasonable amount of time. An ideal source for time resolved photoemission experiments are therefore high repetition rate light sources.

In difference to the probe spacecharge, the pump beam intensity is given on the physical effects under study. Typically it is not possible to tune it towards a compromise and spacecharge caused by the pump beam must be accepted. Simulations and analytical calculations as summarized above, can help to understand the influence of the pump-spacecharge effects on the data[55][56].

2.1.4. Photoemission Spectroscopy at the Free Electron Laser FLASH

In the presented work we make use of the Free Electron Laser FLASH in Hamburg as a photon source for the TR-PES measurements[57][19]. It is an accelerator based source of short pulses of synchrotron radiation. Electrons are accelerated in a superconducting linear accelerator. In an undulator, the accelerated electrons are forced on sinusoidal traces. Caused by this wiggling movement they emit synchrotron radiation. Since the undulator of FLASH is 26 m long, the resulting photon pulse have a very high peak brilliance and coherence. Due to compressed electron pulses, the pulselength can be tuned to very short durations below 100 fs. The concept and working principles of Free Electron Lasers are summarized in text books, e.g. from Saldin et al. [58] or Schmüser et al. [59]. A recent collection of articles in [60] gives a great introduction into practical challenges for experiments at FELs. The FEL FLASH at DESY in Hamburg used in this work

can provide photon pulses with fundamental photon energies between 4.2 to 45nm (295 to 27.6eV) with several orders of even and odd higher harmonic contributions[61].

For a TR-PES experiment, two major factors are of relevance for the experiment: The pulse duration and the energy resolution. The duration of the FLASH photon pulses can be tuned to values ranging from few tens to several hundreds of femtoseconds[62]. The spectral bandwidth of the FEL radiation lies in the order of 0.5-1%[61][63][64]. In case of Photoemission experiments from solids at FLASH, the use of a monochromator for wavelength selection reduces the bandwidth[47][36]. In the presented XUV pump TR-PES experiment a monochromator can't be used because two modes of the FEL (fundamental and third harmonic) have to pass the beamline to the sample. Therefore the energy resolution of the PES experiment is limited by the natural bandwidth of the FEL.

FLASH provides photon pulses with a pulse scheme as depicted in figure 2.4: Every 100ms (10Hz) a pulse-train consisting of up to 800 pulses with a repetition rate of up to 1MHz is created. Due to the probabilistic nature of the SASE process, the properties of the FEL photon spectrum varies slightly for every FEL pulse. In addition to that, long term drifts of the machine settings occur which possibly influences the average spectrum as well (see section 5.2.2).

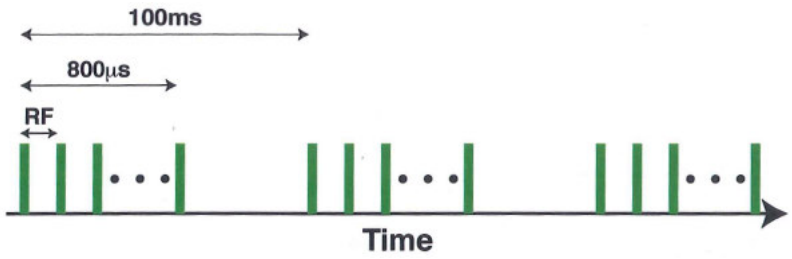

Figure 2.4.: Figure taken from [65]. Pulse Pattern of the Free Electron Laser FLASH. Every 100ms (10Hz) a pulse-train consisting of up to 800 pulses with a repetition rate of up to 1MHz is created.

Since few FEL sources are available worldwide, the experimental time is limited. To allow a post analysis with high flexibility (as presented e.g. in [47] or [36]), many parameters of the experiment and the FEL are saved for every single pulse[3]. A specially designed data acquisition system allows to measure and correlate many experimentally determined properties of the photon beam as well as the electron beam, as e.g. their arrival time jitter or the photon pulse intensity[66][67].

2.2. Dynamical Effects in Semiconductors after Excitation with Short Pulses

In semiconductors the electrons at the Fermi Level are caught in the gap between the conduction and valence band. This special situation leads to the distinct properties of semiconductors and

[3] As the beamtime is limited, it is not always possible to tune the FEL to the very perfect conditions. Instead the tuner has to weight between time-consumption and spectral properties. This limit of time and the complexity of the setup is contributing to the need of careful post-analysis.

their applicability as transistor devices e.g. in computer processors, lasers and solar cells. When the equilibrium distribution of the electrons is altered by an ultrashort pulse of x-ray light, these properties are affected until the excitations decay. In this section, experimental (optical reflectivity, surface photovoltage measurements) and theoretical studies (Drude model based Monte Carlos simulations) on semiconductors after ultrashort excitation and the processes that lead to energy dissipation are summarized.

2.2.1. General

After an x-ray pulse hits the surface of a semiconductor it will partially be absorbed. Most of the absorbed part will lead to excitations in the electronic system of both surface and the bulk[4]. Due to the photoelectric effect, photoelectrons will leave the sample. Additionally and at much higher numbers, excited electrons and holes are created. They will occupy states which weren't occupied before, causing a non-thermal population of the electronic density of states. After thermalization, this electronically excited state and the energy stored therein can be described by an effective increase of the electronic temperature. The band bending at the surface of the semiconductor will partially be screened and a surface photovoltage (SPV) arises. Details on both effects and typical time-scales for the relaxation processes are summarized in this section.

2.2.2. Scattering Processes - Electronic Temperature Increase and Bandgap Shrinking

Within the absorption process, the photons scatter with the atoms of the lattice and hereby liberate core electrons into the unoccupied states above the chemical potential. The scattering and initial excitation process takes place within the first 10-100 as[26]. Parts of the electrons will leave the crystal via photoemission but most of the created high energy electrons will remain bound. Figure 2.5 sketches this relaxation as a function of the time after excitation (taken from [17]). As the situation of highly excited electrons and the respective core-holes is energetically unfavorable ("Coherent regime" in figure 2.6), the high energy electrons/holes will redistribute their energy via electron-electron scattering ("Non-thermal regime"). After few 100 fs, the density of states will resemble a thermal distribution with temperatures of the electronic system of several 1000 K. Since the systems of holes and electrons are embedded in the periodic environment of the crystal and coupled to each other as well, they will not stay at the high temperature. Instead the electrons and holes will start to scatter via electron-hole scattering to level out hole- and electron-temperatures during the next 2 ps ("Hot-excitation regime"). The electrons will start to deposit their energy to the lattice via electron-phonon coupling with typical timescales of few 1 ps. Ultimately the electrons and holes will recombine with time constants in the few 100 ps regime. The system will be back to its original state after ns ("Isothermal regime"). An additional summary of the processes and their timescales taken from J. Shah's book on "Ultrafast Spectroscopy of Semiconductors and

[4]The 1/e-attenuation length of gallium arsenide is δ_{normal} = (35-62)nm for wavelength of 10.3-31nm (120-40eV)[68].

Semiconductor Nanostructures" [69] is shown in figure 2.6. The above summarized response of the electronic system of semiconductors to pulsed optical excitations and the relaxation pathways are under study for long and reviewed e.g. in [70][71][69][72]. Theoretical investigations based on Monte-Carlo models by Medvedev et al. in [73] and [18] and Ziaja et al. in [74] extend the viewfield to higher energy excitations with X-rays.

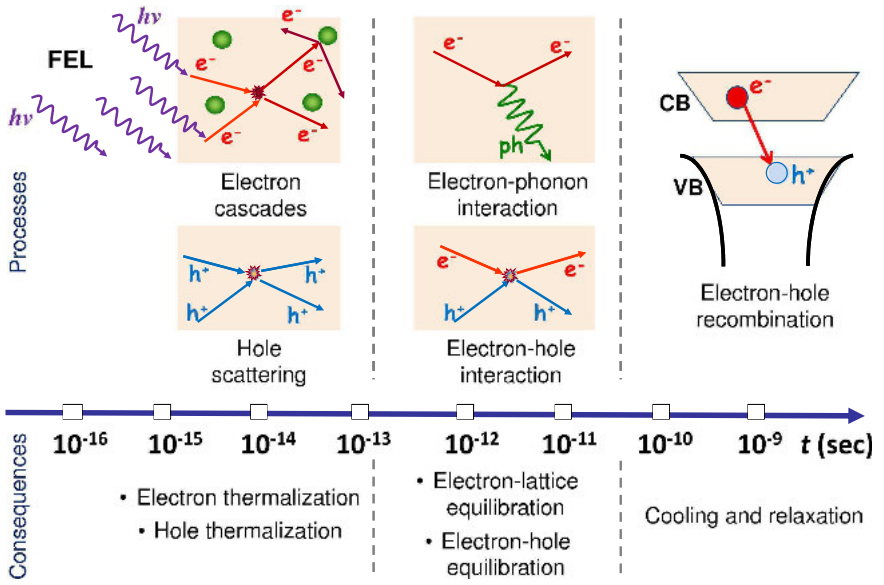

Figure 2.5.: Figure taken from Ziaja et al. in [17]/url. Processes and their timescales describing the energy dissipation in a semiconductor after short pulsed-XUV excitation.

Optical Reflectivity Experiments

With optical reflectivity measurements it is possible to probe excitations of the valence electronic structure[75][76][17]. This phenomenon is utilized in devices applied in short pulsed x-ray sources, to determine the temporal overlap of an optical pump and the x-ray probe beam[16][77][78]. By modeling the experimental data, it is possible to resolve signatures of the above summarized time scales. Figure 2.7 shows the optical reflectivity of Gallium arsenide after excitation with an ultrashort XUV pulse. The data are reproduced by a theoretical model with high accuracy. After the reflectivity drops very fast within the first ≈1 ps and recovers within the next few ps. The fast drop occurs while the excited electrons thermalize and has its minimum when the electronic temperature reaches its maximum. After thermalization within the electronic system, the charge carriers couple to the lattice. The slow recovery is dominated by the characteristic times needed for electron-phonon coupling. For some of the curves it overshoots the original value after relaxation which is due to a shrinking of the band gap due to the increased total temperature. This effect

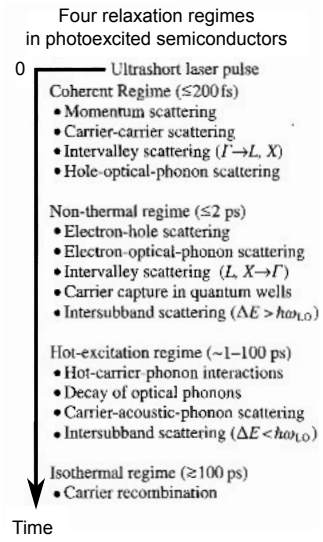

Figure 2.6.: Figure taken from Shah's book of "Ultrafast Spectroscopy of Semiconductors and Semiconductor Nanostructures" [69]. Processes and their timescales describing the energy dissipation in a semiconductor after short pulsed-optical excitation.

decays slowly with rates of several 10 ps. With the theoretical modeling in [17] (solid lines in the graphs), it is possible to extract as a fitting parameter the electron-lattice coupling time-constants from the experimental traces. Depending on the initial electron temperature ($\hat{=}$minimum in reflectivity curve) values of $\tau_{\text{el-lattice}} = 2-3$ ps are reported. The long-term dynamics showing the reflectivity overshooting is matching the expected time scales due to the band gap shrinking. Only the origin of the ealry time-scales ($\approx 0-1$ ps), describing the process of electron thermalization, are not described in detail by the theory in [17] and manually adjusted to match the data. To unravel the exact processes in these first 1 ps more direct methods for measuring the electronic excitation spectrum are required (this work).

2.2.3. Surface Photovoltage

Gallium arsenide as a semiconductor shows the appearance of a surface photovoltage[80][81] in case of photoexcitation of the surface. The effect of surface photovoltage results from the Fermi-Level Pinning of semiconductors which causes a band-bending at the surface relative to the bulk value (see band level sketch in figure 2.8). While the Fermi-Level E_F^{surface} of the surface is found to be pinned to the center of the band gap[5], the bulk Fermi-Level E_F^{bulk} depends on the doping level[6]. The difference of the Fermi-Level in the bulk and that on the surface results in a band bending by $\Delta E = E_F^{\text{surface}} - E_F^{\text{bulk}}$. If free carries are generated by the illumination with photons of sufficient energy, this band bending is temporarily compensated. By measuring the surface photovoltage of a

[5]The Fermi Level pinning at the surface is independent of the doping configuration doping concentrations $\leq 10^{18}/\text{cm}^3$[82].

[6]For $p-$doped semiconductors it lies below the band gap center, and for $n-$doped above the band gap center.

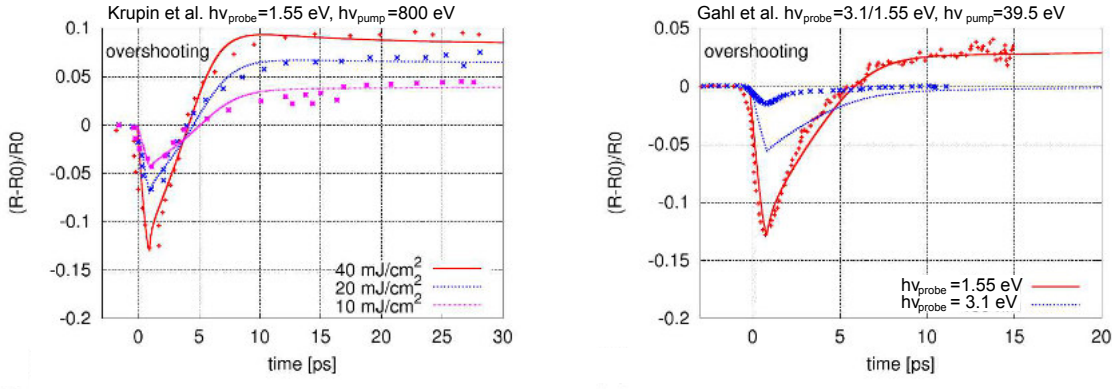

(a) Figure taken from [17]. The sample was excited with a pump photon energy of $h\nu_{\text{pump}} = 800\,\text{eV}$ and varying fluences (see legend) at the LCLS free electron laser source. The probe photon energy was $h\nu_{\text{probe}} = 1.55\,\text{eV}$.

(b) Figure taken from [17]. The sample was excited with a pump photon energy of $h\nu = 39.5\text{eV}$ from the FLASH free electron laser. Two probe photon energies ($1.55\,\text{eV}$ and $3.1\,\text{eV}$) are shown.

Figure 2.7.: Figures taken from [17]. Experimental data on the relative optical reflectivity ($\Delta R/R$) of gallium arsenide after X-ray excitation (original papers [79] and [16]). The solid lines represent the results of calculations based on an extended Drude-model[17].

semiconductor under constant illumination with different frequencies it is possible to extract carrier diffusion times from the bulk towards the surface within the surface photovoltage spectroscopy (SPS)[83].

For photoelectron spectroscopy, the shift of the voltage at the surface, relative to the vacuum level (Surface Photovoltage SPV) will results in a shift of the measured kinetic energy. A $p-$ [$n-$] doped crystal with a bulk Fermi Level below [above] the center of the band gap will exhibit a negative [positive] SPV resulting in an effective increase [decrease] of the measured kinetic energy of the electrons. This can be deduced from the band level diagram in figure 2.8 and is also shown in experiments e.g. in [84]. The footprint of SPV in time resolved photoemission experiments is discussed below.

Surface Photovoltage in TR-PES

Tanaka pointed out in [85], that the determination of the grow-rate of the SPV with a TR-PES experiment is not possible by simply extracting the grow-rate of the negative-delay side of the delay traces. Reason for that is, that the SPV field is an electrostatic phenomenon and affecting the trajectories of the electrons for all possible delays and all positions in space. It will still influence the electrons although they left the sample several ps before ($\hat{=}$negative delays) the SPV field was induced by the pump beam. A major consequence of the considerations in [85] is the spot size dependency of the negative-delay tail time-scales which are measured in a TR-PES experiment. A bigger radius results in a slower grow rate in the observed delay traces. The positive-delay decay rate of TR-PES traces instead resemble the decay rate of the SPV (same physics as the spot size dependency of the pump spacecharge effects summarized in figure 2.2).

Experimentally determined delay traces Yang et al. recorded TR-ARPES (Time Resolved Angular Resolved Photoemission spectroscopy) spectra of $p-$Gallium arsenide[7] in a pump-probe experiment. They use an 800 nm IR laser for pumping the SPV and a frequency quadrupled $h\nu_{\text{probe}} = 6\,\text{eV}$ beam to probe the ARPES spectrum. Figure 2.9 shows the resulting delay-traces. In separate plots, one can see the influence of the pump beam excitation onto (a) the conduction band and (b) the valence band. Additionally the authors proofed in (c) the calculations presented by Tanaka at the negative-delay dynamics tail of the valence band edge. All three determined traces (figura (a) HEE, LEE and figure (b) VBM) show a maximum kinetic energy at temporal overlap and an exponential decay with a similar rate of $\tau_{\text{slow}} \approx 1.5\,\text{ps}$. This slow rate, which all electrons leaving the sample have in common, is attributed to the duration of the SPV decay. An additionally observed fast decay rate of the optically populated HEE states in the CB (see figure description) is attributed to intravalley scattering enabled via electron-phonon coupling, similar to that described in Silicon[87].

Signature of of the SPV in TR-PES With the above summary of the experimental signature of the SPV in a time resolved Photoemission experiment, three major aspects relevant for the TR-PES experiments shall be highlighted:

1. The SPV effect shows its maximum at perfect temporal overlap of pump- and probe beam.
2. The decay rates of the kinetic energy shifts on the negative-delay side depend on the radius of the pump beam. In the above summarized experiment, a pump beam radius of $r_0 = 57\,\mu\text{m}$ leads to an observed grow rate of $\tau_{\text{negative}} \approx 100\,\text{ps}$. For larger spot sizes this decay rate is bigger.
3. The decay rate of the SPV in Gallium arsenide was measured to different values, all with $\tau^{p-\text{GaAs}}_{\text{SPV-decay}} \geq 1.5\,\text{ps}$ and $\tau^{n-\text{GaAs}}_{\text{SPV-decay}} \geq 7\,\text{ps}$:
   $\tau_{\text{SPV-decay}} \approx 1.5\,\text{ps}$ in [86] ($p = 1.2\times10^{19}\,\text{cm}^{-3}$), $\tau_{\text{SPV-decay}} \approx 15\,\text{ps}$ in [84] ($p = 3\times10^{19}\,\text{cm}^{-3}$),
   $\tau_{\text{SPV-decay}} \approx 7\,\text{ps}$ in [88] ($n = 1\times10^{16}\,\text{cm}^{-3}$), $\tau_{\text{SPV-decay}} \approx 8\,\text{ps}$ in [89] ($n = 4.85\times10^{17}\,\text{cm}^{-3}$).

[7] The $p-$doping concentration in [86] is $p = 1.2\times10^{19}\,\text{cm}^{-3}$.

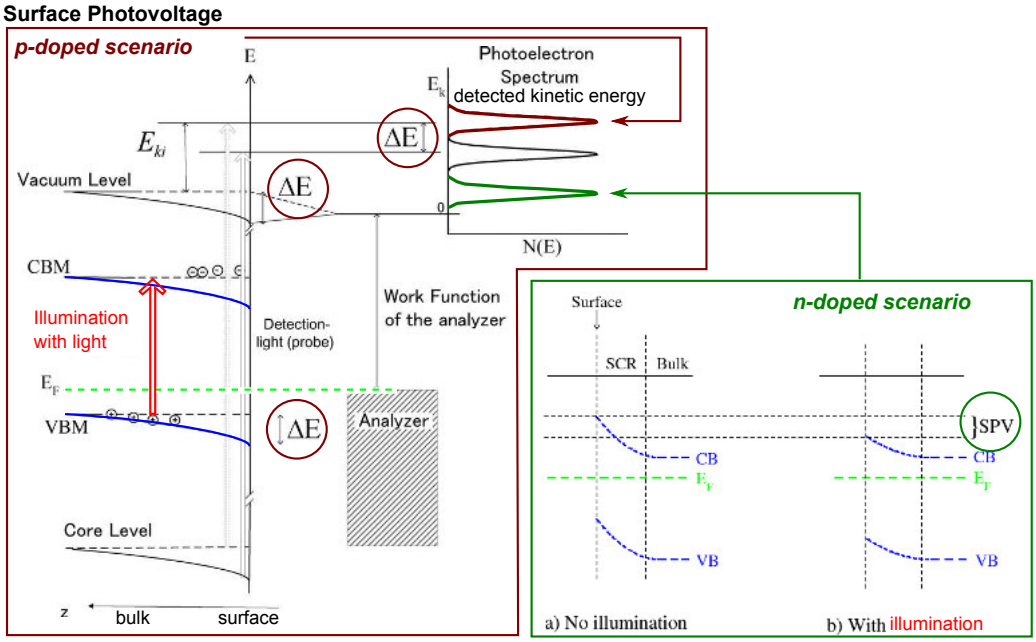

Figure 2.8.: Left figure reprinted and adapted from [85]. Right figure reprinted and adapted from Wikipedia (url). Level scheme of a semiconductor depending on the distance z from the surface. The Fermi Level E_{F} is pinned to the band gap center at the surface. In the bulk instead it is determined by the doping level. Consequently the bands bend by an energy ΔE to align Fermi Level of bulk and surface. When free carriers are created by illumination with light, the band bending is temporarily compensated. For a photoemission experiments this results in a change of the detected kinetic energy. The sign of this change depends on the doping of the bulk semiconductor. In the red frame the scenario for a $p-$doped case is depicted and with a green frame that for the $n-$doped case.

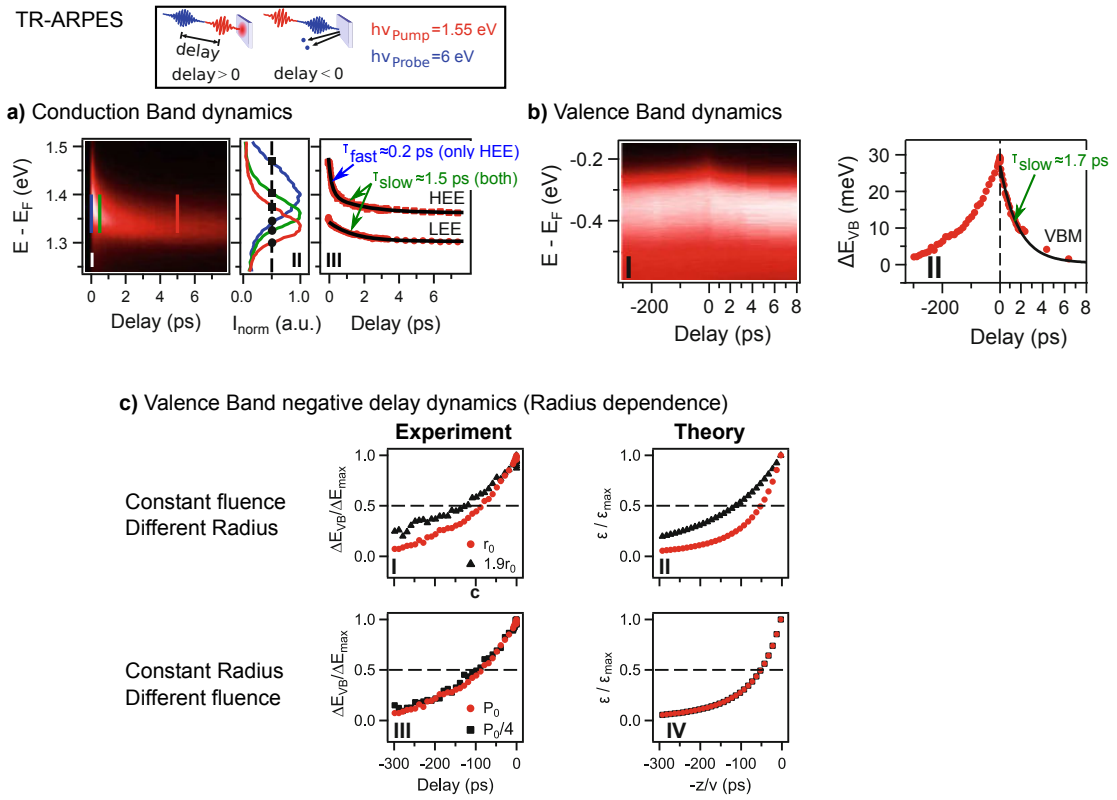

Figure 2.9.: Figures taken from [86]. Results of a TR-ARPES experiment on Gallium arsenide by Yang et al. The spectra are divided into: a) Photoelectrons of the conduction band with a high kinetic energy electron edge (HEE) and a low kinetic energy edge (LEE). Both traces (HEE and LEE) show an exponential decay with a rate of $\tau_{\text{slow}} \approx 1.5\,\text{ps}$. The HEE show a second decay with $\tau_{\text{fast}} = 0.2\,\text{ps}$. b) Photoelectrons of the valence band with the highest electronic level at the valence band maximum (VBM). At positive delay, the exponential fit results with a rate of $\tau_{\text{slow}} = 1.7\,\text{ps}$. The change of the signal at negative delay with a rate of $\tau_{\text{negative}} = \approx 100\,\text{ps}$, is attributed to the electrostatic nature of the SPV and studied in c. c) Negative delay dynamics of the VBM electrons for different pump beam radii at constant fluence and constant fluence at different radii in both, experiment and theory after [85]. Experimental parameter: pump beam radius in units of $r_0 \approx 57\,\mu\text{m}$, time resolution $\tau \approx 160\,\text{fs}$, pump fluence $P_0 = 25\,\mu\text{J/cm}^2$, $p-$doped GaAs(110) samples, hemispherical electron analyzer.

3. Experimental Setup and Sample Characterization

The Free Electron Laser FLASH can provide short pulses of x-rays with high brilliance at photon energies between 28 eV and 295 eV in the fundamental at pulse durations below 100 fs[90][19]. This energy range includes our desired pump photon energy of $h\nu_{\mathrm{pump}} = 40$eV. In addition, higher harmonics of this fundamental energies are included in the spectrum. The third harmonic appears with intensities of ≈0.5% of the fundamental[61][90]. We use this capability of the Free Electron Laser providing x-rays at several harmonics to perform an x-ray pump (fundamental) x-ray probe (3^{rd} harmonic) experiment. For that purpose the FEL beam is split into two arms within an Auto-Correlator setup, named "Split and Delay Unit" (SDU) provided by the FLASH facility at the PG2 beamline[91]. The travel-length of the x-rays within the two arms can be varied individually which allows to introduce a timing delay between the beams of the two arms. We used the resulting x-ray beams to perform pump probe photoemission spectroscopy experiments. Within this chapter, the FEL beamline with the SDU and the PES endstation are described and important parameter calibrated (Sections 3.1-11). In the last section 3.7 of this chapter, the sample preparation is presented.

3.1. FEL Beamline and Diagnostic Tools

Figure 3.1 summarizes all x-ray optics which were required to record and analyze time resolved photoemission spectra. The intensity of the photon beam, which contains several harmonics of the fundamental photon energy of $h\nu = 40$ eV is determined in gas cells (gas monitor detector, GMD). Two of these GMDs are used at FLASH. One before and one after the nitrogen filled gas attenuator (GMD "Tunnel"[1] and "BDA"[2]). The beam can be attenuated with the mentioned gas attenuator and filter foils. When using the gas attenuator (also called gas absorber) it can happen, that the FEL beam is too weak at the GMD BDA and the GMD can not provide intensity data. After the first beamline-switching mirror in the FLASH experimental hall (called mirror *M0*), the beam is steered into the PG2 beamline[92][93][64]. The central part of the beamline is the name-giving Plain Grating (PG) monochromator and the split and delay unit (SDU). Since the first and third harmonic are needed to perform the experiments, the monochromator is not in use

[1] The FEL intensity is measured right after the undulator still located in the Tunnel of the linear accelerator.
[2] The acronym BDA stands for **B**eam **D**istribution **A**rea.

during our pump probe experiments. The Split and Delay unit is used to divide the beam into two arms by applying a wavefront cutting scheme. Different filter foils in the two arms enable photon energy selection of the pump- and probe photon energy. At the sample position the two beams are overlapped and the photoelectrons detected with an electron time-of-flight spectrometer. No intensity monitor is available at the sample position. During the presented experiments the only possibility to determine the intensity at the sample is to propagate that measured at the GMD Tunnel by using the transmission values of the optical elements on the beam path (section 3.6.1).

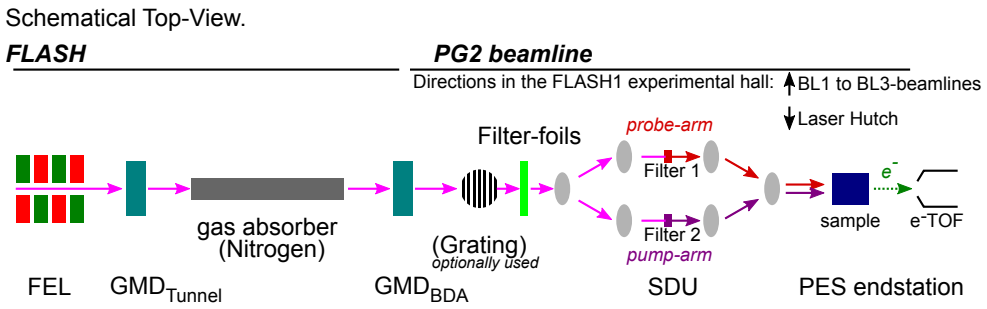

Figure 3.1.: A simplified overview of the experimental layout. Only relevant parts of the beamline and the endstation are included in this sketch. The distances are not scaled to real distances.

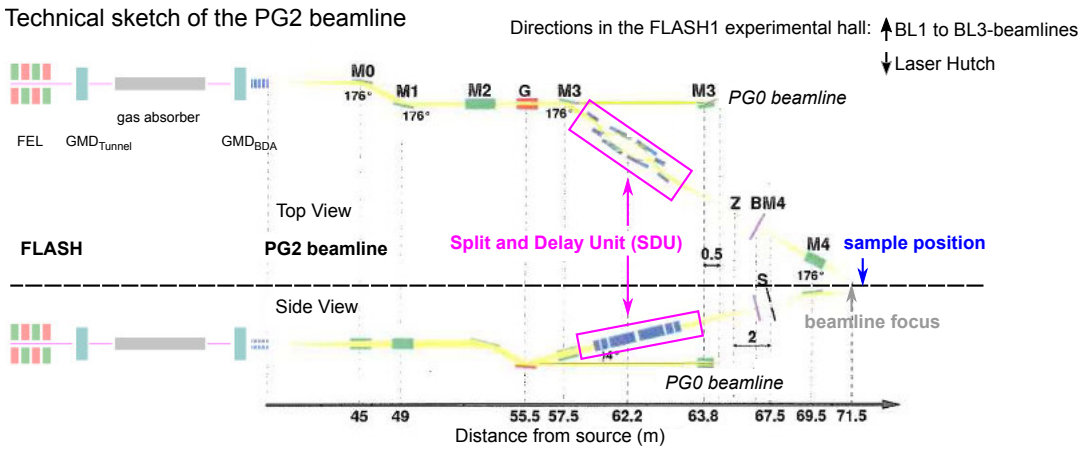

Figure 3.2.: Figure taken and modified from [65]. Sketch of the PG2 beamline at FLASH with all relevant optical elements. The sample of the Photoelectron spectroscopy endstation is located 25cm after the focus of the beamline.

To determine the spectrum of the FEL, it is possible to disperse the beam with a grating and send the photon energy dispersed beam on an in-vacuum CCD detector to record a spectrum[92][64]. An example spectrum of the FEL beam while tuned to a nominal photon energy of $h\nu = 40\,\mathrm{eV}$ is shown in figure 3.3. The spectrum is averaged over several FEL shots and shows a central energy of $h\nu = 39.8\mathrm{eV}$ an a relative spectral bandwidth of 0.55%.

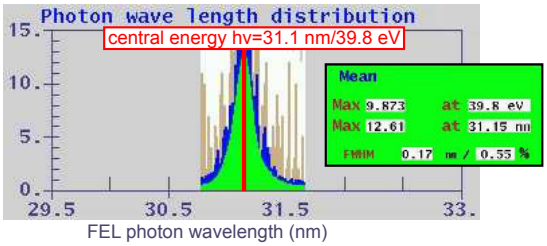

Figure 3.3.: Spectrum of the FEL with a fundamental photon energy of $h\nu$=39.8eV recorded with the spectrometer of the PG2 beamline. Note that this is the spectrum of FEL shot number 100 averaged for several bursts of the FEL (see timing scheme in figure 2.4).

3.2. Split and Delay Unit (SDU)

The split and delay unit (SDU) at the PG beamline at FLASH allows jitter-free pump-probe experiments with two XUV pulses in the photon energy range of FLASH[91]. The technical realization and calibration measurements are summarized in the PhD thesis of F. Sorgenfrei [65] as well as in [91]. In this section, a short summary on the relevant technical aspects is given. After that, the influence of beam pointing variations on the transmission of the SDU is discussed. At the end of this section, an auto-correlation measurement is analyzed in order to determine the time-zero and the FEL pulselength.

3.2.1. Technical Realization

To distribute the XUV beam in two different arms, a wavefront splitting design is applied. A sketch is shown in figure 3.4. One can see, that the incoming photon beam passes the edge of the beam-cutting mirror. Hereby the beam is spatially split into two. The length of the optical path through the two arms can be changed by moving the mirrors DL.1 to DL.4 transverse to the photon beam. The achievable delay is limited by the travel length of the mirror and an overall delay of 6.4ps ($\rightarrow \pm$3.2ps) can be achieved with this setup. Due to the design, the two beams are inherently synchronized and no time-resolution loss due to temporal jitter occurs.

3.2.2. Filters for Photonenergy Selection

For spectral separation within the arms, the absorption characteristics of thin metal foil filters as proposed in [65] is utilized. The transmission spectrum of the chosen filter foils are shown in figure 3.5(a) and are tabulated in table 3.1. Since the pump beam photon energy and that of the probe are coupled via the synchrotron radiation formula, the choice of possible filters and pump and probe frequencies is limited. To match the experiments on the optical reflectivity by Gahl et al. in [16], we selected a fundamental frequency of $h\nu_{\mathrm{pump}} = 40\,\mathrm{eV}$ as pump frequency. The probe photon energy is than restricted to $h\nu_{\mathrm{probe}} = 3 \cdot \mathrm{h}\nu_{\mathrm{pump}} = 120\,\mathrm{eV}$.

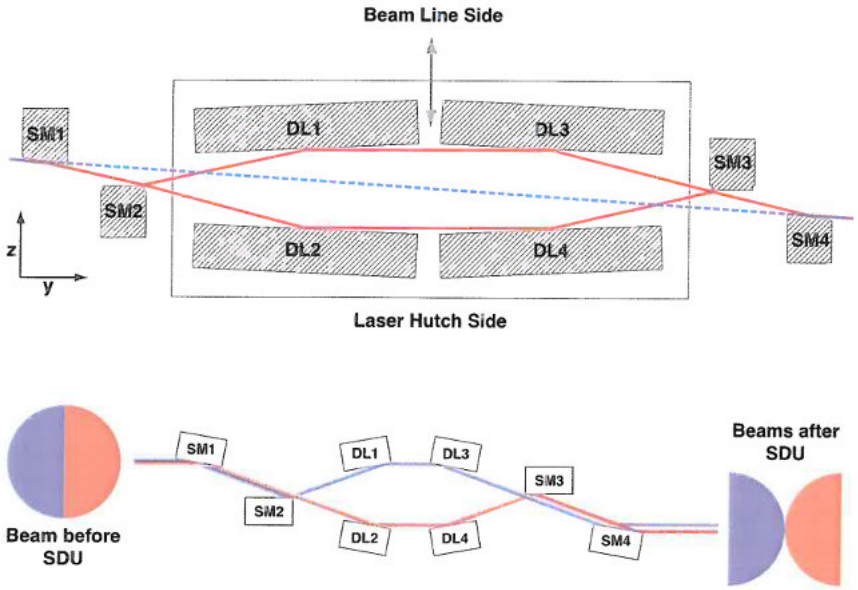

Figure 3.4.: Figure taken from [65]. Sketch of the beam path in the SDU. If the beam arrives closer to the laser hutch side on the beam cutting mirror (*SM2*) more intensity will be cut and less intensity will travel through the laser hutch side arm of the SDU.

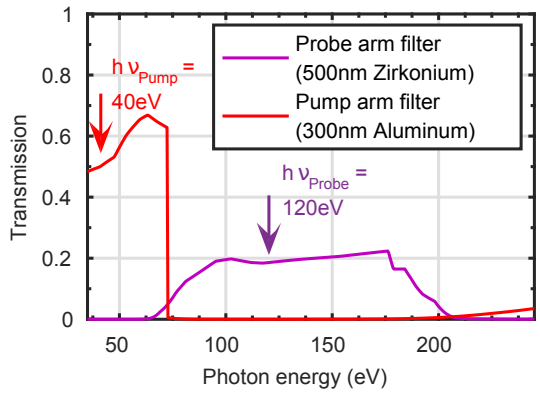

(a) Filters used in the SDU to select pump- and probe beam photon energies. Within the pump-arm the third FEL harmonic is cut with the 300 nm aluminum filter (red), while in the probe-Arm a 500 nm zirconium filter (purple) is used to cut the fundamental of the FEL radiation.

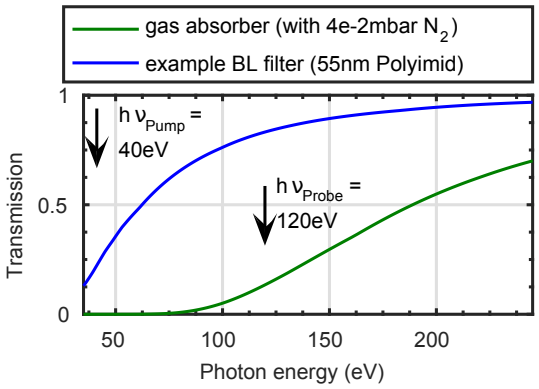

(b) Transmission of a 55 nm thick polyimid filter located after the SDU (blue) and that of the 15 m long gas absorber filled with 4e-2 mbar nitrogen and located before the SDU (green).

Figure 3.5.: Transmission curves of the relevant filters[68]. As the filter-holder mount in the SDU forbids the mounting of more than one filter, it is not possible to tune the pump- and probe arm intensity independently. It is fixed to the values in figure (a). For tuning the pump fluence, the common beamline filtering options (gas absorber and beamline filters) have to be chosen such, that the probe fluence is changed as little as possible. The absolute transmission values of the two arms are tabulated in tables 3.1 and 3.3.

3.2.3. Qualitative Relation of FEL Pointing and SDU Transmission

The intensity ratio in the two arms of the SDU is determined by the pointing of the FEL on the beam cutting mirror of the SDU ("SM2" in figure 3.2). To be able to measure the effective intensity ratio for every FEL shot, an online monitor of the FEL pointing would be required. Such a device is not foreseen in the setup. Instead, the beam position is permanently measured at the gas monitor detectors of the beamline[94][3]. The pointing relation of the beam at the cutting mirror is the same as at the GMD, since the number of horizontally relevant mirrors between the GMD and the cutting mirror is even (4 pcs, see figure 3.2). This means, that an increase in the GMD Position X corresponds, causes a reduction of the intensity fraction in the pump arm.

3.2.4. Splitting Ratio Determination

In his PhD thesis[65], F. Sorgenfrei proposed a method to determine the beam splitting ratio by measuring the photocurrent induced in a gold mesh. This method allows a shot-wise evaluation of the intensity splitting ratio of the two beams with a repetition rate of 1 MHz. For technical reasons[4] we could not use this technique. Instead I determined the splitting ratio by analyzing the size of the beam when hitting a florescence screen in the beam path.

To determine the exact splitting ratio, which is important to calculate the pump fluence at the sample, an image of the beams in the two arms was taken, making use of the integrated beam monitors. The image recorded with a camera directed onto the beam monitors is shown in figure 3.6. To extract the splitting ratio, I assume a gaussian intensity distribution of the beam at the splitting mirror. This gaussian intensity distribution is split in two beams and the splitting ratio between pump- and probe-arm of the SDU is proportional to the ratio of the width in the two arms. The width of the two beams is extracted with a gaussian fit to the intensity distribution as explained in the figure. Finally the splitting ratio is determined to $I_{\text{pump}}/I_{\text{probe}} = h_{\text{LH-side}}/h_{\text{BL-side}} = 1.38$ at a position of the FEL in the GMD-Tunnel of $X_{\text{Tunnel}} = (0.52 \pm 0.05)mm$.

3.2.5. Temporal Overlap and Pulselength Characterization

With the help of an autocorrelation measurement of the FEL beam, measured in 1^{st} order of the Mmonochromator at a photon energy of hν = 120eV, it is possible to determine the pulselength and the temporal overlap (t_0). The Auto-Correlation trace is determined by measuring the occurrence and strength of interference fringes which appear when the two beams of the SDU are overlapped on a screen (example picture in figure 3.7(a)). The strength of the interference fringes ("Fringe-Visibility") varies with the delay. It is biggest for perfect temporal overlap of the pulses. Figure 3.7(b) shows the fringe visibility V as a function of the delay between the two arms (details on

[3] The position of the FEL beam passing the gas cell (X and Y values) is saved in the data stream for every FEL burst. Increasing values in X means a movement towards the laser hutch, increasing values in Y correspond to a movement towards the hall roof (E-Mail Correspondence with U. F. Jastrow).

[4] The MCP readout with the FLASH Data Acquisition system was not working properly during the measurement campaign.

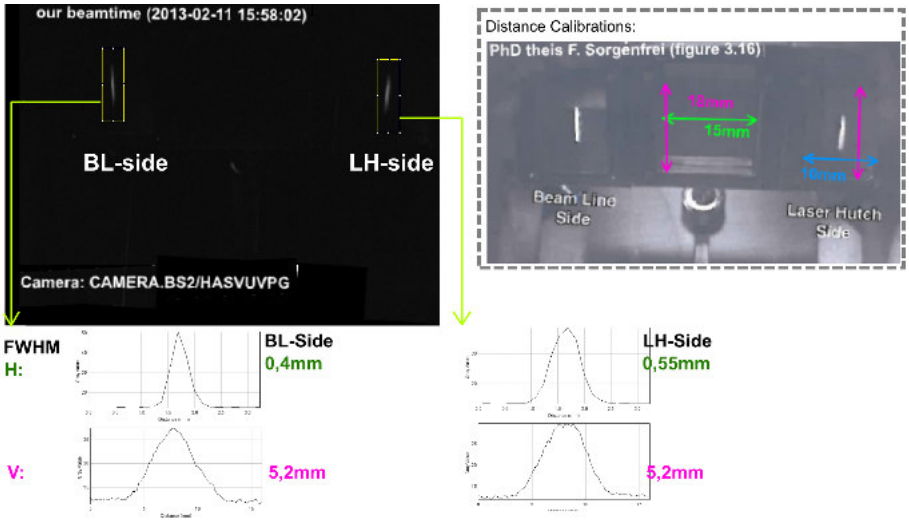

Figure 3.6.: Right figure taken from [65]. Image of the beam monitors in the SDU showing the beam profile in the two arms. To relate pixels with real space distances I used figure 3.16 from [65]. The beam size is extracted by fitting the summed and projected image intensity with a gaussian. The following FWHM sizes of the two beams are extracted (vertical $v\times$ horizontal h): LH-Side $v_{\text{LH-side}} = 0.55\,\text{mm} \times h_{\text{LH-side}} = 5.2\,\text{mm}$. BL-Side $v_{\text{BL-side}} = 0.4\,\text{mm} \times h_{\text{BL-side}} = 5.2\,\text{mm}$. The intensity ratio of the two arms follows that of the width of the two beams: $I_{\text{pump}}/I_{\text{probe}} = h_{\text{LH-side}}/h_{\text{BL-side}} = 1.38$ which is equivalent to a splitting ratio at the cutting mirror of 0.58:0.42 (pump:probe). The GMD BDA showed at the time when the image was recorded (11.02.2013, 15:58 o´clock) a position of the beam in the gas cell of $X_{\text{Tunnel}} = (0.52 \pm 0.05)\,\text{mm}$ and $X_{\text{BDA}} = (0.53 \pm 0.07)\,\text{mm}$. The error is the standard deviation of the position during the 60 seconds within the relevant minute of saving the picture.

the extraction are summarized in Appendix A.2.2). The signal is fitted with a Gaussian line and an autocorrelation time constant of $\tau_{\text{autocorrelation}} = (359 \pm 39)$fs extracted. The maximum autocorrelation signal occurs at the encoder position of $t_0^{\text{SDU control software}} = -3.77ps$. Any delay value in this work refers to this experimentally determined time zero. The width of the measured autocorrelation trace is connected with the pulse length of the incoming τ_{FEL} pulse, which is already stretched by the grating monochromator:

$$\tau_{\text{autocorrelation}} = \sqrt{2}\tau_{\text{FEL stretched}} \tag{3.1}$$

For the initial pulse-length τ_{FEL} this means:

$$\tau_{\text{FEL}} = \sqrt{\frac{\tau^2_{\text{autocorrelation}}}{2} - \Delta T^2}. \tag{3.2}$$

Here ΔT is the pulse stretching caused by the monochromator (see end of this section). With the experimentally determined autocorrelation time-constant $\tau_{\text{autocorrelation}}$ and the approximated pulse stretching it is possible to approximate the pulselength of the original FEL pulse with equation 3.2:

$$\tau_{\text{FEL}} = (170 \pm 102)\,\text{fs} \tag{3.3}$$

and the overall time resolution to:

$$\tau^{\text{FWHM}}_{\text{resolution}} = \sqrt{2}\tau_{\text{FEL}} = (240 \pm 144)\,\text{fs}. \tag{3.4}$$

The big error of this calculation results from the uncertainty of the vertical beam size on the grating σ_y which could only be approximated based on values from [65]. Beside the presented analysis, no further pulse-length characterization was possible during the beamtime.

Expected Pulse Stretching Calculation

To determine the pulse stretching, the equations described by Wellhöfer in [92] are used:

$$\Delta T = \frac{n\lambda\sigma_y k}{c_0\sqrt{1 - \left(\frac{-nk\lambda + \sqrt{1-2c_{ff}^2+c_{ff}^4+c_{ff}^2k^2n^2\lambda^2}}{c_{ff}^2-1}\right)^2}} \tag{3.5}$$

$$\tag{3.6}$$

With the stretching contribution ΔT one can determine the final pulse length $\tau_{\text{FEL stretched}}$ with a squared sum (assuming Gaussian profiles):

$$\tau_{\text{FEL stretched}} = \sqrt{\tau^2_{\text{FEL}} + \Delta T^2} \qquad . \tag{3.7}$$

As described in [92], the vertical beam size σ_y is not measured. Therefore it is here approximated[5] with $\sigma_y = (1 \pm 0.3)\,\mathrm{mm}$. The c_{ff} value was set to $c_{ff} = 2$ during the measurement. The measurement was performed in first diffraction order ($n = 1$) at a photon energy of $\mathrm{h}\nu = 120\,\mathrm{eV}$ ($\lambda = 10.33\,\mathrm{nm}$). The used grating had a groove density of 200 lines/mm. Overall this leads to an expected pulse stretching of:

$$\Delta T_{\mathrm{expected}} = (186 \pm 56)\,\mathrm{fs} \tag{3.8}$$

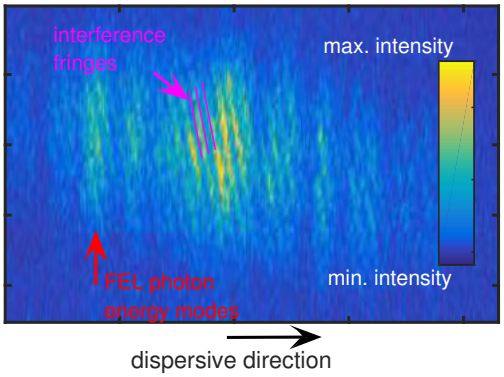

(a) Example image of the interference fringes on the CCD camera at Δt_{SDU}=0ps. The image shows two major features: (1) Along the dispersive direction (200 lines/mm Grating, 1^{st} diffraction order) one can differentiate the different modes of the SASE FEL. An example mode with marked with a red arrow. (2) interference fringes, with an angle of $\approx 20°$. A purple arrow indicates a region where the fringes are well recognizable.

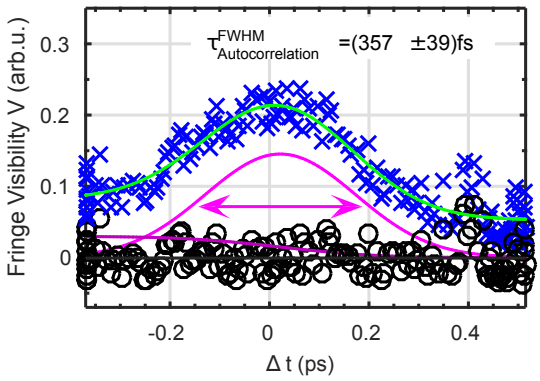

(b) The fringe visibility V shows it's maximum at temporal overlap of the two beams. Experimental data are marked with blue crosses. An arctan-shaped background is subtracted and a gaussian line used to fit the autocorrelation trace (purple lines). The overall fit is shown as a green line and the residuum with black circles. A detailed description on the determination of this curve is summarized in Appendix A.2.2.

Figure 3.7.: Methodology for the time-zero and pulselength determination is depicted. The third harmonic of the FEL beam ($h\nu = 120\,\mathrm{eV}$) is selected with the 200 lines/mm grating and split with the SDU into two beams. These beams are overlapped at an in-vacuum CCD detector (left). The resulting interference fringes and their strength is evaluated and a fringe visibility extracted. This fringe visibility is plotted as a function of the delay and resembles the autocorrelation signal (right). The maximum signal is the time zero. The pulselength can be deduced from the full width at half maximum (FWHM) of the autocorrelation trace $\tau_{\mathrm{Autocorrelation}} = (357 \pm 39)\,\mathrm{fs}$ (see text).

[5] The value of $\sigma_y = 1\,\mathrm{mm}$ is that, used by [65] for a pulse-stretching analysis. In [92] I found values of $\sigma_y > 3\,\mathrm{mm}$. The later one would lead to a pulse stretching bigger than the measured auto-correlation trace and are therefore unphysical in the here presented experiment. The given error of $\Delta\sigma_y = \pm 0.3\,\mathrm{mm}$, was chosen such, that the upper bound value of $\sigma_y^{\mathrm{max}} = 1.3\,\mathrm{mm}$ leads exactly not to a negative number below the root in equation 3.3

3.3. Photoemission Endstation

Figure 3.8 shows a photograph of the experimental endstation. The time-of-flight spectrometer is a commercial THEMIS 1000 with a pre-lens (wide angular lens, WAL) from SPECS GmbH. Including the pre-lens, the spectrometer has a length of 1.5832 m. It is described in detail in the Master thesis of L. Wenthaus [95]. The spectrometer consists of several electron lenses and is designed to collects an emission angle of up to ±30° from the sample surface. Since the lens tables were not correctly programmed, we could not make use of this capability for the presented pump probe measurements. All electron lenses in the spectrometer are on ground during the experiments of this work, which is called the "Drift Mode" of the spectrometer.

To detect the electrons after they fly through the drift tube, a four quadrant delayline detector is used[95]. Different than slower detectors as e.g. CCD chips, it allows to determine the time of flight of the electrons for every individual FEL shot, which allows separation of the spectra in the post analysis. The capability of the detector, to measure the arrival position of all electrons is not used in this work. To avoid saturation of the detector, it is possible to apply a positive voltage on a fine grid located in front of the delaylines ("conversion voltage"[6] U_{conv}). If not commented, we applied a voltage of $U_{\mathrm{Conv}} = -50\,\mathrm{V}$ to avoid saturation of the detector caused by the big amount of secondary electrons emitted from the sample. Although the experimental chamber is equipped with a Mu-metal shielding to compensate external magnetic fields, the trajectories of electrons with kinetic energies below 10 eV can not be detected. Since the Ga3d core levels detected in this experiment arrive with a kinetic energy of $\approx 100\,\mathrm{eV}$ this is not relevant for most of the analysis. Only when the Photoemission spectrum caused by photoemission from the FEL fundamental ($h\nu = 40\,\mathrm{eV}$) is evaluated in section 4.1.2, these losses have to be taken into account. For that purpose, the transmission function of the spectrometer is determined at the end of this section.

3.3.1. Transmission Characteristics of the Spectrometer

Due to electromagnetic fields, slow electrons emitted from the sample can not enter the spectrometer[95]. The experimentally determined functional dependency of the transmission efficiency as a function of electron kinetic energy is depicted in figure 3.9 (details see Appendix A.2.1). A phenomenological fit through the data gives a dependency of the relative Transmission[7] T_{relative} on the electron kinetic energy E_{kin} of:

$$T_{\mathrm{relative}} = 1.34 - 4.5/\sqrt{E_{\mathrm{kin}}}. \tag{3.9}$$

[6] The name conversion voltage comes from the initial purpose of the grid: When used with a low energy electron source (e.g. electron gun measurements) it can increase the efficiency of the MCP based detector to accelerate the electrons before hitting the delayline detector assembly. The conversion of the low energy electrons gave the name to the voltage.

[7] The Transmission is expressed relative to the transmission of the photon peak as explained in the appendix A.2.1.

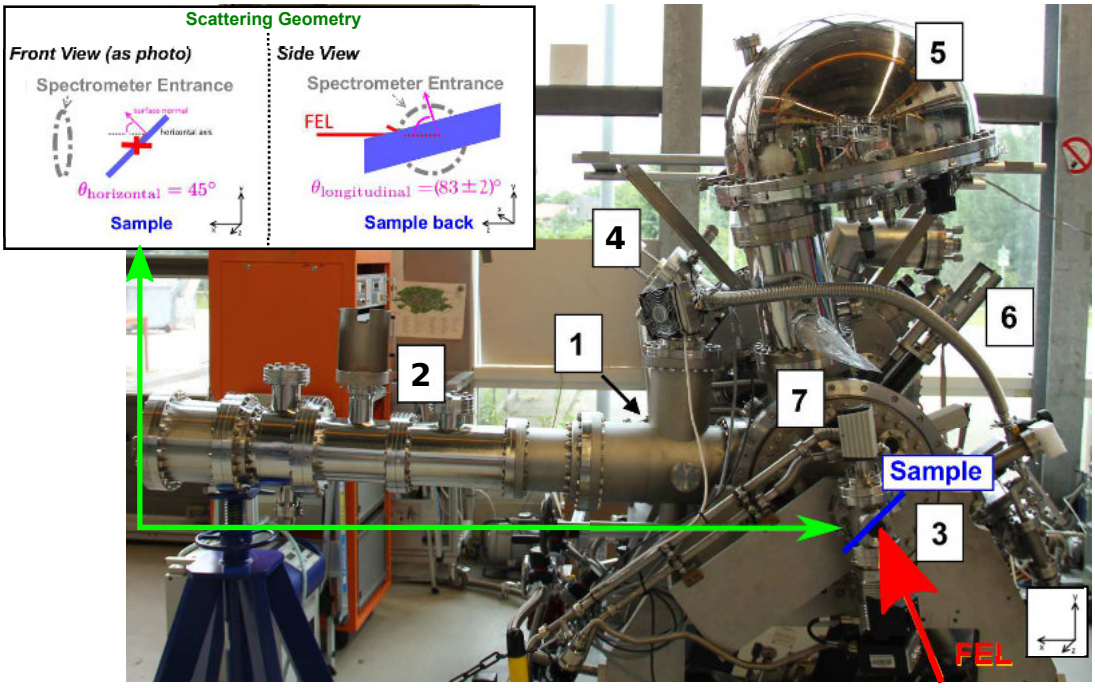

Figure 3.8.: Figure taken and modified from [95]. Photograph of the Photoemission endstation (Hamburg Inelastic X-ray Scattering Station "HIXSS") used for the pump-probe photoemission experiments. The labels are: [1] - Spectrometer wide angular pre-lens (grounded in the presented measurements), [2] - Drift Tube of the time-of-flight spectrometer and Delayline Detector, [3] - beamline flange, [4] - LEED setup, [5] - Hemispherical analyzer (not used in this work) [6] - X-ray gun, [7] - pulsed electron source (not used in this work). The inset in the upper left corner depicts the scattering geometry from two perspectives.

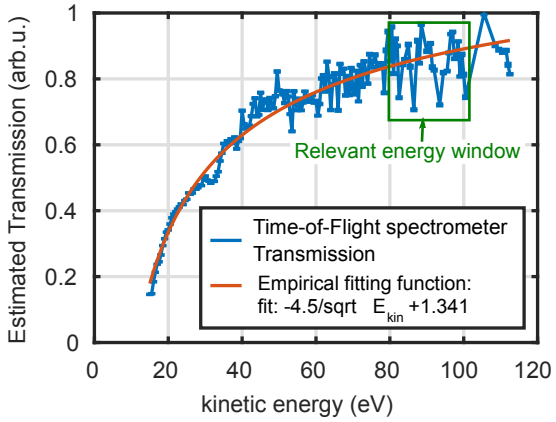

Figure 3.9.: Experimentally determined transmission function of the spectrometer used in drift-mode. The transmission is approximated with the Area of the detected electrons on the Detector as explained in the Appendix A.2.1. A green mark indicates the kinetic energy region of relevance for the study of the Ga3d photoelectron lines where the transmission is almost constant $T_{80\text{-}100\,\mathrm{eV}} = 83\%$.

3.3.2. Time-of-flight to Energy Conversion

For conversion from time of flight to kinetic energy the relation:

$$E_{\text{kin}} = \frac{m_e}{2} v^2 = \frac{m_e}{2} \left(\frac{s}{t}\right)^2 \tag{3.10}$$

is used. Here m_e is the electron mass, v the velocity, s the drift distance and t the time of flight. For the length of the spectrometer I used $s = 1.5885\,\text{m}$ which is the sum of spectrometer length and distance between sample and analyzer entrance[95].

3.4. Transmission Values of the Beamline Optics

To determine the intensity at the sample, one has to propagate the intensity measured at the GMD Tunnel to the sample by calculating the transmission of the optical path. In this section, the theoretical transmission values for all elements for both, pump and probe photon energy ($h\nu = 40/120\,\text{eV}$) are tabulated.

3.4.1. Determination of the Transmission of the Gas attenuator for the Third Harmonic

The transmission of the gas attenuator for the first harmonic of the FEL can be determined experimentally by measuring the intensity before and after the gas attenuator. This is not the case for the third harmonic, as the signal in the GMD is dominated by the fundamental wavelength. To determine the missing transmission of the third harmonic through the nitrogen absorber is calculated with[8]:

$$T_{\text{Absorber}}(40\text{eV}) = I_{\text{FEL}}^{\text{BDA}} / I_{\text{FEL}}^{\text{Tunnel}} \tag{3.11}$$

$$T = \exp\left(-\sigma_{\text{Photo}} \rho_T x\right) \tag{3.12}$$

$$T_{\text{Absorber}}(120eV) = \exp\left(\frac{\sigma_{\text{Photo}}(120eV)\ln\left(T_{\text{Absorber}}(40eV)\right)}{\sigma_{\text{Photo}}(40eV)}\right) \tag{3.13}$$

$$[\text{with:} \quad \sigma_{\text{Photo}}(120\text{eV}) = 1.07\text{Mb and } \sigma_{\text{Photo}}(40\text{eV}) = 12\text{Mb.}] \tag{3.14}$$

Here σ_{Photo} is the absolute N_2 Photoabsorption Cross Section[96], ρ_T the particle volume density, k_B the Boltzmann constant, T the temperature, x the length of the attenuator.

3.4.2. General Losses in X-ray Optics

For redirecting the X-ray beam from the undulator to the experimental endstation, several mirrors are used. While in the optical frequency range mirrors exist which reflect 100 % of the beam

[8] Since the absolute pressure in the attenuator is not measured, the transmission of the third harmonic has to be calculated by determining the gas pressure with the measured transmission of the fundamental in equation 3.13.

intensity, this is not the case for x-ray frequencies. To reduce the losses at x-ray mirrors, they are coated with Carbon and are used with a very grazing angle of incidence (typically $< 2.5\,°$). Under these circumstances the reflectance is > 0.9 for all energies below the Carbon 1s edge at $\approx$280 eV[9]. Anyhow, the theoretical transmission of both, the beamline and the split and delay unit is determined by the amount of mirrors ($N_{\text{mirrors}}^{\text{PG2-BL}} = 5$, $N_{\text{mirrors}}^{\text{SDU pump/probe arm}} = 5$). The theoretical transmission value of the SDU including the design angles of incidence can be found in [91]. For the beamline additionally the transmission of the grating has to be taken into account[10].

3.4.3. Transmission Tables

The overall transmission T_{total} depends on the wavelength and is different for both arms of the SDU. It can split into several factors:

$$T_{\text{total}}^{\text{SDU-arm}} = T^{\text{common}}(\text{Attenuator, BL filter}) \cdot T_{\text{SDU}}^{\text{cutting mirror SDU-arm}} \cdot T_{\text{SDU}}^{\text{filter SDU-arm}}. \tag{3.15}$$

Here T_{common} refers to the parts of the beamline (BL), which both beams pass either before or after the Split and delay unit:

$$T^{\text{common}}(\text{Attenuator, BL filter}) = T_{\text{BL}}^{\text{attenuator}}(p_{\text{set}}^{\text{att}}) \cdot T_{\text{BL}}^{\text{filter}} \cdot T_{\text{BL}}^{\text{losses}} \cdot T_{\text{SDU}}^{\text{losses}}. \tag{3.16}$$

This common transmission depends on the set point pressure $p_{\text{set}}^{\text{att}}$ of the attenuator and the chosen filters of the beamline. The numerical values of the individual factors and the references are listed in table 3.1.

[9] The exact reflectance values for an angle of incidence of 2.5 ° are: $R_{30\,\text{nm Carbon}}(\text{AOI} = 2.5\,°, 40\,eV) = 0.94$ and $R_{30\,\text{nm Carbon}}(\text{AOI} = 2.5\,°, 120\,eV) = 0.94$[68].

[10] The grating transmission in 0^{th} order is calculated by Wellhöfer et al. in [63] to $T_{\text{Grating 0th order}}(40\,\text{eV})$=0.46 and $T(120\,\text{eV})$=0.14 at an incidence angle $\alpha = 87\,°$. The grating transmission at 1^{st} FEL order is estimated with the experimentally determined value of 0.075 for $h\nu$=88.3 eV in [92] (c_{ff}=2).

Beschreibung	$T(40\,\mathrm{eV})$	$T(120\,\mathrm{eV})$	reference
$T_{\mathrm{BL}}^{\mathrm{attenuator}}(p_{\mathrm{set}}^{\mathrm{att}}$ =5.5e-2 mbar)	9.7e-3	1.08e-1	40eV: measured 120eV: eq. 3.13
$T_{\mathrm{BL}}^{\mathrm{attenuator}}(p_{\mathrm{set}}^{\mathrm{att}}$ =5.0e-2 mbar)	1,59e-2	1,37e-1	
$T_{\mathrm{BL}}^{\mathrm{attenuator}}(p_{\mathrm{set}}^{\mathrm{att}}$ =4.7e-2 mbar)	2,02e-2	7,06e-1	
$T_{\mathrm{BL}}^{\mathrm{filter\ Al}}(200\,\mathrm{nm})$	6.3e-1	6.6e-3	[68]
$T_{\mathrm{BL}}^{\mathrm{filter\ Polyimid}}(55\,\mathrm{nm})$	2e-1	8.3e-1	[68]
$T_{\mathrm{BL\ 0^{th}\text{-}order}}^{\mathrm{losses}}$ ($\alpha_{\mathrm{Grating}} = 87\,°$)	0.34	0.1	[92] and footnote 10
$T_{\mathrm{BL\ 1^{st}\text{-}order}}^{\mathrm{losses}}$ (c_{ff}=2, $h\nu$=88.3 eV)	0.0	0.075	[92] and footnote 10
$T_{\mathrm{SDU}}^{\mathrm{losses}}$ (per arm)	0.65	0.72	[91]
$T_{\mathrm{SDU}}^{\mathrm{filter\ pump\text{-}arm\ Al}}(300\,\mathrm{nm})$	5e-1	7.7e-5	[68]
$T_{\mathrm{SDU}}^{\mathrm{filter\ probe\text{-}arm\ Zr}}(500\,\mathrm{nm})$	1e-28	1.9e-1	[68]
$T_{\mathrm{SDU}}^{\mathrm{cutting\ mirror\ pump\text{-}arm}}$	0.58		figure 3.6
$T_{\mathrm{SDU}}^{\mathrm{cutting\ mirror\ probe\text{-}arm}}$	0.42		figure 3.6

Table 3.1.: Theoretical transmission values at first ($h\nu_{\mathrm{pump}}$=40 eV) and third harmonic ($h\nu_{\mathrm{probe}}$=120 eV) wavelength of all relevant optical elements of the beamline (BL) and the split and delay unit (SDU). The transmission of the gas attenuator and the beamline is determined as described in the text. Three settings of the attenuator are distinguished with the set point pressure: $p_{\mathrm{set}}^{\mathrm{att}}(N_2)$ =5.5e-2 mbar for dataset number II | $p_{\mathrm{set}}^{\mathrm{att}}(N_2)$ =5.0e-2 mbar for datasets 9117, III, IV and V | $p_{\mathrm{set}}^{\mathrm{att}}(N_2)$ =4.7e-2 mbar for dataset number 9100.

3.5. Spot Size Determination

For determining the fluence at the sample, it is crucial to know the spot size of the pump beam at the sample. To measure the beam diameter of a single FEL shot within the 1MHz burst of 400 pulses a camera with a readout speed as fast as 1μs would be required. Such tools are not available in the setup. Instead we measured the burst integrated fluorescence signal on a Cerium doped YAG screen with a standard CCD camera. The camera readout is triggered with 10Hz repetition rate. A single burst image is shown in figure 3.11. To determine the size of the beam imprint on the sample, one has to take the geometry difference between the sample and that of the screen with respect to the FEL into account, which is depicted in figure 3.10). The footprint on the sample can be determined by projecting the dimensions onto the tilted sample:

$$x_{\text{long}} = \frac{1}{\cos\left(\theta_{\text{longitudinal}}\right)} \times tx_{\text{vert}} = 8.2 \times x_{\text{vert}} \tag{3.17}$$

$$x_{\text{trans}} = \frac{1}{\cos\left(\theta_{\text{horizontal}}\right)} \times tx_{\text{horz}} = 1.4 \times x_{\text{horz}} \quad . \tag{3.18}$$

Here $x_{\text{vert/horz}}$ refers to the beam dimension on the screen and $x_{\text{long/trans}}$ the dimension on the sample (see footnote 11). The angles $\theta_{\text{long/horz}}$ measure the tilt of the sample relative to the vertical/horizontal axis (see figure 3.10). When the beamline is used in 1$^{\text{st}}$ diffraction order the spot size varies. The beam size of the FEL on the sample[11] is shown in figure 3.11 and table 3.2. The beam size difference for the two beamline settings is quantified in figure 3.12.

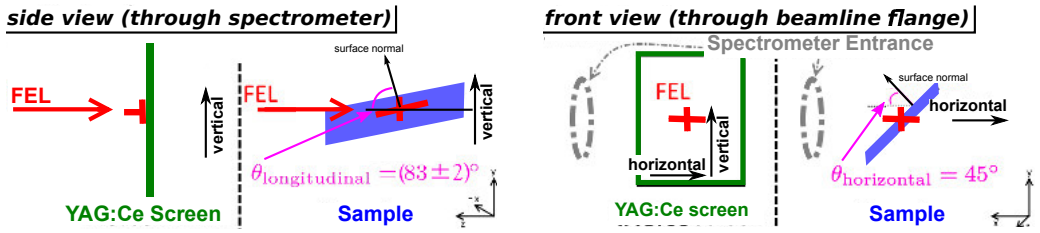

(a) Side View. The sample surface normal is tilted with respect to the beam direction by $\theta_{\text{longitudinal}} = (83 \pm 2)\,°$ while the screen surface normal is parallel to it.

(b) Front View (perspective of the photons). The sample surface normal is tilted relative to the horizontal axis by $\theta_{\text{horizontal}} = 45\,°$.

Figure 3.10.: Measurement geometry for the beam size determination: A picture of the FEL intensity distribution is taken when the beam hits the YAG:Ce screen. The spot sizes on the sample can than be calculated. Therefore the longitudinal ($\theta_{\text{longitudinal}}$, left figure) horizontal tilt ($\theta_{\text{horizontal}}$, right figure) of the sample with respect to the screen must be taken into account.

[11] While the beam size on the YAG can be described in the natural coordinates (horizontal and vertical), the ones of the sample have to be expressed relative to the sample surface coordinates (this is caused by the sample tilt relative to the horizontal as sketched in figure 3.10). I differentiate the axis in FEL direction as longitudinal sample direction (x_{long}) and that perpendicular to the FEL direction and sample surface normal, as transversal sample direction (x_{trans}).

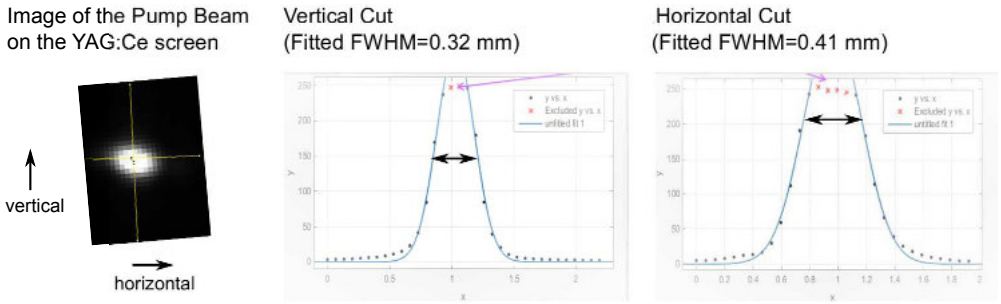

(a) First order FEL (pump) imprint on the YAG:Ce screen with the beamline set in 0^{th} diffraction order. The beam size is (FWHM-values of Gaussian Fit with 95% fitting confidence interval): $x^{\text{pump}}_{\text{vert}} = (0.32 \pm 0.01)\,\text{mm}$ and $x^{\text{pump}}_{\text{horz}} = (0.41 \pm 0.02)\,\text{mm}$. Not, that the YAG:Ce crystal was saturating. Therefore I excluded the saturated pixels from the data fitting which is therefore relying on the slope at the shoulders.

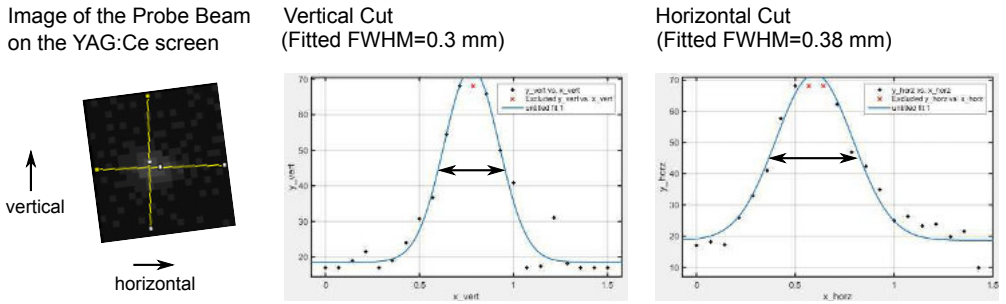

(b) Third order FEL (probe) imprint on the YAG:Ce screen (FWHM-values of Gaussian Fit and 95 % fitting confidence interval): $x^{\text{probe}}_{\text{vert}} = (0.3 \pm 0.05)\,\text{mm}$ and $x^{\text{probe}}_{\text{horz}} = (0.38 \pm 0.07)\,\text{mm}$.

Figure 3.11.: The evaluated pictures of the YAG:Ce screen illuminated with the FEL passing the pump/probe arm of the SDU (top/bottom). The image resembles the averaged beam size of the 400 pulses arriving within one burst. The images were saved right after Run 9113 (Run 9113 ends at 03:48 o'clock 12.2.2013).

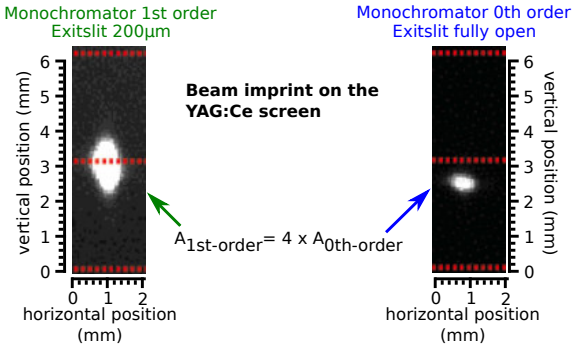

Figure 3.12.: Image of the 1^{st} diffraction order beam (left, BL settings: $h\nu_{\text{Monochromator}}$=120 eV, Exitslit WSU=200 μm, $c_{ff} = 2$, α=87.875 °) compared to that at 0^{th} diffraction order of the grating (right, BL settings: α=87°). The beam in of the 0^{th}-order geometry is smaller than that in 1^{st}-order ($A_{1^{st}\text{-order}} = 4 \cdot A_{0^{th}\text{-order}}$).

SDU arm	size on screen (vertical and horizontal)	size on sample (longitudinal and transversal)	Area on sample
Pump	$x_{\text{vert}} = (0.32 \pm 0.01)\,\text{mm}$	$x_{\text{long}} = (3 \pm 1.2)\,\text{mm}$	$A_{\text{pump}} = (1.5 \pm 0.6)e\text{-}6\,\text{m}^2$
	$x_{\text{horz}} = (0.41 \pm 0.02)\,\text{mm}$	$x_{\text{trans}} = (0.7 \pm 0.02)\,\text{mm}$	
Probe	$x_{\text{vert}} = (0.3 \pm 0.05)\,\text{mm}$	$x_{\text{long}} = (2.5 \pm 2.2)\,\text{mm}$	$A_{\text{Probe}} = (1.3 \pm 1)e\text{-}6\,\text{m}^2$
	$x_{\text{horz}} = (0.38 \pm 0.15)\,\text{mm}$	$x_{\text{trans}} = (0.53 \pm 0.02)\,\text{mm}$	

Table 3.2.: Pump- and probe spot at the vertical screen and the estimated size at the sample. Beamline settings: Diffraction order: 0^{th}, α=87 °. The image is the integrated intensity image of one FEL burst containing 400 pulses. The errors are calculated with the standard propagation of uncertainty. Numerical values for the error of the screen size represent the 95 % confidence interval of the fit (see figure 3.11). Numerical value of of the longitudinal tilt angle uncertainity $\Delta\theta_{\text{long}} = \pm 2\,^\circ$ is given by the measurement precision (see figure 3.10(b)). The pump beam area on the sample is bigger than that of the probe beam by a factor $A_{\text{pump}}/A_{\text{probe}} = 1.15$.

3.6. Fluence of Pump and Probe Beam

3.6.1. Pump Fluence Determination

A common quantity to classify the amount of absorbed pump power is the absorbed energy per area, the fluence Φ^{pump}:

$$\Phi^{\text{pump}} = I^{\text{pump}}_{\text{sample}} \, / A \; . \tag{3.19}$$

The fluence Φ^{pump} is a time and area integrated measure for the amount of absorbed pump photons per pulse. Here I_{Sample} denotes the pump beam energy and A the spot size of the pump beam at the sample. In our setup it is not possible to determine the pump beam energy. Also the PG beamline provides no calibrated beam energy monitor.

To determine the FEL beam energy at the sample position, the beamline transmission is calculated and the beam energy measured at the gas monitor detector (GMD) $I^{\text{FEL}}_{\text{tunnel}}$ propagated to the sample which is located 15 m downstream. For that purpose, the transmission $T^{\text{pump-arm}}_{\text{total}}$ of all optical elements between sample and GMD (see equation 3.15) has to be taken into account. The pump beam energy on the sample $I^{\text{pump}}_{\text{sample}}$ can than be calculated:

$$I^{\text{pump}}_{\text{sample}} = I^{\text{pump-arm}}_{\text{sample}} = T^{\text{pump-arm}}_{\text{total}} \cdot I^{\text{FEL}}_{\text{Tunnel}} \quad . \tag{3.20}$$

The total beamline transmission depends on the absorber settings as well as on the filters and general looses. Additionally one has to take into account, that the transmission in the two arms of

the split and delay unit (SDU) is not necessarily constant. Due to pointing fluctuations of the FEL at the beam cutting mirror a variation of the horizontal FEL pointing X^{FEL} will translate into a variation of the Transmission $T_{\mathrm{total}}^{\text{pump-arm}} = T_{\mathrm{total}}^{\text{pump-arm}}(X^{\mathrm{FEL}})$ (sketch and qualitative description in section 3.2.3). An additional, technically unexpected source for transmission variations was recognized during the data analysis. A variation of the transmission with different delay settings of the SDU $\Delta t_{\text{pump-probe}}$ was found, which leads to $T_{\mathrm{total}}^{\text{pump-arm}} = T_{\mathrm{total}}^{\text{pump-arm}}(X^{\mathrm{FEL}}, \Delta t_{\text{pump-probe}})$. For the following transmission determination I will separate the overall transmission $T_{\mathrm{total}}^{\text{pump-arm}}$ into three factors and describe their determination subsequent in this section:

$$\begin{aligned} &T_{\mathrm{total}}^{\text{pump-arm}}(X^{\mathrm{FEL}}, \Delta t_{\text{pump-probe}}, \text{BL settings}) = \\ &T_{\mathrm{F1}}(\text{BL settings}) \cdot T_{\mathrm{F2}}(X^{\mathrm{FEL}}) \cdot T_{\mathrm{F3}}(\Delta t_{\text{pump-probe}}) \ . \end{aligned} \tag{3.21}$$

Transmission Factor 1 (Beamline Settings)

This factor is determined with help of referenced transmission values. The referenced transmissions T for both first and third FEL harmonic ($h\nu$=40/120eV) for all elements are summarized in table 3.1. Table 3.3 summarizes the transmission values of the two arms of the SDU resulting from the different settings of the beamline for the discussed pump probe experiments.

Strategy for the Experimental Determination of the Transmission Factor 2 and 3

While the beamline setting dependent Factor T_{F1} of the transmission can be calculated with tabulated values, this is not the case for the two factors describing the transmission dependence on beam pointing and delay. Instead, the transmission factors $T_{\mathrm{F2/F3}}$ of equation (3.21) are determined experimentally using the photon peak and relation:

$$T_{\mathrm{F2/F3}}^{\text{relative}}(X^{\mathrm{FEL}}, \Delta t) = \frac{I_{\mathrm{Sample}}^{\text{relative}}}{I_{\mathrm{FEL}}^{\text{relative}}}(X^{\mathrm{FEL}}, \Delta t_{\text{pump-probe}}). \tag{3.22}$$

It is $I_{\mathrm{Sample}}^{\text{relative}}$ the relative beam energy measured at the sample, (photonpeak area, see figure 5.3). $I_{\mathrm{FEL}}^{\text{relative}}$ denotes the relative beam energy of the FEL measured at the GMD. The following formula is used to calculate these quantities with the measured beam energy of the FEL in the GMD I_{FEL} and the photonpeak intensity $I_{\mathrm{Photonpeak}}$:

$$\begin{aligned} I_{\mathrm{Sample}}^{\text{relative}} &= \frac{I_{\mathrm{Photonpeak}}}{I_{\mathrm{Photonpeak}}(\text{reference})} \\ I_{\mathrm{FEL}}^{\text{relative}} &= \frac{I_{\mathrm{FEL}}}{I_{\mathrm{FEL}}(\text{reference})}. \end{aligned} \tag{3.23}$$

If the reference transmission is known, the absolute transmission can be calculated:

$$T_{\mathrm{F2/F3}}(X^{\mathrm{FEL}}, \Delta t_{\text{pump-probe}}) = T_{\mathrm{F2/F3}}(\text{reference}) \cdot T_{\mathrm{F2/F3}}^{\text{relative}}(X^{\mathrm{FEL}}, \Delta t_{\text{pump-probe}}). \tag{3.24}$$

As reference value for the beampointing, the value which was measured when the splitting ratio was determined ($X^{\mathrm{FEL}}_{\mathrm{Tunnel}}(\mathrm{reference}) = 0.52\mathrm{mm}$ see figure 3.6) is chosen. To increase the amount of evaluable data the reference delay is not a single value but all delays within $-3ps < \Delta t(\mathrm{reference}) < -1.5\mathrm{ps}$. This choice is justified because the transmission variation can be neglected for these delay settings (see figure 3.15). The transmission $T_{\mathrm{F2/F3}}(\mathrm{reference})$ at these reference values for $X^{\mathrm{FEL}}(\mathrm{reference})$ and $\Delta t_{\text{pump-probe}}(\mathrm{reference})$ is assumed to be 1:

$$T_{\mathrm{F2/F3}}(\mathrm{reference}) = T_{\mathrm{F2/F3}}(X^{\mathrm{FEL}}_{\mathrm{Tunnel}} = 0.52\mathrm{mm}, \text{-}3 < \Delta t_{\text{pump-probe}} < \text{-}1.5\mathrm{ps}) = 1. \tag{3.25}$$

Transmission Factor 2 (Beam Pointing)

The beam pointing at the cutting mirror of the SDU determines the ratio of beam energy in the two arms (see section 3.2). Since the beam position is measured in the GMD Tunnel, it is possible to trace the transmission as a function of position. The recorded relative transmission for different positions of the FEL in the GMD Tunnel is shown in figure 3.13[12]. A linear regression gives the relation between transmission and beampointing:

$$T^{\mathrm{relative}}_{\mathrm{F2}}(X^{\mathrm{FEL}}_{\mathrm{Tunnel}}, \Delta t \in \{\text{-}3\mathrm{ps}; \text{-}1.5\mathrm{ps}\}) = 1.4 - 0.76 \cdot X^{\mathrm{FEL}}_{\mathrm{Tunnel}} \quad . \tag{3.26}$$

Additionally to the pointing drifts measured on a 10Hz basis in the GMD Tunnel, the pointing fluctuates systematically during the FEL burst (1 MHz). In figure 3.14 the relative transmission $T^{\mathrm{relative}}_{\mathrm{F2}}$ is plotted as a function of FEL-shot number. The observed systematic change of transmission during the burst must be connected to a pointing variation of the FEL beam a the cutting mirror. As no functional dependency is expected, a smoothed curve through the data points is used for defining the transmission of the pump beam for the different FEL shot numbers.

Transmission Factor 3 (Pump-Probe Delay)

While a linear relation between beampointing and transmission could be found in figure 3.13, this is not possible for the relation of transmission and SDU delay $\Delta t_{\text{pump-probe}}$. Instead an interpolation table is used to define the relative transmission $T^{\mathrm{relative}}_{\mathrm{F3}}$ for every setting of the SDU delay $\Delta t_{\text{pump-probe}}$. This relation and the interpolated trace is shown in figure 3.15.

Discussion of the Transmission Variation and Experimental Boundaries

The strong variation of the transmission with the set delay between the two arms SDU figure 3.15 is unexpected. A possible reason is that the aluminum filter, is not homogeneous in thickness. If the delay is changed, the position of the beam on the filter is changed. In case of an inhomogeneous

[12] Note, that the position of the beam in the GMD Tunnel is not determined for every shot of the FEL. Instead it is integrated for all shots in one burst and available only with a 10 Hz repetition rate.

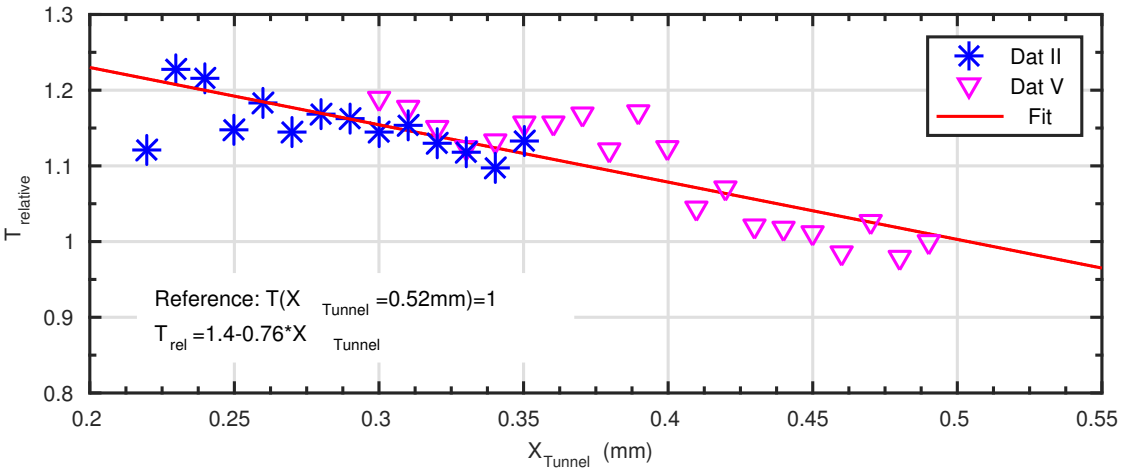

Figure 3.13.: The relative transmission $T_{\mathrm{F2}}^{\mathrm{relative}}(X_{\mathrm{Tunnel}}^{\mathrm{FEL}})$ of the pump arm of the SDU as a function of beam pointing. The pointing $X_{\mathrm{Tunnel}}^{\mathrm{FEL}}$ of the FEL beam is measured in the GMD Tunnel. The transmission of the datasets II and V was measured at delay values between $-3\,\mathrm{ps} < \Delta t_{\mathrm{SDU}} < -1.5\,\mathrm{ps}$ where the delay dependence of the transmission can be neglected (see next paragraph). It is normalized to the (extrapolated) transmission value at position $X_{\mathrm{Tunnel}}^{\mathrm{FEL}} = 0.52$. For this position, the splitting ratio is known from figure 3.6 (pump/probe: 0.58/0.42).

thickness, this would lead to a reduced transmission. The thickness of the used filter-foils could not be characterized, so this hypothesis could not be verified.

An additional fact has to be commented. The setup of the SDU does not allow a separate blocking of the probe arm, while the pump arm is unblocked. This means, that all described transmission measurements are done with both, pump- and probe beam arriving at the sample. It is not expected, that the low fluence of the probe-arm beam at the sample ($\Phi_{\mathrm{max}}^{\mathrm{probe}} < 0.01\,\mu\mathrm{J/cm^2}$) induces changes in the reflectivity. I assume, that the reflected fraction of the pump beam, measured with the photon peak intensity $I_{\mathrm{Photonpeak}}$ is independent of the probe beam appearance.

Fluence Calculations

Knowing the pump beam energy at the sample $I_{\mathrm{Sample}}^{\mathrm{Sample}}$ (see previous sections and equation (3.20)) and the spot size A of the beam at the sample (section 3.5), the pump fluence can be calculated with equation 3.19. The average pump fluence for the four datasets are summarized in table 5.3.

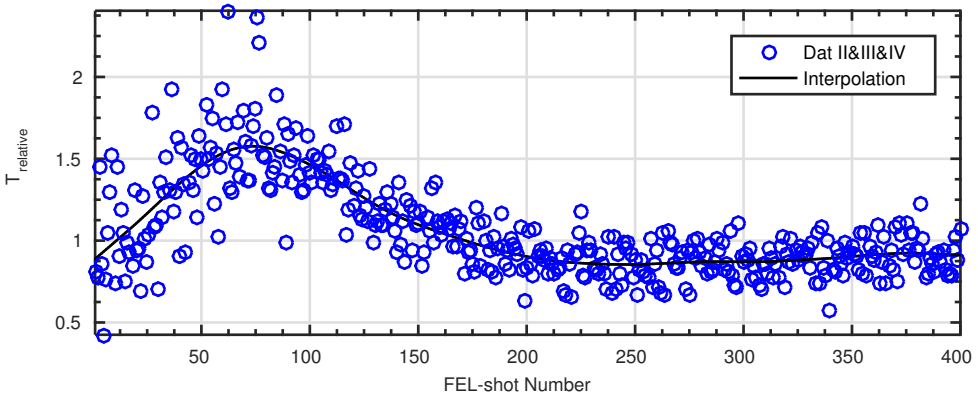

(a) Intra-burst transmission for the first three saved experiments (II-IV). Blue circles mark the average transmission for all datasets. The black line shows an interpolation, used as a look-up table for the intra-burst transmission.

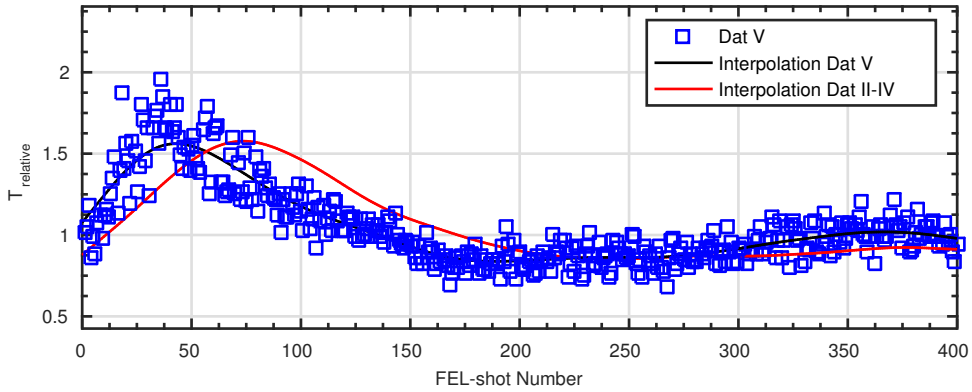

(b) Intra-burst transmission for the last saved experiment (V). Blue Squares mark the average transmission for all datasets. The black line shows an interpolation, used as a look-up table for the intra-burst transmission. The red line shows the curvature for the first three experiments from the figure above.

Figure 3.14.: The relative transmission $T_{\mathrm{F2}}^{\mathrm{relative}}(X^{\mathrm{FEL}})$ of the setup varies systematically during the FEL burst (1 MHz). The dependency is described with a smoothed curvature which is saved as a look-up-table for correcting the data. It varied during the data-acquisition. Therefore two look-up tables are saved.

Dataset	$I^{\text{FEL}}_{\text{Tunnel}}$ * (μJ/pulse)	SDU arm	Transmission T_{F1}		probe beam energy $I_{\text{Sample}}(\mu J/\text{pulse})$	
			$h\nu =$ 40eV	= 120eV	$h\nu =$ 40eV**	= 120eV***
II	7.1	pump	6.4e-4	1.5e-8	5.9e-3	-
		probe	0	2.6e-5	-	0.9e-6
III	6.6	pump	1.3e-4	1.2e-8	1.0e-3	-
		probe	0	2.1e-5	-	0.7e-6
IV	6.9	pump	3.9e-4	1.4e-8	3.4e-3	-
		probe	0	2.4e-5	-	0.8e-6
V	7.2	pump	1.0e-3	2.2e-6	9.2e-3	-
		probe	0	3.9e-3	-	140e-6
9115	6.6	pump	blocked			
		probe	0	1.4e-4	-	4.5e-6
9117	10.0	pump	1.6e-4	7.8e-8	1.3e-3	-
		probe	0	1.4e-4	-	6.8e-6
9100	6.1	BL$^{\diamond}$	0	0.3e-4	-	1.1e-6

Table 3.3.: Beamline transmission and the time averaged FEL beam energy of all datasets. *...The FEL beam energy is measured in the GMD Tunnel. **...The pump beam energy ($h\nu = 40\,\text{eV}$) in this table corresponds to the "central" part of the saved data (see figure 5.5). ***...The probe beam beam energy is approximated with equation (3.27). $^{\diamond}$...Dataset 9100 is recorded with the grating set to 1$^{\text{st}}$ diffraction order and the beam was directly traveling to the sample without passing any of the SDU arms.

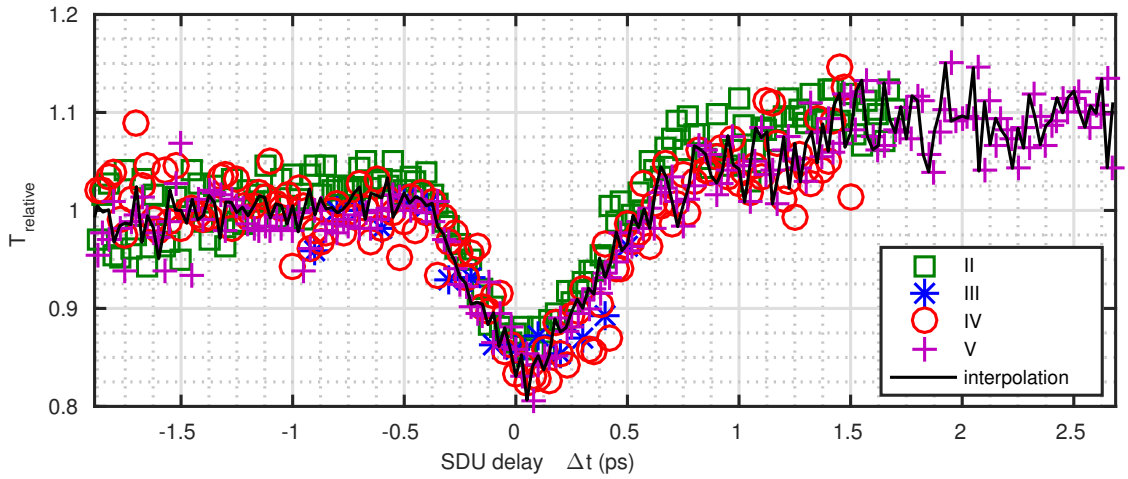

Figure 3.15.: Relative transmission of the pump arm of the SDU as a function of the delay $T_{\mathrm{F3}}^{\mathrm{relative}}(\Delta t_{\mathrm{pump\text{-}probe}})$. No functional relation can express the dependency. Therefore transmission and delay are correlated by using a nearest neighbor interpolation which is shown in black.

3.6.2. Probe Fluence Determination

Knowing the absolute probe beam energy at the sample is important to classify the expected and measured probe spacecharge effects. It is calculated with the Transmission values T_{F1} tabulated in 3.1 and the following equation:

$$I_{\mathrm{Sample}}^{\mathrm{probe}} = T_{\mathrm{F1}}(h\nu = 40\,\mathrm{eV}) \cdot I_{\mathrm{Tunnel}}^{\mathrm{FEL}} \cdot f_{3^{\mathrm{rd}}\text{-harmonic}} \ . \tag{3.27}$$

Here $I_{\mathrm{Tunnel}}^{\mathrm{FEL}}$ is the beam energy of the 1$^{\mathrm{st}}$-harmonic of the FEL measured in the GMD-Tunnel and $f_{3^{\mathrm{rd}}\text{-harmonic}}$ the beam energy fraction of the third harmonic relative to that of the first one. This ratio is assumed to be:

$$f_{3^{\mathrm{rd}}\text{-harmonic}} = 0.5\,\% \tag{3.28}$$

which was experimentally determined in [61] and [92]. Variations of the probe beam energy, as they are caused by beam pointing fluctuations etc. (see section 3.6.1) are not taken into account for the probe fluence determination. The probe beam intensities $I_{\mathrm{Sample}}^{\mathrm{probe}}$ of the different datasets are tabulated in table 3.3.

3.7. Sample Characterization and Conditions

As sample for our experiments, a $1 \times 1\,\mathrm{cm}^2$ sized piece of a standard waver gallium arsenide (GaAs) (100)$\pm 0.1\,^\circ$ with a thickness of $625 \pm 25\,\mu$m is used. The waver piece is clamped on a sample holder which provides a tungsten filament for heating. An electrical connector allows the sample to be

biased which enables heating with electron bombardment. To assure that the crystal does not charge up during the photoemission measurements we chose a Silicon doped crystal with a Si doping density of $n = (1-5)10^{18}\,\mathrm{cm}^{-3}$. For a rough surface cleaning, the $1 \times 1\,\mathrm{cm}^2$ piece the latter one is cleaned in an ultrasonic bath with Aceton and 2-Propanol. Subsequent it is placed into the UHV system. Once in vacuum, the sample surface is cleaned from surface oxide layers with subsequent cycles of sputtering (Argon, sample current $I_{\text{sputter-current}} \approx 20\,\mu A$, duration 20 min) and annealing ($T_{\text{sample}} \approx 550°\mathrm{C}$). The cleaning procedure is described in the master thesis of L. Wenthaus [95] and is similar to that used by J. Wolan et al. in [97].

The surface reconstructions of Gallium arsenide show a rich phase diagram. With LEED measurement in combination with an analysis of XPS spectra (figure 3.16) it is possible to monitor the reconstruction[98][99]. Our sample preparations shows a $c(2 \times 8)$ reconstruction of the surface. With a base pressure of $p \approx 1 - 3 \times 10^{-9}\,\mathrm{mbar}$ in the experimental chamber, it is not possible to maintain the clean surface for long times. Instead we accepted the grow of a surface-adlayer of physisorbed H_2O. With XPS on the O1s level and the valence states compared to literature values of an UPS study in [100], we determined the water layer thickness to be below 0.5 monolayer.

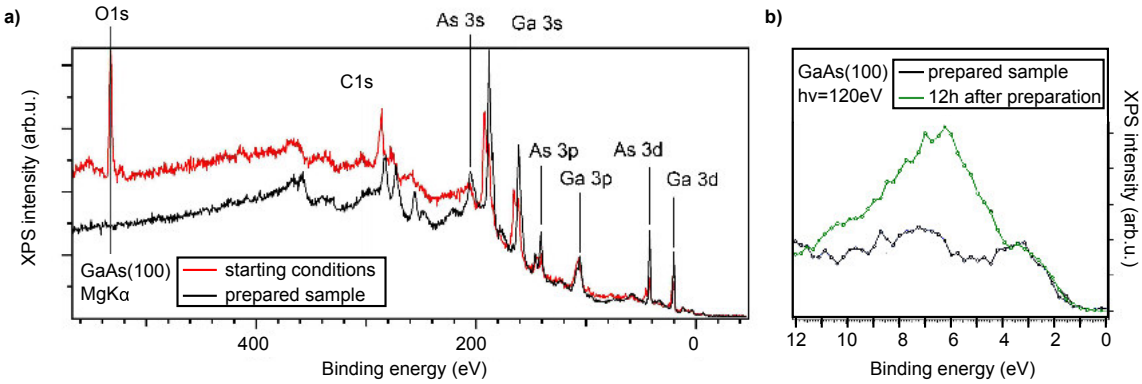

Figure 3.16.: Figure taken and modified from [95]. X-ray spectra of the sample to show the sample cleanliness. a) Core Level Spectrum of the Gallium arsenide crystal recorded with the x-ray gun and the Hemispherical analyzer after the sample is brought to the UHV system (red) and several cleaning cycles (black). b) Valence band spectrum of the sample recorded with the third FEL harmonic (Monochromator settings: $h\nu = 120\,\mathrm{eV}$, 200 lines/mm grating, $c_{ff} = 2$, $WSU = 200\,\mu\mathrm{m}$, only spectra with one count/FEL-shot at the detector assuring low spacecharge effects). Black lines show the spectrum after preparation and green after 12 hours in the UHV chamber. A comparison with UPS spectra in [100] shows, that the increase in valence state intensities is caused by a surface adlayer of H_2O molecules. The O1s levels were not recorded under this conditions.

3.7.1. Sample Mounting

The endstation is equipped with a flexible sample holder mounted on a 4-axis manipulator including a Helium cryostat. A sketch is shown in figure 3.17. It is described in detail e.g. in [101][95]. During the measurements described in this work, the sample position was not changed.

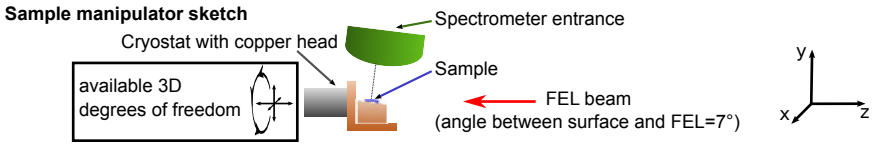

Figure 3.17.: Sketch of the UHV manipulator setup which holds the samples. It can be moved in three dimensions and rotated around the z-axis. The scattering geometry is also shown in the inset in figure 3.8 and 3.10.

4. Simulated Effects - Pump Induced Spaceharge

As explained in the previous section 2.1.3, the spacecharge field caused by the pump beam electrons affects the spectral shape of the detected probe beam electrons. To disentangle pump-induced effects in the sample, which are of interest in the performed experiments, and these caused by pump beam induced spacecharge, spacecharge tracking simulations are performed. The influence of different parameters of the pump beam electrons (pulse length, spot size, spatial distribution) onto the detected spacecharge distortions of the probe electrons is investigated. With the conclusions drawn from these simulations, it is possible to partly interpret the performed pump-probe experiments in chapter 5. For the simulation of the pump beam induced spacecharge, a numerical simulation is done with the open source "Astra" code[102]. The Astra program is capable of tracking particles under external and internal fields. A short summary of the relevant settings can be found in the appendix chapter A.1.1. The results of the simulations and a discussion are presented in in this chapter. After introducing the simulated particle distributions, the spatial evolution of the spacecharge induced electrical fields is shown. To understand the delay independent influence of the spacecharge effects, simulations at constant delay with variations in the pump beam distribution (pump beam radius and pump beam spectral distribution) are presented. Finally, the results of a delay dependent spacecharge analysis are summarized.

4.1. Input Electron Distributions

In this section, the spectra used as input for the simulations are referenced. The photoelectrons which have to be used as an input for the Astra-program can be divided into two classes:

- probe beam photoelectrons ("passive" particles, see section A.1.1)
- pump beam photoelectrons.

4.1.1. Probe Beam Electrons

In the experiments, only the Ga3d lines are analyzed. Therefore, the same lines are studied with the simulations. A reference spectrum for the probe electrons is shown in figure 4.1. It results of experimental data which were recorded with only the probe beam hitting the sample. An arctan-shaped background is subtracted from the experimental data before they were used as input data for the simulations. The direction/momentum distribution of the probe beam electrons was

adapted to the experimental conditions. It is defined by the angular acceptance of the spectrometer $\alpha_{\text{acceptance}} = \pm 0.9°$ and the sample mounting with respect to the spectrometer (see section 3.3). Therefore the fraction of detectable directions in the phase space is represented by a cone with an opening angle of $\alpha_{\text{probe-electrons}} = 0.9°$ centered at the detection angle of $\Phi_{\text{detection}} = 45°$ relative to the surface normal (see figure 4.2).

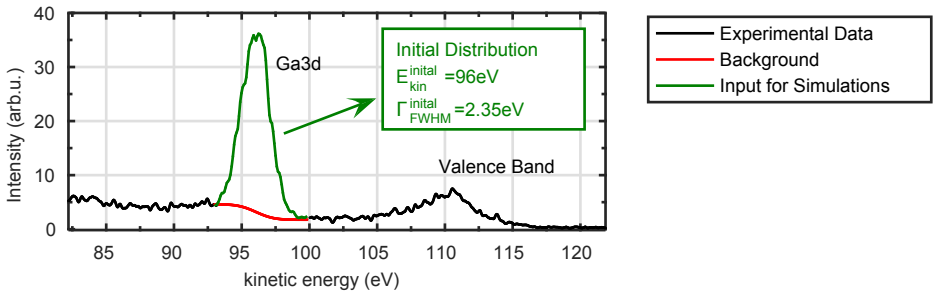

Figure 4.1.: Original spectrum of the Ga3d lines resulting from PES with the 3rd FEL harmonic (Run 9115, $h\nu^{\text{probe}}_{\text{FEL } 1^{st} \text{ pulse}}$ =120.27 eV). An arctan-shaped background is subtracted from the data. A Gaussian fit gives for this initial probe beam electron distribution $E^{\text{initial}}_{\text{kin}}$=96 eV and $\Gamma^{\text{initial}}_{\text{FWHM}}$=2.35 eV.

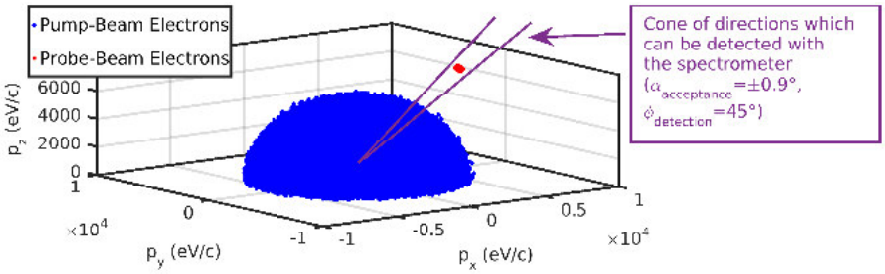

Figure 4.2.: Momentum distribution of the simulated probe beam (red) and pump beam (blue) electron distributions. Only probe electrons reaching the detector with $\alpha_{\text{acceptance}} = 0.9\,°$ centered at the detection angle of $\Phi_{\text{Detection}} = 45\,°$ relative to the surface normal are taken into account. The pump beam electrons momentum is distributed isotropic among the three momentum directions.

4.1.2. Pump Beam Electrons

While the probe beam electron spectrum is reduced to the Ga3d lines, the full spectral distribution of the pump beam electron spectrum is required for the spacecharge simulations. Figure 4.3 shows the spectrum used to simulate the pump beam electrons. Due to the transmission limitations of the spectrometer, the pump beam spectrum could only be measured for electrons with a kinetic energy above $E_{\text{kin}} > 13$ eV. For this region of the kinetic energy, the transmission function of the spectrometer as described in section 3.3.1 shows a significant variation which was compensated by

normalizing the spectrum with the transmission function (equation 3.9). At kinetic energies below $E_{\mathrm{kin}} > 13\,\mathrm{eV}$, no electrons could be detected. As no characteristic emission lines are expected, it is possible to approximate this low kinetic energy part of the pump beam electron spectrum with a secondary electron tail. The amount of secondary electrons is quantified with the secondary electron yield (SEY):

$$\mathrm{S.E.Y.} = N_{\text{secondary electrons}}/N_{\text{all electrons}}. \tag{4.1}$$

To model the Intensity distribution dependence on the kinetic energy of the secondary electrons $I_{\mathrm{secondaries}}(E_{\mathrm{kin}})$ I used a formula which was used by Henke et. al. in[51]. They used it to fit the secondary electron tails of metal substrates.

$$I_{\mathrm{secondaries}}(E_{\mathrm{kin}}) \propto \frac{E_{\mathrm{kin}}}{(E_{\mathrm{kin}} + 2.6)^4}. \tag{4.2}$$

The resulting pump beam spectra used in the simulations are shown in figure 4.3 for three different S.E.Y. (30%, 50% and 60%). The momentum distribution of the simulated pump beam electrons is approximated with an isotropic distribution (figure 4.2).

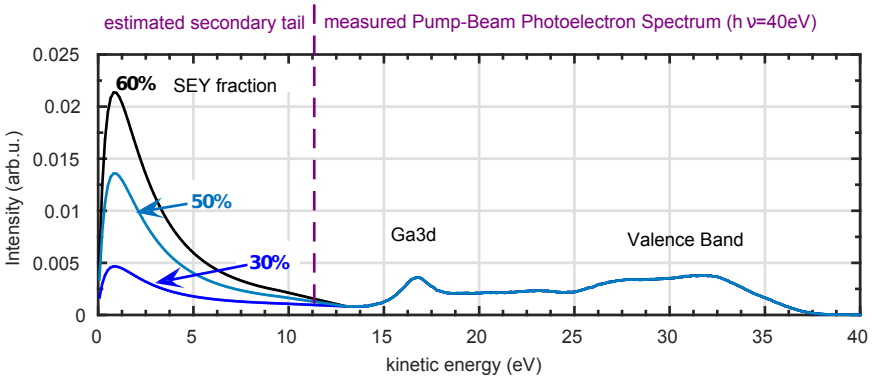

Figure 4.3.: Original spectrum of the Ga3d line resulting from PES with the 1st FEL harmonic (Run 9117, $\mathrm{h}\nu^{\mathrm{pump}}_{\mathrm{FEL}\ 1^{st}\ \mathrm{pulse}}$ =40.09eV, spectrometer transmission function is compensated [see section 3.3.1]). The transmission of electrons with kinetic energy E_{kin}<13eV is zero. Therefore the Secondary electron tail is estimated with equation (4.2). The secondary electron yield (SEY) quantifies the relative amount of secondary electrons (equation (4.1)). The highest kinetic energy is $E_{\mathrm{cutoff}} \approx 37.5\,\mathrm{eV}$.

4.2. Spatial Evolution of Typical Spacecharge Fields

The field strengths arising from typical charge densities as they are emitted in the photoemission process is spatially inhomogeneous. To illustrate this, figure 4.4 shows the radial and longitudinal field components E_{r} and E_{z} of a realistically chosen pump beam electron distribution.

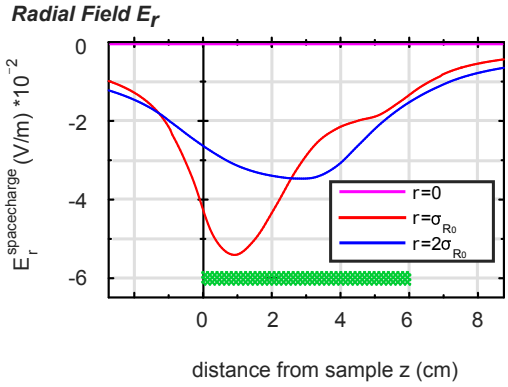

(a) Radial component of the spacecharge field E_r as a function of the longitudinal positions z. The field strength is displayed for three different distances r from the center of the electron cloud at $r_\mathrm{center} = 0$ (r$\in \{0, \sigma_{\mathrm{R0}}, 2\sigma_{\mathrm{R0}}\}$, $\sigma_{\mathrm{R0}} = 20.9\,\mathrm{mm}$).

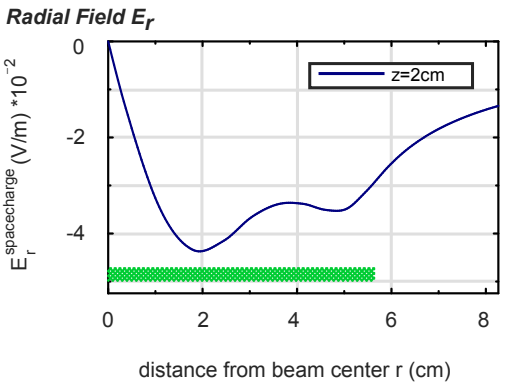

(b) Radial component of the spacecharge field E_r at constant longitudinal position (z=2 cm) as a function of the radial distance r from the electron cloud center.

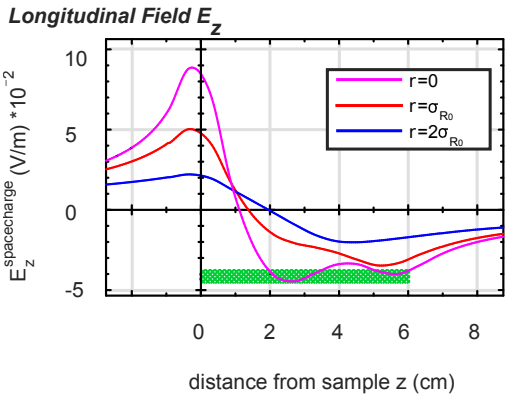

(c) Longitudinal component of the spacecharge field E_z as a function longitudinal positions z. The field strength is displayed for three different distances r from the center of the electron cloud at $r_\mathrm{center} = 0$ (r$\in \{0, \sigma_{\mathrm{R0}}, 2\sigma_{\mathrm{R0}}\}$, $\sigma_{\mathrm{R0}} = 20.9\,\mathrm{mm}$).

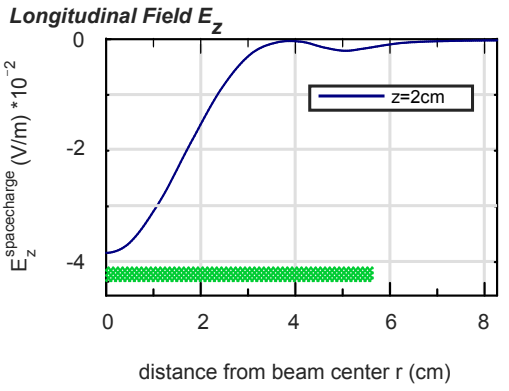

(d) Longitudinal component of the spacecharge field E_z at constant longitudinal position (z=2 cm) for different radial distances r.

Figure 4.4.: Longitudinal and radial component of the spacecharge fields simulated with Astra. A typical pump beam electron distribution was chosen (R_pump=25 μm, $N_\mathrm{pump} = 0.9 \cdot 10^5$electrons, P_pump =normal, $\tau_\mathrm{pump} = \tau_\mathrm{probe}$=10 fs). The fields are evaluated after the beam center of mass arrived at a virtual screen 2 cm after the sample surface. Green crosses mark the spatial extension of the pump- and probe electrons. Note, that the absolute field strength is very small at this long time after the emission. Nevertheless, the shape of the fields and their r/z-dependence is similar to earlier times, where they reach peak intensities of several 10s of kV/m.

4.3. Simulations at Constant Delay

4.3.1. Example Spectrum - Probe Electrons After Spacecharge Tracking

As a reference, figure 4.5 shows the probe beam electron spectrum before (green) and after (blue) being propagated through the spacecharge fields caused by the pump beam electrons. The broadening and shift are not transformed to the spacecharge induced shift $E_{\mathrm{kin}}^{\mathrm{spacecharge}}/\Gamma_{\mathrm{spacecharge}}$ (see equation (2.5)). Instead, for an easier comparison with the experimental data, the total kinetic energy/linewidth ($E_{\mathrm{kin}}^{\mathrm{detected}}/\Gamma_{\mathrm{FWHM}}^{\mathrm{detected}}$) at the detector is stated.

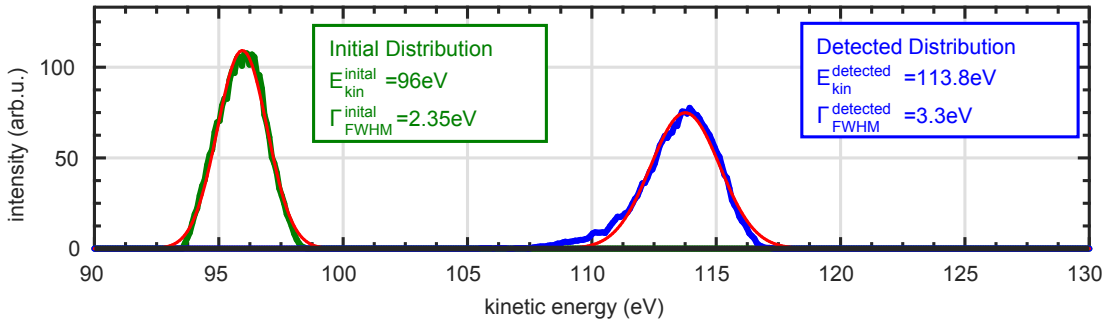

Figure 4.5.: Example for the spectral distribution of the Ga3d-line probe electrons before (green) and after (blue) being tracked through the spacecharge fields of the pump distribution. The detected kinetic energy and the linewidth are quantified by fitting with a Gaussian line (red) characterized by central position (E_{kin}) and the Full Width at Half Maximum (FWHM= $2\sqrt{2\log(2)}\sigma$). Parameters for the simulations: Pump electrons: SEY60, R_{pump}=25 μm, P_{pump}=Normal, Δt=0 ps, N_{pump}=9·10^5 electrons, pump-spectrum S.E.Y.=60 % | probe electrons: R_{probe}=10 μm, P_{probe}=Normal.

4.3.2. Influence of the Pump Beam Intensity

Figure 4.6 shows the simulated shift and broadening for a typical distribution of pump- and probe beam electrons with different pump beam intensity. With increasing number of pump beam electrons, which is proportional to the pump beam intensity, an increase of spacecharge induced shift and broadening can be observed. Shift and broadening as defined in equation (2.5) increase linearly with increasing number of simulated pump beam electrons N_{pump}.

4.3.3. Influence of the Pulselength

Simulations with different pulselengthes for pump- and probe beam in figure 4.7 show, that the temporal distribution of pump- and probe pulse in the regime of pulses lasting few 10s of 100 fs, plays no role for the spacecharge effects of the detected spectrum. A gaussian pules-shape is used with a pule-length specified as the Full Width at Half Maximum (FWHM) value. The spacecharge

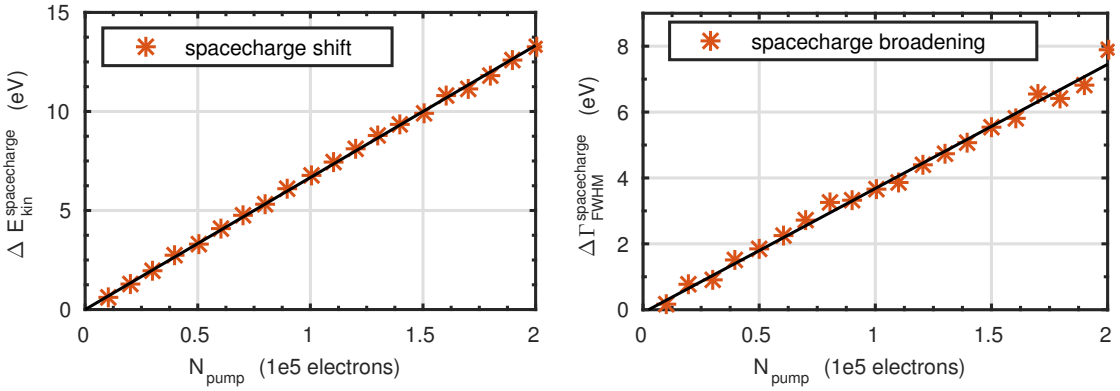

(a) Spacecharge induced shift. The black trace shows as guide for the eyes a linear fit with $\Delta E_{\mathrm{kin}}^{\mathrm{spacecharge}}[\mathrm{eV}] = 6.67 N_{\mathrm{pump}}[1e5\,\mathrm{electrons}]$.

(b) Spacecharge induced broadening. The black trace shows a linear fit with $\Delta\Gamma_{\mathrm{FWHM}}^{\mathrm{spacecharge}}[\mathrm{eV}] = 3.8 N_{\mathrm{pump}}[1e5\,\mathrm{electrons}] - 0.1$.

Figure 4.6.: Shift and Broadening for a typical distribution of pump- and probe beam Electrons at $\Delta t_{\text{pump-probe}} = 0\,\mathrm{ps}$. Simulation Parameters: $R_{\mathrm{pump}} = 68\,\mu\mathrm{m}$, $R_{\mathrm{probe}} = 63\,\mu\mathrm{m}$, $P_{\mathrm{pump}} = P_{\mathrm{probe}}$ =Normal, pump-Spectrum S.E.Y.=60 %.

induced shifts and broadenings are shown for an increasing amount of pump beam electrons. The simulated spectral shifts and broadenings are identical for pulses with pulselengthes up to τ=100 fs. Only pulses with τ=500 fs show a deviation from the other data.

4.3.4. Spacecharge at Different Distances from the Sample Surface

In figure 4.8 the spacecharge induced shifts and broadenings are plotted relative to the distance of the probe electrons from the sample. The shift [broadening] reaches its final value after 80 μm [500 μm]. As a consequence of this, for all simulations in this chapter the probe electrons are tracked until their distance from the sample surface is at least $z_{\mathrm{min}}^{\text{probe-electrons}} = 6\,\mathrm{cm}$. With this choice of a big minimal distance, all possible effects are surely taken into account.

4.3.5. Influence of the Pump and Probe Beam Spatial Distribution

As summarized in section 2.1.3 the electric field $\vec{E}_{\mathrm{spacecharge}}(\varrho(\vec{r})$ that results from charged particles distributed in vacuum can be calculated by solving the integral:

$$\vec{E}_{\mathrm{spacecharge}}(\varrho^{\mathrm{PES}}) = \frac{1}{4\pi\varepsilon_0\varepsilon_r}\int \varrho^{\mathrm{PES}}(\vec{r'})\frac{\vec{r}-\vec{r'}}{|\vec{r}-\vec{r'}|^3}dx'dy'dz' \quad \text{(Equation (2.3))}.$$

It is $\varepsilon_0/\varepsilon_r$ the vacuum/relative permittivity, $\varrho(\vec{r})$ the charge density at position $\vec{r}$ and x, y, z the three spatial dimensions. The fields and therefore the observed spacecharge induced changes in the

[1] The time delay between start and the arrival at position z can be approximated by assuming the Ga3d line is constant at $E_{\mathrm{kin}} = 100\,\mathrm{eV}$ (which corresponds to a velocity v of $v = 5.86e6\,\mathrm{m/s}$).

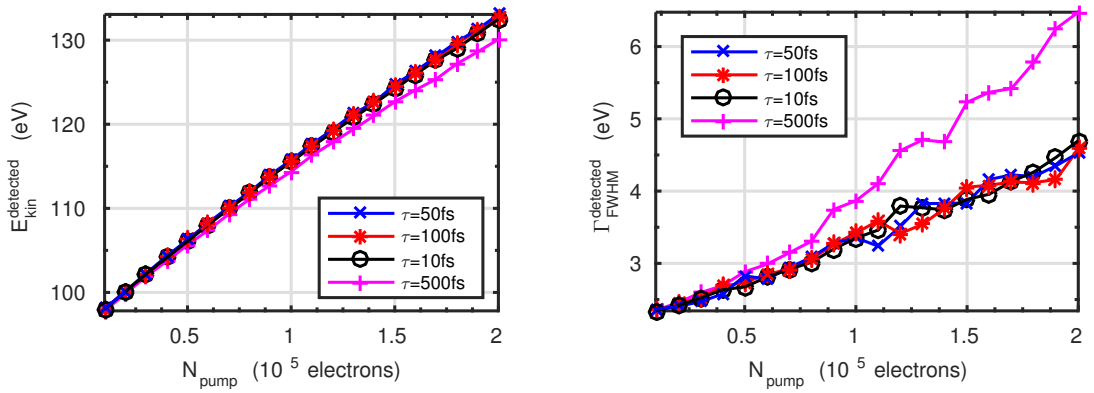

(a) The spacecharge induced shift is equal for $\tau \in \{10, 50, 100\}$fs. For pulses of $\tau = 500$fs, a reduced shift, at the same number of pump beam electrons N_{pump} is observed.

(b) As well as the shift also the spacecharge induced broadening is equal for $\tau \in \{10, 50, 100\}$fs. For pulses of $\tau = 500$fs, an increased broadening, at the same number of pump beam electrons N_{pump} is observed.

Figure 4.7.: Simulated spacecharge effects on the probe beam electron spectrum for an increasing number of pump electrons N_{pump} with different pulse lengths $\tau_{\text{pump}} = \tau_{\text{probe}} \in \{10, 50, 100, 500\}$ fs. The pulselength variations below $\tau_{\text{pump/probe}} \leq 100\,\text{fs}$ don't not affect the spacecharge induced changes. In the regime under study in the experiments ($\tau_{\text{FEL}} \approx 150\,\text{fs}$) this holds also true. A gaussian pules-shape is used with a pule-length specified as the Full Width at Half Maximum (FWHM) value. Simulation parameter: $R_{\text{pump}} = 25\mu$m, $R_{\text{probe}} = 10\mu$m, $P_{\text{pump}} = P_{\text{probe}}$ =Normal, N_{pump}=$0.5{\cdot}10^5$electrons, pump-spectrum S.E.Y.=60%.

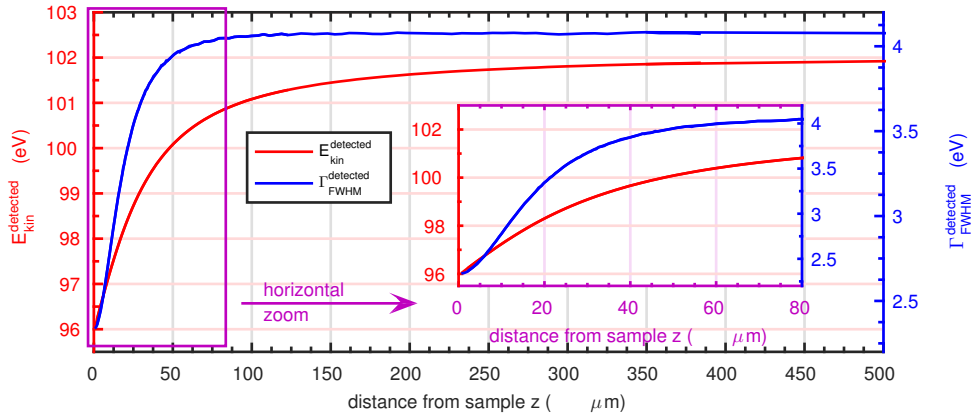

Figure 4.8.: Detected kinetic energy (red) and linewidth (blue) of the probe beam electrons at different positions after they left the sample surface. The broadening reaches its final value at $z^{\text{final}}_{\text{broadening}} \approx 100\,\mu$m ($t^{\text{final}}_{\text{broadening}} \approx 17\,\text{ps}$)[1]. The kinetic energy at $z^{\text{final}}_{\text{shift}} \approx 500\,\mu$m ($t^{\text{final}}_{\text{shift}} \approx 84\,\text{ps}$). For all other simulations shown in this chapter the probe-Ga3d electrons are tracked until they reached at least $z^{\text{probe-electrons}}_{\text{min}} = 6\,\text{cm}$ distance from the sample. Simulation parameter: $R_{\text{pump}} = 68\mu$m, $R_{\text{probe}} = 63\,\mu$m, $P_{\text{pump}} = P_{\text{probe}}$ =normal, $N_{\text{pump}} = 10^5$, τ =50 fs.

spectra depend on the spatial distribution $\varrho(\vec{r})$ of the charges. All spot shapes in this chapter are cylindrical symmetric as the spacecharge tracking relies on cylindrical symmetry. Two properties of the spatial distribution of the spacecharge inducing pump beam electrons can be varied in the simulations:

- pump beam distribution function (e.g. Normal, Flat-Top)
- beam radius.

In this section the role of these two properties on the pump beam induced spacecharge effects of the probe-electrons are analyzed.

Pump Beam Electrons Spatial Distribution

The spectral changes for three different starting distributions were simulated in this section. A flat-top distribution, a normal distribution and a beta-function like distribution (see figure 4.9). The results are summarized in figure 4.10. It turns out, that the distribution has a strong influence on the spacecharge effects. While all three distributions show a similar increase in kinetic energy for increasing number of electrons, the broadening is very different. The flat-top distribution causes no detectable broadening throughout the full region of simulated number of electrons. The intermediate dense beta-like distribution function causes a slight variation. Only the normal distribution causes a strong increase of the linewidth.

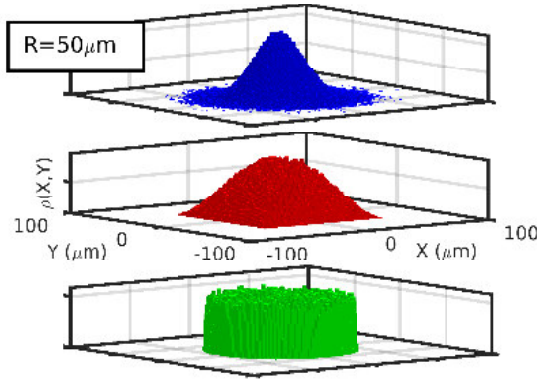

(a) Two dimensional histogram of the starting point distributions for the simulated electron clouds. The meaning of the "Radius" is depicted in the right figure.

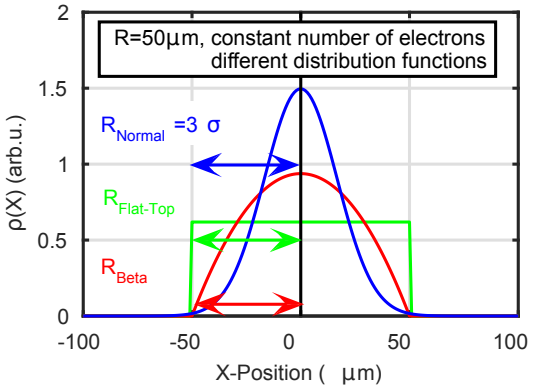

(b) A cut through the distributions along the X-axis for Y=0. The radius of all three distributions is $R_{\text{Flat-Top}} = R_{\text{Normal}} = R_{\text{Beta}(\alpha = \beta = 2)}$=50$\mu$m.

Figure 4.9.: This picture shows the three distribution functions used for the starting point distribution of the pump electrons. The left panel shows the 2D distribution, the right one a cut through the z-x plane along y=0. The three displayed distributions are a normal distribution (blue), a beta distribution (red, with $\alpha = \beta = 2$) and a flat-top distribution (green). The starting positions of the pump electrons in the simulations were spatially sorted following one of the these distribution curves. Each distribution is characterized with a radius. The definition of the readius for the different distributions is shown with arrows.

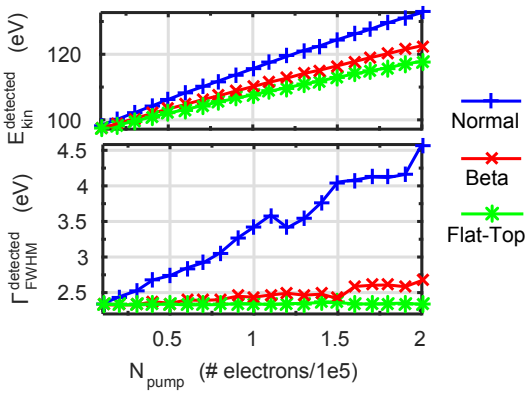

(a) Detected kinetic energy $E_{\mathrm{kin}}^{\mathrm{detected}}$ and linewidth $\Gamma_{\mathrm{FWHM}}^{\mathrm{detected}}$ with increasing number of pump electrons N_{pump}.

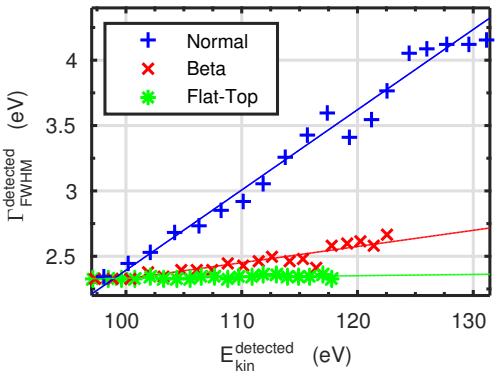

(b) Detected linewidth $\Gamma_{\mathrm{FWHM}}^{\mathrm{detected}}$ scattered vs. the detected kinetic energy $E_{\mathrm{kin}}^{\mathrm{detected}}$. The solid lines are a guides for the eye. Their slope varies for the different starting distributions.

Figure 4.10.: Different spatial distributions affect the shift and broadening differently. Both spacecharge effects are strongest for the normally distributed starting positions of the pump electrons. The flat-top distribution causes almost no broadening of the line. Simulation parameter: R_{pump}=25μm, P_{pump}=[Normal, Flat-Top and Beta], Δt=0ps | Probe electrons: R_{probe}=10μm, P_{probe}=Normal, pump-spectrum S.E.Y.=60%, τ =50fs.

Ratio of Pump and Probe Beam Radius

The spacecharge fields of the pump beam electron distribution are different for different distances r from the beam center (see figure 4.4). Therefore the ratio of probe beam to pump beam radius $R_{\mathrm{probe}}/R_{\mathrm{pump}}$ is influencing the spectral distribution of the detected probe electrons. For the same pump beam conditions, different probe radii were evaluated in figure 4.11 for normally distributed pump and probe beam electrons. While the shift is not influenced by the choice of the radius, the broadening caused by spacecharge effects is strongest in the case of equal spot radii.

Beside the relative spot sizes, also the absolute spot size alters the strength of detected spacecharge effects. Figure 4.12 shows the shift and broadening of the probe electrons for different pump spot sizes. Subfigure (a) shows, that in the case of a constant number of pump beam electrons N_{pump}, the spacecharge effects reduce with increasing spot size. In case of a constant ratio of $N_{\mathrm{pump}}/R_{\mathrm{pump}}$, shown in subfigure 4.12(b), the spacecharge effects for different pump beam radii are unaltered. The same relation was shown by Hellmann et al. in [49] for probe beam induced spacecharge.

4.3.6. Influence of the Pump Beam Secondary Electron Tail

The influence of the spectral distribution of the pump beam electrons is investigated by varying the intensity ratio between Ga3d line and secondary electron tail. This ratio is proportional to the secondary electron yield (S.E.Y.) introduced in equation (4.2). Figure 4.13 shows the spacecharge caused spectral shifts and broadenings for different values of the S.E.Y. (30%, 50% and 60%). No

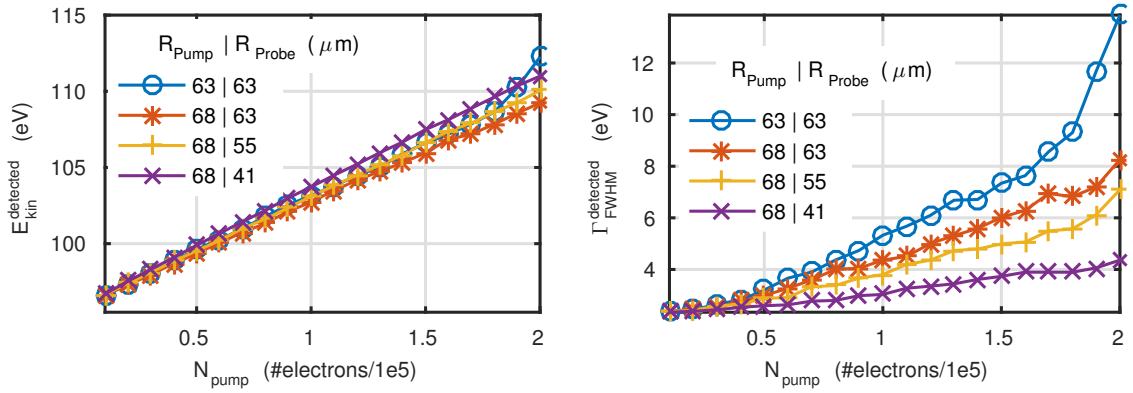

(a) The spacecharge induced shift is equivalent for all simulated spot radii.

(b) The spacecharge induced broadening is increasing with increasing number of pump beam electrons N_{pump} for all simulated radii. At constant N_{pump} the broadening is increasing with the radius of the probe beam.

Figure 4.11.: Simulated spacecharge effects on the probe beam electron spectrum for an increasing number of pump electrons N_{pump} for different Ratios of the spot radii $R_{\mathrm{pump}}/R_{\mathrm{probe}}$. Simulation parameter: $P_{\mathrm{pump}} = P_{\mathrm{probe}}$ =Normal, pump-spectrum S.E.Y.=60 %, τ =50 fs.

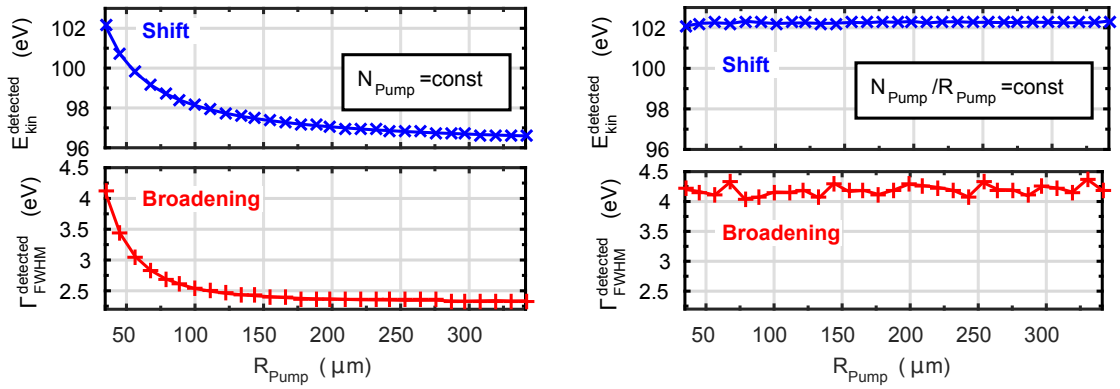

(a) The spacecharge induced shift (blue x) and broadening (red +) for a constant radius ratio and constant number of pump beam electrons ($R_{\mathrm{probe}}/R_{\mathrm{pump}} = 1.09, N_{\mathrm{pump}} = 0.5 \cdot 10^5$ electrons).

(b) The spacecharge induced shift (blue x) and broadening (red +) for a constant radius ratio and constant ratio of pump beam radius to pump beam electrons $N_{\mathrm{pump}}/R_{\mathrm{pump}} = 1449\,\mathrm{electrons}/\mu\mathrm{m}$.

Figure 4.12.: $R_{\mathrm{pump}}/R_{\mathrm{probe}}$ =1.09. Simulation parameters: $P_{\mathrm{pump}} = P_{\mathrm{probe}}$ =Normal, pump-spectrum S.E.Y.=60 %, τ =50 fs.

differences are observed. The energy distribution of the same amount of electrons N_{pump}, with the same constant maximum kinetic energy ("cut-off" energy $E_{\text{cutoff}} = 37.5\,\text{eV}$, see spectrum in figure 4.3) has no influence on the spacecharge effects.

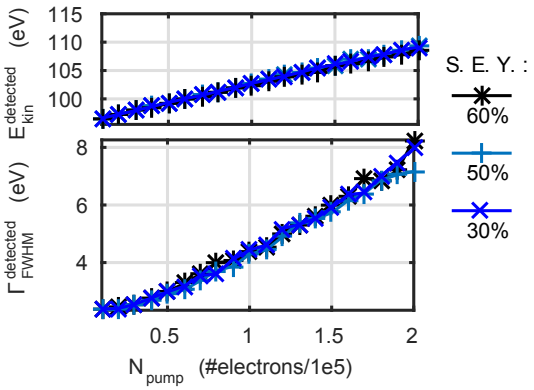

(a) Detected kinetic energy $E^{\text{detected}}_{\text{kin}}$ and linewidth $\Gamma^{\text{detected}}_{\text{FWHM}}$ with increasing number of pump electrons N_{pump}. All three secondary electron tail configurations show the same spacecharge effects.

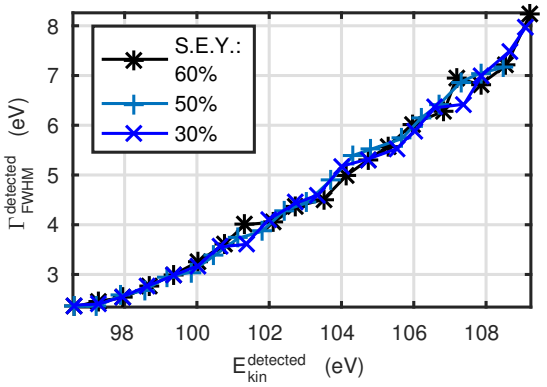

(b) Detected linewidth $\Gamma^{\text{detected}}_{\text{FWHM}}$ scattered vs. the detected kinetic energy $E^{\text{detected}}_{\text{kin}}$. Variations in the S.E.Y. cause no differences in the spacecharge effects.

Figure 4.13.: Simulated spacecharge effects on the probe beam electron spectrum for an increasing number of pump electrons N_{pump} for different secondary electron yields (S.E.Y.) of the pump beam electron distribution (see figure 4.3). Simulation parameter: $P_{\text{pump}} = P_{\text{probe}}$ =Normal, τ_{pump} =50 fs, R_{pump} =68 μm, R_{probe} =63 μm, τ_{probe} =50 fs.

4.4. Simulations with Different Pump-Probe Delays

The delay between pump- and probe pulse Δt is defined like:

$$\begin{aligned} \Delta t_{\text{pump-probe}} &= t^{\text{probe electrons}}_{\text{start}} - t^{\text{pump electrons}}_{\text{start}} \\ \rightarrow &\begin{cases} \Delta t_{\text{pump-probe}} < 0: & \text{probe electrons leave first} \\ \Delta t_{\text{pump-probe}} > 0: & \text{pump electrons leave first.} \end{cases} \end{aligned} \tag{4.3}$$

For different values of this delay, the pump induced spacecharge effects on the probe beam electrons are different (see section 2.1.3). In this section, the delay dependent behavior for different pump radii is described and quantified. After that, the influence of the pump beam intensity on the delay-dependence is analyzed.

4.4.1. Pump Beam Spot Size

In figure 4.14, the evolution of the spacecharge effects as a function of the pump-probe delay is shown for three different pump beam radii between 34.5 μm and 103.5 μm. The region relevant for

experiments with the SDU setup ($\approx \pm 3$ps) is marked with a purple box. Both, shift and broadening show the biggest variation from the initial spectrum at the temporal overlap at $\Delta t = 0$ ps. The delay dependence for shift and broadening is asymmetric for all three simulated pump beam radii. For delay values smaller than zero, the initial-values are reached faster than for delay values bigger than zero. Shift and broadening reach their initial values fastest for the smallest radius (dashed red line, $R_{\text{pump}} = 34.5\,\mu$m) and slowest for the biggest pump beam radius (solid blue line, $R_{\text{pump}} = 103.5\,\mu$m).

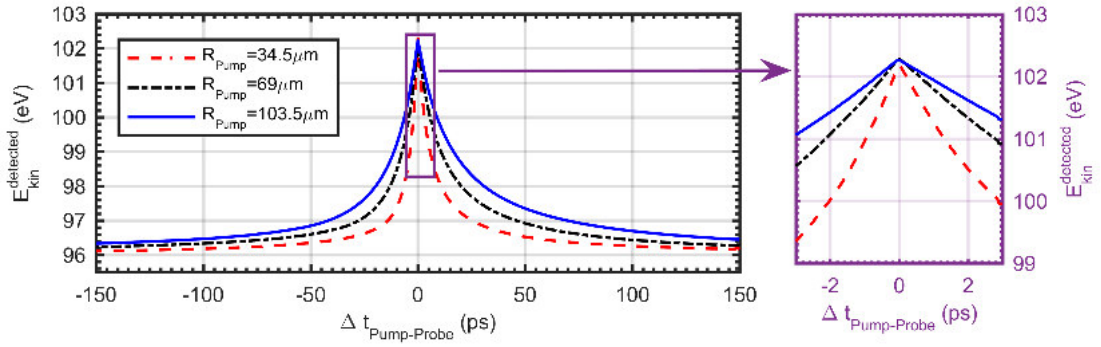

(a) Detected kinetic energy $E_{\text{kin}}^{\text{detected}}$ of the probe electrons.

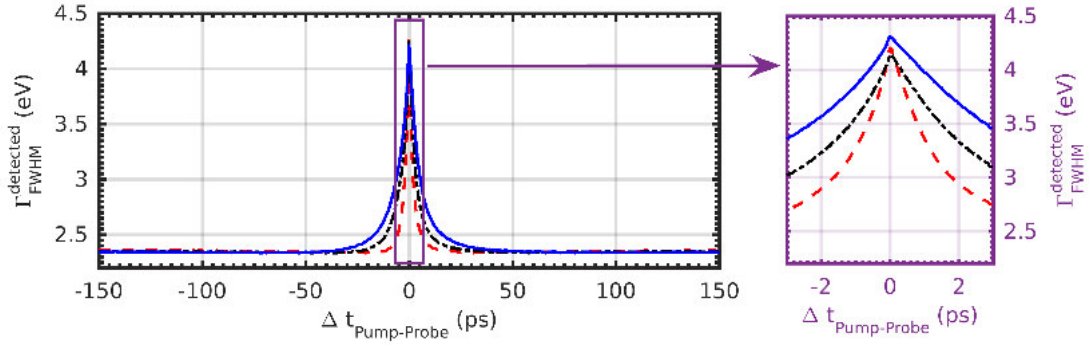

(b) Detected linewidth $\Gamma_{\text{FWHM}}^{\text{detected}}$ of the probe electrons..

Figure 4.14.: Simulated spacecharge induced shift (a) and broadening (b) of the probe electrons at different time-delays between pump and probe pulse (see equation (4.3)). The simulations were performed for three different spot sizes of the pump beam. The variation of the spacecharge effects is different for different pump radii. The detail on the right side, shows the region of delays accessible with SDU ($\pm$3ps). Simulation parameter: $P_{\text{pump}} = P_{\text{probe}} =$ Normal, $R_{\text{pump}}/R_{\text{probe}} = 1.09$, $N_{\text{pump}}/R_{\text{pump}} = 1449$ electrons/μm, $\tau = 50$ fs.

Quantification

To quantify the traces, the evolution within the first ±3 ps is fitted with an exponential function with different exponents for delays bigger or smaller than zero:

$$E_{\mathrm{kin}}(\Delta t) = \begin{cases} Ae^{\Delta t/\tau_1} + B \\ Ae^{\Delta t/\tau_2} + B \end{cases} \quad (4.4) \qquad \Gamma_{\mathrm{FWHM}}(\Delta t) = \begin{cases} Ce^{\Delta t/\tau_3} + D: & \Delta t \leq 0 \\ Ce^{\Delta t/\tau_4} + D: & \Delta t > 0 \end{cases} \quad (4.5)$$

Here Δt is the delay and A, B, C, D and $\tau_{1/2/3/4}$ are fitting parameter. The odd time-constants $\tau_{1/3}$ reflect the rate at the negative delay side, the even $\tau_{2/4}$ that at the positive delay side. An example of the fit for the detected kinetic energy and linewidth of the simulations with radius $R_{\mathrm{pump}} = 69\,\mu$m is shown in the figure 4.15. A complete collection of the fitting values is listed in table 4.1 and the four inverse-exponents/time-constants τ_{1-4} as a function of the pump-probe delay Δt are plotted in the figure 4.16.

The time-constants grow linearly with the radius of the pump beam electron distribution, as shown by a linear fit through the fitting results (see figure 4.15(a)). This reflects the observation from above concerning the radius-dependence. Also the asymmetric evolution is represented by the fit of the delaytraces: For both kinetic energy- and linewidth-delaytrace, the grow rate time-constant is smaller than the recovery rate time-scale. A comparison of the fitted slope reveals a similar relation between grow- and recovery time-constant for both traces: $m_1/|m_2| = 0.72 \approx m_3/|m_4| = 0.75$. Additionally one can observe smaller time-constants for the grow/relaxation of the linewidth as compared to that of the kinetic energy. The ratio of grow/relaxation time-constant of the linewidth-delay-traces compared to that of the kinetic-energy-trace can be determined with the slope of the linear fit. The grow-rate time-constant of the linewidth is smaller by a factor of $m_3/m_1 = 0.23$. That of the recovery-rate time-constants is very similar: $m_4/m_2 = 0.22$.

	E_{kin} Fitparameter (eq. 4.4)				$\Gamma^{\mathrm{detected}}_{\mathrm{FWHM}}$ Fitparameter (eq. 4.5)			
R_{pump}	A^*	B	τ_1	τ_2	C^*	D	τ_3	τ_4
34.5μm	6.228	95.92	0.207	-0.15	1.639	2.578	0.86	-0.741
69μm		96.069	0.11	-0.084		2.49	0.407	-0.328
103.5μm		96.052	0.073	-0.057		2.66	0.299	-0.233
138μm		95.938	0.054	-0.041		2.592	0.223	-0.171

Table 4.1.: Fitting values for the signal evolution for different pump spot radii R_{pump}. *...The pre-factors A/C to the exponential rise/decay is kept constant to a value which was found by fitting the signal of $R_{\mathrm{pump}} = 69\mu$m.

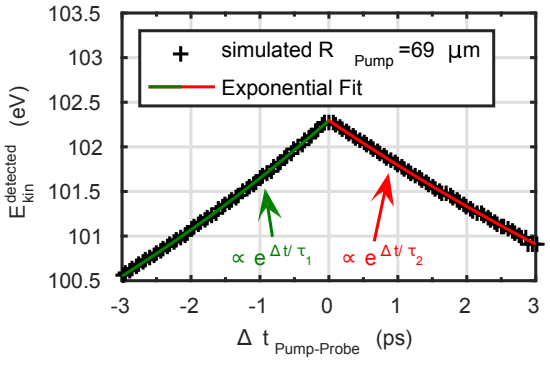

(a) Simulated kinetic energy for different pump-probe delays. The black markers resemble the simulated shifts. Green/red solid lines show the two-case exponential fitting function of eq. 4.4, reflecting the grow/recovery of the delay-trace.

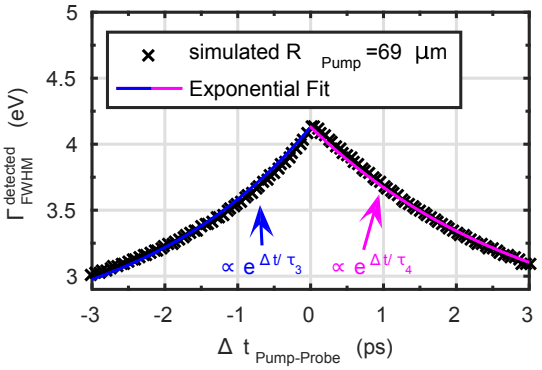

(b) Simulated linewidth for different pump-probe delays. The black markers resemble the simulated linewidth. Blue/magenta solid lines show the two-case exponential fitting function of eq. 4.5, reflecting the grow/recovery of the delay-trace.

Figure 4.15.: Example graph for the fitting functions (solid lines) used to describe the delay-dependence of the spacecharge effects for the delay-regions relevant in the SDU experiments (±3 ps). The data (black markers) stem from the simulation with $R_{\mathrm{pump}} = 69\mu$m, $R_{\mathrm{probe}} = 63\,\mu$m, $N_{\mathrm{pump}} = 1e5$ electrons, S.E.Y.=60 %, $\tau = 50$ fs.

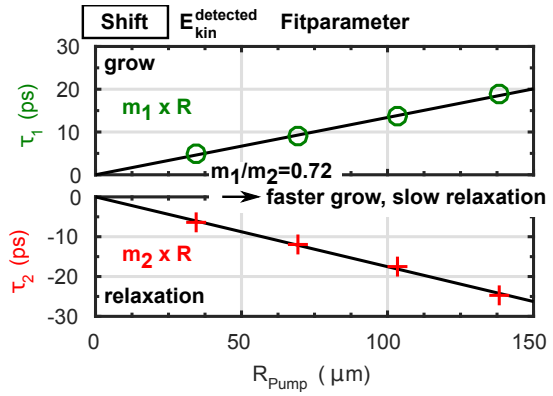

(a) Kinetic energy shift grow/recovery rate (τ_1/τ_2). Linear slope: $m_1 = 0.13$ps/μm, $m_2 = -0.18$ps/μm.

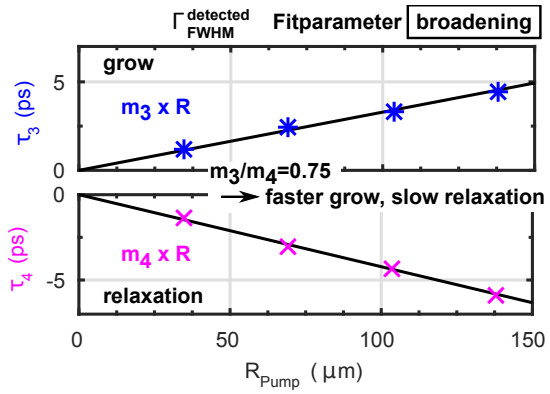

(b) Linewidth Broadening grow/recovery rat (τ_3/τ_4). Linear slope: $m_3 = 0.03$ps/μm, $m_4 = -0.04$ps/μm.

Figure 4.16.: Exponents of the equations 4.4 and 4.5 extracted with a fit of the delay-traces of the spacecharge effects for different pump beam radii. The black solid lines represent a linear fit through the data: $\tau = m \times R_{\mathrm{pump}}$. The slope is used in the text for comparison of the different time-constants. Both, linewidth and kinetic energy appear faster than they recover ($m_1/|m_2| \approx m_3/|m_4| \approx 0.75\rightarrow$ rise time constant is only $0.75\times$ of decay time constant). Additionally, the broadening comes and disappears faster than the shift ($m_4/m_2 \approx m_3/m_1 \approx 0.22\rightarrow$ linewidth reaches its inital value with time constants of $0.22\times$ of shift time constants).

4.4.2. Pump Beam Intensity

Both spacecharge effects reduce in strength when the number of pump beam electrons N_{pump} is reduced. This effect was shown for delay $\Delta t = 0$ in the previous section 4.3. In this section, it is analyzed, weather the time-constants τ_{1-4} are affected by variations of the pump beam intensity. Figure 4.17 shows the delay dependent variation of detected kinetic energy and linewidth for different number of pump beam electrons. Note that in difference with prior figures, the graph in figure 4.17(b) shows the relative linewidth broadening $\Delta\Gamma^{\mathrm{spacecharge}} = \sqrt{(\Gamma^{\mathrm{detected}})^2 - (\Gamma^{\mathrm{initial}})^2}$. This has no influence on the principal shape of the curves.

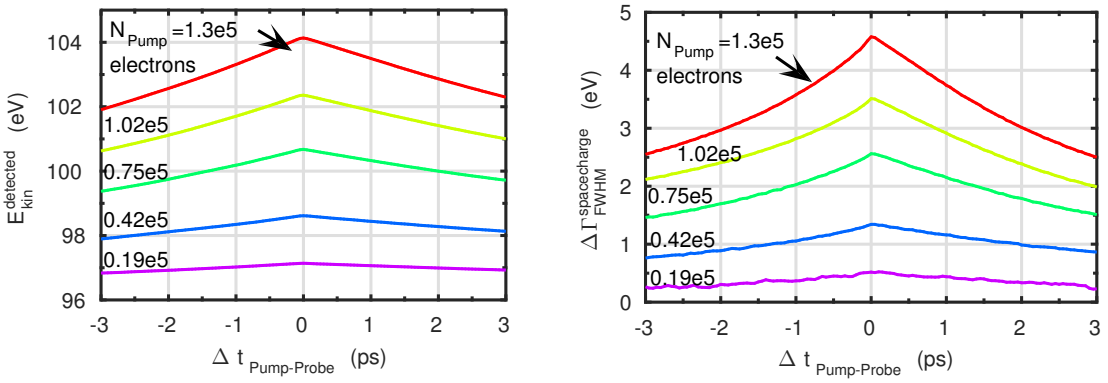

(a) Simulated detected kinetic energy.

(b) Simulated linewidth increase $\Delta\Gamma^{\mathrm{spacecharge}}$ (equation 2.5).

Figure 4.17.: Simulated spacecharge induced shift and broadening of the probe electrons at different delays. The number of pump beam electrons N_{pump} was varied between 0.19e5-1.3e5 electrons (different colored and labeled lines). Simulation parameter: $P_{\mathrm{pump}} = P_{\mathrm{probe}} =$ Normal, $R_{\mathrm{pump}} = 69\,\mu$m, $R_{\mathrm{probe}} = 63\,\mu$m, S.E.Y.=60 %, $\tau = 50$ fs.

Quantification

As in the previous section, both curves for kinetic energy and linewidth vs. delay are fitted with an exponential grow/relaxation (equations 4.4 and 4.5). For fitting $\Delta\Gamma^{\mathrm{spacecharge}}$, the fitting function of equation 4.5 is used without offset (Parameter $D = 0$)[2]. Table 4.2 lists all fitting parameters for the five delay traces. They are additionally plotted as a function of pump beam intensity in figure 4.18. As shown above, the shift and broadening at $\Delta t = 0$ ps grows linearly with N_{pump} (figures 4.18 a and b). The time-constants τ_{1-4} describing the growth and relaxation of the kinetic energy and linewidth broadening with the delay, are not varying for different number of pump beam electrons (figure 4.18 c and d).

[2]The different way of displaying the linewidth variations ($\Delta\Gamma^{\mathrm{spacecharge}}$ vs. $\Gamma^{\mathrm{detected}}$) causes the relaxation timescales $\tau_{3/4}$ to not be comparable with the previously determined ones for the same radius. For the detected kinetic energy and the time-constants $\tau_{1/2}$ a comparison is still possible.

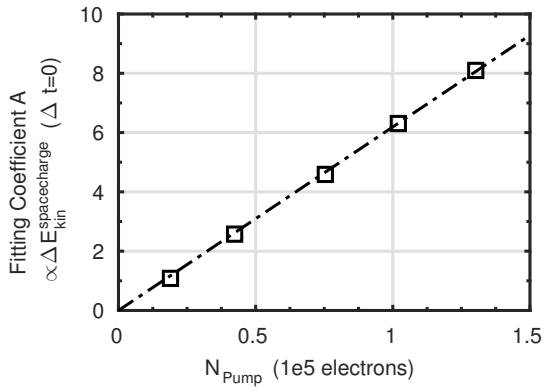

(a) The maximum shift at $\Delta t = 0$ is proportional to the fitting coefficient A. It increases linearly with N_{pump}: $\Delta E_{\mathrm{kin}}^{\mathrm{spacecharge}}[\mathrm{eV}] = 6.2 N_{\mathrm{pump}}[1e5\mathrm{electrons}]$.

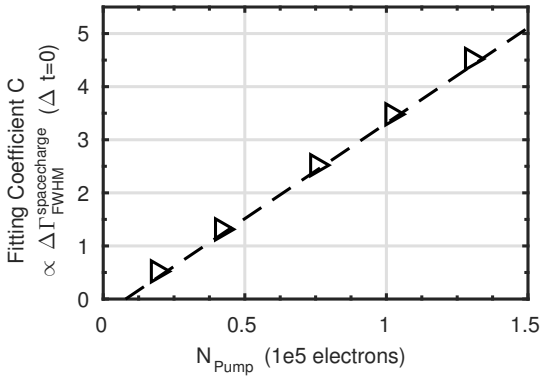

(b) The maximum linewidth increase at $\Delta t = 0$ is proportional to the fitting coefficient C. It increases linearly with N_{pump}: $\Delta\Gamma_{\mathrm{FWHM}}^{\mathrm{spacecharge}}[\mathrm{eV}] = 3.6 N_{\mathrm{pump}}[1e5\mathrm{electrons}] - 0.3$.

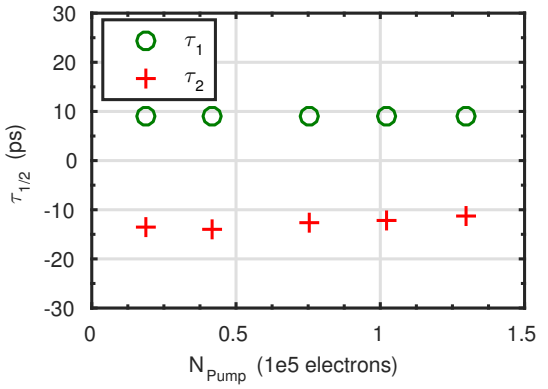

(c) The time-constants $\tau_{1/2}$ for grow/relaxation of the kinetic energy show no significant variation with the number of pump beam electrons. The average values are: $<\tau_1>$=9ps, $<\tau_2>$=-12.8ps.

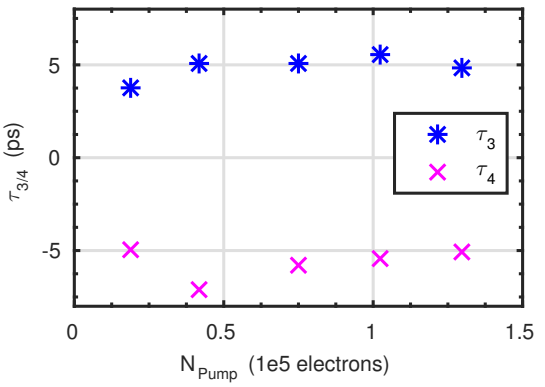

(d) [The time-constants $\tau_{3/4}$ for grow/relaxation of the linewidth increase show no significant variation with the number of pump beam electrons. The average values are $<\tau_3>$=4.8ps, $<\tau_4>$=-5.6ps.

Figure 4.18.: Fitting values for the signal evolution for different number of pump beam electrons N_{pump} at constant spot sizes (fitted with equations 4.4 and 4.5, see also table 4.2).

	E_{kin} Fitparameter (eq. 4.4)				$\Delta\Gamma_{\mathrm{FWHM}}^{\mathrm{spacecharge}}$ Fitparameter (eq. 4.5)			
N_{pump} (1e5 electrons)	A	B^*	τ_1	τ_2	C	D^*	τ_3	τ_4
0.19	1.07	96.069	0.113	-0.073	0.511	0	0.269	-0.202
0.42	2.55		0.11	-0.071	1.321		0.196	-0.141
0.75	4.61		0.11	-0.079	2.531		0.199	-0.172
1.02	6.30		0.11	-0.082	3.459		0.180	-0.183
1.3	8.09		0.11	-0.087	4.513		0.208	-0.197

Table 4.2.: Fitting values for the signal evolution for different number of pump beam electrons N_{pump} at constant spot sizes ($R_{\mathrm{pump}} = 69\mu$m, $R_{\mathrm{probe}} = 63\mu$m). *...The offset B is kept constant to a value which was found by fitting the signal of $N_{\mathrm{pump}} = 1e5$electrons. The offset D to 0.

4.5. Summary and Discussion of the Simulation Results

With the particle tracking software Astra I could simulate the effects of pump beam induced spacecharge on the detected probe electrons of the Ga3d line with an initial kinetic energy of $E_{\mathrm{kin}} = 96\,\mathrm{eV}$ and linewidth of $\Gamma_{\mathrm{FWHM}} = 2.35\,\mathrm{eV}$.

4.5.1. Results at Constant Delay

For pulselengths in the regime of the FEL with $\tau \approx 100\,\mathrm{fs}$, no influence of the pulselength on the spacecharge effects could be observed. It was found, that shift and broadening of the simulated Ga3d line reach their maximum at different times after start ($t_{\mathrm{broadening}}^{\mathrm{final}} \approx 17\,\mathrm{ps}$, $t_{\mathrm{shift}}^{\mathrm{final}} \approx 84\,\mathrm{ps}$ at a pump/probe beam radius of $R_{\mathrm{pump}} = 68\,\mu\mathrm{m}/R_{\mathrm{probe}} = 63\,\mu\mathrm{m}$). The spatial distribution of the pump beam electrons has a strong influence on the broadening. It turned out, that the broadening caused by a flat-top distribution of the pump-electron cloud is much smaller than that caused by a normally distributed pump-electron cloud. In simulations with different ratio of probe-radii it was found, that the broadening increases slower for smaller probe beam radii.

From the above results one can conclude, that the spectral broadening is caused by the spatial inhomogeneity of the pump beam induced spacecharge density in front of the sample. Also temporal inhomogeneity increases the broadening. An increased broadening for pulselengths of $\tau \geq 500\,\mathrm{fs}$. This corresponds to a ratio of $\tau/t_{\mathrm{broadening}}^{\mathrm{final}} \approx 3\,\%$ of the time required to reach the final broadening. For ratios smaller than $\tau/t_{\mathrm{broadening}}^{\mathrm{final}} \leq 0.6\,\%$ (simulated pulselength of 100 fs), the broadening caused by temporal inhomogeneity does not show up. In general, the above conclusion suggests, that part of the pump beam induced broadening can be understood as a deterministic effect of the pump beam induced spacecharge.

The spacecharge effects showed the same quanititative relations for different ratio between sec-

ondary electron tail and characteristic emission line in the pump beam electron spectrum. In all three cases, the number of pump beam electrons is sufficient to describe the detected spacecharge shift, although the mean kinetic energy is different. This finding is different to that stated in [53], where the results of a laser based TR-ARPES experiment on Gallium arsenide are summarized. In there they describe a dependence of the spacecharge shift on the mean energy of the pump-electron spectrum. This is in difference to the simulations in this work, where the mean energy changes with the ratio between emission line and secondary electron tail as well. Propably the different results can be explained by the change in cut-off energy[3] in [53] which appears because of the non-linearity of the multiphotonabsorption processes. In the presented simulations, the cut-off energy is constant.

4.5.2. Results for Different Delays

For delay-regions within the experimentally accessible ±3ps, it was possible to fit the delay dependence of both spacecharge induced shift and broadening with an exponential grow [decay] for negative [positive] values of the pump-probe delay times. The characteristic 1/e-grow [-decay] constants were found to depend linear on the radius of the pump beam, when the ratio of probe- to pump beam radius is constant. For the broadening, time-constants smaller by a factor of ≈0.22 compared to these of the energy shift traces are observed. Both shift and broadening showed a faster grow time-constant compared to that of the recovery. The grow time-constant was found to be smaller by a factor of ≈0.73. At constant spot sizes of pump- and probe beam, a variation of the number of simulated pump beam electrons does not result in a significant variation of the characteristic time-constants.

Oloff et al. present in [53] a linear relation between the grow time-constant and the pump beam radius for experiments at an HHG laser system for negative delays. With a mean field model they could confirm this result. For positive delays it was not possible for Oloff et al. to connect the relaxation time-constant linearly with the radius. This stands in contradiction to the presented results, where also the positive delay-side time-constants stand in a linear relation with the spot radius. The reason for the different result is probably the variation of the pump beam spectrum with increasing pump fluence in [53]. As discussed already above, this spectral variation with fluence is caused by the nonlinear behavior of the underlying multiphoton-photoemission processes.

4.5.3. Implications for TR-PES Experiments

While the probe intensity in an TR-PES experiment can possibly be lowered to values with acceptable spacecharge effects, this is not possible for the pump fluence, since the intensity required to drive a desired phase transition is fixed by physics. To compensate the pump beam induced spacecharge effects in the post analysis, the simulations of the influence of pump beam spacecharge

[3] The cut-off energy means the high-energy edge of the pump-electron spectrum in figure 4.3.

presented in the above chapter can be used. While a shift of the energy is unavoidable in any case, it is possible to reduce the impact on the linewidth by choosing a spatial intensity profile as flat as possible. A flat intensity profile would cause no significant spacecharge broadening. Additionally, a careful characterization of the pump beam intensity profile, combined with simulations as these presented in this chapter, would give the possibility to correct the broadening influence of the pump beam[4].

To reduce the distortions due to the time dependent variation of the spacecharge induced shift of the kinetic energy, it is advisable to use big spots of the pump beam compared to the probe beam[5]. Depending on the time-scales under study, the pump beam spot size should be adjusted such, that the slope due to pump beam spacecharge effects gives only a weak contribution. Since the "negative" delay region is unaffected by true pump effects, it is advisable to record data also at negative time delays. The rising shoulders of the traces can than be used to fit simulation and experiment and ultimately correct the deterministic shifts and broadenings on the positive delay region.

[4] Unfortunately, in the performed TR-PES experiments, no beam shaping devices existed to optimize for the spatial profile. Also a monitor for the spatial intensity profile determination is not foreseen.

[5] In the TR-PES experiment it was not possible to reduce or change the size of the pump beam due to the layout of the split and delay unit.

5. Experimental Data Analysis - Pump Induced Dynamics

As described above, we performed a TR-PES experiment on gallium arsenide (GaAs) with $h\nu_{\mathrm{pump}} = 40\,\mathrm{eV}$ and $h\nu_{\mathrm{probe}} = 120\,\mathrm{eV}$ at the FEL FLASH. In this chapter, a detailed overview on the evaluation of the recorded PES spectra is given. A collection of tables which characterize the measurements can be found in section 5.1. In section 5.2, the beam fluencies are determined with the help of experiment specific measurements. Additionally the experimental, transmission of the pump arm of the SDU is characterized. After these characterizations, the probe and pump beam induced spacecharge effects in the PES experiments are analyzed in sections 5.3 and 5.4. The final analysis and discussion of the pump-probe delay dependent experiments can be found at the end of this chapter in section 5.6. A summary of the results of the experiment is given at the end in section 5.7.

5.1. Summarizing Tables

The recorded experimental data of the performed experiments are saved with the help of the FLASH DAQ. This system is not only saving the data of the used spectrometer, but also a unique time-stamp which allows a correlation of different measured signals. To give reference for the data evaluation an overview of the relevant DAQ-datasets and the respective beamline settings is summarized in three tables this section.

DAQ Runs	duration (min)	comment
9110, 9112 (summarized as II)	156	Pump-probe data sets with varied pump-probe delay at different fluences. Monochromator 0^{th}-order
9114 (III)	113	
9102, 9103, 9104 (IV)	181	
9119 (V)	100	
9100	18	High resolution reference PES acquisition. Monochromator 1^{st} order
9115	8	Pump probe with constant negative delay (=unpumped)
9117	5	

Table 5.1.: Overview of the duration and FLASH-DAQ destination of the recorded datasets. Note, that the naming of the experiments with Run-numbers follows the nomenclature of the DAQ system at FLASH. Since these datasets are stored on tapes and can be accessed for decades for further analysis, the original naming is overtaken.

Dataset	Attenuator Transmission T($h\nu$ = 40eV)*	beamline filters
II	1.6% ($p_{set}(N_2)$=5e-2mbar	Al(200nm)
III	1.6% ($p_{set}(N_2)$=5e-2mbar	Al(200nm) & Polyimid(55nm)
IV	1% ($p_{set}(N_2)$=5.5e-2mbar	Al(200nm) & Polyimid(55nm)
V	1% ($p_{set}(N_2)$=5.5e-2mbar	none
9100	1.6% ($p_{set}(N_2)$=4.7e-2mbar	Al(100nm)
9115	1.6% ($p_{set}(N_2)$=5e-2mbar	Al(100nm) & Polyimid(55nm)
9117	1.6% ($p_{set}(N_2)$=5e-2mbar	Al(100nm) & Polyimid(55nm)

Table 5.2.: Beamline filter settings for the relevant Experiments used in this work. The SDU filters are not changed for the whole set of experiments. The attenuator is filled with nitrogen. Note that set-point pressure $p_{set}(N_2)$ is higher than the real pressure because the regulating gauge is located close to the gas-inlet valve. *...The attenuator transmission of the first FEL harmonic is calculated with the help of the intensity monitors before and after the absorber (see equation (3.13)).

Dataset	Φ_{low}^{pump} ($\mu J/cm^2$)	$\Phi_{central}^{pump}$ ($\mu J/cm^2$)	Φ_{high}^{pump} ($\mu J/cm^2$)
II	0.20-0.24 (5.5%)	0.35-0.39 (13.3%)	0.51-0.55 (5.6%)
III	0.032-0.044 (12%)	0.058-0.064 (14.4%)	0.080-0.092 (12.3%)
IV	0.10-0.15 (9.4%)	0.2-0.22 (12.9%)	0.28-0.32 (11%)
V	0.35-0.39 (4.2%)	0.56-0.58 (5.4%)	0.75-0.79 (4.7%)
9100	pump beam blocked		
9115 9117	0.048-0.068 (17.3%)	0.081-0.091 (17.4%)	0.105-0.125 (17.7%)

Table 5.3.: Selected pump fluence intervals for the space charge analysis. The percentage values in the brackets tells the fraction selected data of the full dataset. A detailed explanation for the reasons of these data-selection regions is given in section 5.2.2.

5.2. Characterizing Measurements

Within this section, PES spectra are shown to give reference for later analysis. A comparison of a spectrum recorded with the usage of a monochromator and one recorded with a filter-foil used for wavelength selection, allows to determine the energy resolution of the PES measurements. After that, general facts concerning the data analysis are summarized. At the end of this section, the pump- and probe beam intensity at the sample are determined, including a experimental transmission determination.

5.2.1. Example PES Spectra

As reference for the following sections, two example Photoemission (PES) spectra of the gallium arsenide sample recorded with the described instrument are shown. Figure 5.1 shows a spectrum of the photoelectrons emitted after the FEL beam passed the monochromator for wavelength selection. The spectrum shows, that the higher harmonics of the FEL are suitable to perform PES until at least the 6^{th} harmonic of the fundamental wavelength. In the presented case, this means a photon energy of $\text{h}\nu^{\text{6th-harmonic}} = 240\,\text{eV}$.

The appearance of higher harmonic induced PES lines becomes more relevant in the PES spectra recorded with only a thin metal filter used for wavelength selection, as shown in the spectrum in figure 5.2. Here PES lines caused by photoemission induced by the 1^{st}, 2^{nd}, 3^{rd}, 4^{th}, 5^{th} and 6^{th} FEL harmonic are visible. Two major differences between the spectra are important:

- PES by 2^{nd}-order FEL radiation ($h\nu$=80 eV) passing the probe arm of the SDU distorts the PES spectrum for detected kinetic energies below $E_{\text{kin}}(h\nu = 120eV) < 80\,\text{eV}$ for spectra taken without monochromator (this forbids an analysis of the As3d lines in the pump-probe experiments).
- The energy resolution is reduced and limited by the FEL natural linewidth for spectra taken without the monochromator for wavelength selection.

As the absorption cross section of gallium arsenide is comparably low for low energetic x-rays in the XUV, the elastically scattered fraction of the fundamental wavelength of the FEL is big enough to detect a signal of the scattered fraction of the pump beam at the detector of the electron spectrometer. The detected photonpeak is shown in figure 5.3. It's area is proportional to the pump beam intensity. This is used in section 3.6.1 for the determination of the transmission function of the beamline elements.

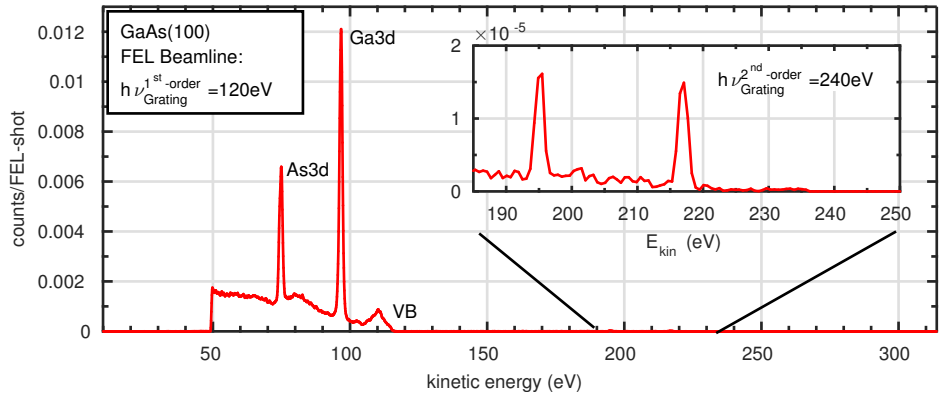

Figure 5.1.: Detected PES spectrum of the GaAs sample with the beamline monochromator used in first diffraction order (200 lines/mm grating, DAQ Run 9100, $h\nu_{\text{Monochromator}}$=120 eV, Exitslit WSU=200 μm, c_{ff} = 2, α=87.875 °, spot size $A_{1^{st}\text{-order}}$=5.6e-6 m^2). The photoelectron spectrum consists not only of electrons induced by radiation passing the first order of the grating (3$^{\text{rd}}$-FEL harmonic), but also radiation passing the grating in second order with a photon energy of $h\nu_{2^{\text{nd}}\text{-order}}$ = 240 eV (6$^{\text{th}}$-FEL harmonic). Both energies fulfill the grating equation at the same optical path. The cut off at E_{kin}=50eV results from a voltage of U_{conv}=50 V in front of the MCPs (see section 3.3).

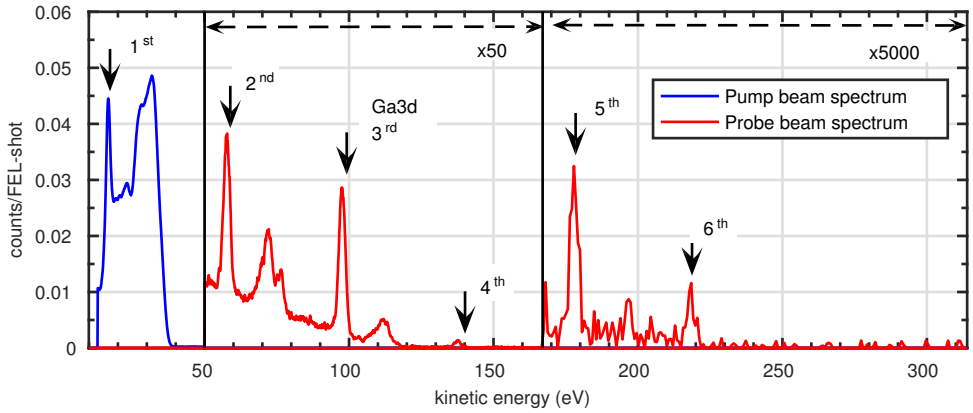

Figure 5.2.: Detected (transmission corrected) PES spectrum of the GaAs sample with the beamline set for 0$^{\text{th}}$-order and SDU usage. Pump and probe beam arrive at the sample (Run 9117, α=87°, $h\nu^{\text{probe}}_{\text{FEL }1^{st}\text{ pulse}}$ =120.27 eV, spot size A_{probe}=1.4e-6 m^2, $h\nu^{\text{pump}}_{\text{FEL }1^{st}\text{ pulse}}$ =40.09 eV, A_{pump}=1.5e-6 m^2, $\Delta t_{\text{pump-probe}}$=0 ps). The photoelectron spectrum is the sum of spectra induced by PES with six orders of higher harmonic radiation of the FEL (1$^{\text{st}}$ to 6$^{\text{th}}$-order). Note that the 1$^{\text{st}}$ FEL harmonic (blue spectrum) reaches the sample through the pump beam, while all higher harmonics (red spectrum) reach it through the probe arm (see transmission tables in section 3.4). The sharp cut off at E_{kin}=13 eV results from the poor transmission of the spectrometer at these energies.

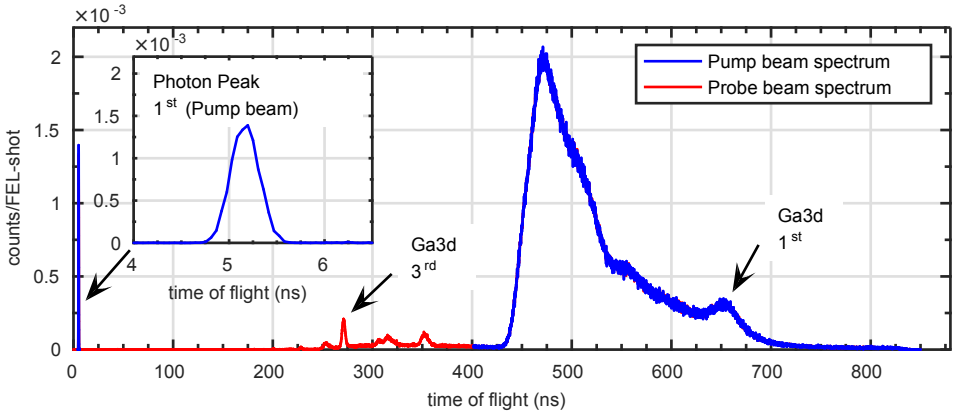

Figure 5.3.: Detected (no transmission correction) PES time-of-flight spectrum of the GaAs sample with the beamline set for 0^{th}-order and SDU usage. Pump and probe beam arrive at the sample (Run 9117, α=87.875 °, $h\nu^{\text{probe}}_{\text{FEL } 1^{st} \text{ pulse}}$ =120.27 eV, spot size A_{probe}=1.4e-6 m^2, $h\nu^{\text{pump}}_{\text{FEL } 1^{st} \text{ pulse}}$ =40.09 eV, A_{pump}=1.5e-6 m^2, $\Delta t_{\text{pump-probe}}$=0 ps, Φ^{pump}=0.085 $\mu J/cm^2$). The photon peak area is proportional to the pump beam intensity arriving at the sample.

5.2.2. General Comments on Data Handling

Different than in the case of most spectroscopic measurements, it is common practice to save many information of the light source in the case of spectroscopy experiments at the SASE FEL FLASH. The saved parameter are not time averaged but saved for every shot of the FEL[1]. This separation of the data into individual shots increases the flexibility for post-analysis.

FEL Feedback Systems - Excluding the First 100 Pulses

For performing the pump probe PES experiments it is crucial, to have stable conditions of the FEL. Several Feedback systems need some time in the early part of a burst to stabilize[103][104]. An example for this is depicted in figure 5.4. One can see, that the FEL electrons kinetic energy (measured after the undulator) is constant after the first 100 photon pules. To exclude possible artifacts caused by unmonitored but relevant changes in the beam parameters, the first 100 pulses of each burst are excluded when analyzing the pump probe PES data.

FEL Intensity Fluctuations

As the FEL intensity fluctuates due to the intrinsic properties of the SASE process the pump fluence at the sample varies while a dataset is recorded. Each recorded pump probe dataset, is separated into three intensity bins as shown in figure 5.5 and summarized in table 5.3.

[1] At a mean pulse-train repetition rate of 10Hz with 400 pulses per pulse this, corresponds to 4000 separately saved spectra per second.

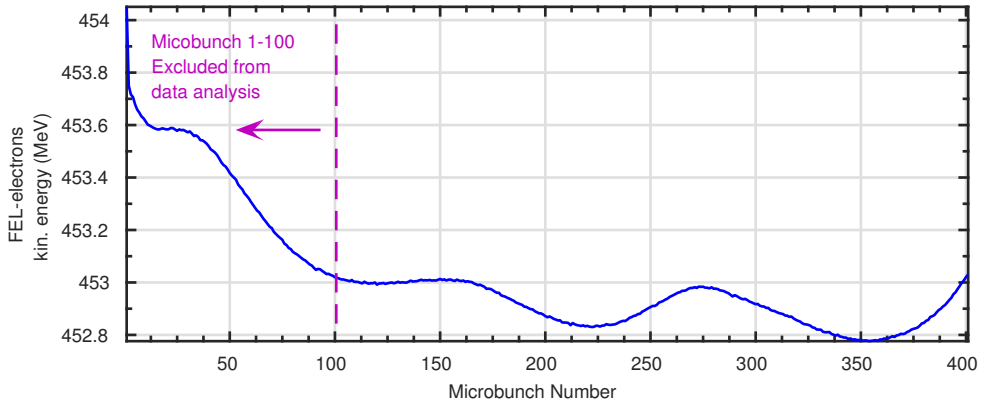

Figure 5.4.: Energy of the lasing electrons of the FEL, measured after the last undulator. An example (5 min average) of the evolution of the kinetic energy during a pulse-train of pulses ("Microbunch Number") is shown above. After a drop of 0.8 MeV after the first 100 pulses it stabilizes at ≈452.9 MeV. This stabilization is caused by feedback systems which automatically optimize the accelerator settings. For analysis of the PES data, the first 100 pulses are excluded, because of possible variations of relevant, but not monitored beam parameters (e.g. photon bandwidth).

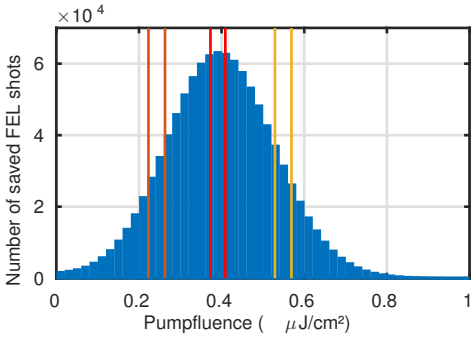

Figure 5.5.: Number of FEL shots saved with a specific pump fluence at the sample (dataset II). To have spectra with a precise pump intensity, not all FEL shots are used for the data evaluation but only small cuts. In the case of dataset II the marked pump fluence intervals are {0.20-0.24, 0.35-0.39, 0.51-0.55} μJ/cm^2. The selected pump fluence regions for the other experiments are shown in table 5.3.

5.3. Probe Induced Spacecharge Effects

The influence of probe beam induced spacecharge on the measured spectra can be reduced by using a sufficiently low probe fluence. In this section I summarize the analysis of the relevant datasets. First I introduce the way of how the probe fluence is estimated with the absolute intensity of the measured Ga3d Photoemission line. After that, a critical probe fluence for the used apparatus is determined with the help of experimental data. Finally, the influence of probe spacecharge on the pump probe datasets is found to be negligible for three of the four recorded datasets.

5.3.1. Probe Fluence Determination

As the FEL beam energy is not monitored at the sample by a beam energy monitor, it is not possible to sort the recorded data by the probe fluence on the sample. Instead it might be estimated with the help of the theoretical transmission as it is done for the pump intensity (section 3.6.1). Since a quantitative comparison between the different experiments is sufficient, another approach is pursued in this section. To compare the probe beam fluence, the Ga3d line intensity is exctracted (see figure 5.6(a)). This is possible, since the amount of detected photoelectrons is proportional to the probe beam fluence[2].

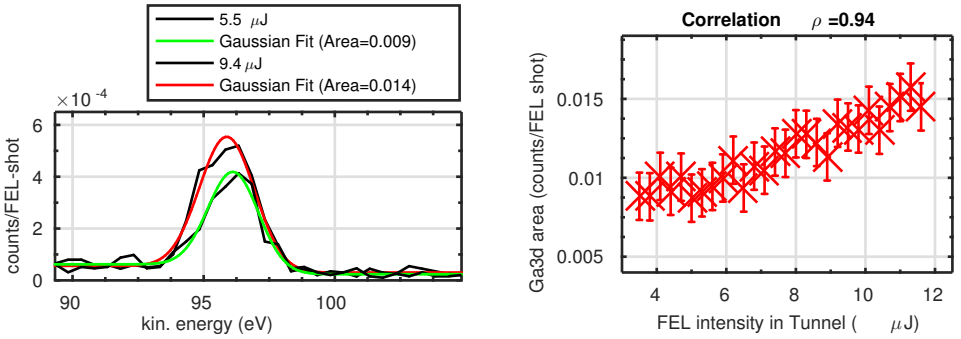

(a) Ga3d photoelectron spectrum for two different intensities of the FEL. The data are fitted with a gaussian line.

(b) The Ga3d area as a function of the FEL beam energy measured in the GMD.

Figure 5.6.: To compare the probe beam fluence on the sample, the intensity (≙area) of the Ga3d Photoemission line is exctracted. The area is determined with a Gaussian fit for different intensities of the FEL measured in the GMD Tunnel (left). The evaluated data were taken without pump beam on the sample (Run 9115). The correlation of area and FEL beam energy is shown in the right figure. The high correlation ($\rho = 0.94$) justifies the strategy.

[2]Note, that the probe intensity can not be separately adjusted to that of the pump. Therefore it is not possible to adjust it to a fixed value for all experiments and characterizations as in this section are mandatory.

5.3.2. Quantitative Probe Spacecharge Evaluation

The signature of probe spacecharge is an increase in linewidth and a shift of the detected kinetic energy (see section 2.1.3). In figure 5.7 both parameters are shown for a dataset within which the probe beam fluence varied around a critical beam energy of the FEL. The figure shows, that the spacecharge effects for the evaluated PES experiment only become important for detected probe beam fluences bigger than a critical fluence I_C:

$$I^{\text{probe spacecharge}}_{\text{C, 1-st Monochromator order}}(A = 5.6\text{e-}6\text{m}^2) = 0.166 \text{ counts/FEL-shot.} \tag{5.1}$$

This fluence is no absolute value for the apparatus but depends on the exact spot size. In the case of this experiment the monochromator was used in first order with a 200 μm exit slit and a central wavelength of $h\nu$ =120 eV. Since the ratio of probe fluence to the beam diameter d is a universal parameter for spacecharge characterization (see section 2.1.3) it is possible to compare this critical countrate for different spot sizes making use of the following relation:

$$I_C^{\text{probe spacecharge}}(A^*) = I_C^{\text{probe spacecharge}}(A) \cdot \sqrt{\frac{A^*}{A}}. \tag{5.2}$$

Here $A = \pi(d/2)^2 \propto d^2$ is the spot size area of a spot with diameter d, $I_C \propto N_{\text{emitted}}$ is the critical probe fluence proportional to the number of totally emitted cloud electrons N_{emitted} as it is used for fluence characterization in [49].

5.3.3. Influence of Probe Spacecharge onto the Data Analysis

Figure 5.6 shows, that the Area of the Ga3d PES line is a good quantity to compare the probe beam fluence of the setup. By expressing the probe beam fluence with this Beamline-setting independent parameter, it is possible to quantitatively compare experiments with different filter settings. A critical probe beam fluence $I^{\text{probe spacecharge}}_{\text{C-extrapolated}}$(A=1.4e-6m^2)=0.083 counts/FEL-shot is found. The probe beam fluence (expressed with the Ga3d line area) of all four relevant pump probe datasets is shown in figure 5.9. Only dataset V shows a probe beam fluence bigger than the critical value.

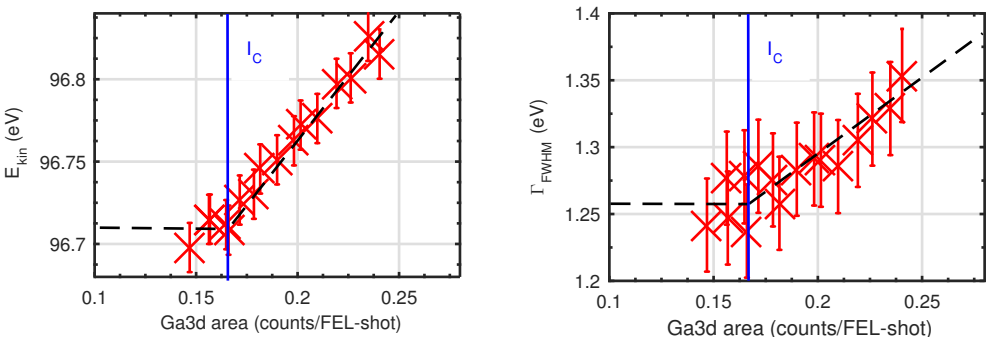

(a) Ga3d detected kinetic energy as a function of line area. While the detected kinetic energy is constant for Ga3d areas below I_C, it monotonically shifts for areas bigger than I_C. The dashed black lines are guide for the eyes.

(b) Ga3d detected linewidth Γ_{FWHM} as a function of line area. As the kinetic energy it is constant below I_C and increases for areas above. The dashed black lines are guide for the eyes.

Figure 5.7.: Linewidth and kinetic energy of Ga3d spectra recorded with the monochromator of the beamline in first order at hν=120 eV (Run 9100, Exitslit WSU=200 μm, c_{ff} = 2, α=87.875°, spot size $A_{1^{st}\text{-order}}$=5.6e-6m^2). The Ga3d kinetic energy E_{kin} and spectral width (Γ_{FWHM}) is plotted as a function of the Ga3d line area. The spectra are created by averaging data of equally sized intervals of FEL beam energy in the GMD. Each spectrum is fitted with a gaussian line (fit see figure 5.6). The errorbars represent the confidence interval of the fit. The critical area below which, the spacecharge effects are not resolvable is $I_{\mathrm{C}}^{\text{probe spacecharge}}(A = 5.6\text{e-}6\mathrm{m}^2)$=0.166 counts/FEL-shot.

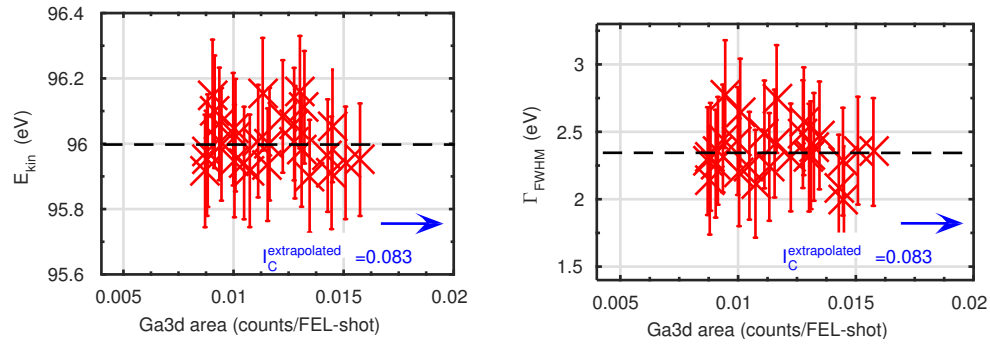

(a) Line Position.

(b) Line Width.

Figure 5.8.: Linewidth and detected kinetic energy of Ga3d spectra recorded with the FEL after passing the probe arm of the SDU (Run 9115, $\mathrm{h}\nu_{\text{FEL }1^{st}\text{ pulse}}^{3^{rd}\text{-harmonic}}$ =120.27 eV, spot size $A_{0^{th}\text{-order}}$=1.4e-6 m^2). The Ga3d kinetic energy and linewidth is plotted as a function of the Ga3d area. The Ga3d kinetic energy E_{kin} and linewidth (Γ_{FWHM}) is plotted as a function of the Ga3d line area. The spectra are created by averaging data of equally sized intervals of FEL beam energy in the GMD. Each spectrum is fitted with a gaussian line (Fit see figure 5.6). The errorbars represent the confidence interval of the fit. The extrapolated critical area (equation 5.2) is $I_{\text{C-extrapolated}}^{\text{probe spacecharge}}(A = 1.4\text{e-}6\mathrm{m}^2)$=0.083 counts/FEL-shot.

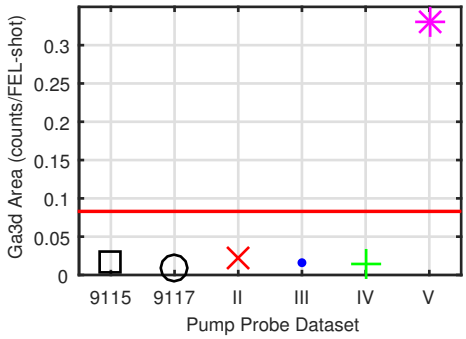

Figure 5.9.: Probe beam fluence expressed by the Ga3d area for all relevant pump-probe datasets. The datasets II to IV show a probe fluence below the critical intensity. Therefore the spectra are unaffected by probe spacecharge effects. Dataset V exceeds the critical fluence with $I^{\text{probe}}_{\text{DatV}} \approx 4 \times I^{\text{probe spacecharge}}_{\text{C-extrapolated}}$.

5.4. Pump Induced Spacecharge Effects

In this section a summary of the experimentally determined effects of pump beam induced spacecharge effects is presented. After that, the measured effects are compared with the simulations of the previous chapter. A quantitative comparison is later used to correct deterministic pump induced spacecharge effects.

5.4.1. Spectral Shifts and Broadening Due to Pump Spacecharge

Two example PES spectra per pump-probe dataset are shown in figure 5.10. The blue spectrum shows the lowest and the red spectrum the highest pump fluence interval within the dataset (see table 5.3). The probe beam fluence of the datasets II to IV is below the critical value for probe spacecharge effects. Therefore all differences in spectral shape must be attributed to changes in the pump beam fluence. The Ga3d line (labeled with I in the spectra) for all three fluences of table 5.3 at a delay of $\Delta t_{\text{pump-probe}} = 0 \pm 0.1\,\text{ps}$ is fitted with a gaussian line to determine the detected kinetic energy E_{kin} and linewidth Γ_{FWHM}. In figure 5.11 the resulting parameters of the Ga3d line are plotted for the different pump beam fluences. Both, kinetic energy and linewidth increase monotonically with increasing fluence. The dataset V fits well in the trend, which suggests that a pump spacecharge analysis is possible for this run. Nevertheless, probe spacecharge could not be excluded to contribute to the observed broadening and shift, as shown in the previous section. Therefore this datatset V is not taken into account for further analysis.

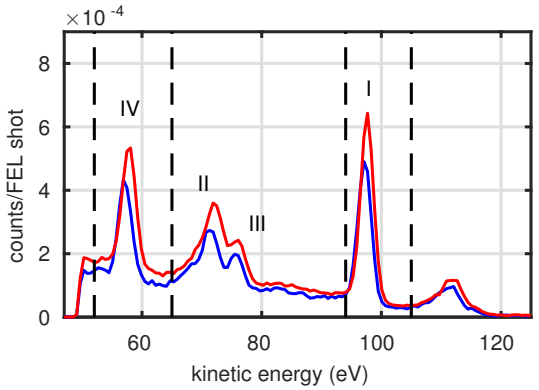

(a) Dataset III: Φ^{pump}=0.04 (blue) and 0.09μJ/cm^2 (red).

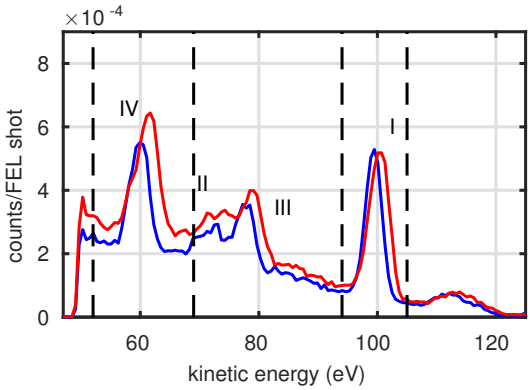

(b) Dataset IV: Φ^{pump}0.13 (blue) and 0.3μJ/cm^2 (red).

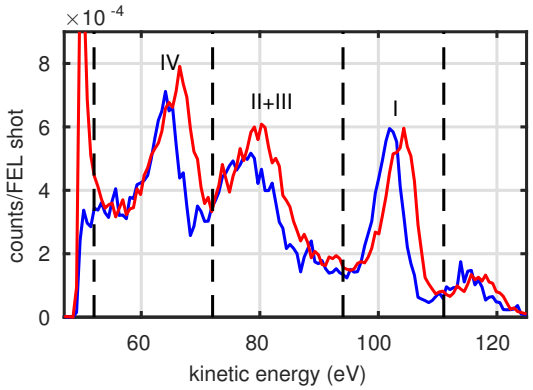

(c) Dataset II: Φ^{pump}0.22 (blue) and 0.53μJ/cm^2 (red).

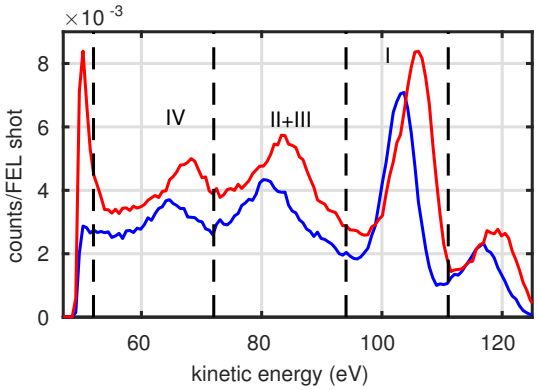

(d) Dataset V: Φ^{pump}0.37 (blue) and 0.77μJ/cm^2 (red). Note the different probe beam intensity ($\propto$Y-scaling) for this graph compared to the others.

Figure 5.10.: PES spectra of the GaAs crystal for different pump fluences Φ^{pump}. This picture is showing the changes of the spectra due to the pump induced spacecharge effects. Additionally the spacecharge variation within the datasets is illustrated (blue vs. red spectra). The peaks labeled I-IV correspond to the following emission lines I=Ga3d (PES from $3^r d$ FEL harmonic hν=120 eV), II=As3d (hν=120 eV), III=Valence Band (PES from $2^n d$ FEL Harmonic hν=80 eV), IV=Ga3d (hν=80 eV). The data shown are from a delay rang of (-1.9 ps< Δt <-1.4 ps) for II, IV and V and (-1 ps< Δt <-0.5 ps) for III.

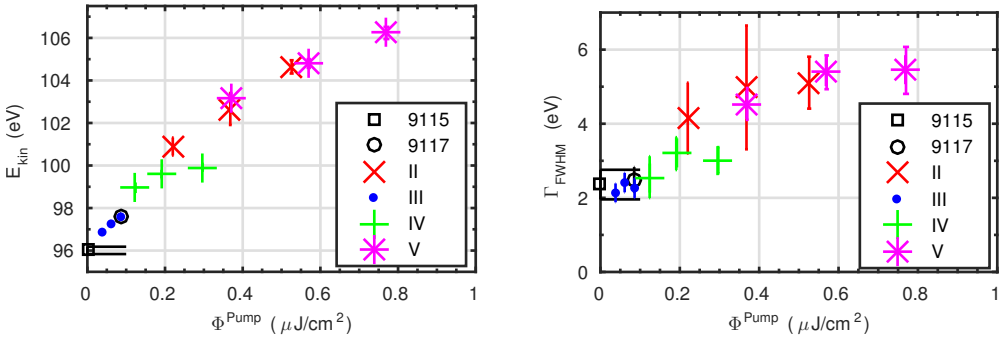

(a) Line Position.

(b) Line Width.

Figure 5.11.: Detected kinetic energy and linewidth of the Ga3d spectra recorded with pump and probe beam at the sample (except 9115) ($h\nu^{probe}_{FEL\ 1^{st}\ pulse}$ =120.27 eV, spot size A_{probe}=1.4e-6 m^2, $h\nu^{pump}_{FEL\ 1^{st}\ pulse}$ =40.09 eV, A_{pump}=1.5e-6 m^2, $\Delta t_{pump\text{-}probe}$=0±0.1 ps). The Ga3d kinetic energy and linewidth is plotted as a function of the estimated pump fluence on the sample. The Ga3d kinetic energy E_{kin} and spectral width Γ_{FWHM} is plotted as a function of the Ga3d area. The errorbars represent the confidence interval of the Gaussian fit. As expected (see section 2.1.3), the spacecharge induced shift and broadening increase monotonically with the pump fluence.

5.4.2. Comparison with Simulations

A comparison of the experimentally determined spacecharge effects and these that were simulated in the previous chapter 4 is given in this section.

To allow a system independent comparison, the linewidth and shift are not separately plotted as a function of fluence. Instead the linewidth is correlated with the detected energy shift in one graph. Figure 5.12 shows this graph for the experiments (markers) compared to that of Astra simulations with a ratio of radii of R_{pump}/R_{probe} = 1.09 (dashed line). The simulated relation between shift and broadening for this simulations is similar to that found in the experiments (ratio of areas $A_{pump}/A_{probe} = 1.15$).

For comparing the fluence dependency of the spacecharge effects of the simulated with these found in the experiments, the intensities have to be normalized. This is done in the last two columns of table 5.4 and plotted in figure 5.13. Here the detected kinetic energy is plotted as a function of the normalized fluence for the simulations (normalized to 0.51e5 electrons) and the experiment (normalized to 0.21 $\mu J/cm^2$).

The observed excellent agreement between simulated and measured pump-spacecharge effects is used below to predict the delay dependent spacecharge component of the experimentally determined kinetic energy shift in section 5.6.

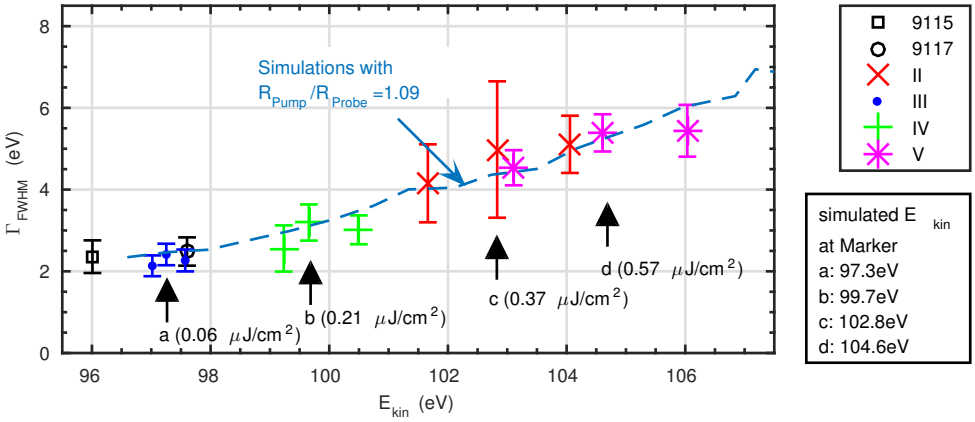

Figure 5.12.: Experimentally determined linewidth and detected kinetic energy of the Ga3d spectra with pump and probe beam at the sample (except 9115) (data as in figure 5.11). The dashed blue lines shows the simulated spectral shift for different number of pump beam electrons at a ratio of pump and probe radius of $R_{\mathrm{pump}}/R_{\mathrm{probe}} = 1.09$ (data as in figure 4.11).

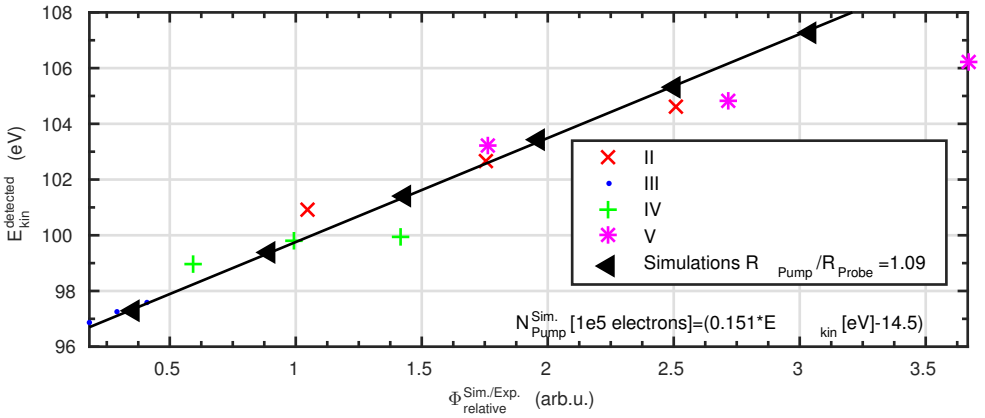

Figure 5.13.: Simulations with $R_{\mathrm{pump}} = 68\mu$m, $R_{\mathrm{probe}} = 63\mu$m (see figure 4.11) and experimental findings as a function of normalized pump beam intensity (see table 5.4). In the lower right corner, the formula is presented which is used to calculate the simulated number of electrons out of the kinetic energy position.

Φ_{pump} (μJ/cm^2)	Marker (fig. 5.12)	$N_{\text{pump}}^{\text{Sim}\ *}$ (1e5 el.)	$\Phi_{\text{relative}}^{\text{Exp}}$	$\Phi_{\text{relative}}^{\text{Sim.}}$
0.06 (III)	a (97.3 eV)	0.19	0.3	0.3
0.21 (IV)	b (99.7 eV)	0.56	*1*	*1*
0.37 (II)	c (102.8 eV)	1.02	1.8	1.8
0.57 (V)	d (104.6 eV)	1.3	2.7	2.3

Table 5.4.: Datapoints marked in figure 5.12 with a,b,c, and d. At each marker the simulated kinetic energy is shown in the figure. To compare the simulated fluence values at these points, this table is used. It shows the number of simulated electrons that were required to achieve the marked kinetic energy in the simulations. The relation between $E_{\text{kin}}^{\text{Sim}}$ and the simulated countrate $N_{\text{pump}}^{\text{Sim}}$ is explained here: *...The connection of N_{pump} and the kinetic energy at the Markers a-d (second column) is determined applying the equation and the linear fit as shown in figure 5.13.

5.5. Summary and Discussion of the Probe and Pump Induced Spacecharge Effects

Probe spacecharge effects can be neglected for three of four of the recorded pump-probe datasets (figure 5.9). Dataset V shows a probe fluence above the critical value. In this dataset fluctuations of the probe fluence could alter the detected kinetic energy and linewidth. Therefore this dataset is excluded from the analysis.

The pump induced spacecharge effects can't be neglected for any of the pump-probe dataset. Pump beam spacecharge causes strong shifts of the detected kinetic energy and linewidth of the Ga3d lines which increases the error in the fitting precision. The experimentally determined pump beam spacecharge effects could be reproduced with a very good agreement with Astra simulations of the previous chapter. This agreement allows to predict the expected delay dependent spacecharge effects with simulations and correct the measured data in the next section.

5.6. Pump-Probe Results after Spacecharge Correction

In this section, the final results of the TR-PES experiment are presented. As discussed in the previous sections, not only the effects of interest influence the detected binding energy. The detailed analysis of pump and probe induced spacecharge effects in the previous sections led to a set of simulations comparable to the expeirment and caused the exclusion of one of the recorded (dataset V). The three remaining pump-probe datasets (II, III and IV) are analyzed in this section. Delay dependent, pump beam induced spacecharge effects as they were simulated in section 4.4, are taken into account.

5.6.1. Kinetic Energy Analysis

The sorted data are evaluated with gaussian fit to the Ga3d spectrum (example spectra are shown in Appendix A.2.3). Kinetic energy and linewidth of the Ga3d line are extracted from this fit. The resulting delay depended kinetic energy for three pump beam fluences (0.06, 0.21 and 0.37 μJ/cm^2) at the sample are shown in figure 5.14. The errorbars represent the 95% confidence interval of the Gaussian fit. This error is big for mainly two reasons: First, the pump-induced spacecharge increases the width of the peak, which reduces the absolute peak height and therefore the signal-to-noise ratio. Therefore the error reduces with reducing pump fluence. A second reason for the low precision is the small effective measurement time contained in each delay-data bin. This is because many data have to be cut from the dataset due to beam energy fluctuations of the FEL pump beam. The effective measurement time per 100 fs data bin is only 37 s for the highest fluence dataset (see table 5.5).

Φ^{pump} (μJ/cm^2)	#	total measurement time	effective measurement time*	measurement time/100fs-data bin **
0.06	III	113 min	16 min	102 s
0.21	IV	181 min	23 min	41 s
0.37	II	156 min	21 min	37 s

Table 5.5.: Due to the strong pump fluence variations caused by the inhomogeneous beam energy distribution during the SASE process many data have to be cut from the measured datasets. *...The effective measurement time is the fraction of time remaining after the data with a not-matching pump beam energy are cut out (see table 5.3). **The effective measurement time per dataset can be expressed as the number of FEL shots per 100 fs-data bin. As the delay-range was varied between the experiments this time is not linearly connected to the effective measurement time.

Each of the three curves in figure 5.14 represents the superposition of two contributions which alter the detected kinetic energy: (1) Spacecharge induced shifts and (2) shifts caused by excitations in the sample. The excitation results in a shift of the electronic binding energy $\Delta E_{\text{excitation}}(\Delta t, \Phi^{\text{pump}})$ of the excited system (Ga3d*) relative to the groundstate system:

$$E_{\text{Binding}}^{\text{Ga3d*}}(\Delta t, \Phi^{\text{pump}}) = E_{\text{Binding}}^{\text{Ga3d-groundstate}} + \Delta E_{\text{excitation}}(\Delta t, \Phi^{\text{pump}}). \tag{5.3}$$

It is Δt the pump-probe delay and Φ^{pump} the pump fluence on the sample. With this nomenclature, the overall detected kinetic energy $E_{\text{kin}}^{\text{detected}}$ can be expressed as the sum of three substitutes:

$$E_{\text{kin}}^{\text{detected}} = E_{\text{kin}}^{0} + \Delta E_{\text{kin}}^{\text{spacecharge}}(\Delta t, \Phi^{\text{pump}}) - \Delta E_{\text{excitation}}(\Delta t, \Phi^{\text{pump}}). \tag{5.4}$$

Here E_{kin}^{0} describes the kinetic energy which is expected after Photoemission without spacecharge and excitation which solely depends on the photon energy and the samples work function (see basic formula of photoemission in equation 2.1). With $\Delta E_{\text{kin}}^{\text{spacecharge}}$, the expected spacecharge

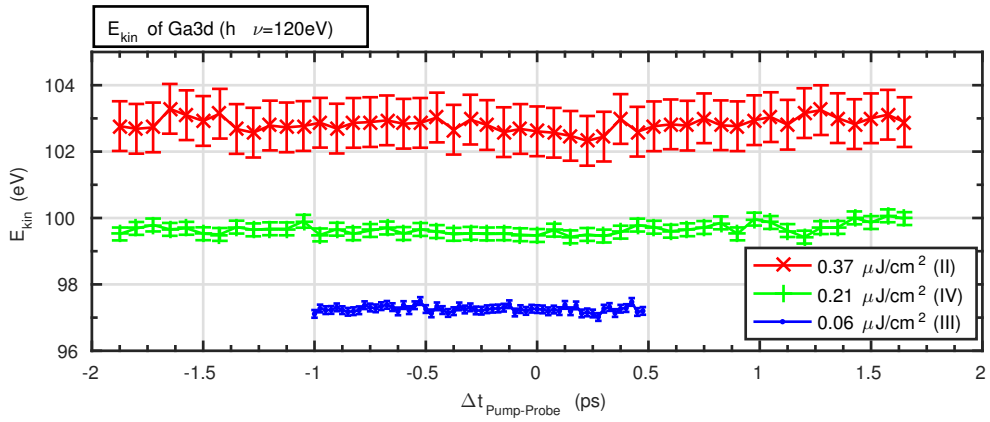

Figure 5.14.: Kinetic energy of the Ga3d line as a function of pump-probe delay for three different excitation fluences (Φ^{pump}=0.06-0.37 μJ/cm^2) detected with the time-of-flight spectrometer. The different base level values have their origin in the different pump induced spacecharge effects for the used fluences (see section 5.4). Photon energies: h$\nu_{\text{pump}} = 40\,\text{eV}$, h$\nu_{\text{probe}} = 120\,\text{eV}$. Spot size on the sample: $A_{\text{pump}} = 1.5e\text{-}6\,\text{m}^2$, $A_{\text{probe}} = 1.4e\text{-}6\,\text{m}^2$.

shift is taken into account. As expressed in the introduced equation (5.4), a determination of the excitation signal is possible only if the spacecharge effects are known.

Subtraction of a Delay Dependent Spacecharge Component

In this section, the spacecharge induced variations of the detected kinetic energy are determined by comparing the measured spacecharge effects to simulations of chapter 4. These simulations show, that the spacecharge induced shift can be modeled with an exponential rise [decay] for delays smaller [bigger] than zero (equation (4.4)). The exponents τ_{1-2} are linearly connected to the radius of the pump beam R_{pump}. This allows to introduce a fitting parameter r, describing the translation of the simulated exponents to that expected in the experiments:

$$\tau_i^{\text{exp}} = r \times \tau_i^{\text{sim}}. \tag{5.5}$$

For τ_i the values found in section 4.4.2 (table 4.2) are used. This choice of the time-constants is justified because the spacecharge behavior at $\Delta t = 0\,\text{ps}$ of simulations and experiment are identically as it was found in the pump spacecharge analysis in the previous section 5.4 (figure 5.12). Since the radius in the experiment in bigger than the simulated ones, the parameter r was determined by fitting eq. (4.4) with r and A as fitting parameter to the highest fluence experiment (figure 5.15, dataset II). For fitting the remaining two datasets (III and IV), only the pre-factors A/C are fitting parameters. The resulting traces for the expected spacecharge dependent shifts are shown in figure 5.15 for the highest pump fluence and in the Appendix figure A.5 for the two other experiments. The fitting values are tabulated in table 5.6.

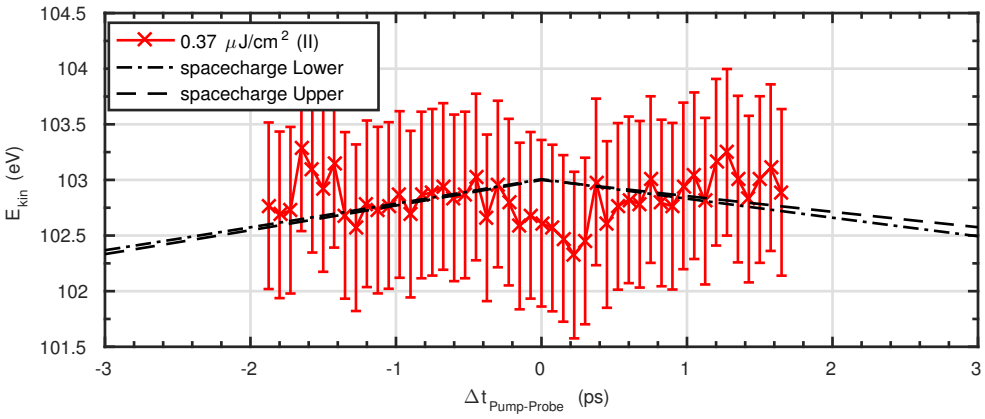

Figure 5.15.: Detected kinetic energy for a pump fluence of $0.37\,\mu\mathrm{J/cm^2}$ and varying pump-probe delay. The expected spacecharge-shift is, beside a free fitting factor r (see equation 5.5), predicted by simulations. The black bi-exponential curves represent the result of this fit and resemble the expected delay-dependent spacecharge shift of the spectra plus the initial kinetic energy: $E^0_{\mathrm{kin}} + \Delta E^{\mathrm{spacecharge}}_{\mathrm{kin}}$ (see eq. (5.4)). The measured data are subtracted from the expected ones to evaluate the pump-probe effects. Figure 5.16 shows this difference signal. To determine the error of this method, the exponents $\tau_{1/2}$ were fixed to the upper and lower boundary values and two fits with equation (4.4) were performed. The resulting expected spacecharge shifts are plotted as dashed (with the upper bounds for $\tau_{1/2}$) and dot-dashed (lower bounds of $\tau_{1/2}$) black lines. The difference of this two curves is added to the error of the spacecharge corrected energy shift curves.

Quantification of Delay Dependent Shift

After the pump beam spacecharge contribution to the delay dependent signal is subtracted from the measured detected kinetic energy, an analysis of the pump induced variation of the binding energy $\Delta E_{\mathrm{Excitation}}$ is possible. Figure 5.16 shows the binding energy shift for the highest evaluated pump fluence as a function of the pump-probe delay. The spacecharge corrected delay-traces of the two lower fluence are shown at the end of this section in figure 5.18. All three graph show a variation of the binding energy which can be fitted with a bi-exponential function:

$$\Delta E_{\mathrm{excitation}}(\Delta t, \Phi^{\mathrm{pump}}) = \begin{cases} I(\Phi^{\mathrm{pump}}) \cdot e^{(\Delta t - t_{\mathrm{max}})/\tau_{\mathrm{drop}}(\Phi^{\mathrm{pump}})} & : \Delta t \leq t_0 \\ I(\Phi^{\mathrm{pump}}) \cdot e^{(\Delta t - t_{\mathrm{max}})/\tau_{\mathrm{recovery}}(\Phi^{\mathrm{pump}})} & : \Delta t > t_0 \end{cases} , \tag{5.6}$$

with free fitting parameter I, τ_{drop}, τ_{recovery} and t_{max}. At the highest pump fluence ($0.37\,\mu\mathrm{J/cm^2}$), a maximum increase of the binding energy of $\Delta E_{\mathrm{excitation}} = 0.7\,\mathrm{eV}$ at $t_{\mathrm{max}} = 240\,\mathrm{fs}$ is extracted. par

The resulting values for all three fluences are tabulated in table 5.7 and plotted as a function of the pump fluence in figure 5.17.

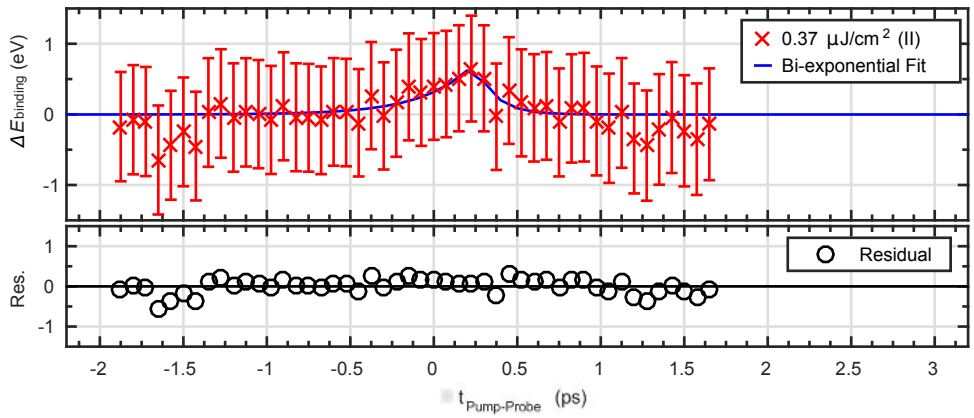

Figure 5.16.: Experimentally determined delay dependent variation of the binding energy of the Ga3d line at a fluence of $0.37\,\mu\mathrm{J/cm^2}$ (red crosses). The trace results from subtraction of the simulated spacecharge shifts from the experimental data as explained in the text. The error-bars resemble the 95%-confidence interval of the fit plus an error caused by the uncertainty by the spacecharge-correction as discussed in figure 5.15. The error is big, because of the strong spacecharge broadening and the low statistics per delay data-bin (see text). The experimental data are fitted with a bi-exponential function (blue line and eq. (5.6)). The extracted maximum shift of $\Delta E_{\mathrm{excitation}} = (0.7 \pm 0.3)\,\mathrm{eV}$ occurs at $t_{\mathrm{max}} = (240 \pm 70)\,\mathrm{fs}$. The 1/e decay [recovery] time for the presented fluence is: $\tau_{\mathrm{drop}} = (290 \pm 180)\,\mathrm{fs}$ [$\tau_{\mathrm{recovery}} = (120 \pm 110)\,\mathrm{fs}$]. The errors of this three fitting parameter resemble the 95%-confidence intervals of the bi-exponential fit to the data, for which the the errors of the delay-trace were included as weighting factors.

		E_{kin} Fitparameter (eq. 4.4)				
Φ^{pump} (μJ/cm^2)	#	A	B	$1/\tau_1$	$1/\tau_2$	r
0.06	III	1.2	fixed 96.07 ($E_{\mathrm{kin}}^{\mathrm{initial}}$)	0.112 ±0.002	-0.078 ±0.008	0.296 ±0.002
0.21	IV	3.8				
0.37	II	6.9				

Table 5.6.: Fitting coefficients for the expected spacecharge shifts for the three evaluated datasets. The resulting traces are shown in figures 5.15 the A.5. The final delaytraces are shown in figure 5.16 for fluence 0.37 μJ/cm^2 and figure 5.18 for the fluences 0.06 μJ/cm^2 and 0.21 μJ/cm^2.

Φ^{pump} (μJ/cm^2)	#	$\|\|I\|\|$ (eV)	t_{max} (fs)	$1/\tau_{\mathrm{drop}}$ (1/fs)	$1/\tau_{\mathrm{recovery}}$ (1/fs)
0.06	III	0.14±0.15	0.28±0.07	9±16	-20±42
0.21	IV	0.17±0.15	0.25±0.17	2.7±3.6	-8.7±19
0.37	II	0.7±0.3	0.24±0.07	3.4±2.1	-8.2±7.3

Table 5.7.: Fitting parameter for equation (5.6) for three different pump fluences.

Figures of the Spacecharge Corrected Delay Traces of Fluence 0.06 μJ/cm^2 and 0.21 μJ/cm^2

5.6.2. Linewidth Analysis

The variation of the linewidth for different values of the pump-probe delay for all three discussed fluences is shown in figure 5.19. The errorbars are very big. The reasons for that are the same as discussed in the previous section for the error of the kinetic energy: The big additional broadening of the line caused by the pump beam induced spacecharge and the low statistics within each data bin. While an analysis of the traces was though possible for the kinetic energy, this is not the case for the traces resulting from the linewidth fitting. A quantitative analysis would require a longer measurement series.

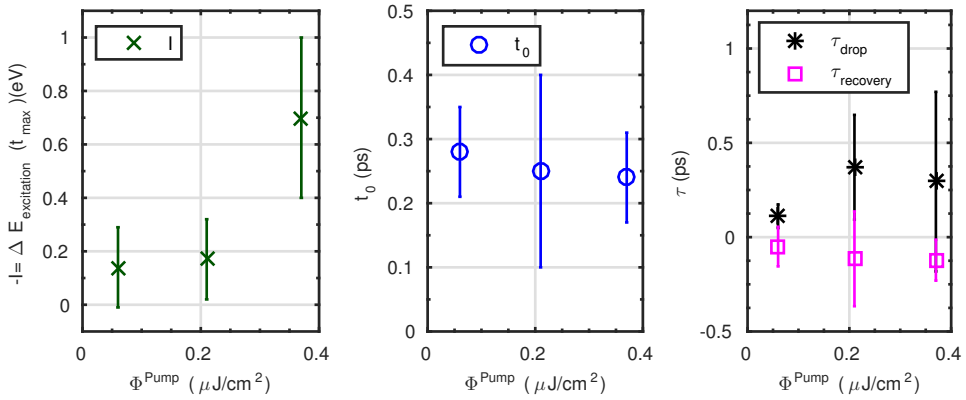

Figure 5.17.: Fitting parameter of table 5.7 for the bi-exponential fit describing the delay-dependent evolution of the binding energy (equation 5.6). The parameter are plotted for the three different pump fluences. The errors resemble the 95%-confidence intervals of the bi-exponential fit to the data. The left graph shows with green crosses, the strength of the maximum binding energy variation $\Delta E_{\text{excitation}}$. It shows an increase with increasing fluence with a strong non-linear behavior. The time of appearance of the maximum variation $t_{\max}$, shown in the central graph with blue circles, is constant within the errorbars for all fluences with an average value of $<t_{\max}> = 257 \pm 103$fs. The 1/e decay [recovery] time constants are plotted in the right graph with black stars [pink squares]. Both parameter are constant within the errorbars with the following average values: $<\tau_{\text{drop}}> = (259 \pm 272)$ fs and $<\tau_{\text{recovery}}> = (96 \pm 155)$ fs.

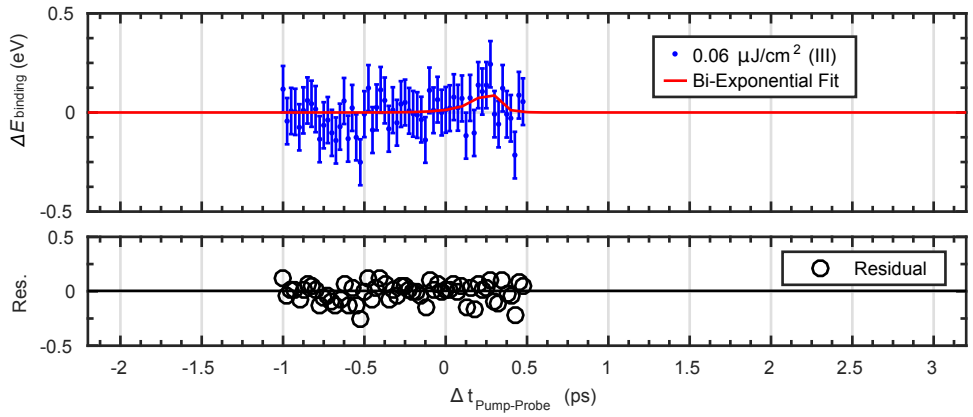

(a) Φ^{pump}=0.06μJ/cm^2 (Dataset III)

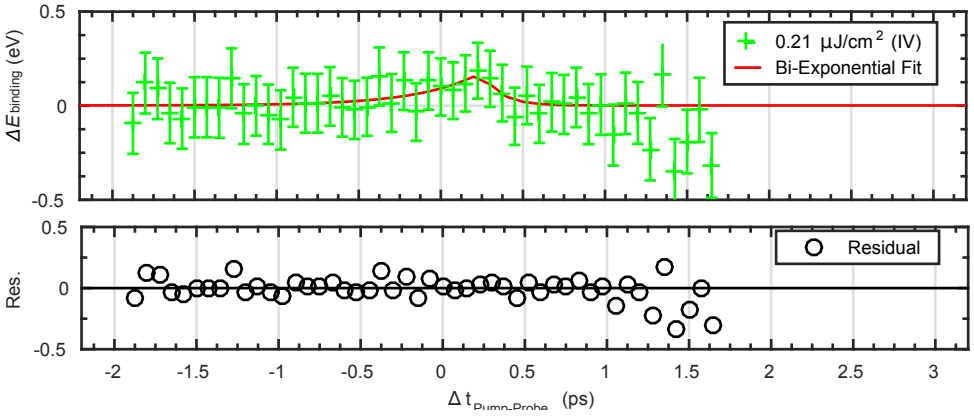

(b) Φ^{pump}=0.21μJ/cm^2 (Dataset IV)

Figure 5.18.: Spacecharge corrected delay dependent shifts of the detected kinetic energy for the two lowest fluences. The red lines represent a bi-exponential fit (equation 5.6). The fitting parameter are tabulated in table 5.7. The detected kinetic energy traces and the subtracted spacecharge component are shown in the Appendix figure A.5.

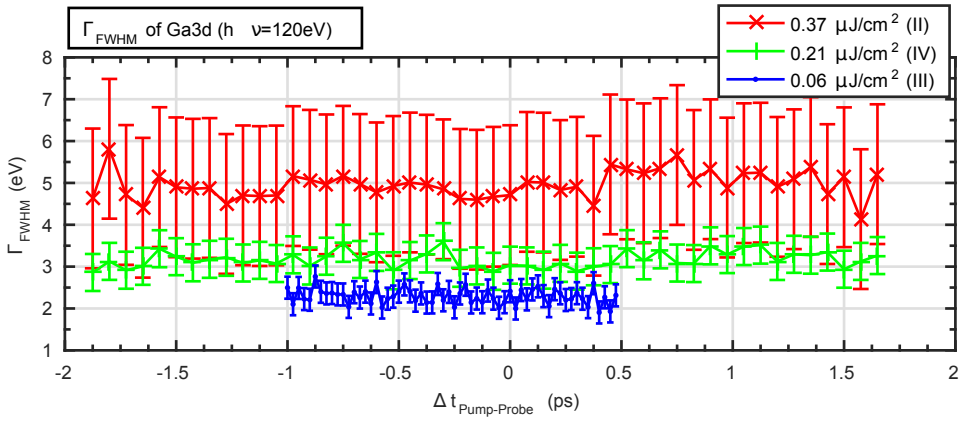

Figure 5.19.: Linewidth of the Ga3d line as a function of pump-probe delay for three different excitation fluences (Φ^{pump}=(0.06-0.37) μJ/cm^2). The different base level values have their origin in the different pump induced spacecharge effects for the used fluences (see section 5.4).

5.6.3. Discussion

The above summarized analysis revealed a delay dependent variation of the Ga3d binding energy in the perforemd XUV pump-probe photoemission experiment. The data analysis showed, that after the gallium arsenide surface is hit by the XUV pulses at a photon energy of $h\nu_{\mathrm{pump}} = 40\,\mathrm{eV}$ with a duration of $\tau_{\mathrm{FEL}} = (170 \pm 102)\,\mathrm{fs}$, the measured binding energy temporarily increases. This increase happens within a rise time of $\tau_{\mathrm{drop}} = (0.2 \pm 0.3)\,\mathrm{ps}$. After reaching its maximum value at $t_{\mathrm{max}} = (0.3 \pm 0.1)$,ps, the binding energy recovers fast within $\tau_{\mathrm{recovery}} = (0.1 \pm 0.1)\,\mathrm{ps}$. The system is found back in its equilibrium state 0.5 ps after the time-zero. While the absolute increase of binding energy depends non-linear on the XUV fluence on the sample, the timescales are similar for all investigated fluences ([0.06, 0.21, 0.37] $\mu\mathrm{J/cm^2}$).

Pump induced spacecharge effects can be excluded as they were corrected by simulations. Photovoltage effects can not explain the transient shift as they have their maximum at the time-zero and decay rates much slower than the observed rates.

As no microscopic picture is available for the observed transient binding energy increase a comparison of timescales allows to draw conclusions on the origin of the effect. According to theoretical investigations (see section 2.2.2) the observed change in binding energy occurs in the time-window at which the electronic subsystem thermalizes into a hot-carrier regime. This thermalization of the electronic system from a non-equilibrium distribution to a high temperature equilibrium state is driven by energy exchange of electrons and holes via electron-electron and hole-hole scattering. Experimental evidence for a thermalization of the photoexcited electron-system within the first 0.5 ps was found e.g. in Terahertz spectroscopy experiments by Leitensdorfer et al.[105] or Beard et al.[106]. In contradiction to that, Kash et al. [107] found electron phonon coupling times of 165 fs in optically pumped time resolved Raman spectroscopy experiments on gallium arsenide. They describe a linear relation between incident energy and population of the observed LO-phonons. Since the here observed transient increase in binding energy shows a non-linear dependence on pump fluence it can not be correlated with a similar phonon excitation mode.

The observed transient increase of the Ga3d binding energy in gallium arsenide within the first 0.5 ps after excitation is attributed to the thermalization process from the non-equilibrium excited state of the electronic system to a state with increased electronic temperature. The photoabsorption seems to cause localization effects in the electronic system. When the excitation density is different at the different ions in the lattice (arsen and gallium atoms), spatially inhomogeneous electrical potentials would arise. Such a local variation of the electric field would explain the observed binding energy shift. During the energy dissipation across the electrons, this localization than disappears (the excitation looses coherence) and after 0.5 ps the electronic excitation gets delocalized. The time-scale of such a screening like effect is on the other hand unexpected slow[108][38]. Repeating the investigations on the arsen atomic sites would provide further insights to verify this picture.

5.7. Summary of the Experimental Results

Utilizing the higher harmonics in the x-ray spectrum of the SASE Free Electron Laser FLASH combined with an autocorrelator setup, allowed us to perform XUV-pump XUV-probe Photoemission experiments (TR-PES) on a semiconductor surface. The time resolution, limited by the FEL pulse duration, could be estimated with an interference-fringe analysis to $\tau_{\mathrm{FEL}} = (170 \pm 102)\,\mathrm{fs}$. With a newly implemented detector, combined with an electron time-of-flight spectrometer we could record photoemission spectra separately for every FEL pulse at a repetition rate of 1 MHz. The influence of probe induced spacecharge was shown to not affect the energy resolution of the experiment. Due to the strong intensity jitter of the SASE FEL causing jitter in the pump-fluence, many datapoints had to be excluded from the analysis. A shot-resolved post analysis combined with a spacecharge correction based on comparison with simulations revealed a time dependent shift of the Ga3d core level binding energies after the sample is excited by the pump pulse. The observed transient increase of the binding energy occurs with a rise time of $\tau_{\mathrm{drop}} = (0.2 \pm 0.3)\,\mathrm{ps}$ and after 0.5 ps the system is found back in equilibrium. A comparison of timescales revealed, that the observed transient shift must be a signature of the non-thermal excitation of the electronic system.

6. Summary - XUV Induced Dynamics in Gallium Arsenide

In the above part of this thesis, the influence of short XUV pulses on the electronic system of a semiconductor is described. The influence of the XUV pulse is exploited by means of a time resolved photoemission experiment (TR-PES). The results of this experiments are subdivided into a simulation- and an experimental chapter and are summarized separately at the end of each individual chapters. To give an overview, in this section the central results of the two chapters are summarized.

Simulations of Pump Induced Spacecharge

Simulations with the particle tracking code Astra showed, that the pump induced spacecharge effects in a TR-PES experiment strongly alter the detected kinetic energy distribution. It was shown, that the broadening in the measured spectra, strongly depends on the spatial and temporal inhomogenity of the pump beam electrons. A flat-top intensity profile shows almost no pump induced broadeneing. In delay dependent simulations it was found, that the time-scales on which the spacecharge effects appear in the pump-probe traces are asymmetric in time and depend linearly on the pump beam radius for both, positive and negative delay side.

Non-equilibrium Dynamics in Gallium Arsenide

Making use of the split and delay unit at the PG2 beamline at the Free Electron Laser FLASH, allowed us to analyze the response of the Ga3d core levels in gallium arsenide (GaAs) after excitation by a short XUV pulses. After sorting the data and applying spacecharge corrections to the pump-probe traces we could show, that the ultrafast excitation of the electronic system with XUV pulses, cause a transient change of the electronic potentials. The non-equilibrium state of the electrons shortly after excitation, manifests in an effective increase of the binding energy of the Ga3d core levels which lasts 0.5 ps. After that time, no more pump induced changes in the binding energies are observable. A comparrison with timescales obtained in theoretical investigations and other experiments indicates, that this transient variation is a signature of the coherence loss during the thermalization process of the photoexcited electrons.

A goal of possible future experiments is the investigation of the response of other core-level lines, e.g. that of the arsen ions (As3d levels) or stronger bound gallium or arsen p-levels. Studies with longer integration times and reduced spacecharge influence, realized e.g. by conditions of the FEL with an improved intensity profile of the pump beam, could allow to additionally track possible transients in the spectral width.

Link between Part I and II

The experiments summarized in the previous part of this work make use of the very short pulse-length which can be delivered by Free Electron Laser (FEL) light sources. For time resolved spectroscopic methods this is a crucial ingredient. Multiple order higher harmonics in the FEL spectrum were shown to be a valuable tool. Choosing different harmonics for pump and probe beam allows to extend the excitation energies in pump-probe kind experiments into the soft X-ray/XUV regime. With a detailed post analysis in combination with spacecharge simulations we successfully performed time resolved Photoemission (TR-PES) experiments at the Free Electron Laser FLASH. A transient change of the electronic potentials during electron thermalization could be observed. While time resolution below 100 fs can easily be achieved with TR-PES experiments at FEL sources, the energy resolution in such experiments will always be limited by spacecharge effects. Time resolved experiments which require a high energy resolution demand for other spectroscopic techniques.

To achieve the energy resolution required to track low-energy excitation in the valence regime, as it is required e.g. for the research on strongly correlated electron systems such as topological insulators, different methods have to be employed. In fact optical spectroscopy methods show partly complementary requirements for spectroscopy at pulsed sources. The biggest difference is, that methods which rely on the detection of photons can not be distorted by external or internal spacecharge fields.

In the following part of this thesis I present experiments guiding the way towards time resolved Resonant Inelastic X-ray scattering (RIXS) at the seeded Free Electron Laser FERMI. As a prototype system for high energy resolution demands, the correlated electron system (Magnetite) was characterized at a high resolution RIXS spectrometer at the Avdanced Light Source (ALS). To find signatures of the important crystal field/dd-excitations, static RIXS experiments resonant to the Fe-M-edge were performed at temperatures below and above the critical Verwey temperature, below which the system changes from a bad metallic to an insulating phase. First M-edge RIXS experiments at FERMI were performed with the Co-containing system $KCoF_3$. The Co-containing sample was chosen instead of Magnetite because of a pronounced RIXS signal at the Co M-edge compared to that at Fe-M-edge. The resulting lower acquisition times makes the Co-compound better suited for proof-of-principle measurements. Ultimately a protocol is proposed to extend the setup scheme towards time resolved RIXS (TR-RIXS) experiments at the iron M-edge of the well characterized Magnetite system.

Part II.

Towards Time-Resolved Resonant Inelastic X-ray Scattering across the Verwey Transition in Magnetite.

1. Introduction

Strongly correlated systems play a leading role in today's solid state physics research[109]. Within this group of condensed matter compounds, the interplay between the electronic subsystem (charge, spin, orbital order) and the lattice is responsible for fascinating effects such as high temperature super-conductivity[3] or metal-to-insulator transitions[10]. Materials composed of open d- and f-shell transition metals (e.g. iron or vanadium) and different kinds of elements (e.g. oxygen) build lot's of such correlated materials[110]. Among the many, the iron oxide magnetite (Fe_3O_4) is one of the oldest examples[111]. While magnetite is a bad metallic conductor above the Verwey temperature $T_V = 125\,K$, it's resistivity jumps to insulating values at temperatures below. This change in conductivity is accompanied by a change in lattice symmetry from cubic at temperatures above to monoclinic at temperatures below the critical temperature. Within several decades of research, still no conclusive theory can explain how exactly the electronic order of the 3d valence electrons is connected to the order of the lattice[112][113]. No theory picture can explain, which of the two systems triggers the phase transition in first place.

In time resolved x-ray diffraction and reflectivity studies on magnetite cooled to temperatures below the transition temperature, it was shown that the Verwey phase transition can be initiated by short pulses of an optical laser[13]. This transient non-equilibrium phase transition is described as the growth and spread of islands of disorder throughout the sample. While the lattice order evolution was mapped with time resolved x-ray diffraction, this non-equilibrium transition is not characterized in terms of its signature in the electronic spectrum. Experimental investigations of the electronic structure can contribute to disentangle the origin of both, the transient non-equilibrium transition as well as the equilibrium Verwey transition in magnetite.

With resonant inelastic x-ray scattering (RIXS) it is possible to gain insights in the electronic structure of the valence electron system. Hereby the bulk sensitivity of this photon-in photon-out technique is useful since the properties of magnetite are attributed to the bulk. Performed in a pump-probe scheme at a short pulsed Free Electron Laser light source, it is possible to achieve time resolutions below typical lattice excitations (time resolved RIXS, TR-RIXS). Therefore by analyzing the time-scales of electronic structure changes observed throughout the non-equilibrium transition, it is possibles to disentangle electronically and lattice driven excitations. Due to the low cross sections, x-ray light sources with high photon flux are required for TR-RIXS experiments. This demand of brilliant light sources with short pulse durations underlines the special suitability of Free Electron Lasers for TR-RIXS experiments.

In the following part of this thesis, a contribution towards the vision of TR-RIXS on magnetite is presented. At the Advanced Light Source synchrotron in Berkeley (ALS), static snapshots of the RIXS spectrum of magnetite were recorded. A sharp signature of the Verwey phase transition is found, which encourages further studies. Further on, we could show in a proof-of-principle experiment on a easy-to-prepare sample of $KCoF_3$, that the seeded Free Electron Laser FERMI allows acquisition of RIXS spectra in the extreme ultraviolet wavelength regime (XUV) without usage of a monochromator.

After a brief literature review on the research on magnetite and the RIXS technique in chapter 2, descriptions of the experimental setup and sample characterizations for the static RIXS measurements on magnetite are shown in chapter 3. In chapter 4, a summary and discussion of the RIXS measurements on magnetite at excitation energies across the iron Fe M-edge is presented. In chapter 5.1, the proof-of-principle experiments of RIXS at the seeded Free Electron Laser FERMI are described.

2. Literature Review

To give reference for different technical and physical aspects, the state of research on magnetite is depicted in the first section of this chapter. It is followed by a summary of technical details of the RIXS technique.

2.1. Magnetite and the Verwey Transition

Iron oxide and iron oxide compounds excellently demonstrate the complexity of atomic and electronic ordering appearing when atoms form condensed matter. While elementary iron in its solid state can be treated as a perfect conductor and many properties can be described with simple models, the complexity of quantum physics comes into play when oxygen is added. Numerous research is performed on iron oxides in many research fields within chemical and physical science, summarized e.g. in [114].

Within this work we contribute to the research of the electronic structure of Fe_3O_4 (magnetite). This iron oxide is famous for its complex phase transition at the so called Verwey temperature $T_V \approx 125\,K$. The transition was described in 1939 and later named by Verwey in [111]. While at temperatures above T_V magnetite is a metallic conductor, it becomes insulating at temperatures below. This change of electrical conductivity is accompanied by a change of lattice symmetry as well as changes in magnetic properties (see figure 2.1). The exact mechanism of the Verwey transition and the interplay of lattice and electronic properties is subject of more than eight decades of research[112][115][116][117]. In this section, selected properties about magnetite are briefly summarized.

2.1.1. Crystallographic Structure

Above the transition temperature T_V the iron and oxygen atoms of magnetite assemble within the so called binary inverse spinel structure of Fe^{2+}, Fe^{3+} and O^{2-} ions with cubic symmetry and a lattice constant $a = 8.397\,Å$[112] (see figure 2.3(a)). In a normal spinel lattice (XY_2O_4) one differentiates between A-sites occupied with X type atoms which are octahedrally coordinated by six oxygen ions. The B-sites are occupied with Y type atoms which are tetrahedrally coordinated by four oxygen ions. A spinel is named inverse if the A-sites are occupied by Y type ions and the B-sites therefore by a mixture of X and Y ions. In case of a binary spinel, the X- and Y-type atoms are of the same species. For magnetite this means an occupation of A-site with Fe^{3+} cations and B-sites with both, Fe^{2+} and Fe^{3+} ion species. At temperatures below T_V the crystal order changes

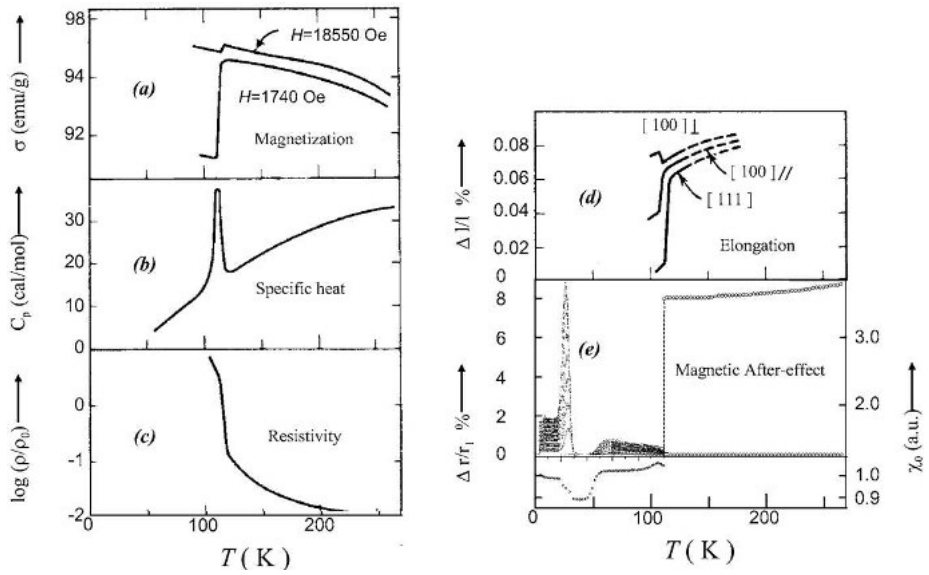

Figure 2.1.: Figure taken and modified from "The Verwey transition - a topical review" by Friedrich Walz in [112]. A collection of the phenomenology of the Verwey transition of magnetite around $T_V \approx 125\,K$: (a) change of magnetization (b) specific heat anomaly (c) electrical resistivity (d) thermal expansion (e) MAE spectrum.

from a cubic symmetry with lattice constant a to a superstructure with monoclinic symmetry and Cc spacegroup[118] with a supercell size of $\sqrt{2}a \times \sqrt{2}a \times 2a$ containing 8 tetrahedral A- and 16 octahedral B-sites. This low-temperature crystal structure is also named as the "Verwey structure" of magnetite.

2.1.2. Electron Configuration

Iron has atomic number 26 and is a transition metal of the fourth row of the periodic table. In its neutral atomic phase, the electron configuration[1] is $[Ar]3d^64s^2$. While the physics of magnetite is dominated by the iron valence electrons, the oxygen configuration is less relevant (atomic number 16, electron configuration $[He]2s^22p^4$). In magnetite the two vacancies in the Oxygen 2p shell are filled up by the two 4s electrons of the iron atoms. The resulting O^{2-} anion has a stable closed shell structure. Consequently the doubly/triply ionized iron atoms have no 4s electrons making the 3d shell with five spin degenerated states in the atom, the outermost shell. It is filled with six (Fe^{2+})/five (Fe^{3+}) 3d electrons as valence electrons (see figure 2.2). Within the crystal structure of Fe_3O_4 the 3d shell degeneracy is reduced due to the crystal field splitting. Hereby the d-orbitals are split into t_{2g} (three times degenerated) and e_g (twice degenerated) levels. Depending on the coordination the t_{2g} (octahedral) or e_g (tetrahedral) states are lower in energy. All 3d states are spin degenerated and filled up according to Hunds rule with five (Fe^{3+}) or six (Fe^{2+}) valence

[1]The complete electron configuration of neutral Fe with 26 electrons: $1s^22s^22p^63s^23p^6\ 3d^64s^2$.

electrons leading to a high-spin configuration at each Fe^{3+} at the A-sites[2]. At the B-sites, which have an average valence of $Fe^{2.5+}$ (11 valence electrons for 10 spin degenerate levels), the shells are filled up to high spin configuration with one remaining minority spin electron per two B-sites.

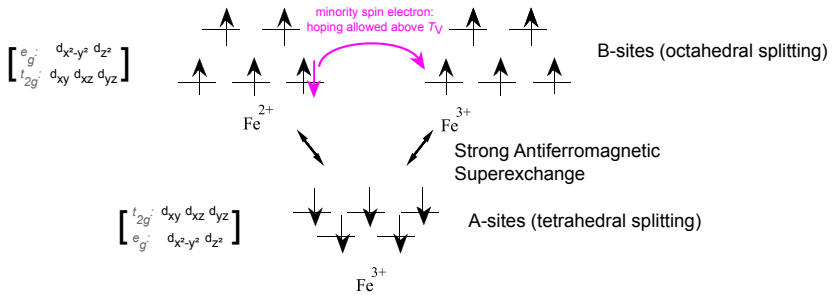

Figure 2.2.: Figure taken and modified from [119]). Level diagram and configuration of the three iron-ion species in magnetite (Fe_3O_4) showing the crystal field induced splitting into t_{2g} and e_g levels. At temperatures above the Verwey temperature T_V the minority spin electron is delocalized between the different B-sites enabling charge transport in this temperature regime. At temperatures below T_V it becomes localized in a trimeron orbital spanning across three iron sites (see figure 2.3(b)). Due to the localization, the charge transport is not possible and the electrical conductivity is lowered.

2.1.3. Electronic Order Below and Above the Verwey Temperature

To explain the conductivity drop at temperatures below T_V, Verwey proposed in 1947 a model of long range charge order (LRCO) along the B-sites[120]. At high temperatures, the sixth 3d electron of the B-site Fe^{2+} ion (=the minority spin electron in figure 2.2) enables charge transport. His model of electronic localization suggests for temperatures below T_V, that the average valency of the B-sites $Fe^{2.5+}$ ions orders to periodic chains of Fe^{2+} and Fe^{3+} ions. Due to the localization, the charge transport is than suppressed below T_V. The model of Verwey would cause an orthorhombic superstructure symmetry below T_V, which was consistent with contemporary crystallographic data. Improvements in crystallography and sample preparations as well as an increase in computational possibilities lead to contradictions with this and upcoming models. Recent examples for the progress in charge order determinations are findings by Wrigth et al. in [121] or these by Blasco et al. in [122]. Both studies report on new insights of the lattice order of the individual iron species gained by x-ray diffraction data. Only after more than seven decades of research in 2012 a model for the exact arrangement of atomic positions connected with a charge ordering scheme was proposed by Senn et al. [113]. Based on x-ray diffraction data with highly oriented micro crystals, they proposed an ordering scheme of magnetite below T_V, which seems to be in line with all published experiments. By measuring the distances between the iron and oxygen ions they found a three iron B-site ions spanning structure with shared electronic orbitals between these B-sites. This object of three iron sites with a common orbital for the minority spin

[2]Five electrons for five spin degenerate energy levels→Hunds rule → all same spin ≙ High spin state

electron is called "trimeron". Its existence in the Verwey phase of magnetite could be confirmed in other experiments by the same authors in [123] and [124]. Similar arrangements of shared localized orbitals involving two atoms are known for longer as "dimers" e.g. in VO_2[125]. To group this kind of orbital order in a solid they are named as "orbital molecules"[119]. Heating the lattice to temperatures above T_V will destroy the long range charge ordering, while a short range charge order (SRCO) was shown to exist also in the metallic phase of magnetite [115].

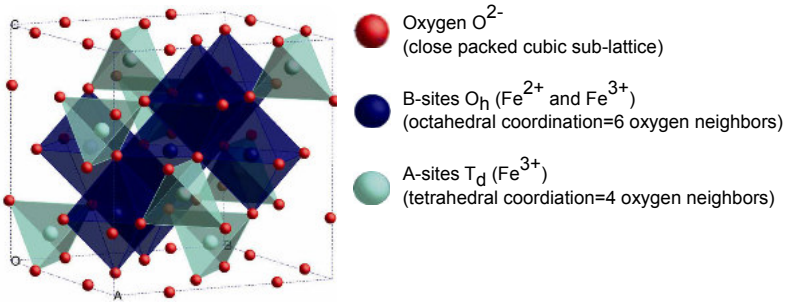

(a) Figure taken from [126]. Sketch of the spinel structure. In case of magnetite both A- and B-sites are occupied by iron ions with different valencies. The lattice constant of the cubic unit cell is $a = 8.397 \circ A$.

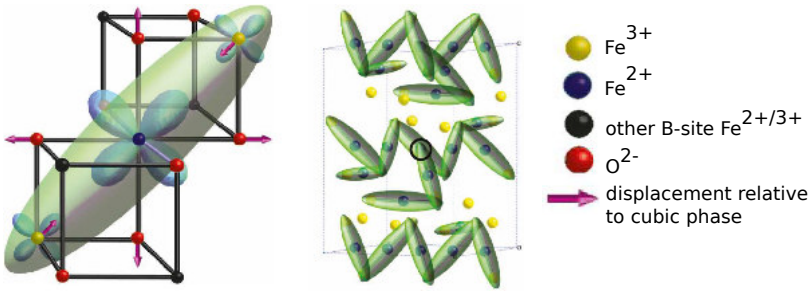

(b) Positions of the B-site $Fe^{2+/3+}$ ions (blue/yellow spheres) in the low temperature super-cell of magnetite. So called trimerons are formed below the Verwey temperature (figure taken from [113]). Within the Verwey phase at $T < T_V$ the minority spin electrons are localized across the three ion "trimeron" structure. The orbital is sketched with green cigar shaped volumes. The shared orbital leads to the identification of the trimeron as an orbital molecule[119].

Figure 2.3.: Crystal structure of magnetite.

2.1.4. Magnetic Structure

All iron ion species in magnetite carry a net spin. For the A- and B-sites one expects due to the filling scheme of the d-shell (figure 2.4) spins of S^{A}_{Fe3+}=-5/2 (down), S^{B}_{Fe3+}=5/2 (up) and S^{B}_{Fe2+}=4/2 (up). At temperatures below the critical Néel temperature $T_N \approx 850\,K$[127] the total spin orders ferrimagnetic. The $S^{A/B}_{Fe3+}$ spins cancel out leaving the system with an expected net magnetic moment of $4\,\mu_B$ per formula unit. The measured value of $4.1\,\mu_B$[112] is close and deviates only little from this expectation value. Figure 2.5c shows the M-edge XMCD spectrum of magnetite

below and above the Verwey temperature. It shows that the spin dependent density of states changes above and below the Verwey temperature.

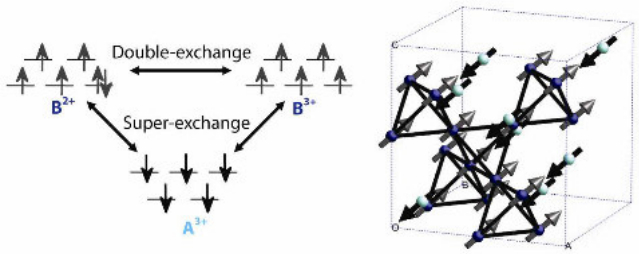

Figure 2.4.: Figure taken from [126]. Left: The 3d-shell of the three different iron species in magnetite (see also figure 2.2). Right: Sketch of the ferrimagnetic ordering of the different iron sites. In this sketch the total A-site spin is S^{A}_{Fe3+}=-5/2 (down) and the total B-site spins are S^{B}_{Fe3+}=5/2 (up) and S^{B}_{Fe2+}=4/2 (up)[117]. The $S^{A/B}_{Fe3+}$ cancel out leading to an expected net magnetic moment of $4\,\mu_B$.

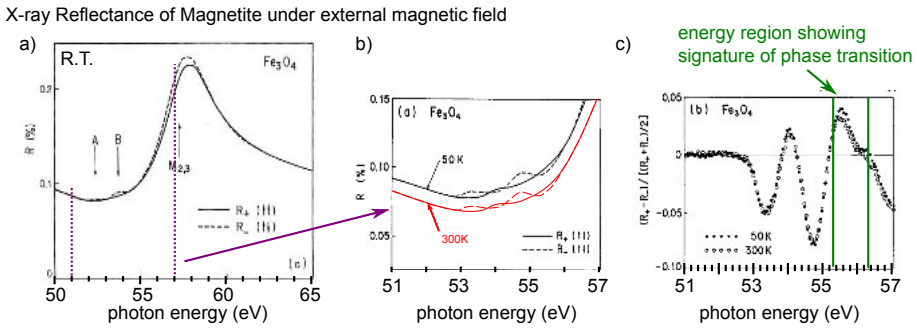

Figure 2.5.: a) Figure taken from [128]. X-ray reflectance spectra (proportional to the x-ray absorption spectrum) of magnetite with different magnetic fields. b) Figure taken from [129]. Detail of the XAS spectrum for different magnetization. c) Figure taken from [129]. XMCD spectrum of magnetite below and above the Verwey temperature.

2.1.5. Theoretical Models for Magnetite

The phase transition of magnetite at $T_V = 125\,K$ is a first order phase transition[112]. As summarized above, its accompanied by changes in electronic and ionic order. The steady state properties within the two phases are investigated for decades. So far no theoretical description exists which is able to explain both temperature phases. A summary of the ongoing research can be found in the review of Walz in [112]. In short, two main ideas explaining the Verwey transition exists today. The "Mott-branch" of theory explains the localization below T_V by the formation of a Wigner crystal of the electrons[130], which changes its phase to a Wigner glass where charge flow is possible at temperatures above T_V. While the low temperature phase is well captured with this

model, the high temperature perspective is better described by the model of Ihle and Lorentz[131]. Within this branch of band based calculations, the charge transport is explained by the sudden appearance of a band gap at temperatures below T_V.

2.1.6. Driving the Verwey Transition with an Optical Laser

To drive the Verwey transition within an optical pump-probe experiment, one can use ultrashort laser pulses. The underlying idea is to increase the energy of the electronic system with the laser pulse, effectively heating the electronic system. This "optical heating" is connected with two characteristic differences compared to a normal temperature increase of the sample: (1) The pure electronic excitation and (2) the ultrashort time-scales needed for this. That magnetite can cross the Verwey phase after irradiation with an IR laser ($h\nu_{\mathrm{Pump}} = 1.5\,\mathrm{eV}$) was shown e.g. in [132][13][133]. A detailed analysis by de Jong et al. in [13] gives insights in the dynamics which occur after the optical laser is absorbed. They propose a model which suggests two subsequent steps occurring after the laser excitation (see figure 2.6). In the low pump-fluence regime (upper part of figure 2.6) the trimeron long range order is not affected. The system relaxes back to groundstate within few ps and the lattice symmetry never gets altered. In the high-pump fluence regime instead (lower part of figure 2.6) the trimeron lattice is disturbed stronger. With an intermediate state of trimeron island, the breakdown of the trimeron long range order is followed by the change of crystal symmetry characterizing the Verwey transition. This model explaining the optically driven Verwey transition with two distinct phases is supported by optical measurements[134][133].

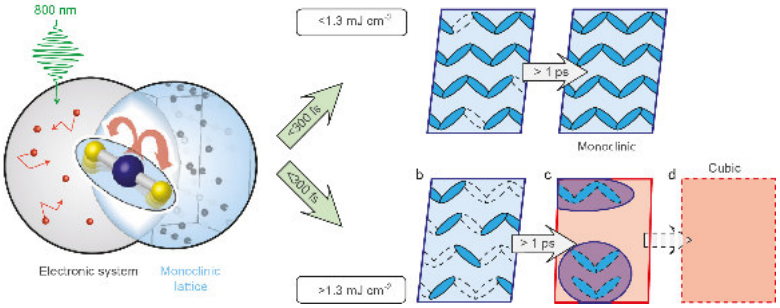

Figure 2.6.: Figure taken and modified from [13]. Sketch of the ordering in magnetite after irradiation with an ultrashort laser pulse. Left: the optical laser heats up the electronic system. Via electron-phonon coupling the lattice is excited and heats up as well. Right: In case of a low pump fluence ($F<1.3\,\mathrm{mJ/cm^2}$) the trimerons remain intact and the crystal remains in the low-temperature phase. When the fluence is sufficiently high ($F>1.3\,\mathrm{mJ/cm^2}$) the lattice changes towards the high temperature phase.

2.2. Resonant inelastic X-ray scattering spectroscopy (RIXS)

Resonant inelastic x-ray scattering (RIXS) is a spectroscopic method based on inelastic scattering of x-ray photons with matter[3]. By analyzing the change of energy, polarization or momentum of photons after scattering within the object of interest, one can learn about the driven excitations. Many books and thesis deal with this technique (e.g. [135][136][5][137][138]). A detailed review of the technique applied to condensed matter systems is given in "Resonant inelastic x-ray scattering studies of elementary excitations" by Luuk Ament et al. (2011) [7]. In this thesis, the RIXS technique is used to determine the excitation spectrum of magnetite. The momentum or polarization dependency of RIXS was not relevant. Within this sectio, that part of the RIXS theory relevant to follow my analysis in the chapter 4.3.

2.2.1. The RIXS Technique

RIXS in the soft x-ray regime is a tool used to study the valence electronic structure of matter. The goal of performing RIXS is to measure possible excited states of the object under study. These excitation spectra of the object under study can be extracted from the difference of incoming and outgoing photon. Since x-ray photons, with escape depths in the order of several 100 nm in the soft x-ray regime are used, it is possible to probe the state within the object of interest without destroying it. Additionally, due to the big inelastic mean free path of x-ray photons, the RIXS technique is bulk sensitive.

In RIXS the energy of the incident photon is tuned to a specific atomic resonance (e.g. a $2p_{1/2}$ to valence transition). The overall scattering cross section for the incident photons within the object under study, is than dominated by the cross section of this very atomic species. If the object under study consist of different atomic species, this property of RIXS can be used to selectively probe the electronic state of only the resonance-fulfilling atomic species. All other species bound in the object under study, which don't share the chosen resonance level, contribute less intense to the scattering cross section.

When scattering with the object under study, the energy of the incoming photon gets altered. The difference in energy ΔE of incoming and outgoing photon is characterized by the amount of energy required for driving the system from the ground state with energy E_g into the final ($\hat{=}$excited state) with total energy E_i:

$$\Delta E = E_\mathrm{i} - E_\mathrm{g} = \hbar(\omega_\mathrm{in} - \omega_\mathrm{out}). \tag{2.1}$$

Here $\hbar\omega_{\mathrm{in/out}}$ refer to the photon energy of the incoming/outgoing ($\hat{=}$scattered) photon. Which exact excitations were the reason for the energy loss is can not be seen from measuring the energyloss of equation 2.1. For an interpretation of RIXS spectra from solids, some knowledge on the spectrum of possible excitations is required. An exemplary excitation spectrum for a strongly

[3]The same technique is called Raman spectroscopy when photons in the optical range are applied.

correlated condensed matter system is shown in figure 2.8. Examples of the success of RIXS to determine the excitation spectrum of solids are [139][140][141][142][143]. The strength of a time resolved RIXS experiment (TR-RIXS) is summarized e.g. in [144].

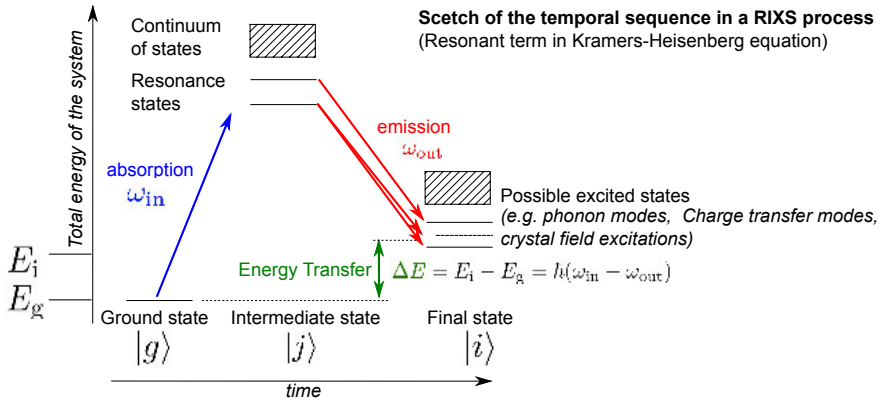

Figure 2.7.: Figure taken and modified from [145]. Temporal evolution of a RIXS process. The total energy of the system is altered twice: After being excited from the ground state $|g\rangle$ by absorption of a photon with energy $\hbar\omega_{\text{in}}$ (blue arrow) the energy is increased to a high value of the intermediate state $|j\rangle$. As this situation is energetically unfavorable, the system decays under emission of a photon with $\hbar\omega_{\text{out}}$ (red arrow) to its final state $|i\rangle$. The energy difference ΔE (green arrow) is paid by the photon. Analyzing the loss of energy of the photon allows to determine the energy of the excited state.

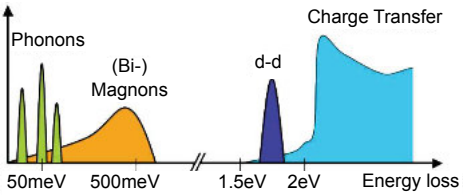

Figure 2.8.: Figure taken and modified from [7]. Example spectrum for possible charge neutral excitations in a correlated condensed matter system. In RIXS, energy of the photon is reduced by the amount of energy needed to excite the system into the state with the excited quasi-particle.

2.2.2. Theoretical Description

The quantum mechanical description of light scattering with atoms goes back to Kramers and Heisenberg[146]. They analyzed the response of the electrons of an atom within a second order perturbation theory. The resulting Kramers-Heisenberg formulas describe the scattering of photons with the incoming energy $\hbar\omega_{\text{in}}$ with the double differential cross section. This cross section is

proportional to the probability of emission of photons with energy $\hbar\omega_{\mathrm{out}}$ within in the solid angle $d\Omega$. Following the nomenclature of [147] with $\hbar = 1$ this cross section is given by:

$$\frac{d^2\sigma}{d\omega_{\mathrm{out}}d\Omega} = \frac{\omega_{\mathrm{out}}^2}{c_0^4}\left(\frac{1}{2\pi}\right)^3 W_{12} \tag{2.2}$$

With c_0 the speed of light and $W_{\mathrm{in,out}}$ the transition rate. The transition rate, also referred to as the scattering amplitude is determined by solving:

$$\begin{aligned} W_{12} = \sum_j \Bigg(& \frac{(2\pi)^3}{\omega_{\mathrm{in}}}\left(\frac{e^2}{m_{\mathrm{e}}}\right)^2 \delta\big(E_{\mathrm{j}} - E_{\mathrm{g}} + \omega_{\mathrm{out}} - \omega_{\mathrm{in}}\big)\times \\ \textit{(I - direct term)} \quad & \Big|\Big[\langle j|\,\rho_{\mathbf{k}_{\mathrm{in}}-\mathbf{k}_{\mathrm{out}}}\,|g\rangle\,(\eta_{\mathrm{in}}\eta_{\mathrm{out}}) + \\ \textit{(II - resonant term)} \quad & \frac{1}{m_{\mathrm{e}}}\sum_i \left(\frac{\langle j|\,\mathbf{p}(\mathbf{k}_{\mathrm{out}})\eta_{\mathrm{out}}\,|i\rangle\,\langle i|\,\mathbf{p}(-\mathbf{k}_{\mathrm{in}})\eta_{\mathrm{in}}\,|g\rangle}{E_{\mathrm{i}} - E_{\mathrm{g}} - \omega_{\mathrm{in}}} + \right. \\ \textit{(III - non-resonant term)} \quad & \left.\left.\left.\frac{\langle j|\,\mathbf{k}_{\mathrm{in}}\eta_{\mathrm{in}}\,|i\rangle\,\langle i|\,\mathbf{p}(-\mathbf{k}_{\mathrm{out}})\eta_{\mathrm{out}}\,|g\rangle}{E_i - E_g + \omega_{\mathrm{out}}}\right)\right]\right|^2 \Bigg) \end{aligned} \tag{2.3}$$

With m_{e} the electron mass, e the electron charge, $|g\rangle$, $|i\rangle$ and $|j\rangle$ describing the system in its ground, intermediate and final state. $E_{\mathrm{g,i}}$ are the corresponding energies. The dipole operator is defined as $\mathbf{p}(\mathbf{k}) = \sum_n \mathbf{p}_n \exp -i\mathbf{k}\mathbf{r}_n$ and $\rho_{\mathbf{k}} = \sum_n \exp -i\mathbf{k}\mathbf{r}_n$. The two sums run over all possible final (j-) and intermediate (i-) states. The photons are described by their energy ω, polarization η and wavevector $\mathbf{k}$. The equation 2.3 can be separated into three terms (labeled with *(I-III)*) describing different pathways through the excitation. These pathways are depicted in figure 2.9. The weight of each of them depends on the photon energies, polarization and momentum. Term *(I)* describes the direct scattering, also called Thomson scattering. No intermediate state is excited. Terms *(II)* and *(III)* are referred to as "indirect" RIXS in [7]. X-ray emission of atomic lines is described by the non-resonant term *(III)*. When using photon energies in resonance with an atomic excitation ($\hbar\omega_{\mathrm{in}} = E_g - E_j$) the second term *(II)* becomes relevant. Since atomic resonances can be separated for all elements and chemical states of the same elements, it is this property of the scattering process, that enables RIXS to probe site selective. While spin flip transitions aren't accessible in low energy optical methods as reflectivity measurements[148] they become allowed under circumstances in RIXS due to crystal field interactions[149][150][151]. The excitation spectra measured with RIXS depend on the local surrounding of the atoms and the resulting crystal fields and symmetries. Knowing the exact chemical state of all individual atoms forming of a material, allows to determine the atomic excitation spectra with the help of atomic multiplet calculations[152][153][154][155]. Possible interaction between different degrees of freedom as e.g. electron-phonon coupling require advanced theoretical approaches[156][157][158][159] and cause broadenings of the effectively measured excitation spectra. An example for a calculated RIXS spectrum of dd-excitations with and without phonon interaction is shown in figure 2.10.

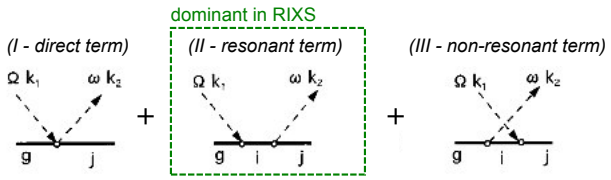

Figure 2.9.: Figure taken and modified from [147]. Feynman like graphs for the three terms of equation 2.3. For RIXS of most relevance is the resonance term, marked with a green box. Its weight is big, when the incoming photon energies corresponds to that of an atomic resonance. Another sketch of the resonant process is shown above in figure 2.7.

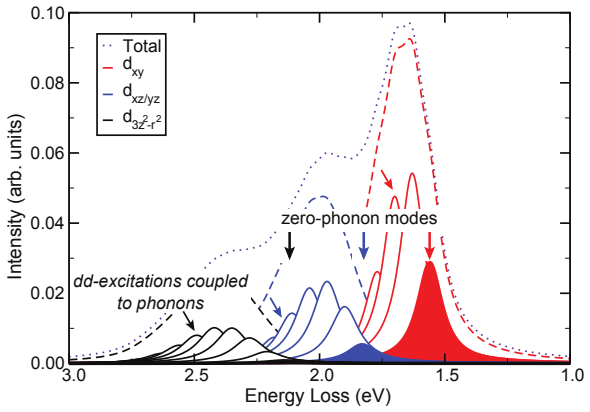

Figure 2.10.: Figure taken and modified from [160]. Calculated excitation spectrum of $Ca_2Y_2Cu_5O_10$ determined for excitation at the Cu L-edge. This figure is supposed to illustrate the consequences of electron-phonon coupling on the RIXS spectrum. If the system would not show a coupling between electronic system and the ion lattice, the excitation spectrum would be resembled by three distinct modes with a lorentzian line shape (filled peaks). When electron-phonon coupling is included in the calculations, differently shifted copied of the zero-phonon excitations appear. The sum of these excitations can be described with Gaussian lines (dashed lines).

2.2.3. RIXS in the XUV Wavelength Region

The resonance condition for performing RIXS is fulfilled when incident photon energies at the absorption edges of the elements are chosen. Depending on the principal quantum number n of the initially excited electron, one differentiates the different absorption edges (see figure 2.11. In transition metal compounds[4] one is typically interested in excitations of the weakly bound valence states. In case of the first row transition metals (from Ti to Cu) these valence states involve contributions from the weakly bound 3d-states and are accessible in the dipole-allowed regime with absorption at the L (2p→3d) and M (3p→3d) edges, while the K edge (1s→4p) doesn't involve them. As the elastic REXS contribution is low in the L edge photon energy region of transition metals, many studies are performed at the L edge[5]. From theoretical point of view, no principal difference is made between the L- and M-edge RIXS. In [161] and [162] a reduced charge transfer and shake-up contribution to the M edge RIXS spectrum compared to measurements at the L edge are highlighted as a strength of RIXS at the M edge. Another rather technical reason for choosing M edge RIXS compared to L edge RIXS is the achievable absolute energy resolution: At a resolving power $R = E/\Delta E \approx 10000$, which is a realistic value for current soft x-ray instrumentation one can achieve a $\Delta E = 6\,\mathrm{meV}$ resolution[163] at $h\nu = 60\,\mathrm{eV}$. XUV RIXS at the transition metal M edge was applied e.g. in [164] and [156] to study the crystal field/dd-excitation spectrum of different transition metal compounds.

[4] Transition metal compounds are of special interest in the field of condensed matter research due to their complex phase diagrams including high T_C superconductivity phases and other correlated effects as metal-to-insulator transitions (see e.g. [109]).

[5] Although the REXS terms are not only caused by reflectivity one can already see clear difference from a comparison of the reflectivity of the materials which is comparably high in the XUV: E.g. the reflectivity of pure iron under 45° incidence angle is $R_{60\,\mathrm{eV}} = 4e\text{-}2/R_{700\,\mathrm{eV}} = 8e\text{-}8$ at 60/700 eV incident photon energy corresponding to the M/L absorption edge[68].

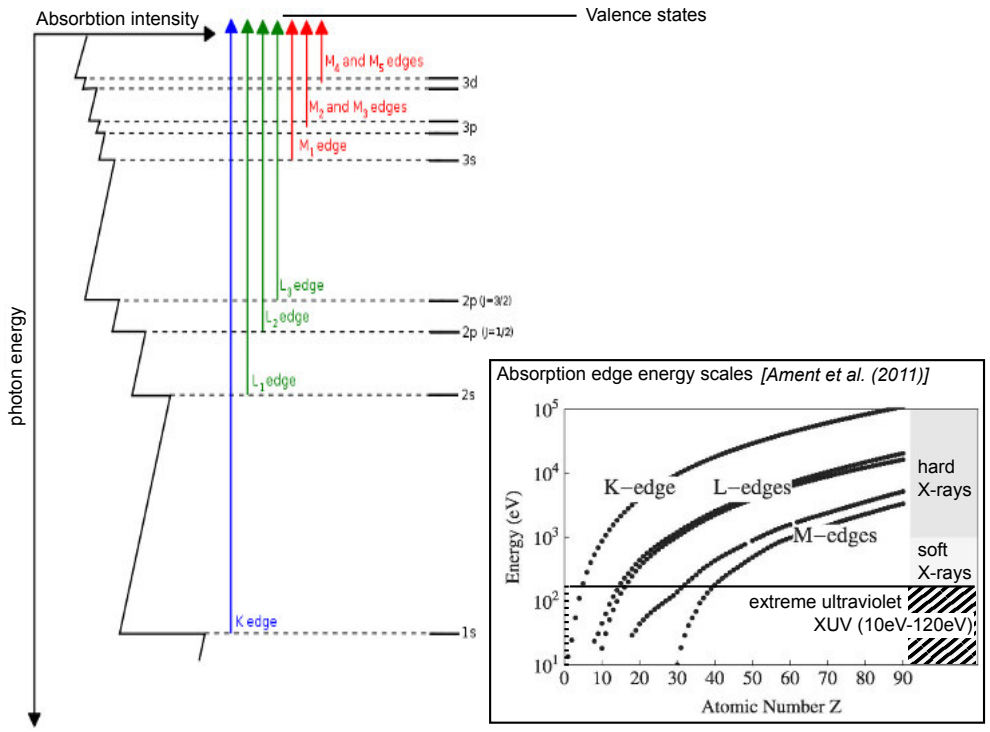

Figure 2.11.: Left: Figure taken from [165]. The absorption edges of elements are classified by the principal quantum number n of the initially excited electronic orbitals (n=1→K-edge, n=2→L-edge, etc.). Right Inset: Figure taken and modified from [7]. Energy scales of the absorption edges depending on the atomic number of the elements..

3. Experimental Setup and Sample Characterization

3.1. High Resolution Beamline and the RIXS Endstation at the Advanced Light Source

All RIXS spectra of the magnetite sample presented in this work were recorded at the high resolution beamline 4.0.3 (**me**V **r**esolution beam**lin**e, MERLIN) of the Advanced Light Source (ALS) Berkeley (U.S.). The MERLIN beamline is optimized for the XUV region and covers the energy range from 10-150 eV. Depending on the settings absolute photon energy resolutions of 0.25-5 meV are achievable by the setup[166]. In the following chapter, the most relevant details of the setup are summarized. Technical details of the overall setup are summarized in table 3.1 at the end of this section.

3.1.1. Beamline Layout

An overview of the technical and optical layout of the beamline can be found in [166]. Figure 3.1 shows a sketch of the beamline taken from [167].

3.1.2. MERIXS Spectrometer - Optical Layout and Technical Realization

The central part of the RIXS endstation of the MERLIN beamline is the custom made x-ray spectrometer. It is optimized for high throughput and constructed for operation without entrance slits. The beam radius on the sample is optimized to be in the order of 5 μm which is important to allow slit less operation[163]. In [168] and [163], the technical design of the spectrometer is described. The spectrometer consists of three optical elements: (1) Spherical mirror for focusing, (2) a variable line spacing (VLS) grating for wavelength dispersion and (3) an in-vacuum CCD detector. A sketch of the optical pathway through the spectrometer is shown in figure 3.2. It's technical realization is shown in a CAD drawing in figure 3.3.

3.1.3. Scattering from sub-mm Facets

The beam size of the beam at the sample at the MERLIN beamline is optimized for very small values of approximately 5 μm. Therefore it is possible to use a RIXS spectrometer without entrance

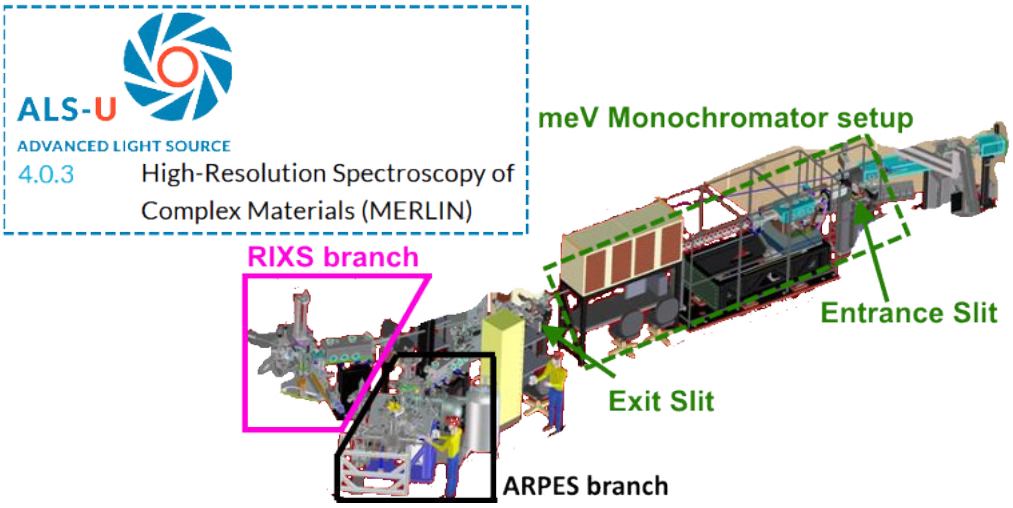

Figure 3.1.: Figure taken and modified from [167]. CAD drawing of the of the MERLIN beamline 4.03 at the Advanced Light Source (ALS) in Berkeley. The beamline has two branches: An ARPES setup and the MERIXS setup for XUV RIXS experiments used for the work in this thesis.

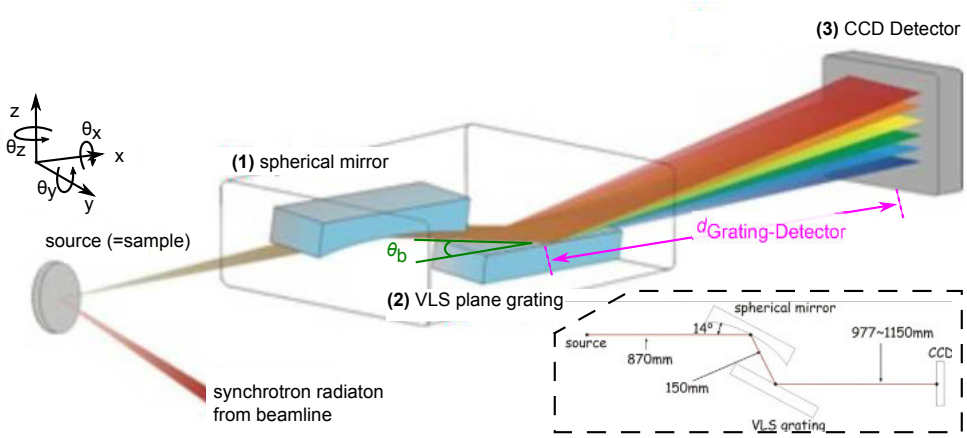

Figure 3.2.: Figure taken from [169]. Optical layout of the spectrograph at the MERIXS endstation. The incident beam is focused on the sample through the beamline optics. This beamline focus, located on the sample resembles the source for the optical design of the spectrometer. From that source the beam is focused with a spherical mirror (1) onto the VLS grating (2) which disperses the beam onto the CCD detector (3). To adapt the spectrometer on the incident photon energy the blazing angle θ_b of the grating and the distance between grating and detector $d_{\text{Grating-Detector}}$ can be varied. The theoretically expected detection efficiency is 2-3$\times 10^{-5}$. Technical details on the optical components are summarized in table 3.1.

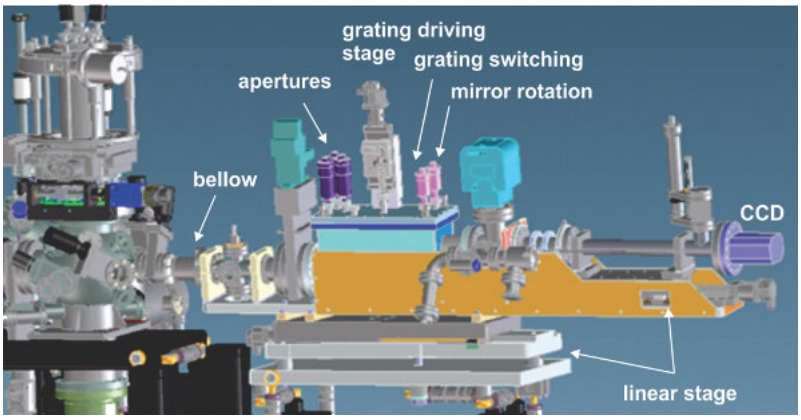

Figure 3.3.: Figure taken from [170]. Technical realization of the MERIXS endstation. The total length of the spectrometer is ca. 2m. A sketch of the optical layout is shown in figure 3.2.

slit. This guarantees a high throughput. A disadvantage of the slitless design of the spectrometer can occur when the source point is not as small and perfect as expected. The occurrence of multiple source points as it could occur on faceted surfaces with facets smaller than the beam diameter, causes multiple copies of the elastically scattered contributions as depicted in figure 3.4. These copies would not arrive at the same CCD positions although their photon energy is identical[171].

3.1.4. Sample Mounting and Geometry

A technical drawing of the vacuum chamber taken from [169] is shown in figure 3.5 including a relative coordinate system. The drawing shows the separation of the setup into three main components: (1) The Preparation chamber where the sample can be cleaved. (2) The x,y,z manipulator for position adjustments. (3) The spectrometer chamber. To attach the sample onto the manipulator, it is glued on a sample holding base plate. This base plate is then screwed into the head of the He-cryostat (see red marked detail in figure 3.5). The whole cryostat is mounted on a 3-axis (x,y,z) manipulator rotatable around the y-axis (yaw, θ). Additionally, the sample head can be adjusted in pitch and roll angle (pitch χ, roll ϕ) relative to the y-axis. For cooling the sample, the He-cryostat can be used. A temperature stabilization is included in the setup guaranteeing a constant temperature at the sample during the measurements. The temperature is measured at the cryostat head which is in direct contact with the sample holding base plate. For high thermal and electrical contact a silver containing paint is put in significant amount at the interface between sample and sample holding base plate. The sample holding base plate is screwed into the He-cryostat head which guarantees thermal contact and justifies the temperature measurement at the Cryostat head.

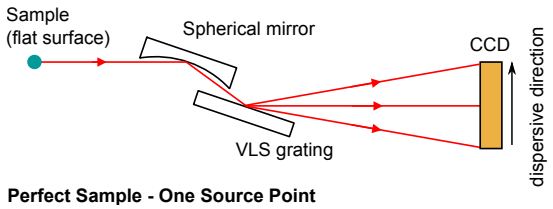

(a) Figure redrawn and modified from [163]. Sketch of the optical path of an ideal flat surface from the sample to the CCD detector.

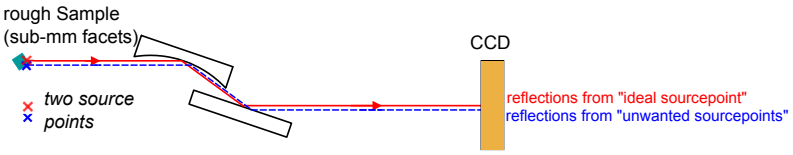

(b) Figure redrawn and modified from [163]. Sketch of the optical path of two distinct source points. Although the photon energy is the same, they appear on different positions on the CCD detector.

Figure 3.4.: Due to the high reflectivity of solids in the XUV wavelength region compared to that in the soft X-rays region, it might happen that very small surface facets appear as multiple source points for the spectrometer. In this case photons with the same wavelength that were scattered at different facets, form distinct source points for facets smaller than the beam diameter ($\approx$50 μm). The slitless optical layout of the spectrometer will than lead multiple elastic lines appearing on different positions on the CCD caused by different source points.

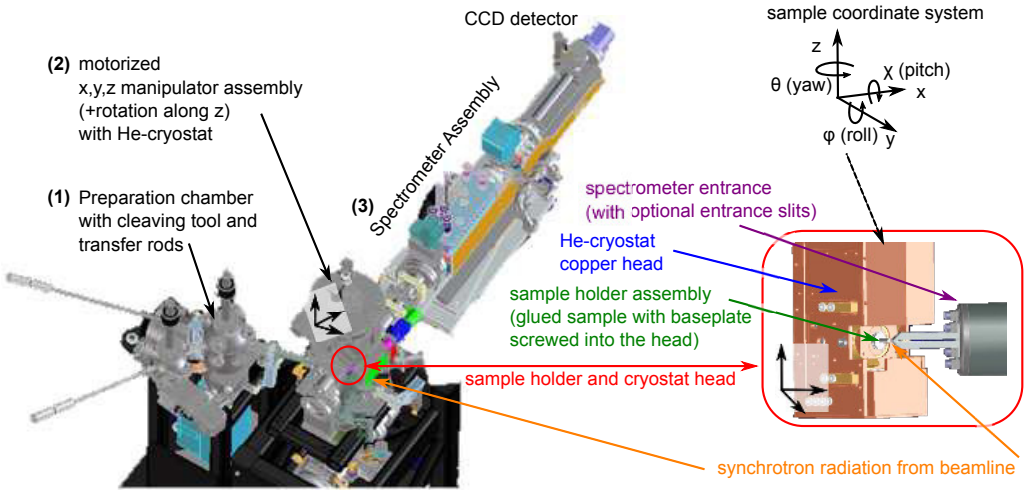

Figure 3.5.: Figure taken from [169]. Technical drawing of the full MERIXS endstation including the preparation chamber, the sample holding x,y,z manipulator and the spectrometer assembly. Further descriptions are given in the text of section 3.1.4.

3.1.5. Data Processing

Before recording a spectrum with the MERIXS setup, the beamline is set to the desired photon energy. Additionally the blazing angle θ_b and the distance between grating and detector $d_{\text{Grating-Detector}}$ (see figure 3.2) are adjusted to achieve optimal resolution in the photon energy region of interest. To acquire data, the CCD is exposed for a freely adjustable amount of time. In the measurements presented in this work, the exposure time was chosen between 400 s and 600 s. The procedure for measuring a spectrum follows always the same protocol, of which summarize most of the steps briefly in the following section:

1. Record Background-image
2. Record several RIXS-images with constant beamline and sample settings
3. Subtract Background-image from every RIXS-image
4. Correct RIXS-images for curvature
5. Apply energy axis
6. Normalize Intensity

Background Subtraction

Several times during the measurements we recorded background images which are subtracted from the spectra. An example image is shown in figure 3.6. The reason for the background intensity is most the temperature of the CCD camera readout electronics which causes thermally induced counts on the detector. As the temperature distribution is constant during the operation, the intensity resulting from that can be subtracted from the spectra which are recorded.

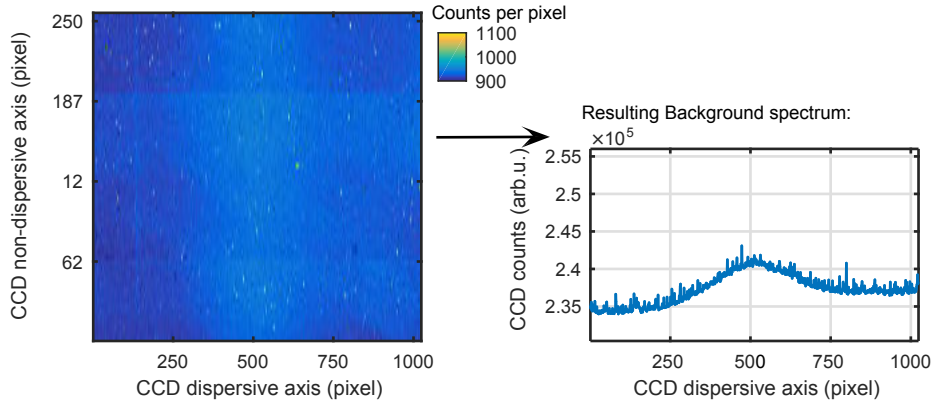

Figure 3.6.: Example for an acquired background image of the CCD detector. The image shows data resulting from a 600 s exposure with closed beamline shutter. The intensity maximum around pixel number 500 results from the finite temperature of the CCD readout electronics which are spatially close to the detector.

Curvature Correction

Due to the use of a spherical mirror for focusing the beam, the dispersed photons arrive on a curved line along the non-dispersive direction of the CCD. This curvature is fitted with a 4^{th}-order Polynomial function and the image corrected with the retrieved function. Example images are shown in figure 3.7.

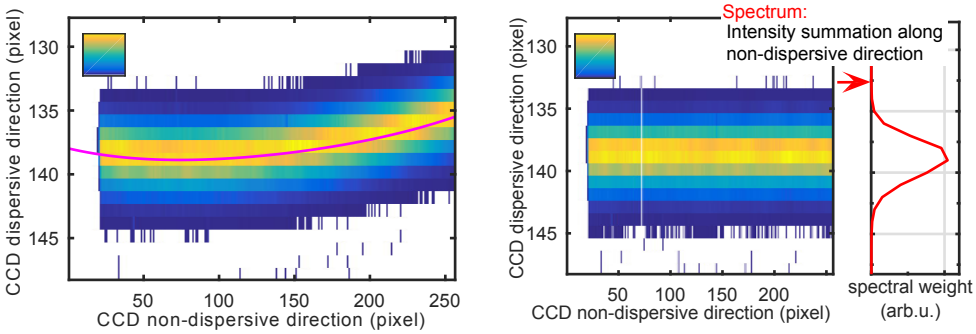

(a) Example raw image. Photons with the same energy arrive on a curved line. The curvature is fitted with a 4^{th}-order polynomial function (magenta line).

(b) Curvature corrected CCD image.

Figure 3.7.: Example for the curvature correction applied to all CCD images (spectrometer set-energy: 48.01 eV, photon energy: $h\nu = 50$eV). The 4^{th}-order polynomial function coefficients used for the curvature correction are tabulated in table B.2 for all used spectrometer settings.

Energy Calibration

The relation between photon energy and position of the detected photons on the CCD detector depends on the settings of the grating blazing angle θ_b and the distance of the detector from the grating. Both has to be changed for every incoming photon energy to achieve optimum energy resolution in the photon energy range from 37 eV to 150 eV. For that reason, a calibration curve was recorded for every setting of the spectrometer that was used in the presented measurements (spectrometer settings are labeled as "spectrometer set-energy" in the LabView based beamline control software). For that purpose, the beamline energy was varied for constant settings of the spectrometer and a calibration curve extracted with a 4^{th}-order polynomial function. An example of such calibration spectra and the extracted calibration fit are shown in figure 3.8(b). Note that the fit through the data points is not based on an analytical concept but purely empirical.

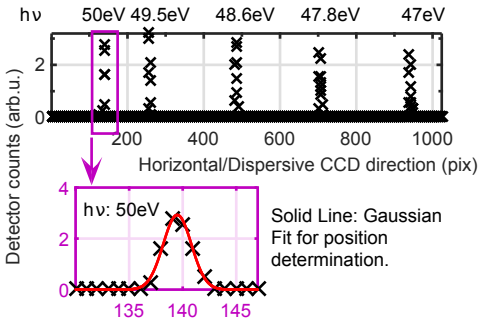

(a) Curvature corrected and background subtracted spectrum of the CCD, summed along the non-dispersive direction (top, black crosses). The magenta marked detail (bottom) shows a Gaussian Fit (red line) which I used for pixel-position determination.

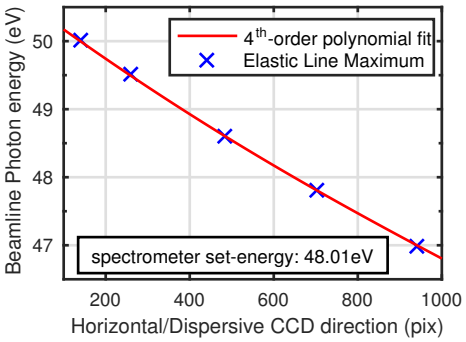

(b) Pixel-position at the detector (retrieved as described in the left figure (a)) for different photon energies (blue crosses). The data points are fitted with a 4^{th}-order Polynomial function (red line). The fit is used as an energy axis for that particular spectrometer set-energy.

Figure 3.8.: To retrieve an energy calibration, a reference spectrum is recorded for each used spectrometer setting. The reference spectrum is the sum of five CCD images with constant spectrometer setting but different photon energies of the beamline. An example is shown in the left figure (a). The energy-axis is retrieved by finding an empirical relation between pixel-position and the known photon energy as shown in the right figure (b). In this figure the calibration is shown for a spectrometer set-energy of 48.01 eV. The beamline energy was varied between 47 eV and 50 eV.

Intensity Normalization

As the beamline intensity varies for different photon energies[1], the count rate of the CCD detector has to be normalized to quantitatively compare spectra recorded at different photon energies. All spectra shown in this work are than normalized to the relative intensity of the beamline following:

$$I_{\text{CCD}}^{\text{relative}}(h\nu) = I_{\text{CCD}}(h\nu)/I_0^{\text{relative}}(h\nu). \tag{3.1}$$

3.1.6. Tables

This section contains tables summarizing technical details of the MERIXS high resolution RIXS setup. Additionaly tables for the energy calibration and curvature correction can be found in the appendix B.1.2.

[1] The photon energy dependence of the intensity is a fundamental property of synchrotron radiation (e.g. [5]).

Optical Element	**Technical details** (from [163])
(1) spherical mirror	◦ Au-coated
	◦ $R_{\text{nominal}} = 4060 \pm 0.2\%\,\text{mm}$
	◦ incident angle 14°
	◦ active dimension $130\times25\,\text{mm}^2$
	◦ collected angle along dispersive direction 35 mrad
(2) VLS grating	◦ Au-coated
	◦ line density: 1850 to 2150 lines/mm
	◦ active dimension $72\times12\,\text{mm}^2$
	◦ blaze angle $\theta_\text{b} = 4 - 6\,°$
(3) in-vacuum CCD detector	◦ 2048×2048 pixels of $13.5\mu\text{m}^2$ size (backthinned Marconi 42-40 sensor)
	◦ collected angle along non-dispersive direction (limited by detector width) 13 mrad
	◦ detection efficiency 30-45 %
	◦ Temperature during operation: -64 °C
	◦ Binning during operation: 2×8 (disp.×non-disp. axis)
overall setup	◦ beam radius in the order of 5μm required
	◦ detectable energies: 37 eV to 150 eV
	◦ overall solid angle: 0.046 % of 4π
	◦ combined efficiency of optics and detector: 4-7%
	◦ detection efficiency (including solid angle): $2\text{-}3\times10^{-5}$
	◦ combined absolute energy resolution (beamline and spectrometer) for photon energies from 42 eV to 59 eV: 7-17 meV

Table 3.1.: Technical details of the elements forming the spectrograph of the MERIXS beamline. A setup sketch is shown in figure 3.2.

3.2. Magnetite Sample Characterizations

In this section, the sample origin and quality is described. After that, optical pump-probe measurements are described to characterize the samples. At the end, as a reference for the RIXS measurements, the results of calculations of the x-ray absorption spectrum (XAS) of magnetite with the "CTM4XAS" software are shown.

3.2.1. Magnetite Samples

As sample for the RIXS measurements we used an ex-vacuum cleaved magnetite (Fe_3O_4) single crystal. The highly stochiometric magnetite samples stem from a collaboration with V. A. M. Braber and are grown with a (111) orientation as described in [172]. The cylindrical crystals have a length of few cm and a diameter of $\approx$3 mm. A photograph of the cleaved sample on the sample holder of the RIXS setup is shown in figure 3.9.

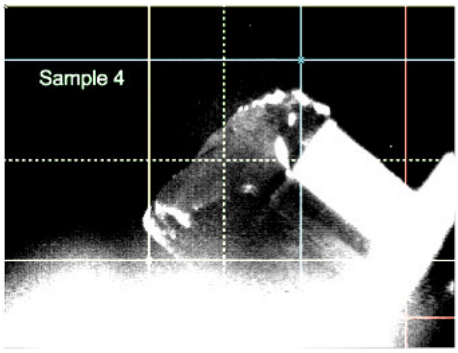

Figure 3.9.: Camera picture of the ex-vacuum cleaved magnetite single crystal mounted on the sample holder. The surface quality could by eye be proofed to consist of flat facets in the order of few mm^2. A position dependent analysis of a x-ray absorption measurements in figure 4.2 could not confirm this facet dimension and proofs them to rather be in the few 0.1 mm^2 region.

3.2.2. Driving the Verwey Transition with a Short Laser Pulse - Time Resolved Optical Reflectivity Measurements

To assure, that the smaples show the transition of interest, we performed optical reflectivity measurements. The optical reflectivity of magnetite below and above the Verwey temperature is different (see figure 3.10). Randi et al. show in [133] that changes in the optical reflectivity $\Delta R/R$ can be used to probe the actual phase of magnetite after being kicked out of equilibrium with an ultrashort laser pulse[134]. We used the experimental setup of Randi et al., to confirm our samples show the same optically driven Verwey transition[2]. In this section, the setup is introduced first.

[2]The samples later used for the RIXS studies are cleaving fragments from the same crystal rods.

After that, the measured reflectivity spectra of our samples are presented. The section ends with a short conclusion.

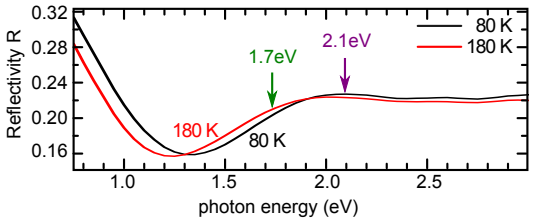

Figure 3.10.: Figure taken and modified from [133]. Reflectivity of magnetite at temperatures below (T=80 K, black line) and above the Verwey temperature (T=160 K, red line). The reflectivity is deduced from ellipsometric measurements. The reflectivity changes for the different temperatures. At 1.7 eV (marked with green arrow) it increases with temperature while at 2.1 eV it reduces (marked with magenta arrow). This signature of the Verwey transition is used for probing the samples phase after optical excitation.

Setup

The time resolved relative optical reflectivity measurements were performed at the IR-pump super continuum probe setup in the laboratory of the TReX[3] group of Prof. F. Parmigiani at the site of the Elettra synchrotron in Trieste (italy). The setup is designed to probe the relative change of optical reflectivity $\Delta R/R$ in the photon energy range of (1.5 eV to 2.6 eV/830 nm to 476 nm) after excitation of the sample with the fundamental 800 nm laser. Knowing this variations allows to disentangle dynamics within correlated electron systems[173][174][175]. Measuring the relative reflectivity $\frac{\Delta R}{R}$ requires no absolute calibration. It can be calculated with:

$$\frac{\Delta R}{R} = \frac{R_{\text{unpumped}} - R_{\text{pumped}}}{R_{\text{unpumped}}}. \tag{3.2}$$

Here $R_{\text{pumped/unpumped}}$ represents the not-normalized reflectivity from the sample with/without optical excitation (see also inset in figure 3.11). The setup and the working principle is described in figure 3.11. In table 3.2 all relevant properties of the laser and the setup are summarized. Energy calibration curves as well as the corrections applied to an energy dependent delay variation are shown in the appendix B.1.3.

Pump-Probe Results

We could measure the optical transient optical reflectivity after excitation with two fluences $F_1 = 0.53\,\text{mJ/cm}^2$ and $F_2 = 3.25\,\text{mJ/cm}^2$. The delay dependent relative changes of the reflectivity for the two fluences are shown in figure 3.12 (full probe energy range) and figure 3.13 (two selected probe energies).

[3]TReX group acronym: Time Resolved X-Ray spectroscopy.

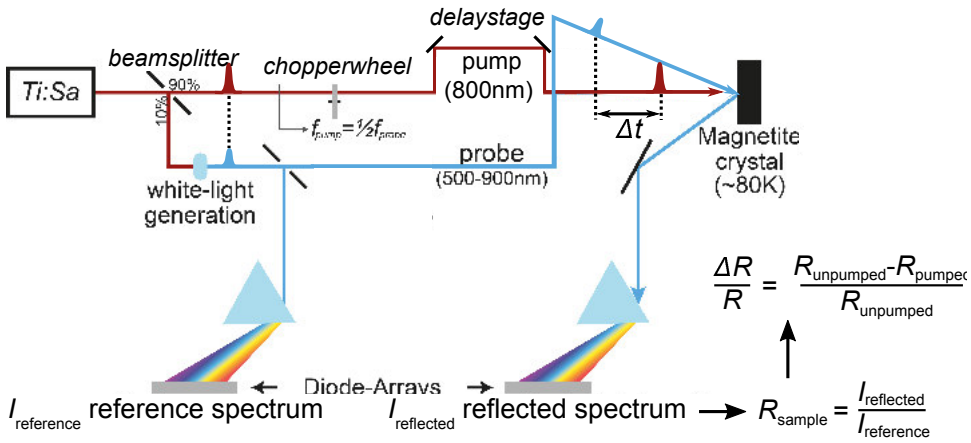

Figure 3.11.: Figure after [176] and [173]. Schematics of the 800 nm pump, supercontinuum probe setup of the T-Rex laboratory in Trieste, IT. The initial pulses (pulse length $\tau_{\mathrm{FWHM}} \approx 70\,\mathrm{fs}$) of the Ti:sapphire laser are divided into a pump- and probe arm. Within the probe-arm the white light ($h\nu_{\mathrm{Probe}} = 1.5\,\mathrm{eV}-2.6\,\mathrm{eV}$) is generated in an optical fiber[177][176]. Within the pump arm a delay Δt can be introduced between the two pulses. At the sample, both beams are overlapped again. The energy dispersed intensity reflected from the sample as well as that of a reference arm is detected with arrays of optical diodes. With this one can retrieve the reflectivity R. The relative pump induced change of optical reflectivity $\Delta R/R$ is then determined by measuring the unpumped and the pumped reflectivity signal $R_{\mathrm{unpumped/pumped}}$ (see equation 3.2). To retrieve the unpumped reflectivity signal, every second shot of the pump beam is blocked with the help of a mechanical chopper wheel.

element	comment	detailed settings
Ti:Sapphire laser	repetition rate	f=40 kHz
	pulselength	$\tau_{\mathrm{FWHM}} = 70\,\mathrm{fs}$
	central wavelength	800 nm/1.55 eV
super continuum source	bandwidth	$h\nu \in \{1.5-2.6\}\,\mathrm{eV}/\{830\text{-}476\}\,\mathrm{nm}$
	pump spot radius	r_{Pump}=130 μm
	probe spot radius	r_{Probe}=73.3 μm

Table 3.2.: Properties of the 800nm pump, supercontinuum probe setup of the T-Rex laboratory in Trieste, IT.

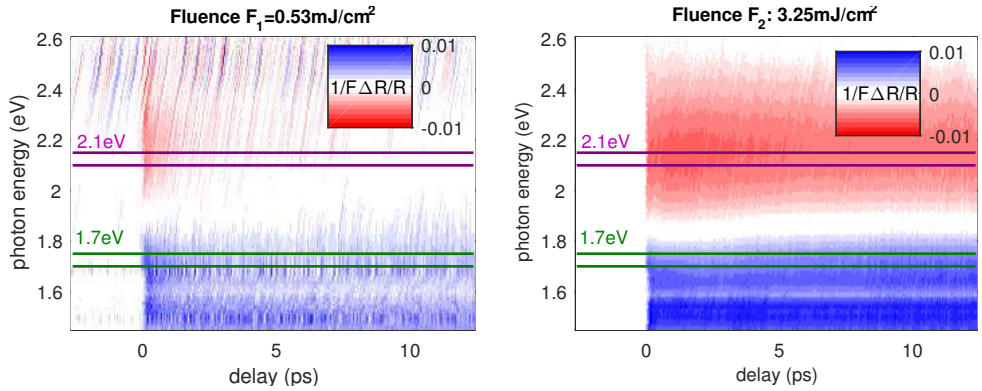

(a) Low fluence: F_1=0.53 mJ/cm^2. (b) High fluence: F_2=3.25 mJ/cm^2.

Figure 3.12.: Time dependent evolution of the relative reflectivity $\Delta R/R$ of magnetite ($T_{\text{sample}} =$ 77K) after excitation with a short laser pulse with different fluences F on the sample (pulse length $\tau_{\text{FWHM}}^{\text{pump}} = 70\,\text{fs}$, $h\nu_{\text{pump}} = 1.55\,\text{eV}$). The reflectivity change is normalized to the fluence. For both fluences one can observe changes. A line plot of the marked photon energies at 2.1eV (magenta marks) and 1.7 eV (green marks) is shown and commented in figure 3.13.

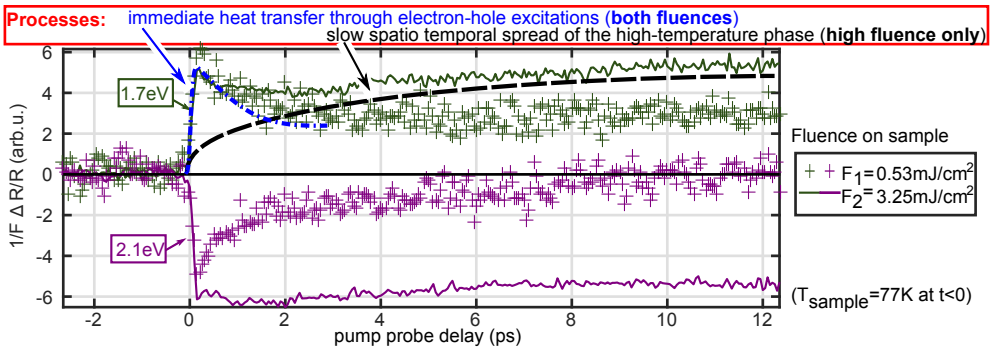

Figure 3.13.: Variation of the normalized change in reflectivity of magnetite at 1.7 eV (green lines) and 2.1 eV (magenta lines) after excitation with a short laser pulse. The sample ($T_{\text{sample}} = 77\,\text{K}$) was excited with two different fluences $F_1 = 0.53\,\text{mJ/cm}^2$ (lines with markers)/$F_2 = 3.25\,\text{mJ/cm}^2$ (solid lines without markers). Both fluences $F_{1/2}$ show an immediate increase (1.7 eV)/drop (2.1 eV) in reflectivity at $\Delta t = 0\,\text{ps}$. The reflectivity at low fluence F_1 recovers almost (1.7 eV)/fully (2.1 eV) after $\tau_{\text{Phase 1}} \approx 4\,\text{ps}$. The reflectivity after high fluence excitation shows the slow grow and saturation of a second phase which is attributed to the spatial spread of the temperature increase[133] at high fluences (see also figure 2.6). As guides for the eyes the intensity evolution connected with the two time scales are labeled with blue dash-dotted (fast response) and black dashed lines (long time response) in the spectrum. Figure 3.14 shows, that the separability of this two processes into a fast and a slow one is connected to an intermediate fluence regime.

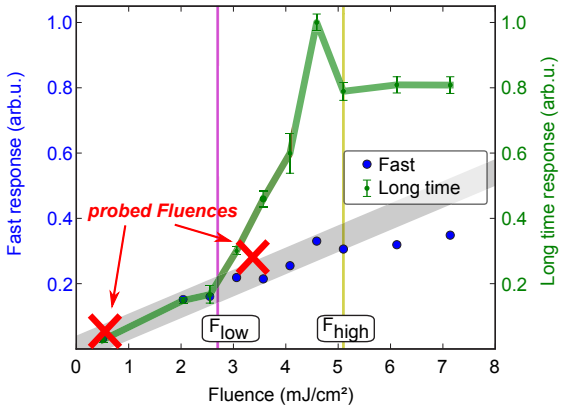

Figure 3.14.: Figure taken from [133]. Time scale separation of the reflectivity signal curves for different fluences. The left axis shows the normalized intensity at $\Delta t = 0.2\,\mathrm{ps}$ (blue marks) as a measure for the first phase. The right axes shows the normalized intensity at $\Delta t = 8\mathrm{ps}$ (green marks)as a measure for the second phase (nucleation). Two characteristic fluences are marked with F_{low} and F_{high}. Below fluences of F_{low} only the first phase is reached and in between F_{low} and F_{high} they occur subsequently. At fluences above F_{high} the first phase and second phase no longer separable. This non-separability manifests in the deviation of the blue dots from the gray shaded linear regime. The different phases of magnetite after optical excitation are summarized in section 2.1.6.

Conclusion

We could show that our samples can be driven from the Verwey state below T_V to the excited state as reported in [13] and [133]. The maximum fluence of $F_2 = 3.25\,\mathrm{mJ/cm^2}$ is in the intermediate regime where two phases of the excited magnetite co-exist: Parts of the sample remain in the Verwey phase (monoclinic symmetry, insulating state) while simultaneously islands of the high temperature phase (cubic symmetry, metallic state) grow. Our measurements thus reproduce these of [133] confirming that our samples are good for time resolved experiments.

3.2.3. Simulated X-ray Absorption Cross Sections

With the help of the "CTM4XAS" code[154] (Charge Transfer Multiplet Calculations for X-ray Absorption Spectroscopy) it is possible to simulate the x-ray absorption cross sections for L- and M-edge transitions of transition metals. The program evaluates the influence of crystal fields onto the atomic multiplets of the transition metal atoms. Also charge transfer influences are taken into account. For magnetite, simulations were perfomred using the symmetry parameter of magnetite in the high temperature phase[153][178]. The spectrum is plotted in figure 3.15. At the low energy side a feature of the Fe^{2+} ions separates at $E = 51\,\mathrm{eV}$ sharply from the others (marked with a blue 1). At the high energy side at $E = 57.5\,\mathrm{eV}$ feature (2) of the Fe_B^{2+} separates clearly. In the energy range of $54.5\,\mathrm{eV}<E<56.5\,\mathrm{eV}$ five features representing absorption at all three possible Fe configurations overlap tightly.

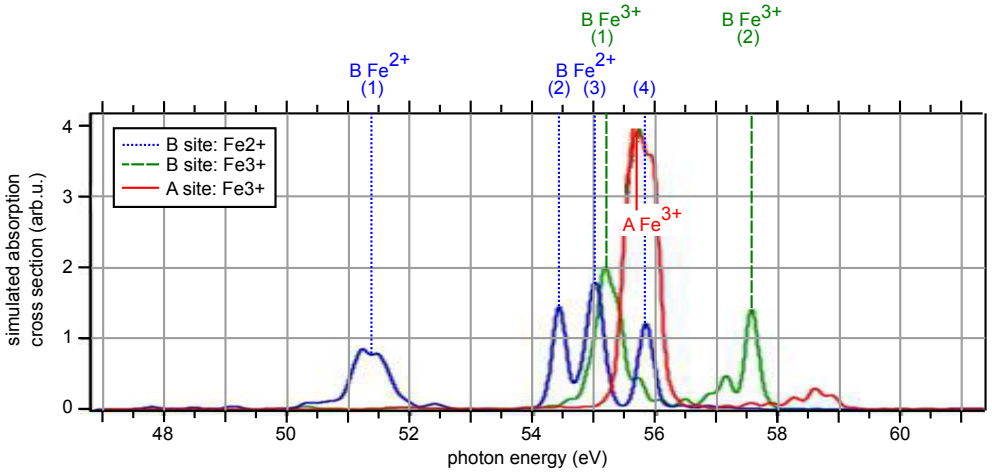

Figure 3.15.: Simulated differential XAS cross section for magnetite (simulated by M. Dell'Angela[179] using "CTM4XAS"[154]). The multiple absorption maxima of the three iron species are clearly separated: 4 Peaks at B site Fe^{2+} (blue), 2 Peaks B site Fe^{3+} (green), 1 Peak at A site Fe^{3+} (red).

4. Magnetite - Signature of the Verwey Transition in the M-edge RIXS Spectrum

In search for a signature for the Verwey transition in magnetite in the XUV RIXS spectrum we recorded a series of RIXS spectra. The excitation energy was resonant to the iron 3p-3d transitions (Fe $M_{2,3}$-edge) between $h\nu = 50\,\text{eV}$ and $62\,\text{eV}$ were recorded at temperatures below and above the Verwey temperature $T_V = 125K$. In this section, the alignment strategy and the experimentally determined x-ray absorption spectrum will be presented first. After that, the results of the RIXS measurements as well as a a quantitative evaluation with an empirical fitting model is presented. Finally, the shape of the spectra is discussed and spectral variations between the two temperatures highlighted.

4.1. Sample Alignment and Scattering Geometry

The sample mounting was described above in section 3.1.4. Figure 4.1 shows a sketch of the scattering geometry. During the whole data acquisition the polarization of the beamline was set to linear polarization. The angle between incoming beam and the detected fraction of the scattered light was $\approx 90\,°$.

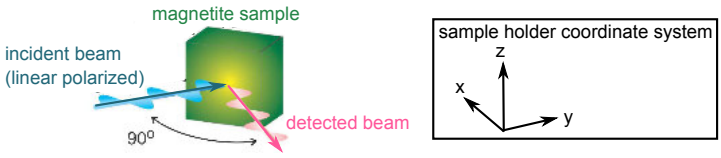

Figure 4.1.: A sketch of the scattering geometry during the presented measurements (figure adapted from [156]). The incident beam was linear polarized. The angle between sample surface normal and incident beam is $\approx 45\,°$ so that the angle between incident beam and spectrometer entrance ($\hat{=}$detected beam direction) is $\approx 90\,°$.

Before being glued on the sample holder (sketch of the sample mounting see figure 3.5) the magnetite samples (described in section 3.2.1) were cleaved out of vacuum by hammering the crystal rod. The cleaving was performed to assure a clean crystal. The sample was transferred into the vacuum chamber after less than 60 min in air. By eye we estimated the size of the facets caused by cleaving to be in the order of $\approx 1\,\text{mm}^2$. This estimated facets dimension could not be confirmed

by a second method presented in figure 4.2. The figure shows the sample current measured during a position scan of the sample. By analyzing the variation of the sample current, which depends on the surface facet orientation, it enables an estimation of the facets dimension. This is possible because the absorption of x-rays due to the sample depends sensitively on the angle of incidence in the XUV wavelength region[161] and therefore is a measure of the facets-surface orientation. The position dependent measurement of the absorption signal (≙sample current) presented in figure 4.2 shows for the facet used in the RIXS measurements a size of ≈0.5×0.8 mm².

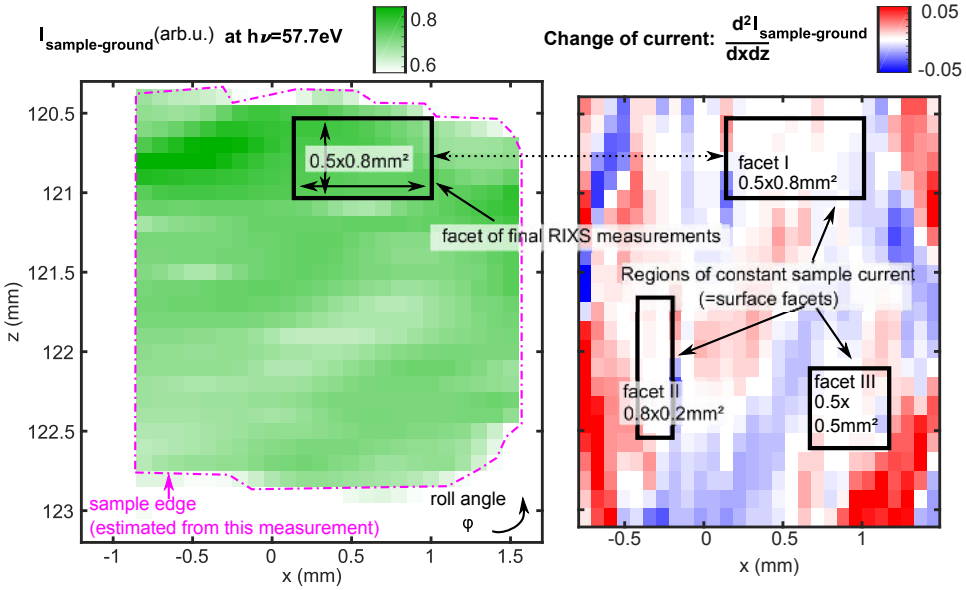

Figure 4.2.: Left: Sample current $I_{\text{sample-ground}}$ at a fixed photon energy above the Fe M-edge ($h\nu$ = 57.8 eV) for different sample x and z-position (y=4.6 mm, $\phi = -90\,°$, $\chi = 2\,°$). Right: Differentiated picture to highlight regions with constant sample current (≙zero in differentiated image). By scanning the sample position at a constant photon energy under the x-ray spot (diameter ≈ 50μm) it is possible to determine the edges of the cleaved magnetite surface (marked with dashed line in the left image). Surface facets cause a different scattering geometry and therefore variations in the sample current. The sample current is thus a measure for the surface flatness. Three regions of constant sample current, corresponding to flat surface facets are marked in the differentiated picture with I, II and III. Facet I (0.8×0.5=0.4 mm²) was chosen for the final RIXS measurements. It is additionally labeled in the left image. Its size is big compared to the beam diameter (R=5 μm). Note that the sample roll and pitch angle (ϕ/χ) were changed from the motor scan to the RIXS measurements ($\Delta\phi = 165\,°/\Delta\chi = -10\,°$). The z- and x-position can therefore not be directly compared.

4.2. Xray Absorption Measurement (Total Electron Yield)

With the RIXS setup at the ALS it is possible to determine the relative absorption cross sections in the XUV region. This is done by measuring the current between sample and ground $I_{\text{sample-ground}}$

while the sample is illuminated with x-rays at different photon energies. The recorded sample current $I_{\text{sample-ground}}$ is related with the relative x-ray absorption cross section $\sigma_{\text{XAS}}^{\text{relative}}$ via:

$$\sigma_{\text{XAS}}^{\text{relative}}(h\nu) = I_{\text{sample-ground}}^{\text{relative}}(h\nu)/I_0^{\text{relative}}(h\nu). \tag{4.1}$$

Figure 4.3 shows the experimentally determined relative absorption cross section spectrum of magnetite in the low temperature phase (T=80 K). Three separate absorption maxima can be identified at ≈51eV, 54 eV and 57.8 eV, while the first one shows a double-peak sub-structure. The pronounced maximum at 57.8eV shows good agreement with the literature data on magnetically oriented samples shown in figure 2.5a. Also the first and second peak can be found in the spectra, assuming that the spectra of this work represent a superposition of the two magnetization directions in figure 2.5.

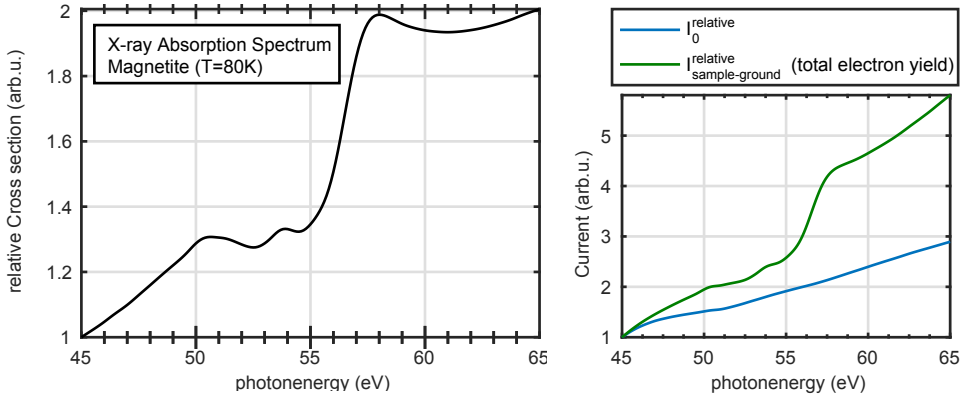

(a) Measured normalized x-ray absorption spectrum (XAS).

(b) Normalized Sample Current and beam intensity.

Figure 4.3.: The left graph in (a) shows the relative x-ray absorption cross section $\sigma_{\text{XAS}}^{\text{relative}}$ of magnetite at T=80 K<T_{Verwey} for different photon energies (black line). To measure this spectrum, the current between sample and ground is recorded as a measure for the total electron yield for different photon energies. This current is than normalized by the relative intensity of the incident photons. The right graph in (b) shows the measured relative/normalized total electron yield (green line) and the relative beamline intensity I_0 measured with a gold mesh (blue line).

4.2.1. Comparison of Experiment and Simulations

The x-ray absorption measurements at magnetically oriented magnetite shown in figure 2.5b show no significant difference above and below the Verwey temperature. This justifies a qualitatively comparison of the simulated (RT) and measured absorption spectra (T=80 K) of magnetite of this work, although the stem from the two different phases. In figure 4.4 the experimentally determined absorption spectrum is compared to the simulated spectra presented in the previous section 3.2.3. After applying a slight rescaling of the energy axis it is possible to match the three

distinct absorption features of the experiment with the simulations. The first maximum with the experimentally determined double structure corresponds to absorption at the Fe_B^{2+} sites which also in the simulations shows a pronounced double-peak structure. Also the separate second maximum corresponds to absorption at the Fe_B^{2+} sites. Feature number three of the experimentally determined spectrum at 57.8 eV corresponds to an absorption feature at the Fe_B^{3+} sites of the simulations. The densely packed absorption maxima of the simulations between 54.5 eV and 56.5 eV are summed up and form the rising edge of the third experimentally determined feature. Here the simulated positions aren't spread across the whole edge but gather at the low energy edge. Maybe this mismatch between simulation and experiment is a consequence of the difference in temperature of simulation (RT) and experiment (T=80 K).

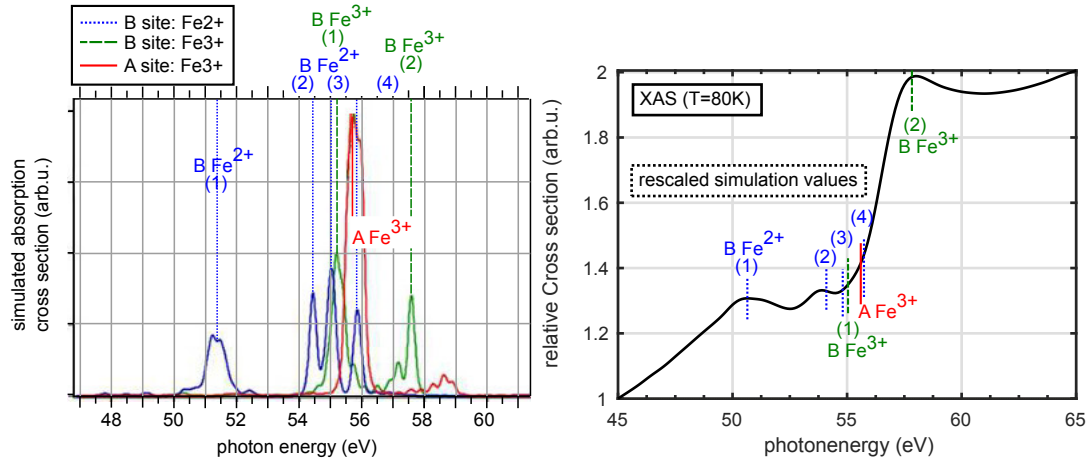

(a) Simulated $M_{2,3}$ edge absorption spectrum (see also section 3.2.3).

(b) To match the absorption peaks of experiment and these obtained in the simulations the simulated energy axis is rescaled.

Figure 4.4.: The simulated XAS spectra of figure 3.15 are overlapped with the measured ones in the left panel. A good match is achieved when scaling the energy axis ϵ by $\epsilon_{\text{rescaled}} = 1.16 \cdot \epsilon_{\text{CTM4XAS}}$ and offsetted to match the peak maxima.

4.3. RIXS Below and Above the Verwey Temperature

Before presenting the RIXS measurements of magnetite starting at this section at 4.3.4, the limitations of our experimental setup which did not allow to study energy loss features between an energy loss range of $0 < \Delta E < 0.3$ eV are described. After that, the RIXS spectra at different temperatures are presented and quantified with an emperical fitting model. At the end of this section, the spectral shape is discussed.

4.3.1. Elastic Contributions in the Spectrum

Figure 4.5 shows an example-spectrum as detected for an excitation energy of hν = 50 eV. To improve the spectral line-shape I use a 10-point averaging function to smooth the inelastic contributions. Interesting to note is the intensity ratio between elastic and inelastic contribution. Due to the high reflectivity of magnetite in the XUV wavelength region, the elastic contribution exceeds the inelastic one by almost three orders of magnitude. This elastic contribution of the scattering signal is termed REXS. Due to the low signal in the inelastic tail of the spectrum, we recorded the spectra for rather long acquisition times which led to saturation of the REXS features. Their analysis is therefore not possible and the following sections deal only with the inelastic (RIXS) contribution of the scattering signal.

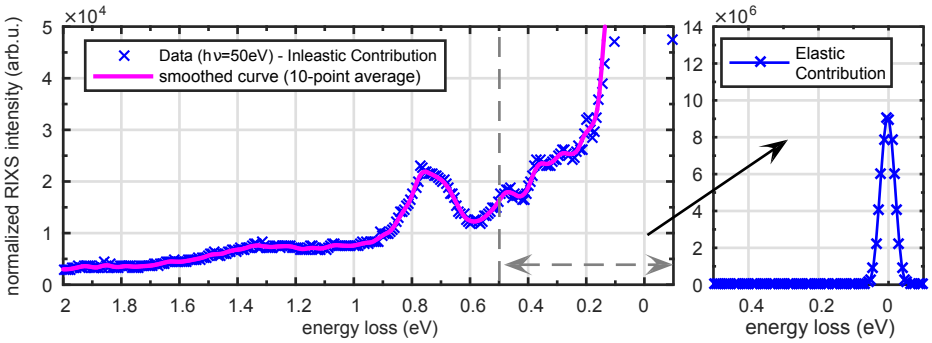

Figure 4.5.: RIXS spectrum of magnetite recorded at T=80 K at an excitation energy of $h\nu = 50$ eV. The right detail shows the elastic contribution to the spectrum. For retrieving this spectrum, the CCD was exposed for 9×10 min to the scattered photons. This figure illustrates A: The used smoothing through the inelastic data with a 10-point-average function and B: The factor of $\approx 10^3$ between the scattering intensity of the elastic relative to the inelastic contributions (right compared to left).

4.3.2. Scattering from Surface Facets - Artifacts in the Low-energy Region

A close up to the tail of the elastic line of the RIXS spectrum in figure 4.6 shows features on the energy gain side ($\Delta E < 0$) of the elastic line. Such energy-gain features can e.g. occur due to energy gain by scattering with a phonon. On the other hand such energy gain features, also called Anti-Stokes lines, are not expected in this energy region. Due to the lack of a physical explanation in the observed energy scale they are treated as features caused by elastic scattering from sub-mm facets of the crystal surface (see section 3.1.3). Since they don't carry physical information the spectral region with energy gain/loss features below/above ±0.3 eV (marked with a green arrow figure 4.6) is excluded from the data analysis. The value of 0.3 eV was chosen because no features appear on the energy gain side above that energy (see figure 4.6).

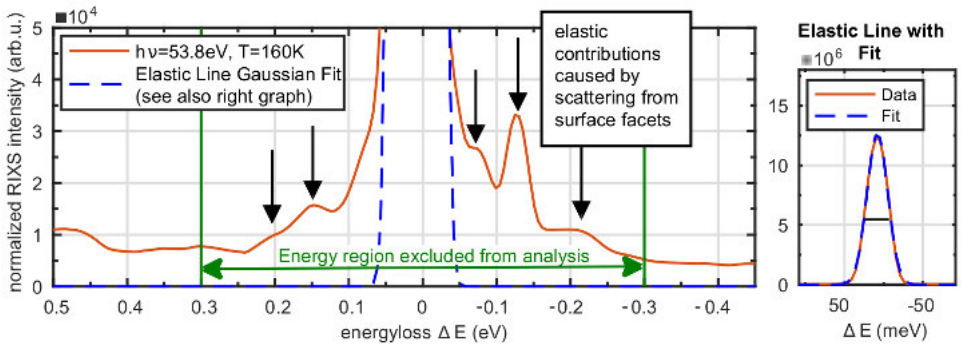

Figure 4.6.: RIXS spectrum of magnetite from the cleaved sample ($h\nu$ = 55.1 eV, T=160 K). The low-energy region around ±0.3 eV from the elastic line shows small elastic contributions. According to the discussion in section 3.1.3 they are attributed to elastic scattering features from sub-mm facets of the crystal surface. As a consequence of this, the energy region is excluded from analysis in the following sections.

4.3.3. Energy Resolution

By determining the linewidth of the elastic line at the detector, one can deduce the overall experimental resolution limited by that of the beamline and the spectrometer. Figure 4.7 shows the elastic linewidth determined for all excitation energies across the RIXS spectrum. The resolution varies for the different spectrometer settings and beamline energies as explained in [163]. The average Full Width at Half Maximum of the combined energy resolution of the spectrometer is determined to:

$$\Delta E^{\mathrm{FWHM}}_{\mathrm{combined}} = (20 \pm 4)\mathrm{meV} \ . \tag{4.2}$$

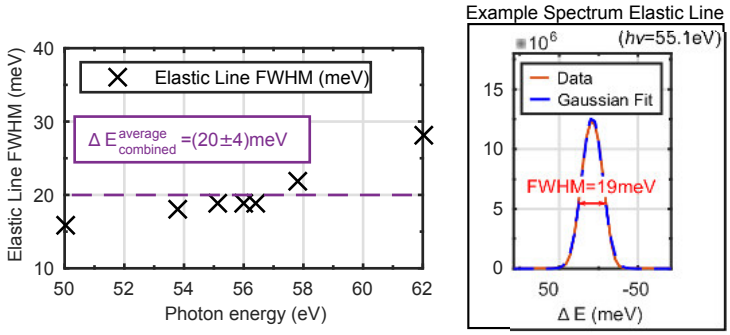

Figure 4.7.: Left: Fitted Full Width at Half Maximum (FWHM) of the elastic line for the different excitation energies. The average energy resolution is marked with a dashed line. Right: Example spectrum with the Gaussian fitting function used to extract the linewidth.

4.3.4. RIXS Spectra at Different Excitation Energies

As the sample alignment required some time, it was not possible to record spectra for more than 10 hours per temperature. The acquisition time per spectrum lies between 60 min and 90 min. As a consequence of this, we recorded spectra at only seven selected photon energies distributed along the Fe3p→3d absorption edge between 50 eV and 62eV (see colored arrows in the inset in figure 4.8). The corresponding RIXS spectra at temperatures of the magnetite sample below (T=80 K) and above (T=160 K) the Verwey temperature are shown in figure 4.8. All seven spectra per temperature show an inelastic contribution at the trustworthy energy region with losses bigger than ΔE>0.3 eV. The intensity of the inelastic features is different for the different excitation energies across the Fe $M_{2,3}$ edge as expected for a resonant measurement. The intensity of the inelastic contribution is bigger for the spectra recorded with a sample temperature of T=160 K compared to these recorded at T=80 K below the Verwey temperature. For an easier discussion of the results I introduce a fitting model in the next section.

4.3.5. Quantification

To quantitatively compare the spectra at the different excitation energies and temperatures, each spectrum is fitted with an empirically chosen fitting function. As the spectra show three distinct maxima, three individual lines are used. The fitting function for an example spectrum at T=80 K[1] is illustrated in figure 4.9. The residuum achieved with this fitting function is acceptable small for all fitted spectra and could not be achieved with similar quality with using Voigt lines. For fitting the spectrum, the three lines were free in all parameter: Peak position, area and linewidth. The numerical values of the fitting parameter for all three lines are summarized in the figures 4.10 (area and peak position) and 4.11 (linewidth) as well as in table 4.1. In the following description of the fitting results, the reference marker $M_{1-3}^{\alpha,\beta,\gamma}$ are used to label excitation energies which show distinct features. The markers are summarized in table 4.10(f). The results concerning peak shape, area, position and linewidth are summarized in this section.

Peak Shape

Theoretically one expects Lorentzian line shapes in RIXS with a linewidth Γ representing the lifetime of the excited states. For the shown RIXS spectra of magnetite it is not possible to use Lorentzian lines to fit the spectra with reasonable quality. Instead a Gaussian line shape and a background consisting of another Gaussian centered at 0 eV energy loss to fit the spectra is used (see figure 4.9). Instrumental broadening as the reason for the unexpected Gaussian line shape can be excluded since the combined energy resolution of 20 meV is much smaller than the observed linewidth. Similar Gaussian Peak shapes were observed by Lee et al. in [160], where they are explained by phonon induced broadening.

[1] An example spectrum of the fitting function applied to the high temperature T=160 K is shown in the appendix figure B.5. The fits of all spectra are shown in the Appendix figures B.6 and B.7.

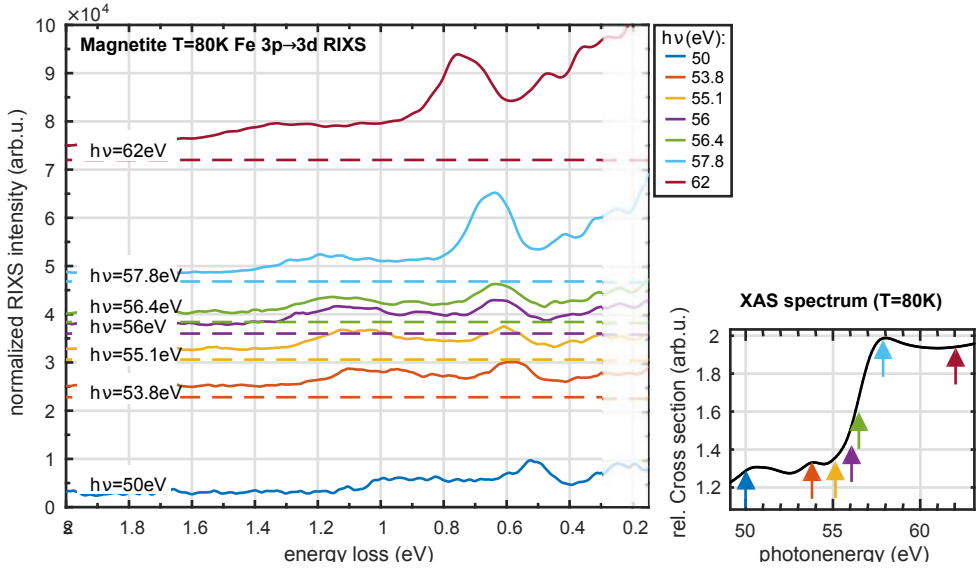

(a) RIXS spectra of magnetite at T=80 K for different excitation energies.

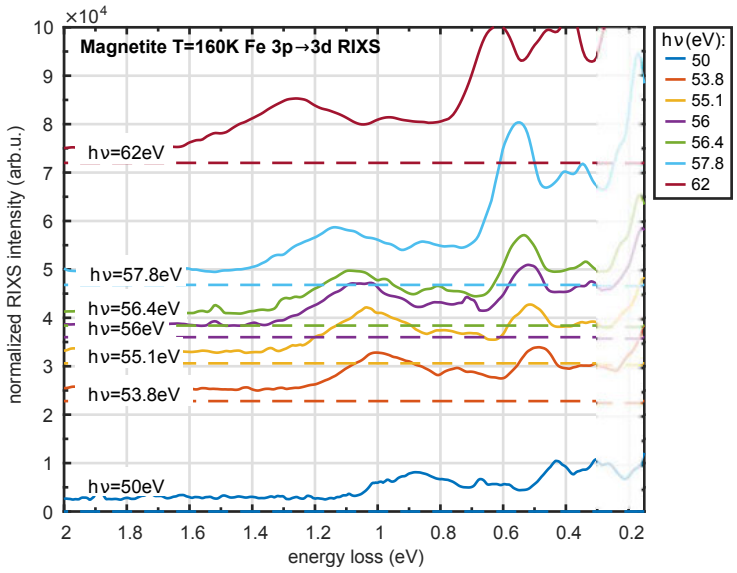

(b) RIXS spectra of magnetite at T=160 K.

Figure 4.8.: RIXS spectra of magnetite recorded at T=80 K (a) and T=160 K (b) at different excitation energies between 50 eV to 62 eV marked with different colors. The spectra are offsetted such, that the distances are proportional to the excitation energy difference. The offset is marked with a dashed line in the respective color. The energy region below ΔE>-0.3 eV can not be trusted because of surface facet scattering. The small inset a the right side in (a) shows the absorption spectrum with small colored marks corresponding to the excitation energies of the RIXS spectra.

Peak Areas

As already discussed on the raw spectra, the peak intensities (≙areas, shown in figure 4.10(c)-(e)) show a dependence on excitation energy and temperature. All three peaks show an intensity increase. On average, the intensity is increased by a factor of ≈2.4 from the spectra at T=80 K to the spectra at T=160 K. Regarding the variation with excitation energy the peaks show different resonance behaviors: Peak 1 at T=80 K shows a similar trend as the absorption spectrum with maxima at $M_1^{\alpha,80\,\mathrm{K}} = h\nu = 53.8\mathrm{eV}$ and $M_1^{\beta,160/80\,\mathrm{K}} = h\nu = 57.8\,\mathrm{eV}$ excitation energy. The first maximum at M_1^{α} vanishes at T=160 K. Peak 2 shows a resonating behavior at $M_2^{\alpha,160\,\mathrm{K}} = h\nu = 56\,\mathrm{eV}$ at T=160 K. At T=80 K instead it exhibits a broad anti-resonance around $M_2^{\beta,80\,\mathrm{K}} = h\nu = 55.1\,\mathrm{eV}$ excitation energy. Peak 3 showing the biggest difference between low and high temperature intensity (factor 3.2) shows a tiny resonance at $M_3^{\alpha,160\,\mathrm{K}} = h\nu = 55.1\,\mathrm{eV}$ for T=160 K. At T=80 K the intensity gradually increases with increasing excitation energy and shows no resonance.

Peak Positions

The fitted RIXS spectra show a linear shift towards higher energy loss with higher excitation energy. The lines connecting the peak positions in figure 4.10(b) are not parallel for the three separate peaks. Instead the slope of the linear shift is gradually increasing. It is lowest for Peak 1 and highest for Peak 3. This effect manifests in increasing distance at low and high excitation energies: $\Delta E^{\text{Peak 1}}_{50\,\mathrm{eV}\text{-}62\,\mathrm{eV}} = 0.2\,\mathrm{eV} < \Delta E^{\text{Peak 2}}_{50\,\mathrm{eV}\text{-}62\,\mathrm{eV}} = 0.28\,\mathrm{eV} < \Delta E^{\text{Peak 3}}_{50\,\mathrm{eV}\text{-}62\,\mathrm{eV}} = 0.36\,\mathrm{eV}$. The shift of energy with increasing excitation energy is monotone for all peaks beside one exception for Peak 2 at T=80 K which shows a sudden drop by 0.2 eV at $M_2^{\gamma,80\,\mathrm{K}} = h\nu = 53.8\,\mathrm{eV}$, jumping back on the line at the next measured excitation energy. The temperature dependence is different for the three peaks: Peak 2 and 3 show a slight difference in position at the two temperatures at $h\nu = 50\,\mathrm{eV}$ which vanishes at $h\nu = 62\,\mathrm{eV}$. Peak 1 instead shows a strong shift of $\Delta^{160\,\mathrm{K}\text{-}80\,\mathrm{K}}_{\text{Peak 1}} = 0.1\,\mathrm{eV}$ towards less energy loss for all spectra at T=160 K compared to the spectra at T=80 K. In a typical RIXS spectrum, the energy-loss position is constant resembling the energy needed to excite the system into an allowed excited state. A mechanism explaining such shifts is a coupling of electronic and lattice degrees of freedom[180][160]. When the excitation has a different spatial distribution the coupling of the ionic and electronic potentials is also different which can lead to shifted excitations. For the observed monotone shift this would imply a monotone shift (e.g. distance increase) of the effective electronic potential in the coordinate system of the ions.

Peak Linewidth

The Gaussian linewidths (Full Width at Half Maximum, FWHM) of the three peaks are shown in figure 4.11. It is in the order of few 100 meV for all three peaks which is much bigger than the measured combined energy resolution of 20meV (section 4.3.3). Beside a slight increase with increasing excitation energy it shows no distinctive variation between the different excitation energies and temperatures for peaks 1 and 3. Only Peak 2 shows a strong variation of the linewidth at the low

temperature spectra, but the big errorbar at these data-points forbids an interpretation of this observed variation. The big error indicates that the fitting function including Peak 2 did not well resemble the spectrum at this points although the residuum of the individual fits shown in figure B.6 is acceptable. A strong increase in temperature would correspond to an increased population of the phonon modes and thus an increase in the observed linewidth. The temperature difference in the two spectra of $\Delta T = 80\,\mathrm{K}$ ($k_B \Delta T = 7\,\mathrm{meV}$) is too small to cause resolvable broadening.

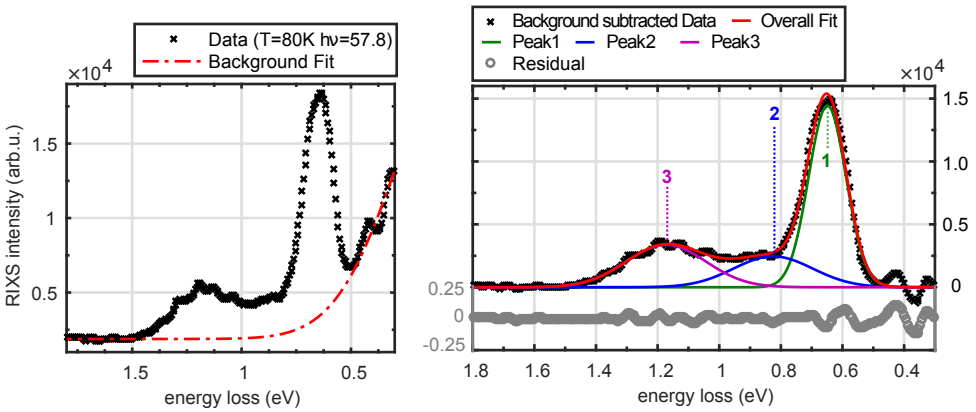

Figure 4.9.: Example of a RIXS spectrum of magnetite recorded at T=80 K (excitation energy of $h\nu = 57.8\,\mathrm{eV}$) illustrating the fitting function used for quantification. Left: The red dash-dotted line shows the shoulder of a Gaussian peak centered at energy loss=0 eV together with a constant offset used to estimate the elastic background contribution. Right: The background subtracted spectrum is fitted with three numbered Gaussian peaks (1-green, 2-blue and 3-magenta). The spectra for the other excitation energies together with the respective fits are shown in figure B.6 (T=80 K) and B.7 (T=160 K). Note that the oscillations in the spectrum are an artifact of the smoothing function.

Peak	relative area (normalized to Peak 2 at 80K)		Position at $h\nu = 50$eV		Position at $h\nu = 62$eV	
	T_{sample}=80K	160K	80K	160K	80K	160K
1	3.4	6.4	0.51eV	0.43eV	0.74eV	0.63eV
2	**1**	2	0.68eV	0.63eV	0.91eV	
3	1.3	4.2	0.95eV	0.88eV	1.26eV	

Table 4.1.: Fitting Results of the RIXS spectra (fitting function see figure 4.9): Peak area (averaged over all photon energies and normalized to that of peak 2 at T=80K) and energy position at the lowest $h\nu = 50\,\mathrm{eV}$ and highest $h\nu = 62\,\mathrm{eV}$ recorded photon energy for three gaussian peaks.

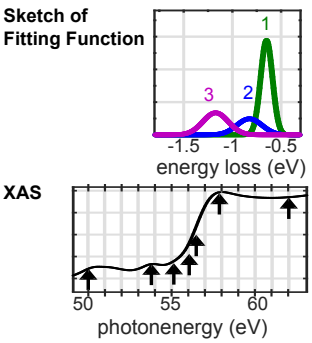

(a) Sketch of the fitting function (top) and XAS spectrum of fig. 4.3 with arrows indicating the excitation energies at 50, 53.8, 55.1, 56, 56.4, 57.8 and 62 eV (bottom).

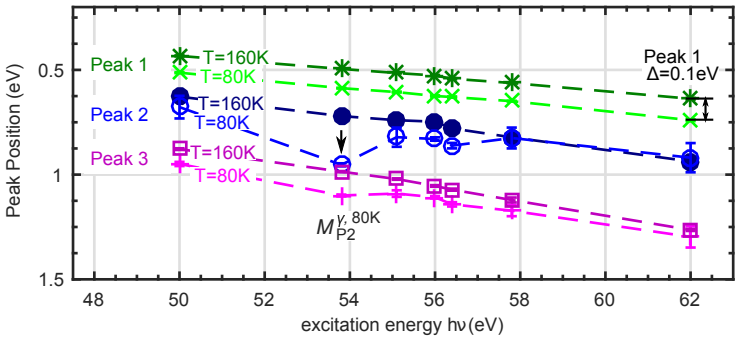

(b) Peak position of the three Gaussian peaks. The dashed lines connect the data points and serve as guides for the eyes. All three peaks disperse with excitation energy. The slope is gradually increasing from peak 1 to 3. A black arrow indicates a shift of $\Delta_{\text{peak 1}}^{\text{160K-80K}} = 0.1$eV the energy position of the peak 1 at the two different temperatures.

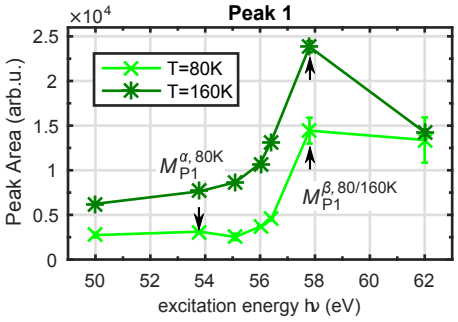

(c) Area peak I.

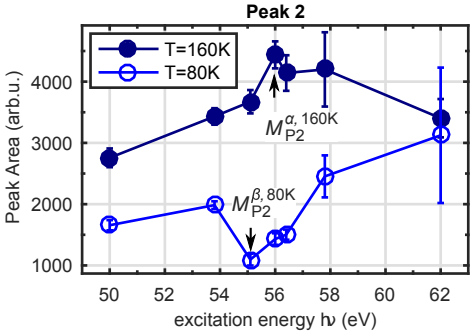

(d) Area peak 2.

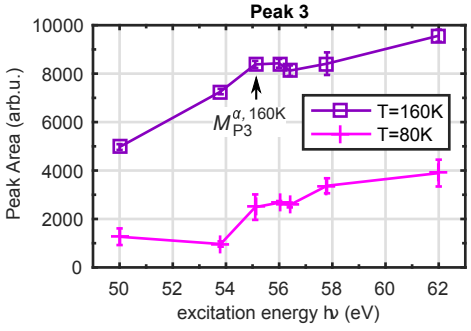

(e) Area peak 3.

Peakmark		T (K)	hν (eV)	description
M_{P1}	α	80	53.8	intensity resonance
	β	80/160	57.8	intensity resonance
M_{P2}	α	160	56	intensity resonance
	β	80	55.1	intensity anti-resonance
	γ	80	53.8	position shift
M_{P3}	α	160	55.1	intensity resonance

(f) Distinct features of the fitting parameter described in the text.

Figure 4.10.: Peak 1/2/3 position (b) and area (c,d,e) of the Gaussian peaks used to fit the RIXS spectra of magnetite at T=80K (bright green, blue and magenta) and T=160K (dark green, blue and magenta) for the different excitation energies. The lines connect the data points and serve as guides for the eyes. A sketch of the fitting function is shown in (a). The errorbars represent the 95% confidence interval of the fit. Most of the fitting results are listed in table 4.1.

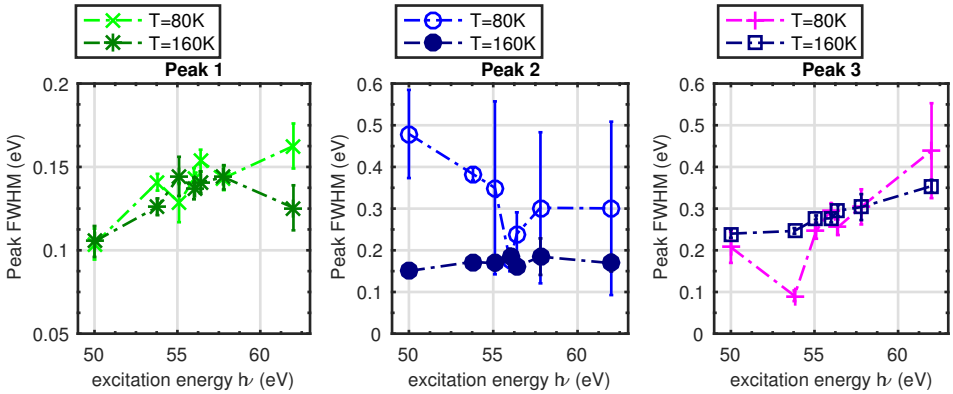

Figure 4.11.: Left/Center/Right: Linewidth (Full Width at Half Maximum FWHM) of the Gaussian peaks 1/2/3 used to fit the RIXS spectra of magnetite at T=80K (bright green, blue and magenta) and T=160K (dark green, blue and magenta) for the different excitation energies. The dashed lines connect the data points and serve as guides for the eyes. The errorbars represent the 95% confidence interval of the fit.

4.4. Discussion and Summary - Verwey Signature in Magnetite

In the above sections, a quantitative description of RIXS spectra of magnetite measured at the Fe $M_{2,3}$ edge was presented. The excitation spectrum obtained with RIXS can be described as the sum of three distinct Gaussian peaks. A discussion of the observed temperature and excitation energy dependencies is given in this section. It is followed by a discussion of their temperature dependent variations and the resulting clear signature of the Verwey transition.

4.4.1. Associating the Fitted Peaks to Microscopic Excitations

Referring to the energy scales of possible excitations in figure 2.8, the energies of the observed three peaks $E_1 \approx 1.1\,\text{eV}$, $E_2 \approx 0.8\,\text{eV}$ and $E_3 \approx 0.6\,\text{eV}$ are too low for having their origin in dd-excitations ($E_{dd} > 1.5\,\text{eV}$) and too big for being caused by magnon excitations ($E_{\text{magnon}} < 500\text{meV}$). Crystal field excitations (=dd-excitations) at energies below 1 eV were found also in [156] where they could be confirmed by atomic multiplet calculations. Also Huang et al. measured excitations between 0.5 eV and 1 eV in RIXS experiments on magnetite at the Fe L edge[181][2]. In their work it is shown, that several atomic multiplet calculations with a wide range of possible crystal field geometries can not reproduce excitations in this energy regime. To interpret the origin of the three distinct peaks, an assignment of the peaks to the different Fe sites, as shown on the XMCD data in figure B.1, would be useful. However, it is not possible to make such an assignment based on the presented data. Instead the three peaks show mixed contributions when comparing their appearance with the simulated absorption spectrum in figure 4.12: peak 1 and 2 show a resonance at the absorption maximum of both B-site species (peak 1: Fe^{2+} at $M_{\mathbf{P1}}^{\alpha,\,80\,\text{K}}$ and Fe^{3+} $M_{\mathbf{P1}}^{\beta,\,80/160\,\text{K}}$, peak 2: Fe^{2+}

[2]They are most prominent at an excitation energy of 706.5 eV.

at $M_{\mathbf{P2}}^{\alpha,\,160\,\mathrm{K}}$ and Fe^{3+} $M_{\mathbf{P2}}^{\beta,\,80\,\mathrm{K}}$). This impossibility to attribute the three peaks in the excitation spectrum to specific Fe-ions in magnetite could be explained by assuming less localized electronic excitations in the trimeron chain of Fe-ions.

The peak shape of the lines, which shows a best fit with a gaussian like peak shape indicates a complex excitation not explainable by pure atomic multiplet excitations. A combination of atomic response (dd-excitation) and lattice excitation (phonon) led to Gaussian peaks in [160] and [159] as also shown in figure 2.10. In favor of such a mixed excitation is the observed shift of the peaks with different photon energy, which also was found in [141][160]. Here the shift is not a shift of the fundamental excitation energies. Instead it's a change of spectral weight of the different separate excitations. I assume a similar effect is taken place in the excitation spectrum of magnetite.

To draw quantitative conclusions from the measured excitation spectra it is necessary to perform calculations of the expected atomic excitations including phonon interaction. Also temperature dependent measurements, including more than two temperature could provide information on the underlying phonon excitations as shown in [141].

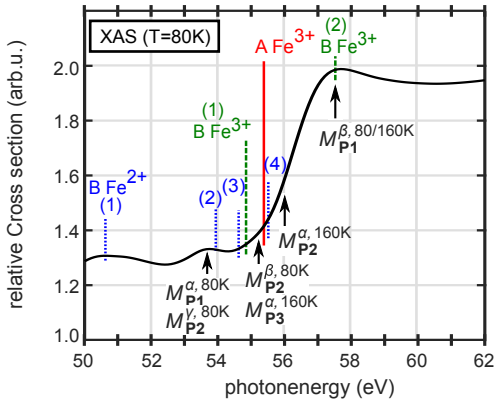

Figure 4.12.: Experimentally determined absorption spectrum with markers (black arrows) for the distinct features of the fitting parameter for the three fitted peaks $M_{\mathbf{P1,2,3}}$ (table 4.10(f)) and the simulated absorption maxima positions. It is not possible to assign any of the three excitation peaks of the RIXS spectrum to a single Fe-site. This may fits in the picture of shared orbitals in the trimeron structure of magnetite.

4.4.2. Signatures of the Verwey Transition - Temperature Dependent Changes

Although the shape of the excitation spectrum obtained in the RIXS spectra can not be fully understood at this point, a temperature dependent change can be described. The principal shape of the RIXS spectrum and its fit with three gaussian lines is not affected by the change in temperature (see e.g. figure 4.14). The energy positions of the three peaks slightly reduce when going towards higher temperatures. When crossing the Verwey temperature ($T_V = 125\,\mathrm{K}$) the overall intensity of the inelastic contribution is increased as summarized in figure 4.13. This increased intensity in

the RIXS spectrum means an increased transition probability for the relevant dd-excitations after x-ray absorption at the M-edge.

In figure 4.13 the integrated spectral weight of the spectra below (blue) and above (red) the Verwey temperature are shown. The black line is the difference between the two curves. The intensity difference shows a clear maximum at an excitation energy of $h\nu = 56.4\,\mathrm{eV}$. This is why this excitation energy was chosen for a direct comparison of the spectral shape below and above the Verwey temperature in figure 4.14. Until no calculations are available which describe the origin of the excitation spectrum, a microscopic explanation of the experimentally determined temperature dependence is not possible.

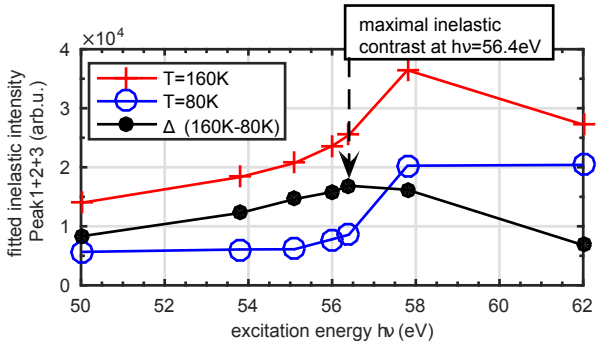

Figure 4.13.: Inelastic intensity below (T=80 K, blue circles) and above (T=160 K, red crosses) the Verwey temperature. The difference between the two signals is plotted with black circles. The maximum difference between the spectra occurred at an excitation energy of $h\nu = 56.4\,\mathrm{eV}$. The corresponding spectra are shown below in figure 4.14.

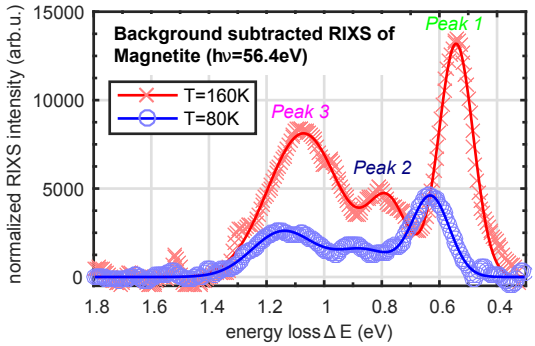

Figure 4.14.: RIXS spectra of magnetite recorded below (T=80 K, blue circles) and above (T=160 K, red crosses) the Verwey temperature T_V at an excitation energy of $h\nu = 56.4\,\mathrm{eV}$. For this excitation energy the intensity contrast of the inelastic part of the spectrum below and above the T_V is maximal (see figure 4.13). The solid lines represent the fitting functions introduced before.

4.4.3. Summary of the Determined Excitation Spectra of Magnetite

Within this chapter of this thesis, RIXS spectra of magnetite recorded at different excitation energies across the Fe $M_{2,3}$-edge, at two temperatures across the Verwey transition were presented. The measurements were performed at the MERIXS endstation of the Advanced Light Source synchrotron in Berkeley with an energy resolution of 20 meV. Due to scattering from surface facets we could not evaluate the contribution of low energy excitations with energies below 300 meV.

The experimentally determined, background subtracted excitation spectra above 300 meV can be expressed with three Gaussian peaks. This shape is reproduced for all measured excitation energies and temperatures. By comparing the excitation spectra resonances with a simulated absorption cross section spectrum, it was not possible to assign the experimentally determined excitations to distinct Fe-ion sites in the magnetite structure. Possibly they resemble non-local excitations of the trimeron orbitals of magnetite.

The Gaussian peak shape as well as the incidence energy dependence of the observed excitations is attributed to electron-phonon coupling contributions in magnetite. Calculations of the RIXS spectra, including electron-phonon coupling should be performed to assign the experimental spectrum to electronic excitations.

A comparison of the spectral shape below and above the Verwey temperature reveals a clear signature of the Verwey transition in magnetite. For temperatures above the transition the spectral weight is strongly increased. This strong temperature dependence encourages time resolved RIXS experiments on the magnetite M-edge combined with advanced theoretical investigations of the electronic excitation spectrum.

5. RIXS at a Seeded Free Electron Laser

The strength of Resonant Inelastic X-ray Scattering (RIXS) in determining the excitation spectrum of correlated solid state systems, surface-adsorbate systems and molecules is used in many fields of physics to unravel correlated electronic effects[144][7][182]. The advances achieved at Free Electron Lasers, being the next generation of synchrotron light sources with pulse durations below 100 fs, pave the way for extending the RIXS technique into the time domain by making use of the ultrashort pulses provided at FEL. Within the following section I summarize a RIXS experiment at the seeded free electron laser FERMI in Trieste (IT) as a proof of principle experiment[183]. The experiment shows, that at a seeded FEL source it is possible to perform high resolution spectroscopy on solids without grating based monochromatization and high intensity stability. The FEL stability is described as well as a detailed analysis of the recorded RIXS spectra of a $KCoF_3$ system. This chapter will end with a summary giving a perspective towards time resolved RIXS at the seeded FEL FERMI.

5.1. RIXS Endstation at the Free Electron Laser FERMI

To perform RIXS experiments at the Free Electron Laser FERMI we utilize a commercial soft X-ray/XUV spectrometer of VG Scienta (XES355) and a multilayer mirror setup focusing the FERMI beam onto the sample. A set of vacuum chambers was designed to enable the experiments. In this section I summarize the experimental setup scheme and the technical realization. Subsequent I introduce relevant instrumentation of the beamline and the data acquisition concept at FERMI. At the end of this section I depict the principal path from the collected raw data to a spectrum. Technical details of the overall setup are summarized in table 5.1 at the end of this section.

5.1.1. Experimental Setup

The vacuum setup consists of three major parts: (1) the X-ray spectrometer, (2) the Sample chamber and (3) the mirror chamber. The pressure in the three chambers was during the experiments in the order of $p = 10^{-8}$ mbar measured with an ion-gauge. Sketches of the optical path through the whole setup from different perspectives are shown in figure 5.1. For a high energy resolution of the spectrometer it is important to use a very small x-ray beam. To achieve a small spot size on the sample we utilize a spherical multilayer mirror (R_{sphere}=40 cm, see figure 5.2 and table 5.1). According to ray tracing simulations the mirror focuses the beam to a focus size at the sample of $20\times13.7\,\mu m^2$ at an angle of incidence of 20 °. It is optimized for photon energies in the range of the

Fe, Co and Ni $M_{2,3}$-edges between 50 eV and 75 eV[184]. The mirror is mounted on a Piezo stage allowing adjustments of the focus position on the sample. For positional adjustments of the sample in front of the spectrometer, the sample holder is mounted on a rotatable x,y,z manipulator. A YAG:Ce crystal is mounted at the same sample holder for beam pointing diagnostics (see figure 5.1d).

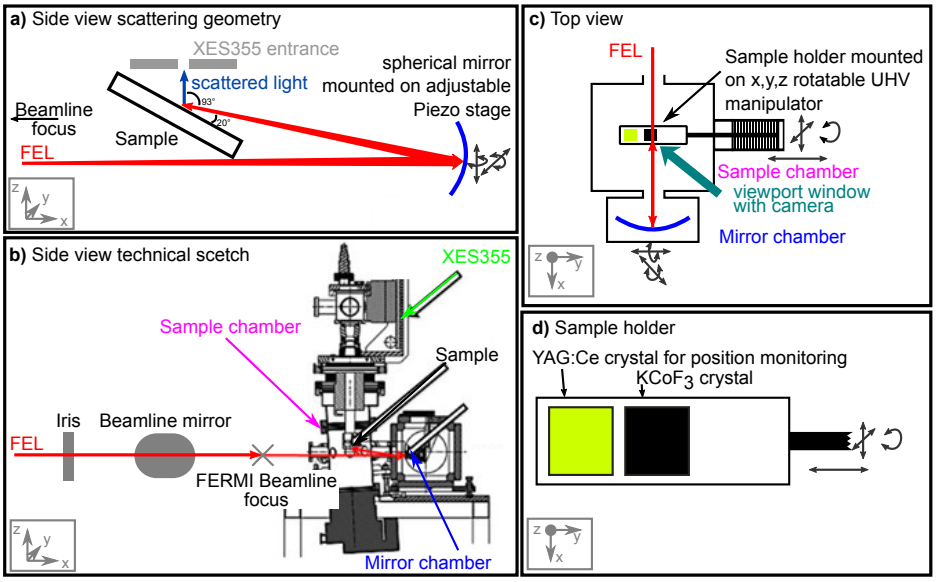

Figure 5.1.: Technical sketches of the RIXS setup. a) The optical path through the setup: The beam from the beamline passes the sample holder from below and hits a spherical mirror. The reflected beam is focused onto the sample. b) Before entering the experimental chamber, the FEL beam passes the iris of the beamline and the elliptical beamline mirror designed to focus the beam into the TIME-X endstation in front of the back reflecting mirror. c) Top view of the setup depicting the sample mounting geometry. A view port window with sample view is equipped with a camera to monitor the sample positioning and the FEL spot on a beam monitor. d) Sketch of the sample holder. The $KCoF_3$ sample is glued on the sample holding plate. As a beam monitor for the FEL position and spot size determination, a Cerium doped YAG crystal is glued onto the sample holder. A photograph of the setup is shown in the appendix figure B.8.

5.1.2. The XES355 X-ray Spectrometer

The XES355 spectrometer[186][187] was manufactured by the VG Scienta company. It is designed in the Rowland-geometry with a detector movable along the Rowland circle of the spherical grating[186]. A sketch of the optical path through the spectrometer is shown in figure 5.3. Technical details are summarized in table 5.1. To detect the dispersed photons, a phosphor screen is combined with an MCP stack at the detector position. When a photon hits the MCPs it will cause a cloud of electrons which hits the phosphor screen. A fluorescence spot is visible at the screen. The phosphor screen is located in front of a glass window and the fluorescence spots are recorded

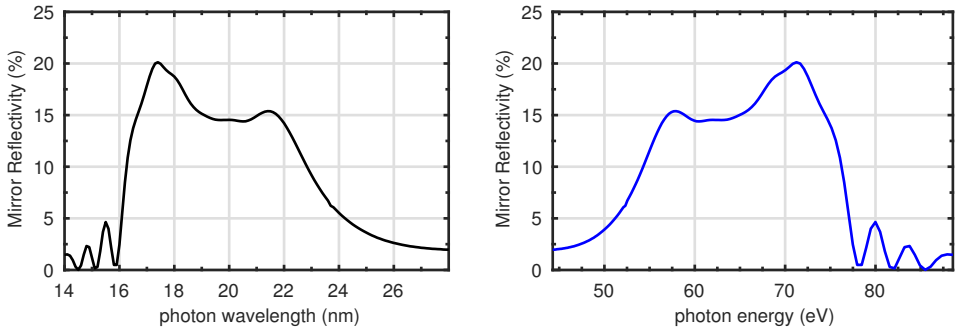

Figure 5.2.: Reflectivity of the multilayer mirror recorded at the PTB XUV reflectometry beamline at Bessy II[185] with the scattering geometry as depicted in figure 5.1a) at an incident angle of 3°. The left graph shows the mirror reflectivity vs. wavelength, the right one the same data vs. photon energy.

with a CCD camera. To correlate the recorded images with the FEL, the image acquisition is triggered externally with the trigger provided by the master trigger of the FERMI facility. For optimizing the energy resolution of the setup it is possible to narrow the opening between the entrance slits of the spectrometer. The slits were set to 50 μm opening resulting in an expected energy resolution of 170 meV. In our experiments, the spot on the sample was focused to a width of 13.7 μm along the dispersive direction of the spectrometer. Ray tracing simulations proof, that this spot size leads to an energy resolution of 130 meV. The same concept of a slitless operation of a X-ray spectrometer is applied at the MERIXS spectrometer introduced in the previous section 3.1.2.

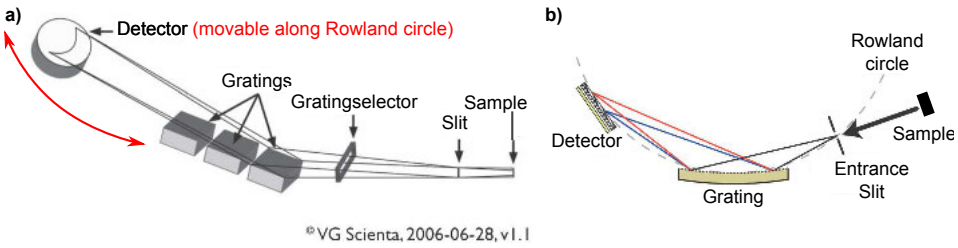

Figure 5.3.: Figures taken from [187] (left) and [188] (right). Note that XES355 has the exact same layout sketch as the XES350. Sketch of the optical path and the technical design of the VG Scienta XES355 spectrometer. In the Rowland geometry of an X-ray spectrometer, the spherical grating is kept at a constant position and the detector is moved to change the energy window of the detector (e.g. in [186]). The entrance slit is only needed, if the source point is big. The entrance slit than increases the resolution of the spectrometer when being narrowed. In the case of the presented experiments, the slit was fully open, since the source point is small due to the focusing mirror (see figure 5.1a). The XES355 was used with 300 lines/mm grating which is optimized for energies around 100 eV (see also table 5.1).

5.1.3. Relevant Beamline Instrumentation and FEL Settings

The RIXS setup described above is designed for usage with any photon source beamline. During the experiments summarized in this thesis, it was installed after the permanent endstation of the EIS-TIMEX beamline at FERMI. A technical sketch of the beamline with all relevant components is shown in figures 5.4 and 5.5. We made use of the Gas absorber which was filled with Nitrogen. and aluminum filter foils of different thickness.

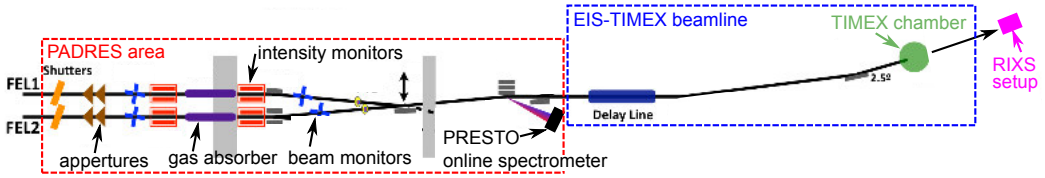

Figure 5.4.: A sketch of the optical path from the FERMI FEL towards the TIMEX (Time resolved experiments under extreme conditions) endstation through the EIS beamline ("Elastic and Inelastic Scattering" beamline, figure taken from [189]). Within the PADRES section ("Photon Analysis Delivery and REduction System") the FEL beam can e.g. be attenuated with a gas absorber or filter foils (not labeled). Also diagnostic tools are available in this section. The FEL photon energy and bandwidth is determined with the online spectrometer PRESTO. It acquires spectra while the RIXS experiments are performed.

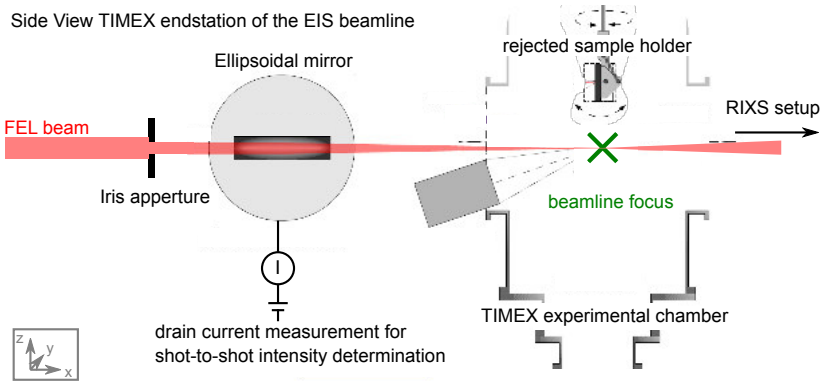

Figure 5.5.: Figure taken and modified from [189]. TIMEX endstation of the EIS beamline at FERMI. The RIXS setup was mounted behind the chamber as indicated with an arrow. The drain current from the ellipsoidal mirror, caused by absorption of FEL radiation is used as a shot-to-shot intensity monitor.

5.1.4. Data Acquisition and Processing

As it is common for FEL sources, the data of the experiments are recorded on a shot-to-shot basis. This allows to sort the data after the beamtime. The data of the XES355 spectrometer are saved as

camera pictures. The FERMI DAQ system combines the camera pictures with data of the beamline as e.g. the data of the intensity monitors and the online spectrometer. For every experiment a hdf5 file is created. To extract a spectrum out of the recorded camera pictures a "blob-finding" routine is applied which identifies the position of the detected photons at the detector. This blob-finding approach reduces the background noise in the final spectra. It is only applicable if the count rate is low so that the different light spots on the CCD don't overlap. The procedure is described e.g. in [188]. While background subtraction is required for the images recorded at the ALS spectrometer in the above section 3.1.5, this has not to be done here. In order to retrieve a spectrum out of the images, the curvature is corrected as described in the previous section 3.1.5. An energy axis can be calculated with the help of the XES355 instrument software. For intensity normalization we use the drain current of the last beamline mirror can be used.

5.1.5. Tables

This section contains a table, summarizing technical details of the FERMI-RIXS setup.

Part	**Technical details**	
XES355 spectrometer	Grating 1 - line density (optimized energy)	1200 lines/mm (400 eV)
	Grating 2	400 lines/mm (275eV)
	Grating 3	300 lines/mm (100eV)
	selected Grating	Grating 3
	selected diffraction order	1^{st}
	slit opening during experiments	50 μm
	slit limited energy resolution[1]	170meV
	camera for detector readout	Baseler
	dispersive axis (coordinate system in fig. 5.1)	x (vertical)
Multilayer Mirror	curvature radius	R=40 cm
	focal length	f=R/2=20 cm
	bandpass (figure 5.2)	56-77 eV/16.1-22.1 nm
	substrate	25.4 diameter round Si crystal (Pilz-Optics), surface roughness 0.4 nm rms (AFM measurements)
	multilayer stack	40 aperiodic multilayer of Mo and Si[190]
	normal focus size (determined with ray-tracing simulations)	20x5 μm^2 (horz.$\times$vert.)
	projected focus size on sample (20 ° incidence angle)	20x13.7 μm^2 (horz.$\times$vert.)

Table 5.1.: Technical data of the RIXS setup at FERMI.

5.2. Performance of the Free Electron Laser During the Campaign

The free electron laser FERMI FEL-1 makes use of a seeding technique to deliver XUV light pulses in the nominal range of 19 eV to 62 eV with relative bandwidths[2] of 5×10^{-4} (r.m.s.)[3] and pulse durations below 100 fs[191][192][193].

For our RIXS measurement campaign the FERMI FEL was tuned to energies around the Cobalt Co $M_{2,3}$ edge between 57 eV and 63 eV. For determining the spectral properties of the FEL radiation an online spectrometer is included in the beamline. The performance of the FEL, concerning bandwidth and stability, during the presented measurement campaign is summarized in this section. After that I describe the results of the successful implementation of an automatized photon energy scanning routine during our measurement campaign.

5.2.1. Intensity Stability

As mentioned in the introduction the intensity stability of the FEL at a constant photon energy is one of the strength of the seeded Free Electron Laser FERMI. Figure 5.6 shows a snapshot of the intensity of the FEL during a 4 min data acquisition at a photon energy of $h\nu = 61$ eV. The deviation from the mean value of 4 μJ/pulse is 23 % r.m.s. and at the same time, the photon energy and average bandwidth is also stable as shown in the next section. At the acquisition cycles during the RIXS experiment we obtained intensity jitter with r.m.s. deviation of 15 %.

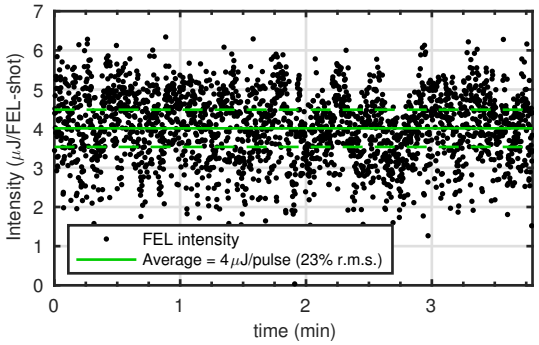

Figure 5.6.: Intensity of the FEL during a 4 min scan at $h\nu = 61$ eV measured with the beamline intensity monitor. The average intensity was 4 μJ/pulse (marked with solid green line) with a statistical deviation of 23 % r.m.s. (marked with dashed green line). During the RIXS spectra acquisition the FEL provided beam intensities at the same level with r.m.s. deviation of 15 %.

[2] The relative bandwidth is the ratio of bandwidth and energy $\Delta E/E$. For a photon energy of $E = 63$ eV the ideally achievable absolute bandwidth is $\Delta E_{\mathrm{FWHM}} = 46$ meV/$\Delta E_{\mathrm{r.m.s.}} = 32$ meV.

[3] To convert from the r.m.s. bandwidth (typical in accelerator physics) to the Full Width at Half maximum value (typical in spectroscopy) the r.m.s. value has to be multiplied by 1.36 ($\Delta E_{\mathrm{FWHM}} = 1.36 \times \Delta E_{\mathrm{r.m.s.}}$).

5.2.2. Spectral Performance Determined with the Online Spectrometer

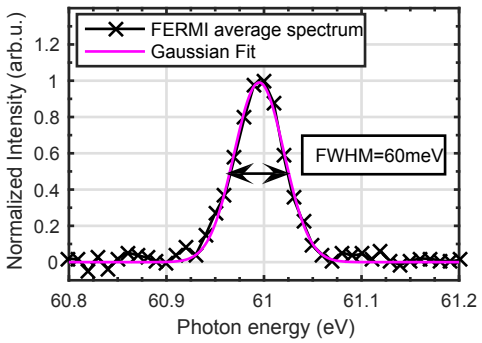

(a) Spectrum of the FEL radiation determined with the online spectrometer PRESTO (black crosses). The average bandwidth, determined with a Gaussian fit (magenta line) is $\Delta E^{\mathrm{FWHM}}_{\mathrm{FEL\text{-}average}} = 60\,\mathrm{meV}$.

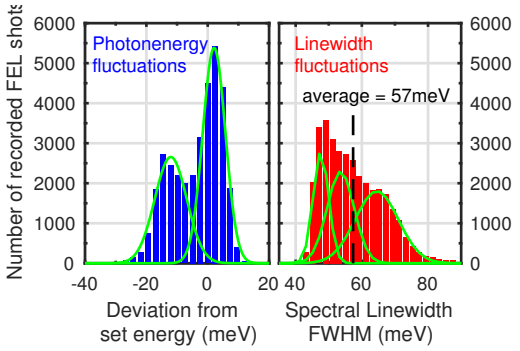

(b) Histograms depict the fluctuations of the FEL central energy (blue bars) and bandwidth (Full Width at Half Maximum, red bars). A set of two Gaussian lines is fitted to the central energy histogram showing that the FEL lased at two modes separated by 10 meV. The bandwidth can be fitted with three Gaussian lines.

Figure 5.7.: Spectral quality of the Free Electron laser spectrum during a data acquisition run lasting 60 min. The FEL was tuned to a constant nominal set-energy of $h\nu_{\mathrm{FEL\text{-}set}} = 61\,\mathrm{eV}$.

Average Bandwidth - FEL Energy Resolution

A 60 minutes average spectrum of the FEL radiation, recorded with the online spectrometer is shown in figure 5.7(a). It was recorded at a set-energy of the FEL of $h\nu_{\mathrm{FEL\text{-}set}} = 61\,\mathrm{eV}$. With a Gaussian line fit through the data, the average energy bandwidth $\Delta E_{\mathrm{FEL\ average}}$ of the FEL is extracted:

$$\Delta E^{\mathrm{FWHM}}_{\mathrm{FEL\ average}} = 60\,\mathrm{meV}. \tag{5.1}$$

For every single FEL shot a spectrum as the presented one is recorded. This allows to analyze the spectral stability during the data acquisition. Additionally it allows to sort the data in the post analysis, as it was extensively done in the first part of this thesis XY. Figure 5.7(b) shows a shot-to-shot analysis of the same data acquisition cycle which lead to the average spectrum of figure 5.7(a). The histograms show the statistical distribution the shot-wise determined FEL bandwidth and central energy. They give insight into the FEL stability.

Central Energy Fluctuations

In the obtained central energy histogram (blue bars in figure 5.7(b)) one can see a double peak structure. The two lines are 10 meV apart. Their appearance shows that the FEL is working in a regime with two distinct spectral modes competing with each other, while the nominal settings are constant (set energy $h\nu = 61\,\mathrm{eV}$).

Bandwidth Fluctuations

Also the bandwidth of the FEL shows fluctuations during the data acquisition presented in the red bars histogram in figure 5.7(b). While the central energy position can be fitted with two Gaussians, the bandwidth can be fitted with three Gaussian lines centered at bandwidths of $\{48; 54; 64\}$ meV. The resulting shot-to-shot averaged bandwidth of the FEL is 57 meV. The comparison of this value, with that obtained from the time-integrated average spectrum ($\Delta E^{\mathrm{FWHM}}_{\mathrm{FEL\text{-}average}} = 60$ meV) shows, that the appearance of two FEL modes being 10 meV apart gives only a very small contribution to the average bandwidth.

Conclusion for the RIXS Data Analysis

The spectrometer resolution is $\Delta E^{\mathrm{FWHM}}_{\mathrm{XES355}} = 104$ meV (shown below in section 5.4.3). It dominates the overall resolution of the RIXS experiment. A sorting of the data according to their FEL central energy is therefore not needed when evaluating RIXS data in the following sections.

5.2.3. Photon Energy Scanning

In a typical FEL experiment at the FERMI facility, the photon energy can be tuned by scientists. Depending on the difference of the actual and desired photon energy this tuning requires some time. During our RIXS measurement campaign we could use a newly developed automatized photon energy tuning tool which allows continuous scanning of the photon energy. With this tool the photon energy can be varied without human interaction within a certain range limited by the seed laser harmonic setting. Figure 5.8 shows the covered photon energy range of the tuning tool.

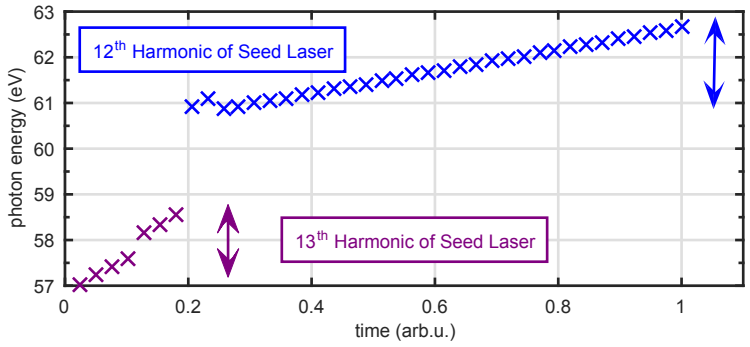

Figure 5.8.: Energy of the FEL determined with the elastic line in the RIXS spectrometer as a function of time during an automatized Energy Scan of the FERMI FEL. The automatic tuning tool was implemented for the first time during a user experiment. The gap in the achieved photon energies arises from a required manual change of the seeding laser harmonic.

5.3. Samples for the FERMI-RIXS Experiment

While it is the long term goal to perform RIXS measurements on magnetite at the Free Electron Laser FERMI (see previous chapter 4) we have chosen another sample in this proof-of-principle experiment. Namely we used the cubic perovskite $KCoF_3$[194][195][196][197][198][199]. The compounds KMF_3 (M=Mn, Fe, Co, Ni) show collective effects as piezo electricity and are of interest for the understanding of correlated electronic effects[200]. The major technical advantage of this system compared to the above investigated magnetite, is the flat crystal surface which requires no surface preparation. When the surface is flat, spectral artifacts caused by scattering from sub-mm facets (see analysis in section 4.3.2) are suppressed. The measured spectra are hence of higher quality making this system a better choice for the proof-of-principle experiments.

5.3.1. Characterizing X-ray spectra of the $KCoF_3$ crystal

We recorded reference RIXS and XAS spectra of the $KCoF_3$ single crystal at the MERIXS beamline at the Advanced Light Source in Berkeley (see experimental description in section 3.1). The XAS spectrum recorded across the Cobalt $M_{2,3}$ edge (figure 5.9(a)) shows four distinct absorption maxima. At two marked photon energies of 61 eV and 62.5 eV we recorded RIXS spectra which shown in figure 5.9(b). They show three distinct spectral features at 0.9 eV, 1.8 eV and 2.3ėV. The low energy excitation has a strong resonating character and appears most sharp at an excitation energy of 61 eV. Both, XAS and RIXS are very similar to the spectra recorded at the parent compound CoO[201][156]. From that we deduce, that the origin of the most pronounced excitation feature at 0.9 eV in the RIXS spectrum are excitations of the final state d-electrons into $^4T_2$ symmetry multiplet states.

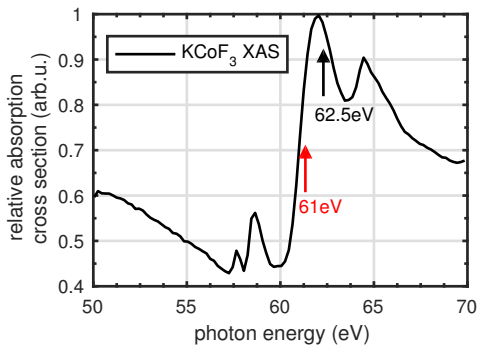

(a) X-ray absorption scan across the Co $M_{2,3}$ edge determined with a total electron yield measurement.

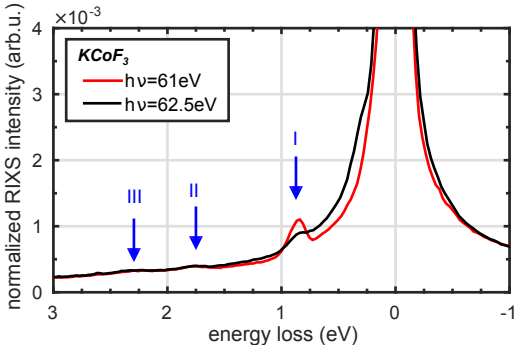

(b) XUV RIXS spectrum at an excitation energy of $h\nu = 61\,\mathrm{eV}$ and $h\nu = 62.5\,\mathrm{eV}$. The three marked features are also observed in the RIXS spectrum of CoO[156]. The sharp line at 0.9 eV energy loss (I) is attributed to an excitation of the final state d-electrons into $^4T_2$ symmetry multiplet states.

Figure 5.9.: Characterizing X-ray spectra of the $KCoF_3$ single crystal at the XUV MERIXS beamline at the ALS synchrotron (setup described in the first part of this thesis-chapter). The combined energy resolution of the RIXS experiment, determined with the width of the elastic lines, is $\Delta E^{\mathrm{FWHM}}_{\mathrm{MERIXS}} = 41\,\mathrm{meV}$.

5.4. RIXS Spectra Recorded at the Seeded Free Electron Laser FERMI

5.4.1. Alignment Strategy and Intensity Determination

To focus the beam on the sample, a curved multilayer mirror is used, which back-reflects the beam from the beamline and focuses it onto the sample (see descriptions in section 5.1). The mirror is mounted on top of a five-axis translation stage allowing it to be shifted and tilted freely (see figure 5.1). With the help of the computer based positioning system of the Elettra Campus technical department, the vacuum chamber was placed exactly in line with the optical path of the beamline by the technical staff. After the FEL was aligned to the ideal path, the beam immediately hit the mirror. Subsequent we used the Piezo stage to move the mirror and thereby scan the beam over the sample. This we did until we could detect the FEL induced fluorescence on the YAG:Ce screen. After we found the beam on the screen we moved the sample holder to hit the $KCoF_3$ crystal with the beam. This strategy immediately gave count rate in the XES355 spectrometer. With the help of filter foils in the beamline and the nitrogen filled gas absorber we attenuated the FEL beam to intensities at which we could not see sample damage. A detailed beam induced damage analysis based on the evaluation of the elastically scattered REXS signal is shown in section 5.4.3. To determine the intensity on the sample we used the beamline integrated intensity monitor and the

transmission values of the optical elements (mirror reflectivity in section 5.1.1, transmission values of the beamline in [202])[4] and determined the fluence at the sample to be F$\leq$ 0.7 J/cm^2 during all relevant data acquisitions presented in this work[5]. Due to the seeding technique the photon energy is very stable in time. A photon energy dependent sorting of the recorded RIXS spectra as it would be required for data recorded at a SASE-FEL, is not necessary. The intensity distribution of the individual FEL shots could still be improved. It lies within a 20 % r.m.s. interval around the mean value.

5.4.2. Crystal field excitations in $KCoF_3$

After the alignment procedure we recorded RIXS spectra of the $KCoF_3$ crystal at two photon energies at constant FEL fluence of F=0.7 J/cm^2 on the sample. The two spectra are shown in figure 5.10 together with these obtained from the very same crystal at the MERIXS synchrotron beamline. The spectra recorded at the FERMI-RIXS at $h\nu$ = 61 eV (dark green) show clearly the $^4T_2$-excitation at 0.9 eV energy loss which was found on CoO and theoretically described by means of atomic-multiplet calculations in [156]. Also at an excitation energy of $h\nu$ = 62.5 eV (bright green) one can see a shoulder at that energy loss position. While this strongly resonating feature can be found, the weak features at 1.8 eV and 2.3 eV are hidden in the background in the FERMI-RIXS data.

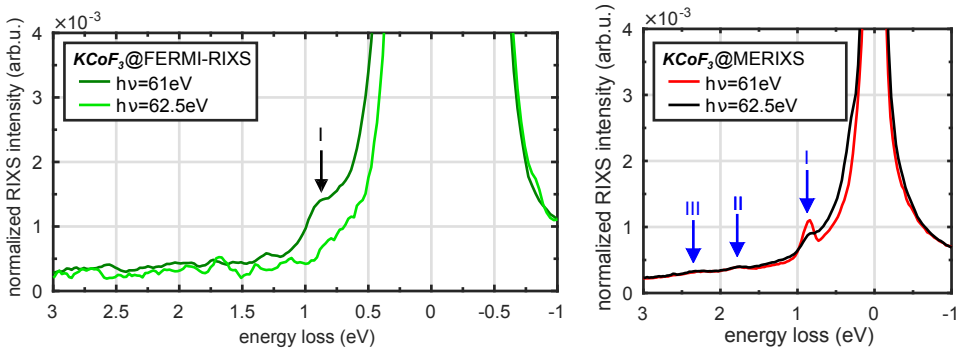

Figure 5.10.: Left: Inelastic tail of the XUV RIXS spectrum of $KCoF_3$ at excitation energies $h\nu$ = 61 eV/$h\nu$ = 62.5 eV recorded within 206 min/60 min at the RIXS setup at the seeded Free Electron Laser FERMI. The x-ray fluence on the sample was F=0.7 J/cm^2. A black arrow at 0.9 eV energy loss indicates the $^4T_2$-excitation observed in high-resolution RIXS spectra recorded at the MERIXS beamline (right graph). The features II and III, observed at the high-resolution data are instead not observable in the spectra recorded at FERMI-RIXS due to the comparably low energy resolution of the FERMI-RIXS setup of 120 meV (determined in figure 5.11).

[4]The intensity estimation was done by Martina Dell'Angela.
[5]The size of the beam on the sample was approximated with the theoretically expected focus size of the used multilayer focusing mirror (see section 5.1.1 and table 5.1).

5.4.3. Elastic Line Evaluations

The RIXS spectrum in the XUV photon energy region is dominated by the elastic contribution which also is referred to as resonant elastic x-ray scattering (REXS) part of the spectrum[161]. The analysis of this elastically scattered light, presented in this section, is used to determine the combined energy resolution of the setup, the absorption cross section spectrum and to track the sample damage.

Energy Resolution and Technical Limitations of the FERMI-RIXS Setup

As described above, it is possible to determine the combined resolution of FEL and spectrometer by measuring the linewidth of the elastic line in the RIXS spectrum. This is done in figure 5.11a. With a Gaussian fit we can determine the overall resolution:

$$\Delta E^{\mathrm{FWHM}}_{\text{FERMI-RIXS combined}} = 120\,\mathrm{meV}. \tag{5.2}$$

The combined energy resolution is the square-root sum of all contributing sources for broadening. Since we know the FEL bandwidth from the online-spectrometer analysis (equation 5.1) it is possible to determine the energy resolution of the spectrometer:

$$\Delta E_{\mathrm{XES355}} = \sqrt{\left(\Delta E^{\mathrm{FWHM}}_{\text{FERMI-RIXS combined}}\right)^2 - \left(\Delta E^{\mathrm{FWHM}}_{\text{FEL average}}\right)^2} = 104\,\mathrm{meV}. \tag{5.3}$$

This value is below the theoretically expected energy resolution of 170 meV at the used slit setting (see table 5.1). Reason for this discrepancy is the very small spot size of $20{\times}13.7\,\mu\mathrm{m}^2$ on the sample obtained with the focusing mirror. The resolving power of the spectrometer as used is $R = \Delta E/E \approx 600$.

On the shoulders of the elastic line, indicated with blue arrows in figure 5.11, one can see intensity at energies where it is not expected in case of an ideal Gaussian beam. Reducing the diameter of the beamline aperture iris (see sketch of the beamline setup e.g. in figure 5.1b) from 22 mm to 7 mm shows clearly, that these shoulders are correlated with the beam shape. A comparison of this experimental finding with ray tracing simulations of the setup presented in figure 5.12 show that the appearance of shoulders in the spectrum and their dependency on the beamline-iris opening, can be explained by a non-Gaussian FEL beam shape contribution.

Absorption Cross Section Spectrum Obtained from REXS Analysis

The photon energy dependency of the elastic REXS signal is proportional to the absorption cross section spectrum. Figure 5.13 shows RXES spectrum obtained during an automatized FEL photon energy scan. As a reference I included the absorption spectrum recorded at the MERIXS beamline. The overlap of the two spectra is very good. The observed shift of 500 meV between the maximum of the REXS signal with respect to the absorption signal is explained by interference effects as discussed in [155]. Fano interference of the contributing resonant and non-resonant excitations

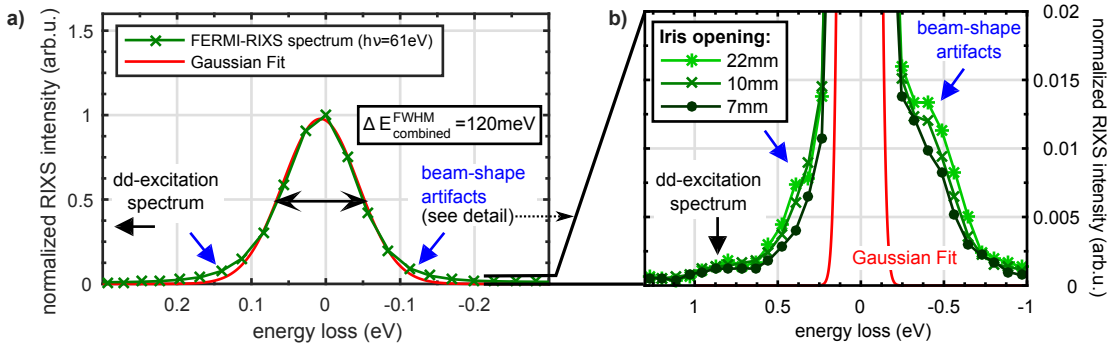

Figure 5.11.: Two detail graphs on the elastic part of the RIXS spectrum of $KCoF_3$ recorded at an excitation energy of $h\nu = 61eV$ at the FERMI-RIXS setup. Left: The elastic line (green line with markers) and a Gaussian fit to determine the combined energy resolution: $\Delta E^{\mathrm{FWHM}}_{\text{FERMI-RIXS combined}} = 120\text{meV}$. The dd-excitations appear on the left side of the spectrum outside the energy range, as indicated with an arrow. At the tail of the spectrum one observes deviations between the ideal Gaussian Fit and the measured data, indicated with blue arrows. Right: The observed shoulders on the tails of the elastic line (marked with blue arrows) reduce in intensity when the beamline aperture iris is closed in three steps from 22 mm to 7 mm (see legend). An influence on the dd-excitation spectrum can not be observed. We conclude, that the shoulders are artifacts caused by imperfections of FEL beam shape on the sample. This argument is supported by ray-tracing simulations presented in figure 5.12.

alter the REXS signal and as a consequence, the REXS spectra are shifted towards higher energies compared to the these obtained with the total electron yield measurements.

Sample Damage

Theoretically, the REXS signal only depends on the samples absorption cross section, the incident photon energy and the scattering geometry. During our measurement campaign we found an unexpected drop of the REXS signal during the measurement when the FEL fluence at the sample exceeded the desired set value of F=0.7 J/cm^2. Figure 5.14a shows the evolution of the elastic line intensity ($\hat{=}$REXS signal) during a 60 min measurement at a critical fluence of F_{critical}=0.84 J/cm^2. Immediately after the opening of the shutter which triggers the start of the data acquisition, the REXS signal drops from $\approx$ 9 counts/FEL-shot to $\approx$ 2 counts/FEL-shot within the first 10 min. Figure 5.14b shows the evolution of the inelastic part of the RIXS spectrum. It turns out, that the intensity ratio of inelastic and elastic line increases with increasing damage. The principal shape of the spectra is not affected. Although an increase of this ratio is in principle useful for XUV RIXS experiments, we attribute the observed loss of REXS intensity in experiments with high fluence to a beam induced damage on the sample surface. To specify the damage mechanism and reasons for the drop in REXS intensity during FEL irradiation with high fluence, further studies are required. The earlier presented RIXS spectra were checked for this effect and showed a constant REXS intensity during the acquisition.

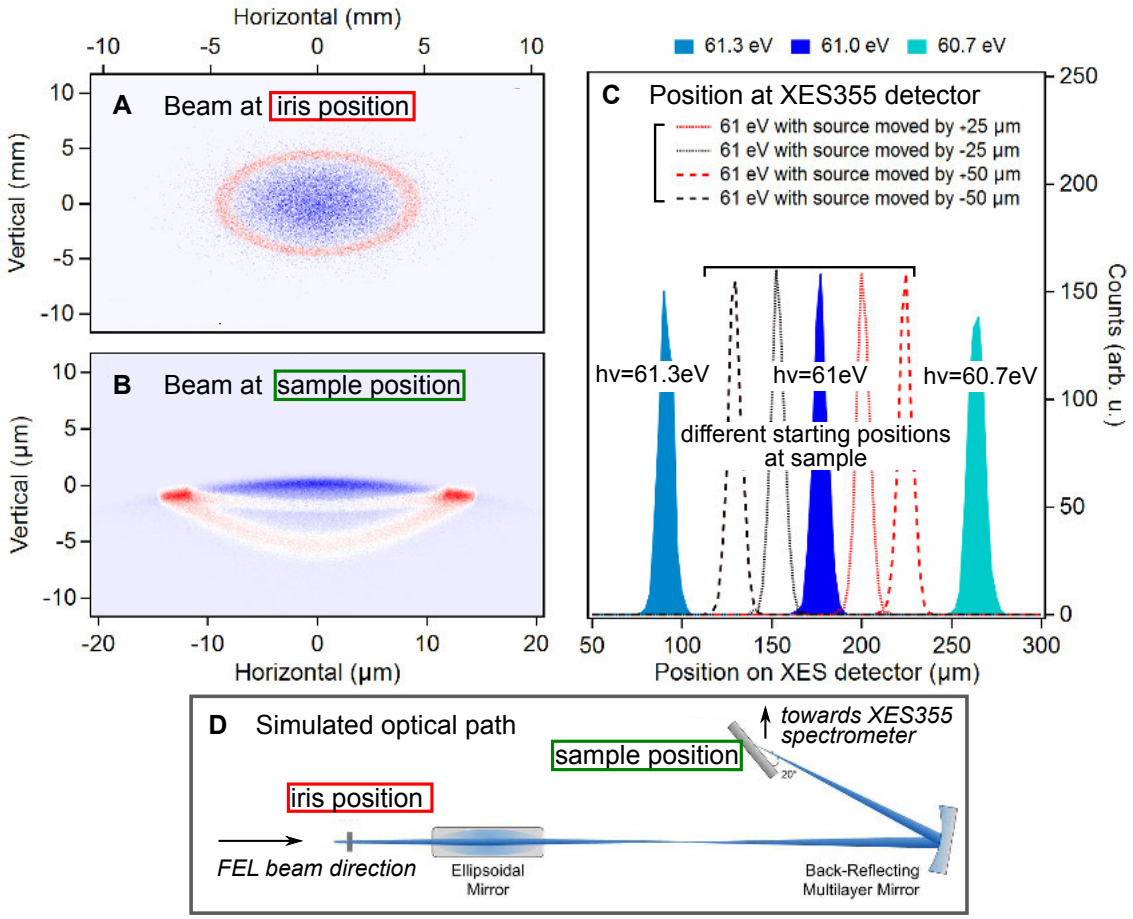

Figure 5.12.: Summary of beam propagation simulations with the x-ray optics ray tracing program "Shadow"[203] performed by M. Dell'Angela et al.[183] **A)** Possible beam shape at the Iris position with a normally distributed contribution marked with blue dots and a second, non-normally distributed contribution marked with red dots. **B)** The beam shown in A is propagated through the back reflecting mirror onto the sample position. The red dotted region of the initial beam cause spatial side peaks on the sample. **C)** Simulation of the position sensitivity of the XES355 spectrometer: A shift of the source point on the sample leads to a shift of the same line at the spectrometer energy-axis. Therefore a beam shape on the sample as that shown in B would appear with shoulders on the energy axis though the photon energy is constant. **D)** Sketch of the optical path.

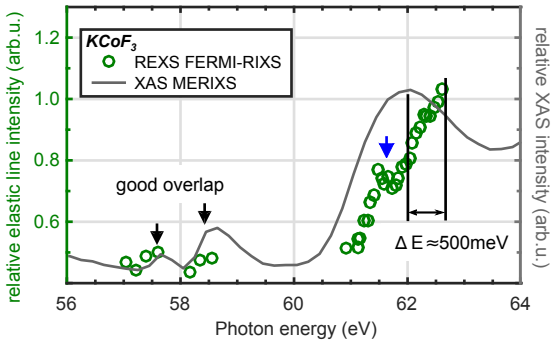

Figure 5.13.: Elastic Line Intensity (REXS-signal) of the $KCoF_3$ spectra recorded for different excitation energies (green circles). The FEL was running in an automatic energy-scanning mode (see section 5.2.3). The REXS is proportional to the absorption cross section of the system which was measured in figure 5.9(a) and is shown as a gray solid line. Both traces overlap excellent at the first two absorption maxima at $h\nu = 57.7$eV and $h\nu = 58.5$ eV. At the third absorption maximum of the XAS spectrum at $h\nu = 62$eV the traces deviate by $\Delta E \approx 500$ meV which is expected due to interference effects of the excitation spectrum causing shift of the REXS signal at the absorption edge[155]. Also the narrow dip at the leading edge, marked with a blue arrow arises from these Fano interference effects.

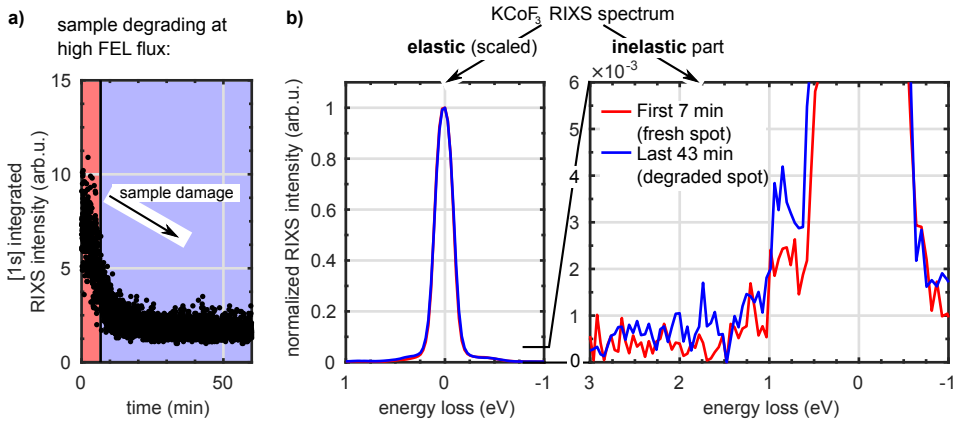

Figure 5.14.: **a)** FEL-shot wise count rate (averaged for 1s) at the detector during a 60 min data acquisition run at $h\nu = 61$ eV. The count rate is dominated by the elastic REXS contribution of the spectrum (ratio elastic/inelastic=$1/1.5\times10^{-3}$). When the shutter opens at the beginning of the acquisition one observes an immediate decrease in count rate which drops from ≈ 9 counts/FEL-shot in the beginning to ≈ 2 counts/FEL-shot after 10 min of measurement. **b)** Comparison of the spectra early (red) and late (blue) in the acquisition (the spectra normalized to the elastic line). One can observe a change of the ratio between elastic/inelastic intensity. It is smaller for the "damaged" sample. Instead no qualitative difference in the spectral weight distribution between the two parts of the data set is found.

5.5. Discussion and Summary - RIXS at FERMI

Discussion

The RIXS spectra obtained at the seeded Free Electron Laser FERMI show a very high quality at acquisition times in the order of several hours. This is comparable to the acquisition time required for spectra recorded at synchrotron light sources (ca. 1 h), while the FEL repetition rate ($f_{FERMI} = 10\,Hz$) is much smaller than that of typical synchrotron ($f_{ALS} = 500\,Hz$). Reason for that is the very high peak brilliance of Free Electron Laser x-ray sources.

The stability of the seeded Free Electron Laser in terms of photon energy and bandwidth makes post-analysis sorting unnecessary when performing RIXS experiments. A stable intensity distribution allows to set the fluence on the sample to values close damage threshold. At SASE Free Electron Lasers, this is not possible when a monochromator is used because the spectral fluctuations can in this case cause intensity fluctuations with up to 100 % .

Sample damage instead could be identified as a possible source to limit the applicability of FERMI as a x-ray source for solid state RIXS experiments. When critical FEL fluences are exceeded at the sample, a sudden drop of the elastic contribution was found and attributed to damage. When the probe fluence has to be attenuated to avoid sample damage, the high intensity of the FEL pulses can not be employed to compensate the lower repetition rate of the source. Upgrades of the FERMI FEL from 10 Hz to 50 Hz repetition rate, as well as progress in the seeding attempts at the high-repetition rate FEL FLASH II are therefore promising for RIXS experiments on sensitive samples.

The FERMI-RIXS setup energy resolution is limited by the contribution of the spectrometer. We determined a resolving power of $R_{spectrometer} \approx 600$. The FEL bandwidth instead would allow a reduction of energy resolution by a factor of two, towards the FEL bandwidth of $\Delta E_{FEL\text{-}average} = 60\,meV$ (FWHM) during our campaign. The desired enhancement in energy resolution is possible by upgrading the spectrometer. State-of-the art x-ray spectrometer allow resolving powers of up to 10 000[163].

A beam shape analysis revealed a non-gaussian intensity distribution of the incident FEL beam which lowers the effective energy resolution because of artifacts in the spectra. In future experiments, an implementation of additional diagnostic tools should be foreseen, which allow the machine physicists to tune the FEL such, that only ideal gaussian modes contribute to the spectrum. Alternatively, additional beam shaping apertures could be used along the beam path to assure maximum energy resolution in RIXS experiments.

Summary of the RIXS Experiments at FERMI

In this chapter, the results of RIXS measurements at the seeded Free Electron Laser FERMI were presented. The Free Electron Laser provided pulses with an average bandwidth of $\Delta E_{FEL\text{-}average} = 60\,meV$ (FWHM) at a photon energy of $h\nu = 61\,eV$ and intensity fluctuations within of 15 % r.m.s. at an intensity of 5 μJ/pulse during the data acquisition cycles. For performing the RIXS

experiments we made use of a specially designed vacuum setup equipped with a commercial Scienta XES355 x-ray spectrometer. A curved multilayer mirror, mounted on a Piezo stage allowed us a precise steering of the beam at the sample. We could determine the energy resolution of the setup to $\Delta E_{\text{FERMI-RIXS combined}} = 120\,\text{meV}$ which is dominated by the spectrometer contribution. Due to a very small focus size on the sample it was possible to achieve a spectrometer energy resolution better than what is theoretically expected. With a systematic variation of a beamline aperture opening we could show, that the FEL beam consists of spatial modes with non Gaussian distributions. With the setup we could determine the RIXS spectrum of $KCoF_3$ at photon energies of $h\nu = 61\,\text{eV}$ and $h\nu = 62.5\,\text{eV}$ across the Cobalt $M_{2,3}$ absorption edge. After averaging for 200 min we could see the expected $^4T_2$ symmetry induced excitation of the Cobalt valence electronic system and its resonance at excitation at a photon energy of $h\nu = 61\,\text{eV}$. It was not possible to resolve weak features with energy losses above 1 eV because of too low energy resolution and limited data acquisition time. The required acquisition times exceeded these of synchrotron measurements by a factor of three. This is a promising result since the repetition rate of the FERMI FEL is only 10 Hz, which much smaller than these of synchrotron x-ray sources with several 100 MHz. Reason for the much higher efficiency in the FEL experiments is the high brilliance of the FEL pulses compared to that of the synchrotron. The absorption cross section spectrum of the sample could be obtained making use of an automatized photon energy scan of the Free Electron Laser.

Because of its low bandwidth and high peak brilliance, the seeded Free Electron Laser FERMI is an excellent x-ray source for RIXS investigations on solids. An increase in repetition rate will help to reduce the data acquisition times from >3 hours per spectrum to shorter times. Due to the seeding technique, no monochromator is required at the FERMI FEL. For the pulse-length of the XUV pulses this means no additional stretching. It is therefore expected to achieve high time resolution in pump probe experiments, which will only be limited by the FEL pulse length which can be shorter than 100 fs. Also the pump laser synchronization is perfect in case of a seeded FEL, since the seed and pump laser are naturally synchronized, which reduces the jitter to a minimum.

5.6. Towards Time Resolved RIXS at Fermi

As mentioned in the above summary, the perspectives towards time resolved RIXS at FERMI are very promising. The monochromatic beam is very stable and a jitter-free implementation of a pump laser is possible[204][202]. The FERMI-RIXS setup used for the experiment described in this chapter and sketched in figure 5.1, foresees several optical view ports which allow the incoupling of a pump laser. An interesting system which may be studied with time resolved RIXS at FERMI is the iron oxide magnetite (Fe_3O_4) as discussed in chapter 4. It shows a clear signature of the Verwey phase transition in the dd-excitation spectrum which could be investigated within a pump probe experiment at FERMI.

6. Summary - Towards TR-RIXS on Magnetite

Within the above presented Part II of this thesis, two experimental campaigns are presented. First, static RIXS experiments on magnetite at the synchrotron (chapter 4) and secondly proof-of-principle RIXS experiments at the seeded Free Electron Laser FERMI (chapter 5). Both chapters end with a compact summary of the results. For a brief overview, the central achievements of the two RIXS campaigns are summarized in this chapter.

Signature of the Verwey Transition in RIXS

With the bulk sensitive resonant inelastic spectroscopy we could find a signature of the Verwey phase transition in the electronic structure of magnetite. The spectral shape and the overall intensity of the excitation spectrum changes when changing the sample temperatures from values below (T=80 K) to values above (T=160 K) the Verwey temperature.

Measurements at different excitation energies between 50 eV and 62 eV across the Fe $M_{2,3}$ absorption edge, combined with simulated absorption spectra did not allow an assignment of the peaks in the excitation spectrum to specific ionic sites. This finding is compatible with the recently proposed orbital ordering scheme in magnetite ("trimeron" structure).

Instrumentation Towards Time Resolved Measurements at FERMI

With a newly designed experimental endstation we could measure RIXS spectra at the seeded Free Electron Laser FERMI without usage of a monochromator. With a natural bandwidth of the FEL of $\Delta E_{\mathrm{FEL}}^{\mathrm{FWHM}} = 60\,\mathrm{meV}$ we recorded spectra of a $KCoF_3$ sample within acquisition times of 1-3 hours at different excitation energies. By analyzing the shot-resolved elastic contribution of the spectrum, we could establish a method for online monitoring of the sample damage.

Towards TR-RIXS on Magnetite

The ultimate goal of performing time resolved RIXS experiments at the Free Electron Laser FERMI is in sight. We showed, that the equilibrium phase transition strongly affects the electronic excitation spectrum. Mapping the evolution of the excitation throughout the laser driven non-equilibrium phase transition will give new insights into the nature of both, the non-equilibrium, as well as the equilibrium Verwey transition.

Conclusions and Perspectives

Within two parts of this thesis, experiments on the application of soft x-ray/XUV spectroscopy on the investigation of different condensed matter systems were presented. Electronic excitations in solids were characterized for systems in- (magnetite experiments, Part II) and out-of thermal equilibrium (gallium arsenide experiments, Part I). A summary and perspectives for future research are given in this chapter.

Time resolved photoemission spectroscopy (TR-PES) is employed in Part I to find signatures of the thermalization of photoexcited electrons in a semiconductor. By monitoring the binding energy of the core level states of the Gallium atoms with time resolved PES, we found a signature of the non-equilibrium excitation of the valence electrons. A 500 fs lasting transient increase of the binding energy at the gallium sites was observed. Possibly it resembles a localized excitation, which looses coherence within the first 500 fs after excitation, It's temporal evolution suggests a connection to the early thermalization of the photoexcited valence electrons. The wide photon energy spectrum of the Free Electron Laser (FEL) FLASH and its higher harmonics, as well as the pulse duration of only (170 ± 102) fs enabled the research on this system. Improvements on the experimental setup towards lower influence of the pump beam spacecharge effects could allow to simultaneously map other core levels, e.g. these of the arsen atoms in gallium arsenide, to unravel site specific, localized effects in the thermalization process.

By following a similar experimental approach as in the above summarized TR-PES experiments, we would like to unravel the electronic contribution to the Verwey phase transition in magnetite. In preparatory static soft x-ray/XUV RIXS experiments at a synchrotron, we characterized the excitation spectrum of magnetite and found a signature of the Verwey transition in the spectrum. The results show a clear, but comparably weak difference in the spectra below and above the Verwey transition, which reminds on the need of high energy resolution which can not easily be achieved in a PES experiment. Time resolved RIXS (TR-RIXS) experiments are therefore a better choice for this system. Along this vision of TR-RIXS experiments on magnetite, we set up a RIXS experiment at the seeded Free Electron Laser FERMI and performed proof-of-principle static RIXS experiments. In a next step TR-RIXS experiments should be performed. It is hereby the goal to determine the time scales at which the electronic signature changes. With a comparison of timescales to theoretical models, as it was done in the Part I of this work, it is possible to disentangle the origin of the changes. Improvements of the RIXS setup instrumentation in terms of beam diagnostics and spectrometer resolution could increase the accessible energy window. Upgrades of the FEL FERMI to higher repetition rates will allow faster data acquisition cycles.

Not only technical improvements are possible. The physical origin of the determined excitation spectra could be further investigated with theoretical calculations of the RIXS spectrum.

In both parts of this thesis, the strength of Free Electron Lasers to provide very short pulses of x-rays, is used or is proposed to be used to compare time scales of the experiment with that expected from theory. Experimental approaches as these utilized (Part I - TR-PES) and proposed (Part II - TR-RIXS) in this thesis will benefit a lot from improvements of stability and repetition rates of Free Electron Lasers. Ongoing improvements in the FEL intensity and wavelength stability will enable spectroscopy with higher energy resolution and lower data loss rates.

Appendix

A. Appendix Part I

Content

A.1. Additional Informations on the Spacecharge Simulations

Contents

A.1.1. Astra Settings

A detailed description of the working principles of the ASTRA code can be reviewed in the software manual[102]. In this section I give a brief overview about details which are relevant for performing the simulations.

Symmetry Constraints

While the particle distributions are treated in a 3D coordinate system, the spacecharge field calculations rely on a cylinder symmetric distribution of the electrons. This reduces the coordinates to a 2D system and therefore the time required for the simulations.

Passive Particles

It is possible to define particles, which are precisely tracked as all others, but are not taken into account for the calculation of spacecharge fields. These particles are called "passive" particles. As the spacecharge arising from the Probe-beam Photoelectrons can be neglected (see section 5.3) they can be treated as "passive" particles.

Input Parameters

Most of the parameters of Astra are used in their default settings (see Astra Manual [102]). The input parameters required for Astra as input used with non-default values are shown in table A.1.

Name	Value	Meaning (cited from [102])
N_min	5000	"average number of particles to be emitted in one step during the emission from a cathode"
H_max	0.5ns	"maximum time step for the Runge-Kutta integration."

Table A.1.: Astra input parameter required to Run the simulations.

A.2. Additional Informations on the Experimental Data evaluation

Contents

A.2.1. Transmissionfunction Determination of the Electron Time-of-Flight Spectrometer

To determine the transmission of the time-of-flight spectrometer I make use of the 2D imaging capability of the Delayline Detector. The photon peak which is fully transmitted by the spectrometer appears as a homogeneously illuminated circle on the spectrometer (figure A.1). A projection of this circle onto the x-axis is fitted with Gaussian line. The width of this Gaussian is taken as the radius of the circle on the detector. I than use the following assumptions:

$$T \propto A \propto R^2_{\text{detected circle}} \tag{A.1}$$

$$\rightarrow T_{\text{relative}} = \frac{R(E_{\text{kin}})}{R_{\text{reference}}(\text{photons})}^2 , \tag{A.2}$$

where T is the transmission of the spectrometer, A the area of the circle on the detector, R the radius of the circle on the detector and $R_{\text{reference}}$ the radius of the photon peak circle at the detector (figure A.1). For the relative transmission as a function of kinetic energy I evaluated the electron detection distribution for all kinetic energies (figure A.2(a)) and apply equation A.2 in figure 3.9.

A.2.2. Fringe Visibility Determination

In section 3.2.5 I present the auto-correlation trace of the FEL beam. This trace is determined by analyzing the fringe visibility on a screen at which the split and delayed FEL beams are spatially overlapped (see figure A.3). To extract the fringe visibility I use a method similar to that described

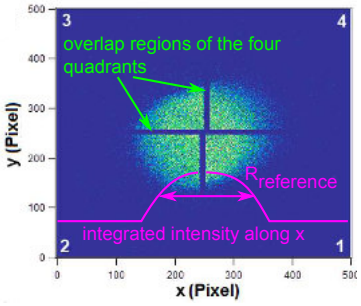

Figure A.1.: Imprint of the photon peak on the 4 Quadrant delayline detector (adapted from [95]). As the transmission is unaffected for photons, the area of the circle is taken as the reference for the experimental determination of the transmission. The magenta line is the integrated intensity along the x-direction. The radius is exctracted with a Gaussian line fit. The same distribution is plotted with color coding in figure A.2(a) for different electron kinetic energies.

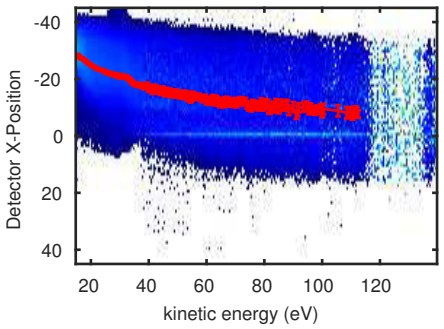

(a) Integrated intensity distribution along the x-axis of the detector for different kinetic energies of the mesured electrons. One can see (I) a shift of the center of mass towards the outer edge of the detector and (II) a reduction of the radius of the distribution.

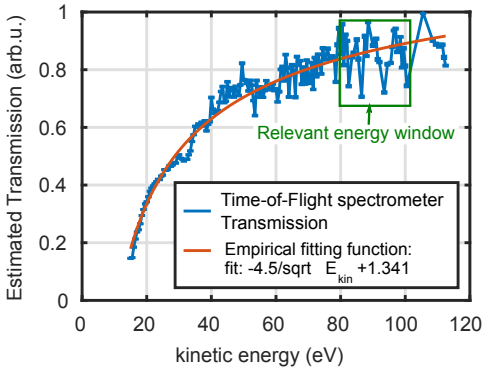

(b) Relative Transmission determined with equation A.2 and fitted with a squar-root fit.

Figure A.2.: The methodology to derive the transmission function of the electron time of fligh spectrometer is depicted in this two figures. See also the descriptions in the text.

in [205][65]. For every image I analyze the Fourier transformed image with a fit of the vertical projection (see figure A.3(c)). The fitting function is composed of two components. The central line resembles the auto correlation intensity I_{AC}, and the two side-peaks resemble the cross correlation intensity I_{XC}. The cross correlation intensity I_{XC} becomes zero when the two beams are not overlapped in time. The auto correlation intensity I_{AC} is proportional to the beam intensity. It only disappears to zero, when the beam doesn't hit the screen. How the two variables are extracted from the camera image is shonw in figure A.3. The fringe visibility V is than calculated with[65]:

$$V = \frac{2 \times I_{\mathrm{XC}}}{I_{\mathrm{AC}}}. \tag{A.3}$$

In the main text the resulting fringe visibility V for different delays of the pump- and probe-arm of the SDU is shown and used to extract the auto-correlation length (figure 3.7).

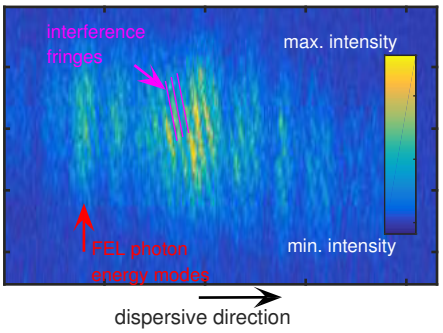

(a) Example image of the interference fringes on the CCD camera at Δt_{SDU}=0ps (same image is shown in the main text figure 3.7

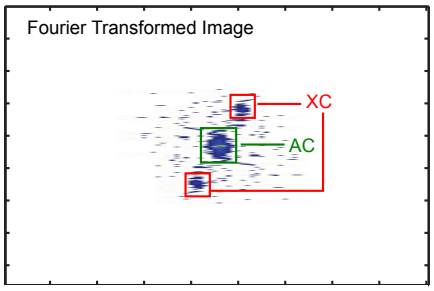

(b) Fourier Transform of the image shown in a. The image is mirrored around the x=0 axis. The two relevant areas resemble the auto correlation signal (AC, marked green) used for normalization, as well as the cross correlation signal (XC, marked red).

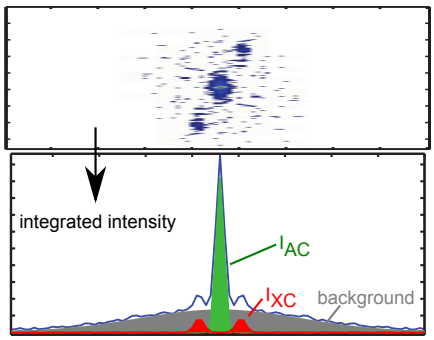

(c) To extract the cross- and auto-correlation intensity, I sum the fourier image intensity along the vertical axis and fit it with three gaussian lines representing a background contribution (grey), the cross correlation intensity I_{XC} (red) and the auto correlation intensity I_{AC} (red).

Figure A.3.: The three steps to evaluate the pictures of the interference fringes after the FEL beam was split and delayed with the SDU. a) Original image, b) Fourier Transform, c) Fitting function.

A.2.3. Example for the Used Fitting Function

The Ga3d lines of the Pump Probe Data were evaluated with a Gaussian line fit with a arc-tan shaped background function for the secondary electron background description[206]. In high resolution spectroscopy the Ga3d line shape is described by the sum of a surface and bulk lorentzian line[99]. Due to the spacecharge broadening the rather coarse Gaussian line-shape is justified. Two examples of the fitting function for spectra with a pump fluences of $\Phi^{\mathrm{Pump}} = 0.22/0.53\,\mu\mathrm{J/cm^2}$ are shown in figure A.4.

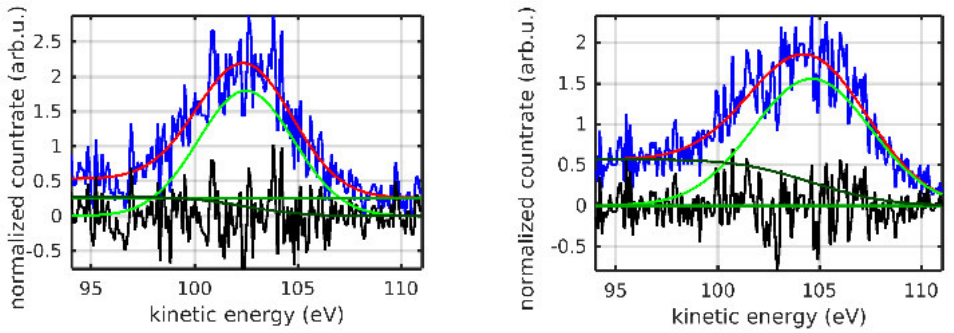

(a) Medium pump fluence - $\Phi^{\mathrm{Pump}} = 0.22\,\mu\mathrm{J/cm^2}$ (b) High pump fluence - $\Phi^{\mathrm{Pump}} = 0.53\,\mu\mathrm{J/cm^2}$

Figure A.4.: Illustration of the fitting function used to fit the Ga3d line. figures a) and b) show XPS spectra of the Ga3d emission line recorded with the electron time of flight and the Free Electron Laser with both, pump and probe beam on the sample (Dataset II, $h\nu_{\mathrm{Probe}} = 120\,\mathrm{eV}$, $h\nu_{\mathrm{Pump}} = 40\,\mathrm{eV}$, different fluences). The experimental data (blue) are fitted with the sum of a Gaussian line (bright green) and a arc-tan shaped background (dark green). The overall fit is shown with a red line and the residuum shown in black is acceptable for all spectra fitted in this work.

A.2.4. Spacecharge Compensations Applied to the Pump-Probe Traces

In the main text of Part I, section 5.6, the strategy to correct the measured pump-probe traces for the spacecharge contributions is described. Figure A.5 shows the correction traces applied to the datasets which were not included in the main text. Figure A.6 shows the spacecharge corrected delay trace of dataset V which was excluded from the data analysis because influence of the probe spacecharge can not be excluded. Probably probe spacecharge effects cause the appearance of delay dependent variations before the time-zero in figure A.6.

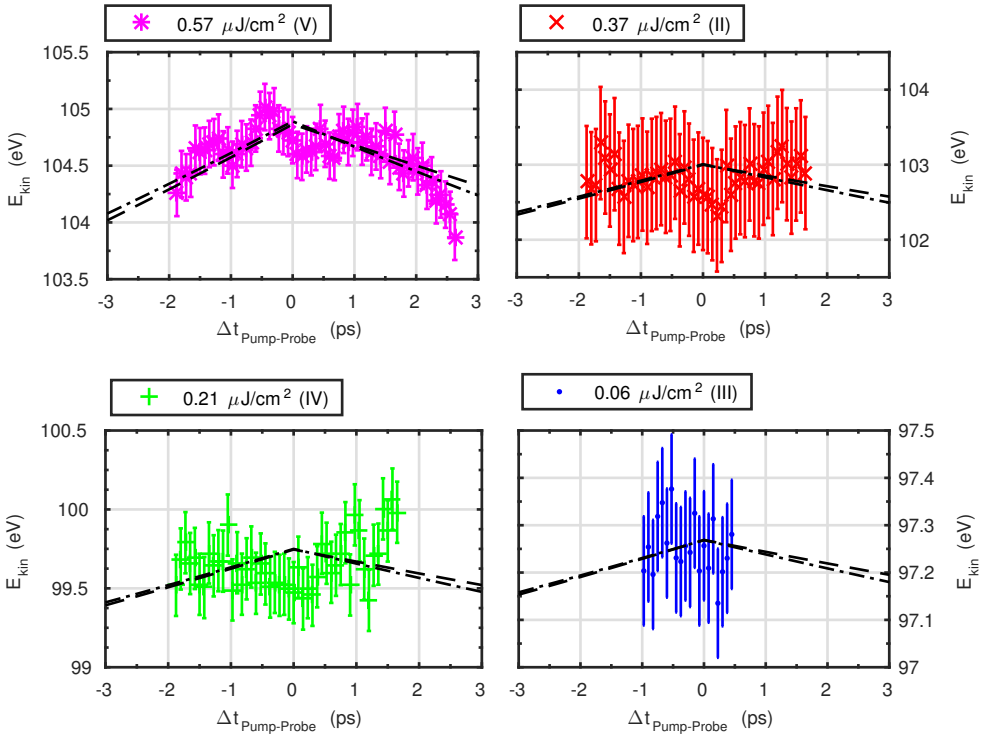

Figure A.5.: The fitting coefficients for II, III and IV are listed in table 5.6, while these of V are not tabulated. The fitting coefficient A of dataset V is determined to: $A = 8.8$.

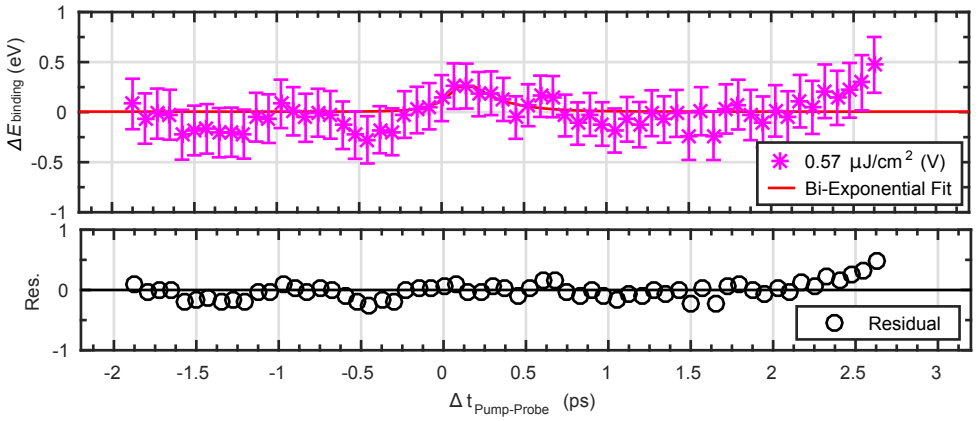

Figure A.6.: Fitting coefficients (eq. (5.6)): $I = -0.34 \pm 0.22$, $t_0 = 0.14 \pm 0.1$, $1/\tau_{\text{drop}} = 8.8 \pm 13.4$, $1/\tau_{\text{recovery}} = -5 \pm 6$.

B. Appendix Part II

Content Appendix Part II

B.1. Additional Information on the RIXS Experiments at Magnetite

Contents

B.1.1. Magnetite Simulated XMCD Spectrum

The XMCD spectrum shown together with simulations in figure B.1 was measured by Koide et al. in [129] and reproduced by Antonov et al. in [207].

B.1.2. Summary Table and Datasets Recorded at MERLIN

The table B.1 summarizes the beamline and endstation settings during the experiments. Tables B.2 and B.3 show fitting parameter used to transfer the CCD detector data of the MERIXS spectrometer into a RIXS spectrum.

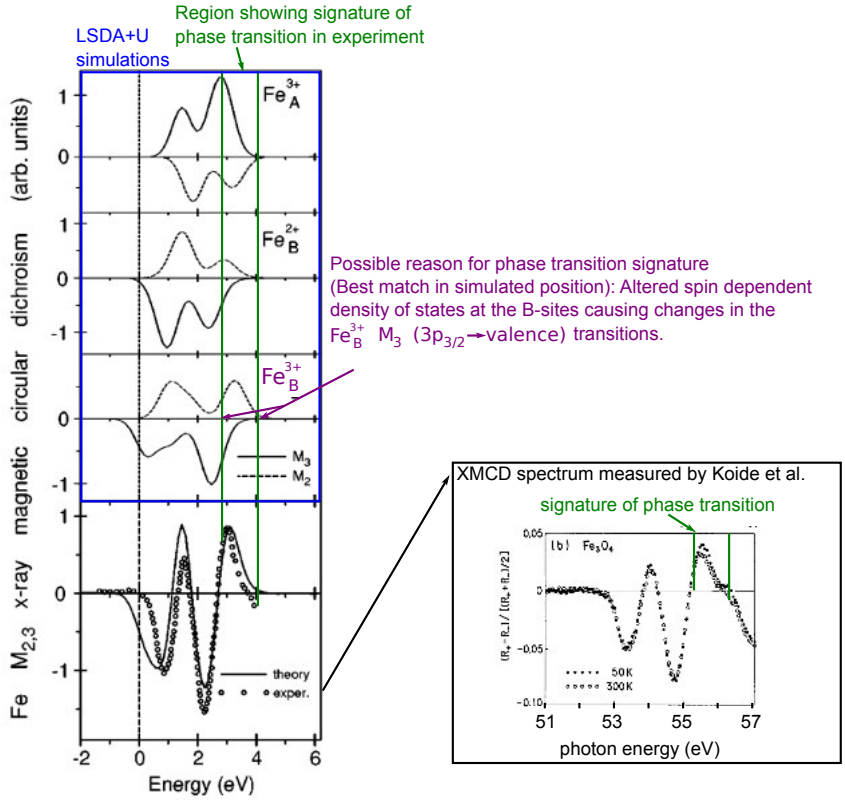

Figure B.1.: Left: Figure taken from [207]. Simulated and measured Fe M-edge XMCD spectrum of magnetite (data of [129]). The XMCD contribution of the three iron sites is displayed individually for all three iron sites (three boxes) as well as the M2 (3The simulations within the LSDA+U approach suggest, that the region which shows a signature of the phase transition is best matched by a contribution of the M2-edge feature of the B site Fe^{3+} ion. Right: Figure taken from [129]. Fe M-edge XMCD spectrum of magnetite below and above the Verwey temperature (shown also in figure 2.5).

Dataset	Infos	Settings
2159	RIXS 7 energies {50; 53.8; 55.1; 56; 56.4; 57.8; 62}eV	◦ T=160K
		◦ x=-0.9 z=122.6 y=4.6 $\theta = -30$Â° $\phi = 75$Â° $\chi = -8$Â°
		◦ CCD exposure/photon energy=8 ($h\nu$=50;53.8;55.1eV)/7 (all other)×400s
		◦ 7 Spectrometer Set Energies (ordered as excitation energies): $E_{\text{spectrometer}} \in$ {48.01; 51.42; 52.58; 53.4; 53.75; 55; 58.77}eV
2135	RIXS 7 energies {50; 53.8; 55.1; 56; 56.4; 57.8; 62}eV	◦ T=80K
		◦ x=-1 z=123 y=4.6 $\theta = -30$Â° $\phi = 75$Â° $\chi = -8$Â°
		◦ CCD exposure/photon energy=9×600s
3506	z-Motor XAS scan	◦ x=0 y=4.6 z=120-125 $\theta = -25$Â°
		◦ $h\nu = 57.8$eV
3515	XAS scan	◦ x=-1 z=123 y=4.6 $\theta = -30$ $\phi = 75$Â° $\chi = -8$Â°
		◦ $h\nu$=45-65eV
		◦ T=80K
0161	x,z-Motor XAS scan	◦ x=-0.8-1.5 z=120-123 y=4.6 $\theta = -25$ $\phi = -90$Â° $\chi = 2$Â°
		◦ $h\nu$=57.8eV
		◦ T=RT

Table B.1.: Overview of the Datasets recorded during the ALS beamtime in 2013. Coordinate system sketched in figure 3.5. Units: [x,y,z] Positions in mm. [θ,ϕ,χ] in Â°.

spectrometer set-energy	**4th-order Polynomial Fit coefficients (formula see caption)**				
	$p1$	$p2$	$p3$	$p4$	$p5$
48.01eV	-1.366e-09	7.994e-07	-2.610e-4	2.776e-2	137.967
51.42eV	-9.168e-10	5.714e-07	-2.190e-4	2.244e-2	137.353
52.58eV	-5.677e-10	3.740e-07	-1.778e-4	1.870e-2	137.372
53.40eV	-7.390e-10	4.416e-07	-1.819e-4	1.763e-2	139.798
53.75eV	-1.103e-09	6.805e-07	-2.359e-4	2.247e-2	138.784
55.00eV	-1.318e-09	8.003e-07	-2.609e-4	2.451e-2	139.987
58.77eV	-1.191e-09	6.755e-07	-2.157e-4	1.722e-2	147.984

Table B.2.: Summary of the curvature-correction fits. Each line along the dispersive direction is shifted by: Δy[pixel](x)=$p1 * x^4 + p2 * x^3 + p3 * x^2 + p4 * x + p5$. Here x is the detector position along the non-dispersive direction.

B.1.3. Experimental Details on the Time Resolved Optical Reflectivity Experiments.

Energy Axis Calibrations

To calibrate the photodiode of the 800nm-pump-supercontiuum-probe setup described in figure 3.11 and section 3.2.2 we put a multipeakfilter into the beampath and search the characteristic transmission points in the spectrum on the diode-assembly. The procedure is described in B.2. The resulting energy calibration (shown in figure B.3) is:

$$E_{\text{reflected}}[eV] = 0.0004x^2 - 0.0202x + 1.6566. \tag{B.1}$$

Here x is the pixel position at the diode assembly which measures the reflected beam spectrum.

spectrometer set-energy	**4th-order Polynomial Fit coefficients (formula see caption)**				
	$p1$	$p2$	$p3$	$p4$	$p5$
48.01eV	-1.862e-13	2.091e-10	6.843e-7	-4.519e-3	50.62
51.42eV	6.047e-13	-1.096e-9	1.494e-6	5.562e-3	54.54
52.58eV	-2.626e-14	-2.054e-10	1.232e-6	-5.906e-3	55.89
53.40eV	7.647e-13	-1.198e-09	1.585e-06	-6.148e-3	56.83
53.75eV	1.277e-12	-2.062e-09	2.104e-06	-6.365e-3	57.25
55.00eV	-1.284e-12	1.65e-09	4.413e-07	-6.472e-3	58.69
58.77eV	6.906e-13	-1.067e-9	2.004e-6	-8.014e-3	63.15

Table B.3.: Summary of the retrieved energy calibration data. The photon energy of the detected photons on the CCD detector can be retrieved from the horizontal position on the CCD with the following formula: $E_{detected}[eV]=p1*x^4+p2*x^3+p3*x^2+p4*x+p5$. In this formula x is the horizontal CCD position in pixel and $E_{detected}$ the photon energy. The fitting parameter $p1$ to $p5$ vary for the different set-energies of the spectrometer as the blazing angle and the distance between detector and VLS grating is varied for different set-energies.

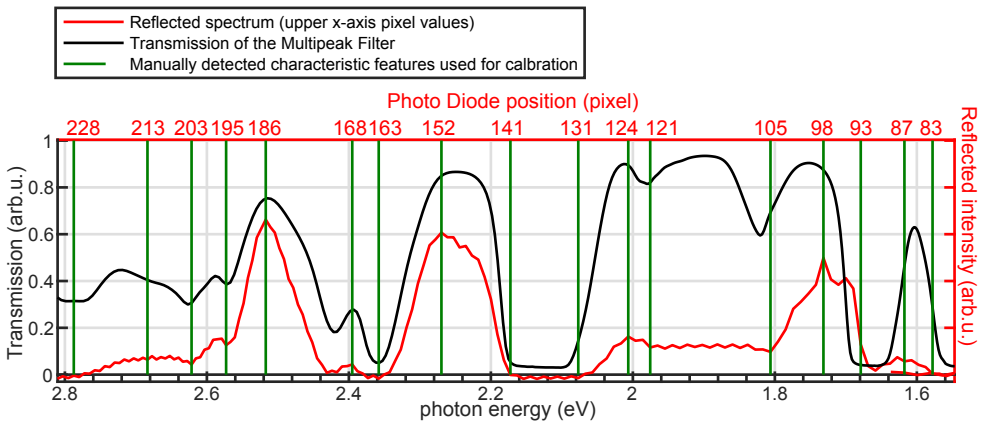

Figure B.2.: Calibration curve of the optical reflecitivity setup. To retrieve a functional relation between pixel of the Photodiode detector and photon energy we insert a multipeak filter into the beam (black line shows transmission of this filter in correspondence with photon energy at the bottom x-axis). After passing the multipeakfilter the beam is sent to the sample and reflected to the energy-analyzing diode. The reflected spectrum is read-out as a function of diode-pixels (red line and upper x-axis) and shows some of the characteristic spikes of the multipeak filter. Some of these spikes are identified by eye (green lines). The resulting correspondence is used to define the energy calibration curve shown in figure B.3.

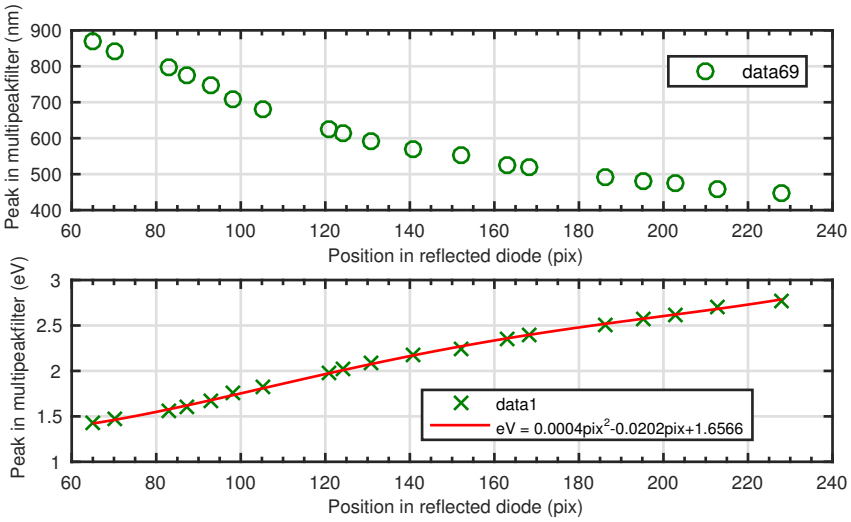

Figure B.3.: Bottom: Green crosses mark the Diode-Pixel Position (pixel) of manually detected characteristic features of the multipeak filter transmission features (eV) (labeled with green bars in figure B.2). The red line represents a 2^{nd} order polynomial fit used to convert from pixel-values to photon energy. Top: The same relation (without fit) for the wavelength dependence.

Correction of Photonenergy Dependent Delay Variation

As reported in [208] the different frequencies of the super-contiuum probe, generated in the optical fibre have a different delays. This can be resolved in the setup and corrected as shown in figure B.4. The curvature is empirically extracted and the data shifted such, that in the corrected spectrum all photon energies appear at the same time-zero.

B.1.4. RIXS Spectra and Their Fits for All Excitation Energies and Temperatures

An example for the fitting function for the spectra at room temperature is shown in figure B.5. All recorded RIXS spectra and their fitting function are shown in figures B.6 and B.7

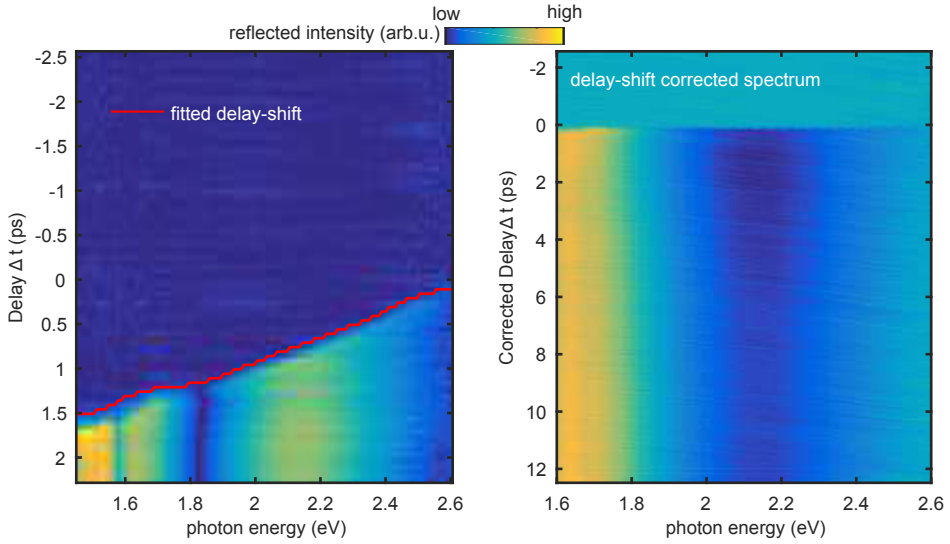

Figure B.4.: Left: The different photon energies arrive at different time delay at the photodiode detector. The arrival is determined as presented with the red line. Right: The arrival time of the spectrum is shifted such that all photon energies arrive at the same time zero. The data stem from the high fluence scan at F=3.25mJ/cm^2.

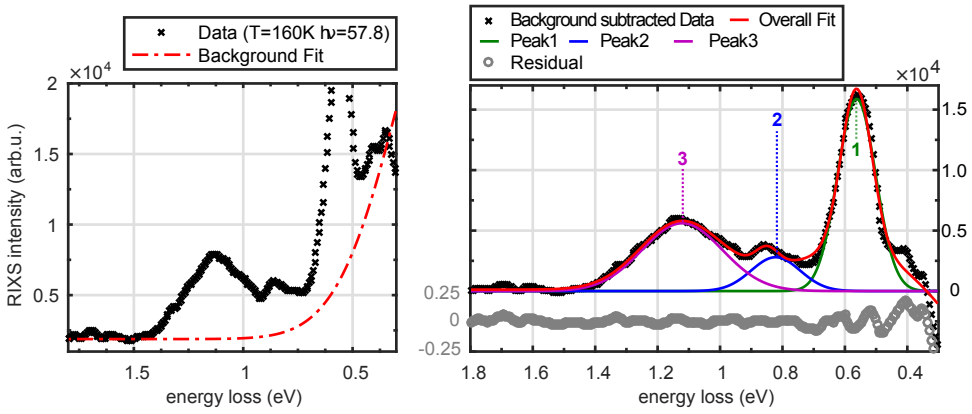

Figure B.5.: RIXS spectrum of Magnetite recorded at T=160K at an excitation energy of $h\nu$ = 57.8eV illustrating the fitting function used for quantification. Left: The red dash-dotted line shows the shoulder of a Gaussian peak centered at energy loss=0eV together with a constant offset used to estimate the elastic background contribution. Right: The background subtracted spectrum is fitted with three numbered Gaussian Peaks (1-green, 2-blue and 3-magenta). The spectra for the other excitation energies together with the respective fits are shown in figure B.6 (T=80K) and B.7 (T=160K).

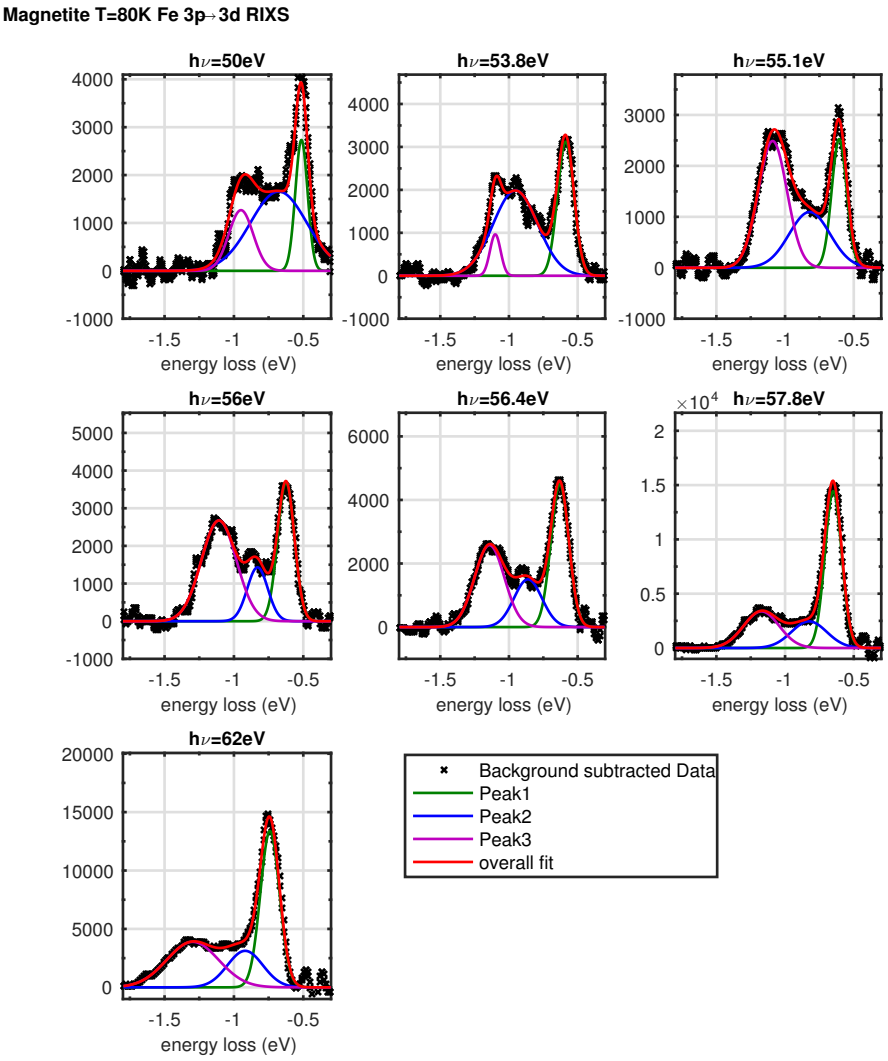

Figure B.6.: RIXS spectra of magnetite (black points) recorded at different excitation energies at a sample temperature of T=80K. The red line shows the fit with the fitting model introduced in the main-text.

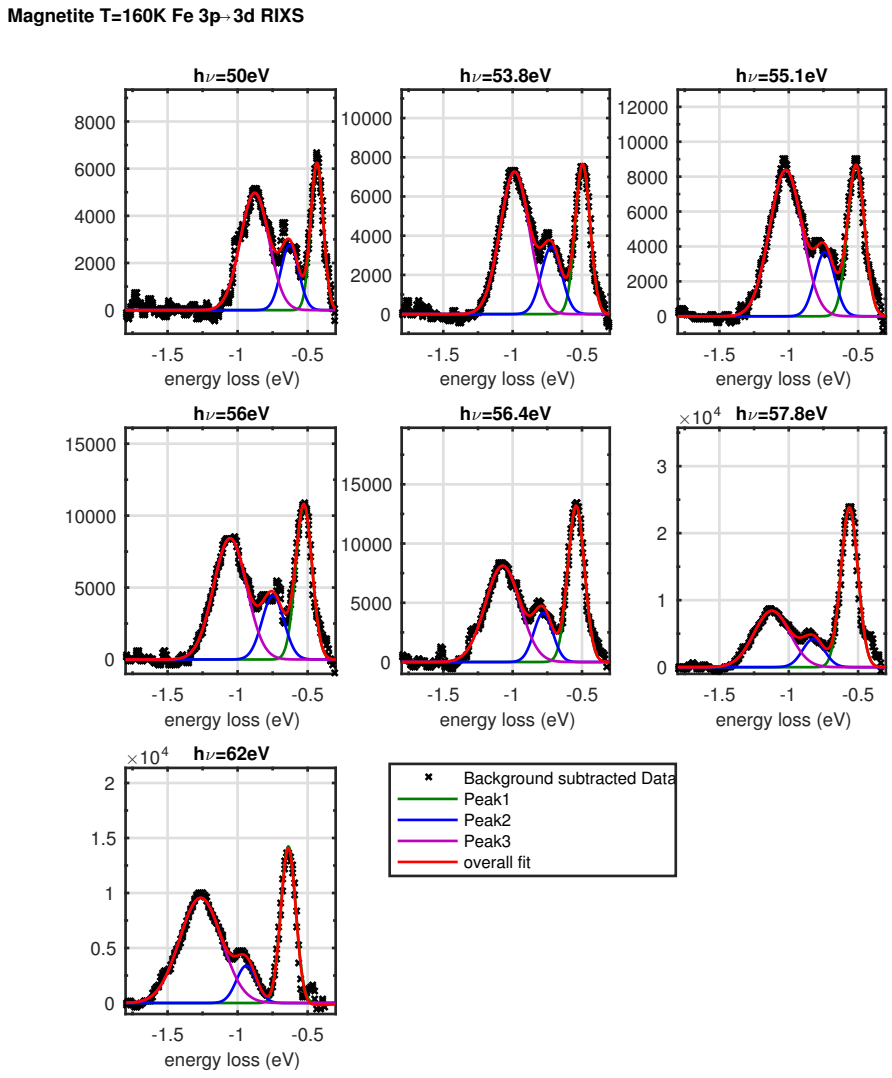

Figure B.7.: RIXS spectra of magnetite (black points) recorded at different excitation energies at a sample temperature of T=160K. The red line shows the fit with the fitting model introduced in the main-text.

B.2. Additional Information On The RIXS Instrumentation at FERMI

Contents

B.2.1. Photograph of the Setup

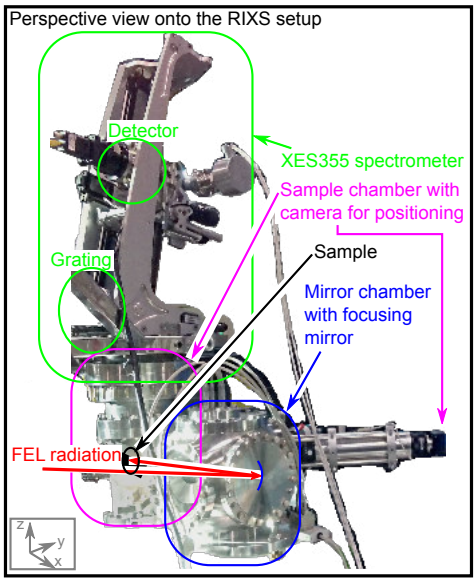

Figure B.8.: A photograph of the RIXS setup at FERMI from a perspective view. The spectrometer, sample and mirror chamber are labeled with arrow.

Eidesstattliche Versicherung

Hiermit erkläre ich an Eides statt, dass ich die vorliegende Dissertationsschrift selbst verfasst und keine anderen als die angegebenen Quellen und Hilfsmittel benutzt habe.

Hamburg, den 05.04.2017 (Florian Hieke)

List of Papers

The following paper is published in a scientific journal and contains a substantial part of this thesis (Chapter 4 of Part II):

Reference Number [183]:
Extreme ultraviolet resonant inelastic X-ray scattering (RIXS) at a seeded free-electron laser. Dell'Angela, M., Hieke, F. , Malvestuto, M., Sturari, L. , Bajt, S., Kozhevnikov, I. V., Ratanapreechachai, J., Caretta, A., Casarin, B., Glerean, F., Kalashnikova, A. M., Pisarev, R. V., Chuang, Y.-D., Manzoni, G., Cilento, F., Mincigrucci, R., Simoncig, A.,Principi, E., Masciovecchio, C., Raimondi, L., Mahne, N., Svetina, C., Zangrando, M., Passuello, R., Gaio, G., Prica, M., Scarcia, M., Kourousias, G., Borghes, R., Giannessi, L., Wurth, W., Parmigiani, F. (published online 12.12.2016) *Scientific Reports*

During my time in the group of Wilfried Wurth, I took part at the following projects which are not explicitly part of this thesis:

Statistical properties of a free-electron laser revealed by the Hanbury Brown and Twiss interferometry Gorobtsov, O. Yu., Mercurio, G., Brenner, G., Lorenz, U., Gerasimova, N., Kurta, R. P., Hieke, F., Skopintsev, P., Zaluzhnyy, I., Lazarev, S., Dzhigaev, D., Rose, M., Singer, A., Wurth, W., Vartanyants, I. A. (accepted 01/2017) *Phys. Rev. A*

Chemical Bond Activation Observed with an X-ray Laser Beye, M., Öberg, H., Xin, H., Dakovski, G.L., Dell'Angela, M., Föhlisch, A., Gladh, J., Hantschmann, M., Hieke, F., Kaya, S., Kühn, D., Larue, J., Mercurio, G., Minitti, M.P., Mitra, A., Moeller, S.P., Ng, M.L., Nilsson, A., Nordlund, D., Nørskov, J., Öström, H., Ogasawara, H., Persson, M., Schlotter, W.F., Sellberg, J.A., Wolf, M., Abild-Pedersen, F., Pettersson, L.G.M., Wurth, W. (2016) *Journal of Physical Chemistry Letters*, 7 (18), pp. 3647-3651.

Ultrafast surface dynamics probed with time resolved photoemission Dell'Angela, M., Hieke, F., Sorgenfrei, F., Gerken, N., Beye, M., Gerasimova, N., Redlin, H., Wurth, W. (2016) *Surface Science*, 643, pp. 197-202

Correction of the deterministic part of space-charge interaction in momentum microscopy of charged particles Schönhense, G., Medjanik, K., Tusche, C., de Loos, M., van der Geer, B., Scholz, M., Hieke, F., Gerken, N., Kirschner, J., Wurth, W. (2015) *Ultramicroscopy*, 159, pp. 488-496

Strong influence of coadsorbate interaction on CO desorption dynamics on Ru(0001) probed by ultrafast X-ray spectroscopy and ab initio simulations Xin, H., Larue, J., Öberg, H., Beye, M., Dell'Angela, M., Turner, J.J., Gladh, J., Ng, M.L., Sellberg, J.A., Kaya, S., Mercurio, G., Hieke, F., Nordlund, D., Schlotter, W.F., Dakovski, G.L., Minitti, M.P., Föhlisch, A., Wolf, M., Wurth, W., Ogasawara, H., Nørskov, J.K., Öström, H., Pettersson, L.G.M., Nilsson, A., Abild-Pedersen, F. (2015) *Physical Review Letters*, 114 (15), art. no. 156101

Probing the transition state region in catalytic CO oxidation on Ru Öström, H., Öberg, H., Xin, H., LaRue, J., Beye, M., Dell'Angela, M., Gladh, J., Ng, M.L., Sellberg, J.A., Kaya, S., Mercurio, G., Nordlund, D., Hantschmann, M., Hieke, F., Kühn, D., Schlotter, W.F., Dakovski, G.L., Turner, J.J., Minitti, M.P., Mitra, A., Moeller, S.P., Föhlisch, A., Wolf, M., Wurth, W., Persson, M., Nørskov, J.K., Abild-Pedersen, F., Ogasawara, H., Pettersson, L.G.M., Nilsson, A. (2015) *Science*, 347 (6225), pp. 978-982

The role of space charge in spin-resolved photoemission experiments Fognini, A., Salvatella, G., Michlmayr, T.U., Wetli, C., Ramsperger, U., Bähler, T., Sorgenfrei, F., Beye, M., Eschenlohr, A., Pontius, N., Stamm, C., Hieke, F., Dell'Angela, M., De Jong, S., Kukreja, R., Gerasimova, N., Rybnikov, V., Redlin, H., Raabe, J., Föhlisch, A., Dürr, H.A., Wurth, W., Pescia, D., Vaterlaus, A., Acremann, Y. (2014) *New Journal of Physics*, 16, art. no. 043031

Ultrafast reduction of the total magnetization in iron Fognini, A., Michlmayr, T.U., Salvatella, G., Wetli, C., Ramsperger, U., Bähler, T., Sorgenfrei, F., Beye, M., Eschenlohr, A., Pontius, N., Stamm, C., Hieke, F., Dell'Angela, M., De Jong, S., Kukreja, R., Gerasimova, N., Rybnikov, V., Al-Shemmary, A., Redlin, H., Raabe, J., Föhlisch, A., Dürr, H.A., Wurth, W., Pescia, D., Vaterlaus, A., Acremann, Y. (2014) *Applied Physics Letters*, 104 (3), art. no. 032402

Acknowledgments

After having finished my Diploma in the group of Wilfried Wurth, I thought a bit and finally took his offer and continued my work on studying time resolved phenomena in his group. I am very happy, to have had this opportunity and that I could spend four more years in science. Being part of the lively community of scientists attracted by Free Electron Lasers, and the growing field of solid state spectroscopy with them was a great experience for me. Beside the position I thank Wilfried for his encouraging and calm perspective on my work. Thank you.Martina Dell'Angela shares place one with Wilfried in the list of irreplaceable partners during the time of my PhD. Together we recorded all data presented in this work. What I know about spectroscopy I learned from her. Together we collected lots of experience in our first FEL experiments at FLASH in Hamburg. In the first year of my PhD she left to Trieste, but we continued our team work in collaborative projects around the world. In the not seldom 48 hours exceeding beamtime shifts at FLASH and FERMI, we found good ways to stay relaxed under stressful conditions and I can not imagine any problem which Martina would not be willy to discuss. Thanks a lot for all your support through my time in science and for your help with this thesis. Less in the center of this thesis, but even more in my daily working life at CFEL, I thank "always-calm-Lukas" and "never-tired-Giuseppe" for the unique team work. Our (finally rewarded) attempts to perform measurements on catalytic systems at FLASH made us a tough and experienced team. Working with you was really a great thing. I thank our technical engineers Sven and Holger for their permanent support and will to listen to our nasty problems with the UHV, and Marlis for the always filled glass of Haribos in her office. The CFEL coffee- and breakfast-gang has of course to be mentioned and overflowed with thanks. A working day without gold-cup coffee with Adrian, Julia, Friedrich, Tiberiu, Henrike, Artur, Dima, Federico, or Hauke was always a bad working day. In this sense, I thank all members of the AG Wurth for small talks during coffee breaks as well as support in the lab or at the beamline: Thank you Ivan, Karo, Steffen, Deniza, Nils G., Torben B., Friedtjof, Friederike, Kaja, Kay, Michael, Teresa and all members I am forgetting in this moment.

Bibliography

[1] Harald Ibach and Hans Lüth. *Festkörperphysik: Einführung in die Grundlagen ; mit 18 Tafeln und 104 Übungen*. Springer-Lehrbuch. Springer, Berlin [u.a.], 7 edition, 2009.

[2] Neil W. Ashcroft and N. David Mermin. *Solid state physics*. Brooks/Cole Thomson Learning, South Melbourne [u.a.], repr. edition, 2012.

[3] Jeffrey W. Lynn. *High Temperature Superconductivity*. Springer Science & Business Media, December 2012.

[4] Gerhard Ertl. Reactions at Surfaces: From Atoms to Complexity (Nobel Lecture). *Angewandte Chemie International Edition*, 47(19):3524–3535, April 2008.

[5] Jens Falta and Thomas Möller. *Forschung mit Synchrotronstrahlung: eine Einführung in die Grundlagen und Anwendungen*. Studium. Vieweg Teubner, Wiesbaden, 1 edition, 2010.

[6] C.S. Fadley. X-ray photoelectron spectroscopy: Progress and perspectives. *Journal of Electron Spectroscopy and Related Phenomena*, 178-179:2–32, May 2010.

[7] Luuk J. P. Ament, Michel van Veenendaal, Thomas P. Devereaux, John P. Hill, and Jeroen van den Brink. Resonant inelastic x-ray scattering studies of elementary excitations. *Reviews of Modern Physics*, 83(2):705–767, June 2011.

[8] A. L. Cavalieri, N. Müller, Th. Uphues, V. S. Yakovlev, A. Baltuška, B. Horvath, B. Schmidt, L. Blümel, R. Holzwarth, S. Hendel, M. Drescher, U. Kleineberg, P. M. Echenique, R. Kienberger, F. Krausz, and U. Heinzmann. Attosecond spectroscopy in condensed matter. *Nature*, 449(7165):1029–1032, October 2007.

[9] M. Dell'Angela, T. Anniyev, M. Beye, R. Coffee, A. Föhlisch, J. Gladh, T. Katayama, S. Kaya, O. Krupin, J. LaRue, A. Møgelhøj, D. Nordlund, J. K. Nørskov, H. Öberg, H. Ogasawara, H. Öström, L. G. M. Pettersson, W. F. Schlotter, J. A. Sellberg, F. Sorgenfrei, J. J. Turner, M. Wolf, W. Wurth, and A. Nilsson. Real-Time Observation of Surface Bond Breaking with an X-ray Laser. *Science*, 339(6125):1302–1305, March 2013.

[10] S. Hellmann, M. Beye, C. Sohrt, T. Rohwer, F. Sorgenfrei, H. Redlin, M. Kalläne, M. Marczynski-Bühlow, F. Hennies, M. Bauer, A. Föhlisch, L. Kipp, W. Wurth, and K. Rossnagel. Ultrafast Melting of a Charge-Density Wave in the Mott Insulator 1 T - TaS 2. *Physical Review Letters*, 105(18), October 2010.

[11] S. Neppl, R. Ernstorfer, A. L. Cavalieri, C. Lemell, G. Wachter, E. Magerl, E. M. Bothschafter, M. Jobst, M. Hofstetter, U. Kleineberg, J. V. Barth, D. Menzel, J. Burgdörfer, P. Feulner, F. Krausz, and R. Kienberger. Direct observation of electron propagation and dielectric screening on the atomic length scale. *Nature*, 517(7534):342–346, January 2015.

[12] Zheng Yang, Changhyun Ko, and Shriram Ramanathan. Oxide Electronics Utilizing Ultrafast Metal-Insulator Transitions. *Annual Review of Materials Research*, 41(1):337–367, 2011.

[13] S. de Jong, R. Kukreja, C. Trabant, N. Pontius, C. F. Chang, T. Kachel, M. Beye, F. Sorgenfrei, C. H. Back, B. Bräuer, W. F. Schlotter, J. J. Turner, O. Krupin, M. Doehler, D. Zhu, M. A. Hossain, A. O. Scherz, D. Fausti, F. Novelli, M. Esposito, W. S. Lee, Y. D. Chuang, D. H. Lu, R. G. Moore, M. Yi, M. Trigo, P. Kirchmann, L. Pathey, M. S. Golden, M. Buchholz, P. Metcalf, F. Parmigiani, W. Wurth, A. Föhlisch, C. Schüßler-Langeheine, and H. A. Dürr. Speed limit of the insulator–metal transition in magnetite. *Nature Materials*, 12(10):882–886, July 2013.

[14] A. Fognini, T. U. Michlmayr, G. Salvatella, C. Wetli, U. Ramsperger, T. Bähler, F. Sorgenfrei, M. Beye, A. Eschenlohr, N. Pontius, C. Stamm, F. Hieke, M. Dell'Angela, S. de Jong, R. Kukreja, N. Gerasimova, V. Rybnikov, A. Al-Shemmary, H. Redlin, J. Raabe, A. Föhlisch, H. A. Dürr, W. Wurth, D. Pescia, A. Vaterlaus, and Y. Acremann. Ultrafast reduction of the total magnetization in iron. *Applied Physics Letters*, 104(3):032402, January 2014.

[15] D. Fausti, R. I. Tobey, N. Dean, S. Kaiser, A. Dienst, M. C. Hoffmann, S. Pyon, T. Takayama, H. Takagi, and A. Cavalleri. Light-Induced Superconductivity in a Stripe-Ordered Cuprate. *Science*, 331(6014):189–191, January 2011.

[16] Cornelius Gahl, Armin Azima, Martin Beye, Martin Deppe, Kristian Döbrich, Urs Hasslinger, Franz Hennies, Alexej Melnikov, Mitsuru Nagasono, Annette Pietzsch, Martin Wolf, Wilfried Wurth, and Alexander Föhlisch. A femtosecond X-ray/optical cross-correlator. *Nature Photonics*, 2(3):165–169, March 2008.

[17] Beata Ziaja, Nikita Medvedev, Victor Tkachenko, Theophilos Maltezopoulos, and Wilfried Wurth. Time-resolved observation of band-gap shrinking and electron-lattice thermalization within X-ray excited gallium arsenide. *Scientific reports*, 5, 2015.

[18] N. Medvedev, B. Ziaja, M. Cammarata, M. Harmand, and S. Toleikis. Electron Kinetics in Femtosecond X-Ray Irradiated SiO_2. *Contributions to Plasma Physics*, 53(4-5):347–354, May 2013.

[19] W. Ackermann, G. Asova, V. Ayvazyan, A. Azima, N. Baboi, J. Bähr, V. Balandin, B. Beutner, A. Brandt, A. Bolzmann, R. Brinkmann, O. I. Brovko, M. Castellano, P. Castro, L. Catani, E. Chiadroni, S. Choroba, A. Cianchi, J. T. Costello, D. Cubaynes, J. Dardis, W. Decking, H. Delsim-Hashemi, A. Delserieys, G. Di Pirro, M. Dohlus, S. Düsterer, A. Eckhardt, H. T. Edwards, B. Faatz, J. Feldhaus, K. Flöttmann, J. Frisch, L. Fröhlich, T. Garvey,

U. Gensch, Ch. Gerth, M. Görler, N. Golubeva, H.-J. Grabosch, M. Grecki, O. Grimm, K. Hacker, U. Hahn, J. H. Han, K. Honkavaara, T. Hott, M. Hüning, Y. Ivanisenko, E. Jaeschke, W. Jalmuzna, T. Jezynski, R. Kammering, V. Katalev, K. Kavanagh, E. T. Kennedy, S. Khodyachykh, K. Klose, V. Kocharyan, M. Körfer, M. Kollewe, W. Koprek, S. Korepanov, D. Kostin, M. Krassilnikov, G. Kube, M. Kuhlmann, C. L. S. Lewis, L. Lilje, T. Limberg, D. Lipka, F. Löhl, H. Luna, M. Luong, M. Martins, M. Meyer, P. Michelato, V. Miltchev, W. D. Möller, L. Monaco, W. F. O. Müller, O. Napieralski, O. Napoly, P. Nicolosi, D. Nölle, T. Nuñez, A. Oppelt, C. Pagani, R. Paparella, N. Pchalek, J. Pedregosa-Gutierrez, B. Petersen, B. Petrosyan, G. Petrosyan, L. Petrosyan, J. Pflüger, E. Plönjes, L. Poletto, K. Pozniak, E. Prat, D. Proch, P. Pucyk, P. Radcliffe, H. Redlin, K. Rehlich, M. Richter, M. Roehrs, J. Roensch, R. Romaniuk, M. Ross, J. Rossbach, V. Rybnikov, M. Sachwitz, E. L. Saldin, W. Sandner, H. Schlarb, B. Schmidt, M. Schmitz, P. Schmüser, J. R. Schneider, E. A. Schneidmiller, S. Schnepp, S. Schreiber, M. Seidel, D. Sertore, A. V. Shabunov, C. Simon, S. Simrock, E. Sombrowski, A. A. Sorokin, P. Spanknebel, R. Spesyvtsev, L. Staykov, B. Steffen, F. Stephan, F. Stulle, H. Thom, K. Tiedtke, M. Tischer, S. Toleikis, R. Treusch, D. Trines, I. Tsakov, E. Vogel, T. Weiland, H. Weise, M. Wellhöfer, M. Wendt, I. Will, A. Winter, K. Wittenburg, W. Wurth, P. Yeates, M. V. Yurkov, I. Zagorodnov, and K. Zapfe. Operation of a free-electron laser from the extreme ultraviolet to the water window. *Nature Photonics*, 1(6):336–342, June 2007.

[20] Stephan Hüfner. *Photoelectron Spectroscopy: Principles and Applications*. Springer Science & Business Media, March 2013.

[21] M. P Seah, I. S Gilmore, and S. J Spencer. Quantitative XPS: I. Analysis of X-ray photoelectron intensities from elemental data in a digital photoelectron database. *Journal of Electron Spectroscopy and Related Phenomena*, 120(1–3):93–111, October 2001.

[22] Kai Siegbahn. Electron spectroscopy for atoms, molecules and condensed matter-an overview. *Journal of electron spectroscopy and related phenomena*, 36(2):113–129, 1985.

[23] A. Einstein. Über einen die Erzeugung und Verwandlung des Lichtes betreffenden heuristischen Gesichtspunkt. *Annalen der Physik*, 322(6):132–148, January 1905.

[24] A. R. Williams and N. D. Lang. Core-Level Binding-Energy Shifts in Metals. *Physical Review Letters*, 40(14):954–957, April 1978.

[25] J. B. Pendry. Theory of photoemission. *Surface Science*, 57(2):679–705, 1976.

[26] C.-H. Zhang and U. Thumm. Streaking and Wigner time delays in photoemission from atoms and surfaces. *Physical Review A*, 84(3), September 2011.

[27] S. Nagele, R. Pazourek, J. Feist, and J. Burgdörfer. Time shifts in photoemission from a fully correlated two-electron model system. *Physical Review A*, 85(3), March 2012.

[28] C. Lemell, S. Neppl, G. Wachter, K. Tőkési, R. Ernstorfer, P. Feulner, R. Kienberger, and J. Burgdörfer. Real-time observation of collective excitations in photoemission. *Physical Review B*, 91(24), June 2015.

[29] E. E. Krasovskii, C. Friedrich, W. Schattke, and P. M. Echenique. Rapid propagation of a Bloch wave packet excited by a femtosecond ultraviolet pulse. *Physical Review B*, 94(19), November 2016.

[30] R. Haight, J. Bokor, J. Stark, R_H Storz, R. R. Freeman, and P. H. Bucksbaum. Picosecond time-resolved photoemission study of the InP (110) surface. *Physical review letters*, 54(12):1302, 1985.

[31] J. Bokor. Ultrafast dynamics at semiconductor and metal surfaces. *Science*, 246(4934):1130–1134, 1989.

[32] Richard Haight. Electron dynamics at surfaces. *Surface Science Reports*, 21(8):275–325, January 1995.

[33] Michael Bauer. Femtosecond ultraviolet photoelectron spectroscopy of ultra-fast surface processes. *Journal of Physics D: Applied Physics*, 38(16):R253–R267, August 2005.

[34] A Pietzsch, A Föhlisch, M Beye, M Deppe, F Hennies, M Nagasono, E Suljoti, W Wurth, C Gahl, K Döbrich, and A Melnikov. Towards time resolved core level photoelectron spectroscopy with femtosecond x-ray free-electron lasers. *New Journal of Physics*, 10(3):033004, March 2008.

[35] M. Dell'Angela, T. Anniyev, M. Beye, R. Coffee, A. Foehlisch, J. Gladh, S. Kaya, T. Katayama, O. Krupin, A. Nilsson, D. Nordlund, W. F. Schlotter, J. A. Sellberg, F. Sorgenfrei, J. J. Turner, H. Ostrom, H. Ogasawara, M. Wolf, and W. Wurth. Vacuum space charge effects in sub-picosecond soft X-ray photoemission on a molecular adsorbate layer. *Structural Dynamics-Us*, 2(2), March 2015. WOS:000354994100009.

[36] M. Dell'Angela, F. Hieke, F. Sorgenfrei, N. Gerken, M. Beye, N. Gerasimova, H. Redlin, and W. Wurth. Ultrafast surface dynamics probed with time resolved photoemission. *Surface Science*, 643:197–202, January 2016.

[37] Zhensheng Tao, Cong Chen, Tibor Szilvási, Mark Keller, Manos Mavrikakis, Henry Kapteyn, and Margaret Murnane. Direct time-domain observation of attosecond final-state lifetimes in photoemission from solids. *Science*, 353(6294):62–67, July 2016.

[38] Renate Pazourek, Stefan Nagele, and Joachim Burgdörfer. Attosecond chronoscopy of photoemission. *Reviews of Modern Physics*, 87(3):765–802, August 2015.

[39] Terry L. Gilton, James P. Cowin, Glenn D. Kubiak, and Alex V. Hamza. Intense surface photoemission: Space charge effects and self-acceleration. *Journal of Applied Physics*, 68(9):4802, 1990.

[40] C. Girardeau-Montaut and J. P. Girardeau-Montaut. Space-charge effect on the energy spectrum of photoelectrons produced by high-intensity short-duration laser pulses on a metal. *Physical Review A*, 44(2):1409, 1991.

[41] S. Passlack, S. Mathias, O. Andreyev, D. Mittnacht, M. Aeschlimann, and M. Bauer. Space charge effects in photoemission with a low repetition, high intensity femtosecond laser source. *Journal of Applied Physics*, 100(2):024912, July 2006.

[42] J. Graf, S. Hellmann, C. Jozwiak, C. L. Smallwood, Z. Hussain, R. A. Kaindl, L. Kipp, K. Rossnagel, and A. Lanzara. Vacuum space charge effect in laser-based solid-state photoemission spectroscopy. *Journal of Applied Physics*, 107(1):014912, 2010.

[43] Dominik Leuenberger, Hirofumi Yanagisawa, Silvan Roth, Jürg Osterwalder, and Matthias Hengsberger. Disentanglement of electron dynamics and space-charge effects in time-resolved photoemission from h -BN/Ni(111). *Physical Review B*, 84(12), September 2011.

[44] X.J. Zhou, B. Wannberg, W.L. Yang, V. Brouet, Z. Sun, J.F. Douglas, D. Dessau, Z. Hussain, and Z.-X. Shen. Space charge effect and mirror charge effect in photoemission spectroscopy. *Journal of Electron Spectroscopy and Related Phenomena*, 142(1):27–38, January 2005.

[45] L. Miaja-Avila, C. Lei, M. Aeschlimann, J. L. Gland, M. M. Murnane, H. C. Kapteyn, and G. Saathoff. Laser-Assisted Photoelectric Effect from Surfaces. *Physical Review Letters*, 97(11), September 2006.

[46] M. Plötzing, R. Adam, C. Weier, L. Plucinski, S. Eich, S. Emmerich, M. Rollinger, M. Aeschlimann, S. Mathias, and C. M. Schneider. Spin-resolved photoelectron spectroscopy using femtosecond extreme ultraviolet light pulses from high-order harmonic generation. *Review of Scientific Instruments*, 87(4):043903, April 2016.

[47] S Hellmann, C Sohrt, M Beye, T Rohwer, F Sorgenfrei, M Marczynski-Bühlow, M Kalläne, H Redlin, F Hennies, M Bauer, A Föhlisch, L Kipp, W Wurth, and K Rossnagel. Time-resolved x-ray photoelectron spectroscopy at FLASH. *New Journal of Physics*, 14(1):013062, January 2012.

[48] A Fognini, G Salvatella, T U Michlmayr, C Wetli, U Ramsperger, T Bähler, F Sorgenfrei, M Beye, A Eschenlohr, N Pontius, C Stamm, F Hieke, M Dell'Angela, S de Jong, R Kukreja, N Gerasimova, V Rybnikov, H Redlin, J Raabe, A Föhlisch, H A Dürr, W Wurth, D Pescia, A Vaterlaus, and Y Acremann. The role of space charge in spin-resolved photoemission experiments. *New Journal of Physics*, 16(4):043031, April 2014.

[49] S. Hellmann, K. Rossnagel, M. Marczynski-Bühlow, and L. Kipp. Vacuum space-charge effects in solid-state photoemission. *Physical Review B*, 79(3), January 2009.

[50] Adriano Verna, Giorgia Greco, Valerio Lollobrigida, Francesco Offi, and Giovanni Stefani. Space-charge effects in high-energy photoemission. *Journal of Electron Spectroscopy and Related Phenomena*, 209:14–25, May 2016.

[51] Burton L. Henke, Jerel A. Smith, and David T. Attwood. 0.1–10-keV x-ray-induced electron emissions from solids—Models and secondary electron measurements. *Journal of Applied Physics*, 48(5):1852, 1977.

[52] G. Schönhense, K. Medjanik, C. Tusche, M. de Loos, B. van der Geer, M. Scholz, F. Hieke, N. Gerken, J. Kirschner, and W. Wurth. Correction of the deterministic part of space–charge interaction in momentum microscopy of charged particles. *Ultramicroscopy*, 159:488–496, December 2015.

[53] L.-P. Oloff, K. Hanff, A. Stange, G. Rohde, F. Diekmann, M. Bauer, and K. Rossnagel. Pump laser-induced space-charge effects in HHG-driven time- and angle-resolved photoelectron spectroscopy. *Journal of Applied Physics*, 119(22):225106, June 2016.

[54] L-P Oloff, M Oura, K Rossnagel, A Chainani, M Matsunami, R Eguchi, T Kiss, Y Nakatani, T Yamaguchi, J Miyawaki, M Taguchi, K Yamagami, T Togashi, T Katayama, K Ogawa, M Yabashi, and T Ishikawa. Time-resolved HAXPES at SACLA: probe and pump pulse-induced space-charge effects. *New Journal of Physics*, 16(12):123045, December 2014.

[55] Søren Ulstrup, Jens Christian Johannsen, Federico Cilento, Alberto Crepaldi, Jill A. Miwa, Michele Zacchigna, Cephise Cacho, Richard T. Chapman, Emma Springate, Felix Fromm, Christian Raidel, Thomas Seyller, Phil D. C. King, Fulvio Parmigiani, Marco Grioni, and Philip Hofmann. Ramifications of optical pumping on the interpretation of time-resolved photoemission experiments on graphene. *Journal of Electron Spectroscopy and Related Phenomena*, 200:340–346, April 2015.

[56] Lars-Philip Oloff, Ashish Chainani, Masaharu Matsunami, Kazutoshi Takahashi, Tadashi Togashi, Hitoshi Osawa, Kerstin Hanff, Arndt Quer, Ryuki Matsushita, Ryutaro Shiraishi, Maki Nagashima, Ayato Kimura, Kotaro Matsuishi, Makina Yabashi, Yoshihito Tanaka, Giorgio Rossi, Tetsuya Ishikawa, Kai Rossnagel, and Masaki Oura. Time-resolved HAXPES using a microfocused XFEL beam: From vacuum space-charge effects to intrinsic charge-carrier recombination dynamics. *Scientific Reports*, 6, October 2016.

[57] V. Ayvazyan, N. Baboi, J. Bähr, V. Balandin, B. Beutner, A. Brandt, I. Bohnet, A. Bolzmann, R. Brinkmann, O. I. Brovko, J. P. Carneiro, S. Casalbuoni, M. Castellano, P. Castro, L. Catani, E. Chiadroni, S. Choroba, A. Cianchi, H. Delsim-Hashemi, G. Di Pirro, M. Dohlus, S. Düsterer, H. T. Edwards, B. Faatz, A. A. Fateev, J. Feldhaus, K. Flöttmann, J. Frisch, L. Fröhlich, T. Garvey, U. Gensch, N. Golubeva, H.-J. Grabosch, B. Grigoryan, O. Grimm, U. Hahn, J. H. Han, M. V. Hartrott, K. Honkavaara, M. Hüning, R. Ischebeck, E. Jaeschke, M. Jablonka, R. Kammering, V. Katalev, B. Keitel, S. Khodyachykh, Y. Kim, V. Kocharyan,

M. Körfer, M. Kollewe, D. Kostin, D. Krämer, M. Krassilnikov, G. Kube, L. Lilje, T. Limberg, D. Lipka, F. Löhl, M. Luong, C. Magne, J. Menzel, P. Michelato, V. Miltchev, M. Minty, W. D. Möller, L. Monaco, W. Müller, M. Nagl, O. Napoly, P. Nicolosi, D. Nölle, T. Nuñez, A. Oppelt, C. Pagani, R. Paparella, B. Petersen, B. Petrosyan, J. Pflüger, P. Piot, E. Plönjes, L. Poletto, D. Proch, D. Pugachov, K. Rehlich, D. Richter, S. Riemann, M. Ross, J. Rossbach, M. Sachwitz, E. L. Saldin, W. Sandner, H. Schlarb, B. Schmidt, M. Schmitz, P. Schmüser, J. R. Schneider, E. A. Schneidmiller, H.-J. Schreiber, S. Schreiber, A. V. Shabunov, D. Sertore, S. Setzer, S. Simrock, E. Sombrowski, L. Staykov, B. Steffen, F. Stephan, F. Stulle, K. P. Sytchev, H. Thom, K. Tiedtke, M. Tischer, R. Treusch, D. Trines, I. Tsakov, A. Vardanyan, R. Wanzenberg, T. Weiland, H. Weise, M. Wendt, I. Will, A. Winter, K. Wittenburg, M. V. Yurkov, I. Zagorodnov, P. Zambolin, and K. Zapfe. First operation of a free-electron laser generating GW power radiation at 32 nm wavelength. *The European Physical Journal D*, 37(2):297–303, February 2006.

[58] E. L. Saldin, E. A. Šnejdmiller, and M. V. Yurkov. *The physics of free electron lasers*. Advanced texts in physics. Springer, Berlin [u.a.], 2000.

[59] Peter Schmüser, Martin Dohlus, and Jörg Roßbach. *Ultraviolet and soft X-ray free electron lasers: introduction to physical principles, experimental results, technological challenges*. Number 229 in Springer tracts in modern physics : Ergebnisse der exakten Naturwissenschaften. - Berlin : Springer, 1965-. Springer, Berlin [u.a.], 2008.

[60] Eberhard J. Jaeschke, Shaukat Khan, Jochen R. Schneider, and Jerome B. Hastings, editors. *Synchrotron Light Sources and Free-Electron Lasers*. Springer International Publishing, Cham, 2016.

[61] S. Düsterer, P. Radcliffe, G. Geloni, U. Jastrow, M. Kuhlmann, E. Plönjes, K. Tiedtke, R. Treusch, J. Feldhaus, P. Nicolosi, and others. Spectroscopic characterization of vacuum ultraviolet free electron laser pulses. *Optics letters*, 31(11):1750–1752, 2006.

[62] S. Duesterer, M. Rehders, A. Al-Shemmary, C. Behrens, G. Brenner, O. Brovko, M. DellAngela, M. Drescher, B. Faatz, J. Feldhaus, U. Fruehling, N. Gerasimova, N. Gerken, C. Gerth, T. Golz, A. Grebentsov, E. Hass, K. Honkavaara, V. Kocharian, M. Kurka, Th Limberg, R. Mitzner, R. Moshammer, E. Ploenjes, M. Richter, J. Roensch-Schulenburg, A. Rudenko, H. Schlarb, B. Schmidt, A. Senftleben, E. A. Schneidmiller, B. Siemer, F. Sorgenfrei, A. A. Sorokin, N. Stojanovic, K. Tiedtke, R. Treusch, M. Vogt, M. Wieland, W. Wurth, S. Wesch, M. Yan, M. V. Yurkov, H. Zacharias, and S. Schreiber. Development of experimental techniques for the characterization of ultrashort photon pulses of extreme ultraviolet free-electron lasers. *Physical Review Special Topics-Accelerators and Beams*, 17(12):120702, December 2014. WOS:000346437200001.

[63] M Wellhöfer, M Martins, W Wurth, A A Sorokin, and M Richter. Performance of the

monochromator beamline at FLASH. *Journal of Optics A: Pure and Applied Optics*, 9(7):749–756, July 2007.

[64] Natalia Gerasimova, Siarhei Dziarzhytski, and Josef Feldhaus. The monochromator beamline at FLASH: performance, capabilities and upgrade plans. *Journal of Modern Optics*, 58(16):1480–1485, September 2011.

[65] Florian Sorgenfrei. *Time-resolved jitter-free experiments at FLASH: from longitudinal coherence studies to nonlinear dynamics*. PhD thesis, Dr. Hut, München, 2013.

[66] A. Agababyan, G. Grygiel, B. Fominykh, O. Hensler, R. Kammering, K. Rehlich, V. Rybnikov, L. Petrosyan, G. Asova, G. Dimitrov, and others. The Data Acquisition system (DAQ) of the FLASH facility. In *11th International Conference On Accelerator And Large Experimental Physics Control Systems (ICALEPCS 2007)*, pages 564–566, 2007.

[67] A. Agababyan, G. Grygiel, O. Hensler, R. Kammering, V. Kocharyan, L. Petrosyan, and K. Rehlich. EVOLUTION OF THE FLASH DAQ SYSTEM. In *12th International Conference On Accelerator And Large Experimental Physics Control Systems (ICALEPCS 2009)*, 2009.

[68] B. L. Henke, E. M. Gullikson, and J. C. Davis. X-Ray Interactions: Photoabsorption, Scattering, Transmission, and Reflection at E = 50-30,000 eV, Z = 1-92. *Atomic Data and Nuclear Data Tables*, 54(2):181–342, July 1993.

[69] Jagdeep Shah. *Ultrafast Spectroscopy of Semiconductors and Semiconductor Nanostructures*. Springer Science & Business Media, November 2013.

[70] Arthur J. Nozik. Spectroscopy and hot electron relaxation dynamics in semiconductor quantum wells and quantum dots. *Annual review of physical chemistry*, 52(1):193–231, 2001.

[71] Fausto Rossi and Tilmann Kuhn. Theory of ultrafast phenomena in photoexcited semiconductors. *Reviews of Modern Physics*, 74(3):895, 2002.

[72] L. Wang, R. Long, D. Trivedi, and O.V. Prezhdo. Time-domain ab initio modeling of charge and exciton dynamics in nanomaterials. In *Green Processes for Nanotechnology: From Inorganic to Bioinspired Nanomaterials*, pages 353–392. Springer International Publishing, Cham, 2015. DOI: 10.1007/978-3-319-15461-9_13.

[73] N. Medvedev and B. Rethfeld. Transient dynamics of the electronic subsystem of semiconductors irradiated with an ultrashort vacuum ultraviolet laser pulse. *New Journal of Physics*, 12(7):073037, 2010.

[74] Beata Ziaja, David van der Spoel, Abraham Szoeke, and Janos Hajdu. Auger-electron cascades in diamond and amorphous carbon. *Physical Review B*, 64(21), November 2001. arXiv: cond-mat/0109430.

[75] A. J. Sabbah and D. M. Riffe. Femtosecond pump-probe reflectivity study of silicon carrier dynamics. *Physical Review B*, 66(16), October 2002.

[76] S. S. Prabhu. Dynamics of the pump-probe reflectivity spectra in GaAs and GaN. *Journal of Applied Physics*, 95(12):7803, 2004.

[77] Theophilos Maltezopoulos, Stefan Cunovic, Marek Wieland, Martin Beye, Armin Azima, Harald Redlin, Maria Krikunova, Roland Kalms, Ulrike Frühling, Filip Budzyn, Wilfried Wurth, Alexander Föhlisch, and Markus Drescher. Single-shot timing measurement of extreme-ultraviolet free-electron laser pulses. *New Journal of Physics*, 10(3):033026, March 2008.

[78] S. Eckert, M. Beye, A. Pietzsch, W. Quevedo, M. Hantschmann, M. Ochmann, M. Ross, M. P. Minitti, J. J. Turner, S. P. Moeller, W. F. Schlotter, G. L. Dakovski, M. Khalil, N. Huse, and A. Föhlisch. Principles of femtosecond X-ray/optical cross-correlation with X-ray induced transient optical reflectivity in solids. *Applied Physics Letters*, 106(6):061104, February 2015.

[79] O. Krupin, M. Trigo, W. F. Schlotter, M. Beye, F. Sorgenfrei, J. J. Turner, D. A. Reis, N. Gerken, S. Lee, W. S. Lee, G. Hays, Y. Acremann, B. Abbey, R. Coffee, M. Messerschmidt, S. P. Hau-Riege, G. Lapertot, J. Lüning, P. Heimann, R. Soufli, M. Fernández-Perea, M. Rowen, M. Holmes, S. L. Molodtsov, A. Föhlisch, and W. Wurth. Temporal cross-correlation of x-ray free electron and optical lasers using soft x-ray pulse induced transient reflectivity. *Optics Express*, 20(10):11396, May 2012.

[80] Hans Lüth. *Solid Surfaces, Interfaces and Thin Films*. Graduate Texts in Physics. Springer International Publishing, Cham, 2015.

[81] Winfried Mönch. *Semiconductor surfaces and interfaces*. Number 26 in Springer series in surface sciences. - Berlin : Springer, 1985-. Springer, Berlin [u.a.], 3., rev. ed., [softcover version of original hardcover edition 2001]. edition, 2010.

[82] M. D. Pashley, K. W. Haberern, R. M. Feenstra, and P. D. Kirchner. Different Fermi-level pinning behavior on n-and p-type GaAs (001). *Physical Review B*, 48(7):4612, 1993.

[83] Leeor Kronik and Yoram Shapira. Surface photovoltage phenomena: theory, experiment, and applications. *Surface Science Reports*, 37(1):1–206, 1999.

[84] P. Siffalovic, M. Drescher, and U. Heinzmann. Femtosecond time-resolved core-level photoelectron spectroscopy tracking surface photovoltage transients on p–GaAs. *EPL (Europhysics Letters)*, 60(6):924, December 2002.

[85] Shin-ichiro Tanaka. Utility and constraint on the use of pump-probe photoelectron spectroscopy for detecting time-resolved surface photovoltage. *Journal of Electron Spectroscopy and Related Phenomena*, 185(5-7):152–158, August 2012.

[86] S.-L. Yang, J. A. Sobota, P. S. Kirchmann, and Z.-X. Shen. Electron propagation from a photo-excited surface: implications for time-resolved photoemission. *Applied Physics A*, 116(1):85–90, November 2013.

[87] T. Ichibayashi and K. Tanimura. Ultrafast Carrier Relaxation in Si Studied by Time-Resolved Two-Photon Photoemission Spectroscopy: Intravalley Scattering and Energy Relaxation of Hot Electrons. *Physical Review Letters*, 102(8), February 2009.

[88] Shinji Tokudomi, Junpei Azuma, Kazutoshi Takahashi, and Masao Kamada. Ultrafast Decay of Surface Photo-Voltage Effect on n-type GaAs(100) Surface. *Journal of the Physical Society of Japan*, 76(10):104710, October 2007.

[89] Shinji Tokudomi, Junpei Azuma, Kazutoshi Takahashi, and Masao Kamada. Ultrafast Time Dependence of Surface Photo-Voltage Effect on p -Type GaAs(100) Surface. *Journal of the Physical Society of Japan*, 77(1):014711, January 2008.

[90] DESY. FLASH Parameters, 2016.

[91] F. Sorgenfrei, W. F. Schlotter, T. Beeck, M. Nagasono, S. Gieschen, H. Meyer, A. Föhlisch, M. Beye, and W. Wurth. The extreme ultraviolet split and femtosecond delay unit at the plane grating monochromator beamline PG2 at FLASH. *Review of Scientific Instruments*, 81(4):043107, 2010.

[92] Michael Wellhöfer. *The Monochromator Beamline at FLASH Assembly, Characterization and first Experiments*. PhD thesis, Universität Hamburg, Hamburg, July 2007.

[93] K Tiedtke, A Azima, N von Bargen, L Bittner, S Bonfigt, S Düsterer, B Faatz, U Frühling, M Gensch, Ch Gerth, N Guerassimova, U Hahn, T Hans, M Hesse, K Honkavaar, U Jastrow, P Juranic, S Kapitzki, B Keitel, T Kracht, M Kuhlmann, W B Li, M Martins, T Núñez, E Plönjes, H Redlin, E L Saldin, E A Schneidmiller, J R Schneider, S Schreiber, N Stojanovic, F Tavella, S Toleikis, R Treusch, H Weigelt, M Wellhöfer, H Wabnitz, M V Yurkov, and J Feldhaus. The soft x-ray free-electron laser FLASH at DESY: beamlines, diagnostics and end-stations. *New Journal of Physics*, 11(2):023029, February 2009.

[94] Ulrich Hahn and Kai Tiedtke. The Gas Attenuator of FLASH at DESY. In *AIP Conference Proceedings*, volume 879, pages 276–282. AIP Publishing, January 2007.

[95] Lukas Wenthaus. Charakterisierung eines Elektronen Flugzeitspektrometers zur Photoelektronenspektroskopie, April 2013.

[96] Y. Itikawa, M. Hayashi, A. Ichimura, K. Onda, K. Sakimoto, K. Takayanagi, M. Nakamura, H. Nishimura, and T. Takayanagi. Cross Sections for Collisions of Electrons and Photons with Nitrogen Molecules. *Journal of Physical and Chemical Reference Data*, 15(3):985, 1986.

[97] John T. Wolan, William S. Epling, and Gar B. Hoflund. Characterization study of GaAs(001) surfaces using ion scattering spectroscopy and x-ray photoelectron spectroscopy. *Journal of Applied Physics*, 81(9):6160–6164, May 1997.

[98] R. Z. Bachrach. Surface phases of GaAs(100) and AlAs(100). *Journal of Vacuum Science and Technology*, 18(3):797, April 1981.

[99] A. D. Katnani. Core-level photoemission study of MBE-grown GaAs(111) and (100) surfaces. *Journal of Vacuum Science & Technology B: Microelectronics and Nanometer Structures*, 3(2):608, March 1985.

[100] P Pianetta, I Lindau, P. E Gregory, C. M Garner, and W. E Spicer. Valence band studies of clean and oxygen exposed GaAs(100) surfaces. *Surface Science*, 72(2):298–320, March 1978.

[101] Florian Hieke. *Pump-Probe Photoemissions Spektroskopie am Freie Elektronen Laser FLASH an Ir(111) Oberflächen-Rumpfniveaus*. Diplomarbeit, Universität Hamburg, February 2012.

[102] Klaus Floettmann. *A Space Charge Tracking Algorithm*. DESY, Hamburg, 3 edition, April 2014. The ASTRA program package can be downloaded free of charge for non-commercial and non-military use. Dissemination to third parties is illegal. DESY reserves copyrights and all rights for commercial use for the program package ASTRA, parts of the program package and of procedures developed for the program package. DESY undertakes no obligation for the maintenance of the program, nor responsibility for its correctness, and accepts no liability whatsoever resulting from its use.

[103] S. Palutke, N. C. Gerken, K. Mertens, S. Klumpp, A. Mozzanica, B. Schmitt, C. Wunderer, H. Graafsma, K.-H. Meiwes-Broer, W. Wurth, and M. Martins. Spectrometer for shot-to-shot photon energy characterization in the multi-bunch mode of the free electron laser at Hamburg. *Review of Scientific Instruments*, 86(11):113107, November 2015.

[104] S. Schulz, I. Grguraš, C. Behrens, H. Bromberger, J. T. Costello, M. K. Czwalinna, M. Felber, M. C. Hoffmann, M. Ilchen, H. Y. Liu, T. Mazza, M. Meyer, S. Pfeiffer, P. Prędki, S. Schefer, C. Schmidt, U. Wegner, H. Schlarb, and A. L. Cavalieri. Femtosecond all-optical synchronization of an X-ray free-electron laser. *Nature Communications*, 6:5938, January 2015.

[105] A. Leitenstorfer, S. Hunsche, J. Shah, M. C. Nuss, and W. H. Knox. Femtosecond charge transport in polar semiconductors. *Physical review letters*, 82(25):5140, 1999.

[106] Matthew C. Beard, Gordon M. Turner, and Charles A. Schmuttenmaer. Transient photoconductivity in GaAs as measured by time-resolved terahertz spectroscopy. *Physical Review B*, 62(23):15764, 2000.

[107] J. A. Kash, J. C. Tsang, and J. M. Hvam. Subpicosecond time-resolved Raman spectroscopy of LO phonons in GaAs. *Physical review letters*, 54(19):2151, 1985.

[108] G. Strinati. Effects of dynamical screening on resonances at inner-shell thresholds in semiconductors. *Physical Review B*, 29(10):5718, 1984.

[109] Adolfo Avella and Ferdinando Mancini, editors. *Strongly Correlated Systems*, volume 180 of *Springer Series in Solid-State Sciences*. Springer Berlin Heidelberg, Berlin, Heidelberg, 2015.

[110] Gabriel Kotliar and Dieter Vollhardt. Strongly correlated materials: Insights from dynamical mean-field theory. *Physics Today*, 57(3):53–60, 2004.

[111] E. J. W. Verwey. Electronic Conduction of Magnetite (Fe3o4) and its Transition Point at Low Temperatures. *Nature*, 144:327–328, August 1939.

[112] Friedrich Walz. The Verwey transition - a topical review. *Journal of Physics: Condensed Matter*, 14(12):R285, 2002.

[113] Mark S. Senn, Jon P. Wright, and J. Paul Attfield. Charge order and three-site distortions in the Verwey structure of magnetite. *Nature*, 481(7380):173–176, January 2012.

[114] Rochelle M. Cornell and Udo Schwertmann. *The Iron Oxides: Structure, Properties, Reactions, Occurences and Uses*. Wiley-VCH, Weinheim, 2nd, completely revised and extended ed. edition, 2003.

[115] Victor Antonov, Bruce Harmon, and Alexander Yaresko. *Electronic structure and magneto-optical properties of solids*. Kluwer Academic Publishers, Dordrecht; Boston, 2004. OCLC: 55201413.

[116] Joaquín García and Gloria Subías. The Verwey transition—a new perspective. *Journal of Physics: Condensed Matter*, 16(7):R145, 2004.

[117] J. P. Attfield. The Verwey Phase of Magnetite: A Long-Running Mystery in Ferrites. *??????????*, 61(S1):S43–S48, 2014.

[118] M. Iizumi and G. Shirane. Crystal symmetry of the low temperature phase of magnetite. *Solid State Communications*, 17(4):433–436, August 1975.

[119] J. Paul Attfield. Orbital molecules in electronic materials. *APL Materials*, 3(4):041510, April 2015.

[120] E. J. Verwey, P. W. Haayman, and F. C. Romeijn. Physical Properties and Cation Arrangement of Oxides with Spinel Structures II. Electronic Conductivity. *The Journal of Chemical Physics*, 15(4):181–187, April 1947.

[121] Jon P. Wright, J. Paul Attfield, and Paolo G. Radaelli. Charge ordered structure of magnetite Fe 3 O 4 below the Verwey transition. *Physical Review B*, 66(21), December 2002.

[122] Javier Blasco, Joaquín García, and Gloria Subías. Structural transformation in magnetite below the Verwey transition. *Physical Review B*, 83(10), March 2011.

[123] Mark S. Senn, Jon P. Wright, James Cumby, and J. Paul Attfield. Charge localization in the Verwey structure of magnetite. *Physical Review B*, 92(2), July 2015.

[124] G. Perversi, J. Cumby, E. Pachoud, J. P. Wright, and J. P. Attfield. The Verwey structure of a natural magnetite. *Chemical Communications*, 52(27):4864–4867, March 2016.

[125] Keisuke Shibuya, Masashi Kawasaki, and Yoshinori Tokura. Metal-insulator transitions in TiO 2 / VO 2 superlattices. *Physical Review B*, 82(20), November 2010.

[126] Mark Stephen Senn. *Charge, orbital and magnetic ordering in transition metal oxides*. PhD thesis, University of Edinburgh, Edinburgh, June 2013.

[127] G. A. Samara and A. A. Giardini. Effect of Pressure on the N\'eel Temperature of Magnetite. *Physical Review*, 186(2):577–580, October 1969.

[128] T. Koide, T. Shidara, H. Fukutani, K. Yamaguchi, A. Fujimori, and S. Kimura. Strong magnetic circular dichroism at the M 2, 3 edges in ferromagnetic Ni and ferrimagnetic Fe 3 O 4. *Physical Review B*, 44(9):4697, 1991.

[129] Tsuneharu Koide, Tetsuo Shidara, Katsuhiko Ymaguchi, Atsushi Fujimori, Hirohito Fukutani, Noboru Kimizuka, and Shigeyuki Kimura. Core-level magnetic circular dichroism in Fe3o4 and CoFe2o4. *Journal of Electron Spectroscopy and Related Phenomena*, 78:275–278, May 1996.

[130] N. F. Mott. Materials with mixed valency that show a verwey transition. *Philosophical Magazine Part B*, 42(3):327–335, September 1980.

[131] D. Ihle and B. Lorenz. Small-polaron conduction and short-range order in Fe 3 O 4. *Journal of Physics C: Solid State Physics*, 19(26):5239, 1986.

[132] N. Pontius, T. Kachel, C. Schüßler-Langeheine, W. F. Schlotter, M. Beye, F. Sorgenfrei, C. F. Chang, A. Föhlisch, W. Wurth, P. Metcalf, I. Leonov, A. Yaresko, N. Stojanovic, M. Berglund, N. Guerassimova, S. Düsterer, H. Redlin, and H. A. Dürr. Time-resolved resonant soft x-ray diffraction with free-electron lasers: Femtosecond dynamics across the Verwey transition in magnetite. *Applied Physics Letters*, 98(18):182504, 2011.

[133] F. Randi, I. Vergara, F. Novelli, M. Esposito, M. Dell'Angela, V. A. M. Brabers, P. Metcalf, R. Kukreja, H. A. Dürr, D. Fausti, M. Grüninger, and F. Parmigiani. Phase separation in the nonequilibrium Verwey transition in magnetite. *Physical Review B*, 93(5), February 2016.

[134] Simone Borroni, Edoardo Baldini, Andreas Mann, Christopher Arrell, Frank van Mourik, Jérémie Teyssier, José Lorenzana, and Fabrizio Carbone. On the Verwey transition in magnetite: the soft modes of the metal-insulator transition. *arXiv preprint arXiv:1507.07193*, 2015.

[135] Faris Gel'mukhanov and Hans Ågren. Resonant X-ray Raman scattering. *Physics Reports*, 312(3–6):87–330, May 1999.

[136] Frank de Groot and Akio Kotani. *Core Level Spectroscopy of Solids*. CRC Press, March 2008. Google-Books-ID: HGHzu66i1yoC.

[137] Franz Hennies. *Resonant Inelastic X-ray Scattering at Small Hydrocarbon Molecules: Scattering Dynamics and Bonding to Silicon*. PhD thesis, Dr. Hut, München, 2006.

[138] Martin Beye. *Ultrafast dynamics in solids studied with soft X-rays*. PhD thesis, Verl. Dr. Hut, München, 2010.

[139] G. Ghiringhelli, A. Piazzalunga, X. Wang, A. Bendounan, H. Berger, F. Bottegoni, N. Christensen, C. Dallera, M. Grioni, J.-C. Grivel, M. Moretti Sala, L. Patthey, J. Schlappa, T. Schmitt, V. Strocov, and L. Braicovich. Crystal field and low energy excitations measured by high resolution RIXS at the L3 edge of Cu, Ni and Mn. *The European Physical Journal Special Topics*, 169(1):199–205, March 2009.

[140] M Moretti Sala, V Bisogni, C Aruta, G Balestrino, H Berger, N B Brookes, G M de Luca, D Di Castro, M Grioni, M Guarise, P G Medaglia, F Miletto Granozio, M Minola, P Perna, M Radovic, M Salluzzo, T Schmitt, K J Zhou, L Braicovich, and G Ghiringhelli. Energy and symmetry of dd excitations in undoped layered cuprates measured by Cu L_3 resonant inelastic x-ray scattering. *New Journal of Physics*, 13(4):043026, April 2011.

[141] S Huotari, L Simonelli, C J Sahle, M Moretti Sala, R Verbeni, and G Monaco. Temperature dependence of crystal field excitations in CuO. *Journal of Physics: Condensed Matter*, 26(16):165501, April 2014.

[142] Jungho Kim, M. Daghofer, A. H. Said, T. Gog, J. van den Brink, G. Khaliullin, and B. J. Kim. Excitonic quasiparticles in a spin–orbit Mott insulator. *Nature Communications*, 5, July 2014.

[143] L. Andrew Wray, Shih-Wen Huang, Yuqi Xia, M. Zahid Hasan, Charles Mathy, Hiroshi Eisaki, Zahid Hussain, and Yi-De Chuang. Experimental signatures of phase interference and subfemtosecond time dynamics on the incident energy axis of resonant inelastic x-ray scattering. *Physical Review B*, 91(3), January 2015.

[144] M. Beye, Ph. Wernet, C. Schüßler-Langeheine, and A. Föhlisch. Time resolved resonant inelastic X-ray scattering: A supreme tool to understand dynamics in solids and molecules. *Journal of Electron Spectroscopy and Related Phenomena*, 188:172–182, June 2013.

[145] P. Glatzel, M. Sikora, and M. Fernández-García. Resonant X-ray spectroscopy to study K absorption pre-edges in 3d transition metal compounds. *The European Physical Journal Special Topics*, 169(1):207–214, March 2009.

[146] H. A. Kramers and W. Heisenberg. Über die Streuung von Strahlung durch Atome. *Zeitschrift für Physik*, 31(1):681–708, January 1924.

[147] Akio Kotani and Shik Shin. Resonant inelastic x-ray scattering spectra for electrons in solids. *Reviews of Modern Physics*, 73(1):203, 2001.

[148] A. Schlegel, S. F. Alvarado, and P. Wachter. Optical properties of magnetite (Fe3o4). *Journal of Physics C: Solid State Physics*, 12(6):1157, 1979.

[149] F. M. F. De Groot, Pieter Kuiper, and G. A. Sawatzky. Local spin-flip spectral distribution obtained by resonant x-ray Raman scattering. *Physical Review B*, 57(23):14584, 1998.

[150] S. G. Chiuzbăian, G. Ghiringhelli, C. Dallera, M. Grioni, P. Amann, X. Wang, L. Braicovich, and L. Patthey. Localized Electronic Excitations in NiO Studied with Resonant Inelastic X-Ray Scattering at the Ni M Threshold: Evidence of Spin Flip. *Physical Review Letters*, 95(19), October 2005.

[151] Michel van Veenendaal. Polarization Dependence of L - and M -Edge Resonant Inelastic X-Ray Scattering in Transition-Metal Compounds. *Physical Review Letters*, 96(11), March 2006.

[152] Robert Duane Cowan. *The theory of atomic structure and spectra*. Los Alamos series in basic and applied sciences. - Berkeley, Calif. [u.a.] : Univ. of California Press, 1979- ; [3]. Univ. of California Press, Berkeley, Calif. [u.a.], 1981.

[153] Alessandro Mirone, Maurizio Sacchi, and Susana Gota. Ligand-field atomic-multiplet calculations for arbitrary symmetry. *Physical Review B*, 61(20):13540, 2000.

[154] Eli Stavitski and Frank M. F. de Groot. The CTM4xas program for EELS and XAS spectral shape analysis of transition metal L edges. *Micron*, 41(7):687–694, October 2010.

[155] L. Andrew Wray, Wanli Yang, Hiroshi Eisaki, Zahid Hussain, and Yi-De Chuang. Multiplet resonance lifetimes in resonant inelastic x-ray scattering involving shallow core levels. *Physical Review B*, 86(19), November 2012.

[156] L. Andrew Wray, J. Li, Z. Q. Qiu, Jinsheng Wen, Zhijun Xu, Genda Gu, Shih-Wen Huang, Elke Arenholz, Wanli Yang, Zahid Hussain, and Yi-De Chuang. Measurement of the spectral line shapes for orbital excitations in the Mott insulator CoO using high-resolution resonant inelastic x-ray scattering. *Physical Review B*, 88(3), July 2013.

[157] Takami Tohyama. Resonant inelastic X-ray scattering in strongly correlated electron systems. *Journal of Electron Spectroscopy and Related Phenomena*, 200:209–215, April 2015.

[158] Mohammad Soltanieh-ha. *Interplay Between Charge, Spin, and Phonons in Low Dimensional Strongly Interacting Systems*. PhD thesis, Northeastern University, 2015.

[159] Steve Johnston, Claude Monney, Valentina Bisogni, Ke-Jin Zhou, Roberto Kraus, Günter Behr, Vladimir N. Strocov, Jiři Málek, Stefan-Ludwig Drechsler, Jochen Geck, Thorsten Schmitt, and Jeroen van den Brink. Electron-lattice interactions strongly renormalize the charge-transfer energy in the spin-chain cuprate Li2cuo2. *Nature Communications*, 7:10563, February 2016.

[160] J. J. Lee, B. Moritz, W. S. Lee, M. Yi, C. J. Jia, A. P. Sorini, K. Kudo, Y. Koike, K. J. Zhou, C. Monney, V. Strocov, L. Patthey, T. Schmitt, T. P. Devereaux, and Z. X. Shen. Charge-orbital-lattice coupling effects in the d d excitation profile of one-dimensional cuprates. *Physical Review B*, 89(4), January 2014.

[161] L. Andrew Wray, Shih-Wen Huang, Ignace Jarrige, Kazuhiko Ikeuchi, Kenji Ishii, Jia Li, Z. Q. Qiu, Zahid Hussain, and Yi-De Chuang. Extending resonant inelastic X-ray scattering to the extreme ultraviolet. *Condensed Matter Physics*, 3:32, 2015.

[162] S. G. Chiuzbăian, T. Schmitt, M. Matsubara, A. Kotani, G. Ghiringhelli, C. Dallera, A. Tagliaferri, L. Braicovich, V. Scagnoli, N. B. Brookes, U. Staub, and L. Patthey. Combining M - and L -edge resonant inelastic x-ray scattering for studies of 3 d transition metal compounds. *Physical Review B*, 78(24), December 2008.

[163] Yi-De Chuang, John Pepper, Wayne McKinney, Zahid Hussain, Eric Gullikson, Phil Batson, Dong Qian, and M. Zahid Hasan. High-resolution soft X-ray emission spectrograph at advanced light source. *Journal of Physics and Chemistry of Solids*, 66(12):2173–2178, December 2005.

[164] Pieter Kuiper, J.-H. Guo, Conny S\a athe, L.-C. Duda, Joseph Nordgren, J. J. M. Pothuizen, F. M. F. De Groot, and George A. Sawatzky. Resonant X-ray Raman spectra of Cu dd excitations in Sr 2 CuO 2 Cl 2. *Physical review letters*, 80(23):5204, 1998.

[165] ChmistryLibreTexts. Chemistry Libre Texts: XANES: Theory, October 2013.

[166] Ruben Reininger, John Bozek, Yi-De Chuang, Malcolm Howells, Nicholas Kelez, Soren Prestemon, Steve Marks, Tony Warwick, Chris Jozwiak, Alessandra Lanzara, M. Zahid Hasan, and Zahid Hussain. MERLIN — A meV Resolution Beamline at the ALS. In *AIP Conf. Proc.*, volume 879, pages 509–512. AIP, 2007.

[167] Derek Degian, Jonathan Denlinger, and Keith Franck. Mechanical Engineering Design Review BL ARPES Endstation Derek Yegian, Jonathan Denlinger, Keith Franck 4/18/ ppt download, April 2008.

[168] C. F. Hague, J. H. Underwood, A. Avila, R. Delaunay, H. Ringuenet, M. Marsi, and M. Sacchi. Plane-grating flat-field soft x-ray spectrometer. *Review of Scientific Instruments*, 76(2):023110, 2005.

[169] Tom Miller. Engineering Division 1 MERLIN RIXS Endstation Design Review Tom Miller 6-30-08 90 Deg Scatter Back Scatter (proposed) Forward Scatter (proposed) Sample. - ppt download, June 2008.

[170] Yi-De Chuang, L. Andrew Wray, Jonathan Denlinger, and Zahid Hussain. Resonant Inelastic X-ray Scattering Spectroscopy at MERLIN Beamline at the Advanced Light Source. *Synchrotron Radiation News*, 25(4):23–28, July 2012.

[171] Florian Hieke and Yi-De Chuang. E-Mail Correspondence: Question to MERIXS beamline, April 2016.

[172] A. J. M. Kuipers and V. A. M. Brabers. Thermoelectric properties of magnetite at the Verwey transition. *Physical Review B*, 14(4):1401–1405, August 1976.

[173] Federico Cilento, Claudio Giannetti, Gabriele Ferrini, Stefano Dal Conte, Tommaso Sala, Giacomo Coslovich, Matteo Rini, Andrea Cavalleri, and Fulvio Parmigiani. Ultrafast insulator-to-metal phase transition as a switch to measure the spectrogram of a supercontinuum light pulse. *Applied Physics Letters*, 96(2):021102, 2010.

[174] S. Dal Conte, C. Giannetti, G. Coslovich, F. Cilento, D. Bossini, T. Abebaw, F. Banfi, G. Ferrini, H. Eisaki, M. Greven, A. Damascelli, D. van der Marel, and F. Parmigiani. Disentangling the Electronic and Phononic Glue in a High-Tc Superconductor. *Science*, 335(6076):1600–1603, March 2012.

[175] Federico Cilento, STEFANO Dal Conte, GIACOMO Coslovich, Francesco Banfi, Gabriele Ferrini, Hiroshi Eisaki, Martin Greven, Andrea Damascelli, Dirk Van Der Marel, Fulvio Parmigiani, and others. In search for the pairing glue in cuprates by non-equilibrium optical spectroscopy. In *Journal of Physics: Conference Series*, volume 449, page 012003. IOP Publishing, 2013.

[176] Federico Cilento. *Dinamiche Elettroniche Fotoindotte in Superconduttori ad Alta Temperatura Critica*. Brescia, 2007.

[177] Jinendra K. Ranka, Robert S. Windeler, and Andrew J. Stentz. Visible continuum generation in air–silica microstructure optical fibers with anomalous dispersion at 800 nm. *Optics letters*, 25(1):25–27, 2000.

[178] H. Magnan, P. Le Fèvre, D. Chandesris, P. Krüger, S. Bourgeois, B. Domenichini, A. Verdini, L. Floreano, and A. Morgante. Resonant photoelectron and photoelectron diffraction across the Fe L3 edge of Fe3o4. *Physical Review B*, 81(8):085121, February 2010.

[179] Martina Dell'Angela. Group Seminar Presentation: ALS Beamtime Preparation, June 2014.

[180] J. N. Hancock, G. Chabot-Couture, and M. Greven. Lattice coupling and Franck–Condon effects in K-edge resonant inelastic x-ray scattering. *New Journal of Physics*, 12(3):033001, 2010.

[181] H. Y. Huang, Z. Y. Chen, R.-P. Wang, F. M. F. de Groot, W. B. Wu, J. Okamoto, A. Chainani, J.-S. Zhou, H.-T. Jeng, G. Y. Guo, Je-Geun Park, L. H. Tjeng, C. T. Chen, and D. J. Huang. Jahn-Teller distortion driven magnetic polarons in magnetite. *arXiv:1512.07957 [cond-mat]*, December 2015. arXiv: 1512.07957.

[182] A. Rusydi, A. Goos, S. Binder, A. Eich, K. Botril, P. Abbamonte, X. Yu, M. B. H. Breese, H. Eisaki, Y. Fujimaki, S. Uchida, N. Guerassimova, R. Treusch, J. Feldhaus, R. Reininger, M. V. Klein, and M. Rübhausen. Electronic Screening-Enhanced Hole Pairing in Two-Leg Spin Ladders Studied by High-Resolution Resonant Inelastic X-Ray Scattering at Cu M Edges. *Physical Review Letters*, 113(6), August 2014.

[183] Dell'Angela, M.,, Hieke, F. ,, Malvestuto, M.,, Sturari, L. ,, Bajt, S.,, Kozhevnikov, I. V.,, Ratanapreechachai, J.,, Caretta, A.,, Casarin, B.,, Glerean, F.,, Kalashnikova, A. M.,, Pisarev, R. V.,, Chuang, Y.-D.,, Manzoni, G.,, Cilento, F.,, Mincigrucci, R.,, Simoncig, A.,, Principi, E.,, Masciovecchio, C.,, Raimondi, L.,, Mahne, N.,, Svetina, C.,, Zangrando, M.,, Passuello, R.,, Gaio, G.,, Prica, M.,, Scarcia, M.,, Kourousias, G.,, Borghes, R.,, Giannessi, L.,, Wurth, W.,, and Parmigiani, F. Extreme ultraviolet resonant inelastic X-ray scattering (RIXS) at a seeded free- electron laser. *Scientific reports*, November 2016.

[184] (National Institute of Standards and Technology, Gaithersburg, 2012). NIST X-ray Photoelectron Spectroscopy Database, Version 4.1, 2012.

[185] F. Scholze, J. Tümmler, and G. Ulm. High-accuracy radiometry in the EUV range at the PTB soft x-ray beamline. *Metrologia*, 40(1):S224, 2003.

[186] J. Nordgren, G. Bray, S. Cramm, R. Nyholm, J.-E. Rubensson, and N. Wassdahl. Soft x-ray emission spectroscopy using monochromatized synchrotron radiation (invited). *Review of Scientific Instruments*, 60(7):1690–1696, July 1989.

[187] VG Scienta. SOFT X-RAY EMISSION SPECTROMETER SCIENTA XES 350, July 2006.

[188] Martin Beye. Electronic structure of excited states and electron-phonon coupling: soft X-ray spectroscopy on hot silicon, June 2007.

[189] Elettra Sincrotrone Trieste. EIS-TIMEX setup, November 2016.

[190] I. V. Kozhevnikov, A. E. Yakshin, and F. Bijkerk. Wideband multilayer mirrors with minimal layer thicknesses variation. *Optics Express*, 23(7):9276–9283, April 2015.

[191] E. Allaria, R. Appio, L. Badano, W.A. Barletta, S. Bassanese, S.G. Biedron, A. Borga, E. Busetto, D. Castronovo, P. Cinquegrana, S. Cleva, D. Cocco, M. Cornacchia, P. Craievich, I. Cudin, G. D'Auria, M. Dal Forno, M.B. Danailov, R. De Monte, G. De Ninno, P. Delgiusto, A. Demidovich, S. Di Mitri, B. Diviacco, A. Fabris, R. Fabris, W. Fawley, M. Ferianis, E. Ferrari, S. Ferry, L. Froehlich, P. Furlan, G. Gaio, F. Gelmetti, L. Giannessi, M. Giannini,

R. Gobessi, R. Ivanov, E. Karantzoulis, M. Lonza, A. Lutman, B. Mahieu, M. Milloch, S.V. Milton, M. Musardo, I. Nikolov, S. Noe, F. Parmigiani, G. Penco, M. Petronio, L. Pivetta, M. Predonzani, F. Rossi, L. Rumiz, A. Salom, C. Scafuri, C. Serpico, P. Sigalotti, S. Spampinati, C. Spezzani, M. Svandrlik, C. Svetina, S. Tazzari, M. Trovo, R. Umer, A. Vascotto, M. Veronese, R. Visintini, M. Zaccaria, D. Zangrando, and M. Zangrando. Highly coherent and stable pulses from the FERMI seeded free-electron laser in the extreme ultraviolet. *Nature Photonics*, 6(10):699–704, September 2012.

[192] Enrico Allaria, Bruno Diviacco, Carlo Callegari, Paola Finetti, Benoît Mahieu, Jens Viefhaus, Marco Zangrando, Giovanni De Ninno, Guillaume Lambert, Eugenio Ferrari, Jens Buck, Markus Ilchen, Boris Vodungbo, Nicola Mahne, Cristian Svetina, Carlo Spezzani, Simone Di Mitri, Giuseppe Penco, Mauro Trovó, William M. Fawley, Primoz R. Rebernik, David Gauthier, Cesare Grazioli, Marcello Coreno, Barbara Ressel, Antti Kivimäki, Tommaso Mazza, Leif Glaser, Frank Scholz, Joern Seltmann, Patrick Gessler, Jan Grünert, Alberto De Fanis, Michael Meyer, André Knie, Stefan P. Moeller, Lorenzo Raimondi, Flavio Capotondi, Emanuele Pedersoli, Oksana Plekan, Miltcho B. Danailov, Alexander Demidovich, Ivaylo Nikolov, Alessandro Abrami, Julien Gautier, Jan Lüning, Philippe Zeitoun, and Luca Giannessi. Control of the Polarization of a Vacuum-Ultraviolet, High-Gain, Free-Electron Laser. *Physical Review X*, 4(4), December 2014.

[193] E. Allaria, D. Castronovo, P. Cinquegrana, P. Craievich, M. Dal Forno, M. B. Danailov, G. D'Auria, A. Demidovich, G. De Ninno, S. Di Mitri, B. Diviacco, W. M. Fawley, M. Ferianis, E. Ferrari, L. Froehlich, G. Gaio, D. Gauthier, L. Giannessi, R. Ivanov, B. Mahieu, N. Mahne, I. Nikolov, F. Parmigiani, G. Penco, L. Raimondi, C. Scafuri, C. Serpico, P. Sigalotti, S. Spampinati, C. Spezzani, M. Svandrlik, C. Svetina, M. Trovo, M. Veronese, D. Zangrando, and M. Zangrando. Two-stage seeded soft-X-ray free-electron laser. *Nature Photonics*, 7(11):913–918, October 2013.

[194] W. J. L. Buyers, T. M. Holden, E. C. Svensson, R. A. Cowley, and M. T. Hutchings. Excitations in KCoF3. II. Theoretical. *Journal of Physics C: Solid State Physics*, 4(14):2139, 1971.

[195] T. M. Holden, W. J. L. Buyers, E. C. Svensson, R. A. Cowley, M. T. Hutchings, D. Hukin, and R. W. H. Stevenson. Excitations in KCoF3-I. Experimental. *Journal of Physics C: Solid State Physics*, 4(14):2127, 1971.

[196] Kinshiro Hirakawa, Kazuyoshi Hirakawa, and Takasu Hashimoto. Magnetic Properties of Potassium Iron Group Fluorides KMF3. *Journal of the Physical Society of Japan*, 15(11):2063–2068, November 1960.

[197] H. Onuki, F. Sugawara, Y. Nishihara, M. Hirano, Y. Yamaguchi, A. Ejiri, H. Takahashi, and H. Abe. Absorption spectra of KMF3 (M = Mn, Fe, Co, Ni, Cu, Zn) in the extreme ultraviolet region. *Solid State Communications*, 20(1):35–37, October 1976.

[198] S.L. Wang, W.L. Li, G.F. Wang, D.Y. Dong, J.J. Shi, X.Y. Li, P.G. Li, and W.H. Tang. Crystal structure and electrical transport property of KMF3 (M = Mn, Co, and Ni). *Powder Diffraction*, 28(SUPPL. 1):S3–S6, 2013.

[199] Hayatullah, G. Murtaza, R. Khenata, S. Muhammad, A. H. Reshak, Kin Mun Wong, S. Bin Omran, and Z. A. Alahmed. Structural, chemical bonding, electronic and magnetic properties of KMF3 (M = Mn, Fe, Co, Ni) compounds. *Computational Materials Science*, 85:402–408, April 2014. WOS:000331724000049.

[200] A. Oleaga, A. Salazar, and D. Skrzypek. Critical behaviour of magnetic transitions in KCoF3 and KNiF3 perovskites. *Journal of Alloys and Compounds*, 629:178–183, April 2015.

[201] G. Khaliullin. Orbital order and fluctuations in Mott insulators. *Progress of Theoretical Physics Supplement*, 160:155–202, 2005.

[202] C. Masciovecchio, A. Battistoni, E. Giangrisostomi, F. Bencivenga, E. Principi, R. Mincigrucci, R. Cucini, A. Gessini, F. D'Amico, R. Borghes, M. Prica, V. Chenda, M. Scarcia, G. Gaio, G. Kurdi, A. Demidovich, M. B. Danailov, A. Di Cicco, A. Filipponi, R. Gunnella, K. Hatada, N. Mahne, L. Raimondi, C. Svetina, R. Godnig, A. Abrami, and M. Zangrando. EIS: the scattering beamline at FERMI. *Journal of Synchrotron Radiation*, 22(3):553–564, May 2015.

[203] M. Sanchez del Rio, N. Canestrari, F. Jiang, and F. Cerrina. SHADOW3: a new version of the synchrotron X-ray optics modelling package. *Journal of Synchrotron Radiation*, 18(5):708–716, September 2011.

[204] Miltcho B. Danailov, Filippo Bencivenga, Flavio Capotondi, Francesco Casolari, Paolo Cinquegrana, Alexander Demidovich, Erika Giangrisostomi, Maya P. Kiskinova, Gabor Kurdi, Michele Manfredda, Claudio Masciovecchio, Riccardo Mincigrucci, Ivaylo P. Nikolov, Emanuele Pedersoli, Emiliano Principi, and Paolo Sigalotti. Towards jitter-free pump-probe measurements at seeded free electron laser facilities. *Optics Express*, 22(11):12869–12879, June 2014.

[205] W. F. Schlotter, F. Sorgenfrei, T. Beeck, M. Beye, S. Gieschen, H. Meyer, M. Nagasono, A. Föhlisch, and W. Wurth. Longitudinal coherence measurements of an extreme-ultraviolet free-electron laser. *Optics letters*, 35(3):372–374, 2010.

[206] Surf Tougaard. Practical algorithm for background subtraction. *Surface Science*, 216(3):343–360, 1989.

[207] V. N. Antonov, B. N. Harmon, V. P. Antropov, A. Ya. Perlov, and A. N. Yaresko. Electronic structure and magneto-optical Kerr effect of Fe 3 O 4 and Mg 2 + - or Al 3 + -substituted Fe 3 O 4. *Physical Review B*, 64(13), September 2001.

[208] John M. Dudley, Xun Gu, Lin Xu, Mark Kimmel, Erik Zeek, Patrick O'Shea, Rick Trebino, Stéphane Coen, and Robert S. Windeler. Cross-correlation frequency resolved optical gating analysis of broadband continuum generation in photonic crystal fiber: simulations and experiments. *Optics Express*, 10(21):1215, October 2002.